稿件详细信息 返回

当前状态：排期完成，清样制作中

稿件信息 审稿意见 发票邮寄

稿件编号：ZGYY221010180

稿件信息：临床药师参与抗菌药物相关药物热的诊疗实践 最新稿（208.5KB） 原始稿件 临床试验伦理学批件 自审意见表 基金证明文件

论文授权书：下载授权书 验证方式：在线上传 验证状态：验证通过

单位介绍信：下载介绍信 验证方式：在线上传 验证状态：验证通过

稿件作者：李丹;刘泽清;薛梅;洪玉娇;吴敏江

同意入编数据库：是

稿酬支付方式：转赠期刊

投稿时间：2022-10-12 00:26:33

研究领域：临床药学

费用信息：

审理费：已付款 100.00元 缴费时间：2022-10-12 11:04

出版费：已付款 4820.00元 缴费时间：2023-03-12 11:18

加急费：未付款 0.00元

发票号：未开票 发票号：

提醒：当您付款成功后，此时仍然显示待缴费状态，请等待编辑确认您的付款（通常1-2个工作日内完成确认）。

刊期：《2023年32卷08月16期》 栏目：药事管理 出版日期：2023-08-20

当前阶段信息

稿件状态：清样制作中

起始时间：2023-03-12 11:18:47

截止时间： 2023-03-28 00:00:00

评语及建议：

上一阶段信息

稿件状态： 等待排期，排期完成

时间范围： 2023-03-12 11:18:47 至 2023-03-24 00:00:00

操作时间： 2023-03-13 09:44:49

操作人： 主编1(主编)

评语及建议：

主编1(主编)于2023/3/13 9:44:49将稿件排入《2023年32卷08月16期》。

开票信息

报销人姓名： 刘泽清

报销人单位全称： 惠州市中心人民医院

单位纳税人识别号： 1244 1300 4566 5985 8F

单位地址及电话： (选填)

单位开户行及账号： (选填)

如您的发票需要单位地址、电话、开户行等信息，请在对应处填写。

邮寄信息

收信人： 刘泽清

联系电话（手机）： 15913858800

邮寄地址： 广东省惠州市惠城区鹅岭北路41号

邮政编码： 516001

DOI:10.20037/j.issn.1671-1246.2022.14.26

合作授课模式在临床药物治疗学教学中的效果评价

万　欣[1],刘泽清[2],梁　可[1*]

(1.惠州卫生职业技术学院,广东　惠州　516000;2.惠州市中心人民医院,广东　惠州　516000)

摘　要:临床药物治疗学是一门新兴的实用性学科,为当前药学工作模式由药品模式向患者模式的转变提供有力支持。但在该课程教学中存在课程难度大,学生缺乏学习兴趣;教学方法单一,难以学以致用;实践内容缺乏,与理想有差距等问题。选取惠州卫生职业技术学院110名高职大二年级药学专业学生为研究对象,随机分为实验组和对照组,在临床药物治疗学授课中分别实施专任教师与临床药师合作授课创新模式和传统的专任教师授课模式。通过问卷调查和考试成绩进行教学效果评价发现,专任教师与临床药师合作授课创新模式可以提升学生的自主学习水平,增强学习内容的趣味性和实用性,提升教学效果,值得进一步研究推广。

关键词:临床药物治疗学;合作授课模式;效果评价

中图分类号:G423.04　　**文献标识码:**A　　**文章编号:**1671-1246(2022)14-0067-03

目前,药学工作的重点是新药创制和药学服务,药学服务中心已从原来的以药品为中心阶段过渡至以患者为中心阶段,药学服务工作任务由以药品调配为主,保障患者治疗所需药品转变为保证患者用药合理、安全和有效。药学服务的中心与任务已发生改变,这对传统的药学教育提出了新的要求,医药相关院校对药师的培养模式应适应临床人才的需求[1],同时对临床药物治疗学等强调实践能力的课程要加强重视。临床药物治疗学课程最早由美国的高校在1980年左右开设,21世纪初期在我国本科高校药学专业中开始开设本门课程,近10年高职院校药学专业也陆续开设该课程。目前临床药物治疗学是高职院校药学类专业规定设置的一门专业主干课程,是研究药物预防、治疗疾病的理论和方法的一门课程,集药理学、诊断学、内科学为一体[2]。临床药物治疗学作为基础药学与临床医学的桥梁学科,发挥着非常重要的作用[3]。临床药物治疗学课程涉及范围广、知识点零散、内容枯燥乏味、实践性强,药学专业学生对于基础医学如生理学、病理学等课程掌握不深,在学习与理解临床药物治疗学上存在一定的困难[4]。另外,在临床药物治疗学课程教学中存在许多问题,例如该课程涉及范围广,学生普遍

基金项目:惠州市2019—2020年度职业院校教育科学研究课题(2020hzzjkt31);广东省教育厅高职教育教学改革研究与实践项目(JGZKZ2020143);2019—2021惠州卫生职业技术学院"创新强校工程"教育教学改革类项目建设规划(3.36)

较好地评价专业知识、临床技能,是一种科学的考核方式,值得临床推广。

3　结语

OSCE是一种较科学的考核方式,在国内外得到广泛应用。根据精神科的特点,设计实施了精神科OSCE,突出对精神科临床专业知识、临床技能、临床思维和临床沟通能力的考核和评定,更加客观、准确,同时能够有力促进学生上述能力的培养,对培养综合素质高、实践能力强、适应医改要求的高层次应用型精神医学专门人才很有帮助,值得推广。

参考文献:

[1]HUANG Y,WANG Y,WANG H,et al. Prevalence of mental disorders in China:a cross-sectional epidemiological study [J].Lancet Psychiatry,2019,6(3):211-224.

[2]国务院办公厅.关于转发卫生计生委等部门全国精神卫生工作规划(2015—2020年)的通知[A].国办发[2015]44号.

[3]HARDEN R M,STEVENSON M,DOWNIE W W,et al.Assessment of clinical competence using objective structured examination [J].Br Med J,1975,1(5955):447-451.

[4]PLAKIPTIS C.Objective structured clinical examination(OSCE) in psychiatry education:a review of its role in competency-based assessment[J].Adv Exp Med Biol,2017(988):159-180.

[5]曹玉萍,张亚林,胡晔.客观结构化临床考试在精神病学教学与技能考核中的应用[J].临床心身疾病杂志,2008,14(6):534-535.

[6]杨世昌,张东军,杜爱玲,等.客观结构化临床考试在精神病学临床技能考核中的应用[J].中国高等医学教育,2012(6):91-92.

[7]李晓虹,周方.客观结构化临床考试在北京市精神科住院医师临床技能考核中的应用[J].中国医药导报,2014,11(27):166-169.

[8]何红波,宁玉萍,陈群,等.精神科住院医师结业"5站式"考核评分标准的一致性分析[J].临床精神医学杂志,2017,27(6):385-387.

作者简介:翟金国(1966—),男,硕士,教授,硕士研究生导师。研究方向:临床精神病学。

反映学习难度大；且现在课程教学主要采用传统讲授法，教学方法单一，对于即将步入实习的学生缺乏吸引力，学生学习兴趣不高；课时分配少，实训课基于场地限制，难以同时安排大量学生外出到药店和医院实训，实践内容以案例讨论为主，学生参与度低[5]。20世纪60年代，美国中学之父 William M. Alexander 首次提出“合作教学（Cooperative Teaching）”的概念[6]，其被认为是近几十年间最成功和重要的教学改革方法，自提出后在欧洲和北美国家多个学科中被广泛应用于教学实践[7]。20世纪90年代，我国教育研究者开始引入和介绍合作教学模式[8]，该教学模式在中小学教育改革和英语教育改革中最先开始探索。实践研究表明，合作授课模式在英语教学中成效明显[9]，但其在高职院校临床药物治疗学课程教学中的作用鲜有报道。基于临床药物治疗学课程的重要性以及当前教学中存在的诸多问题，为提升学生的实践技能，帮助药学专业学生完成药学服务中心与工作任务的转化，笔者通过课程改革实践，探索专任教师与临床药师合作授课创新模式在临床药物治疗学教学中的实施方法及效果评价。

1 资料与方法

1.1 研究对象

2020年3月选取惠州卫生职业技术学院2019级药学专业大二年级学生共110名，随机分为实验组（55人）和对照组（55人），实验组采用专任教师与临床药师合作授课创新模式教学，对照组仍采用传统的专任教师授课模式。两组学生的基本情况包括年龄、性别、以往成绩等无显著差异（$P>0.05$）。临床药物治疗学授课时间为大二年级第二学期，此时学生已完成人体解剖学和生理学课程的学习，药理学课程在大二年级分两个学期完成授课，此时已完成药理学大二年级第一学期的授课，还有一半的药理学授课内容与临床药物治疗学均安排在大二年级第二学期。

1.2 教学方法

药学专业学生的临床基础知识较为薄弱，导致临床药物治疗学课程的理解难度增加。同时，大量的药物专业知识和合理用药指导十分枯燥，学生缺乏学习兴趣，鲜少主动学习。当前医药技术迅猛发展，新的药物层出不穷，而《临床药物治疗学》教材收载的药物品种和合理用药指导往往落后于临床实际。面对如此众多的药物，课程教学既要使学生掌握传统的药物治疗原则，又要让他们了解新药在临床应用的情况，以适应临床药物治疗的需要，这为该课程的学习增加了难度。

传统的专任教师授课模式主要采用课堂讲授为主的教学方法。教师以疾病种类为纲，系统讲述疾病的发病机制、临床表现、治疗药物的分类、治疗药物的合理选用及相关临床病例分析等内容。教学方法单一，不易吸引学生注意力，传统教学以教师为主体，较多的知识灌输使得学生接受起来较为缓慢，学生鲜有自主思考的机会，往往只是对药学知识和临床理论死记硬背，难以适应临床实践中面临的各种实际问题，不能学以致用。专任教师与临床药师合作授课创新模式按以下步骤实施教学：（1）与惠州地区排名靠前的“三甲”医院建立紧密持续的合作关系。目前我校已和惠州市中心人民医院、惠州市第一人民医院、惠州市第三人民医院等建立了紧密合作关系，聘请有丰富临床经验与教学心得的临床药师为我院兼职教师。学院对聘请的临床药师进行教学能力和师德师风培训，并指定学院一名本门课程教学时间超过3年的专任教师为临床药物治疗学课程秘书，负责协助临床药师与学生沟通，帮助临床药师了解学生学习情况，安排授课时间和配合临床药师控制授课难度等。（2）系统分析《临床药物治疗学》教材，正式授课前专任教师与临床药师共同探讨实际工作中需要重点掌握的课程内容。以疾病为纲，以合理用药为目的，主要讲解实际工作中接触频繁的、需要重点掌握的疾病相关章节内容，如“特殊人群用药”一章中的“妊娠期和哺乳期妇女用药”，“小儿用药、心血管系统疾病的药物治疗”一章中的“高血压和高血脂用药”，“呼吸系统疾病的药物治疗”一章中的“急性上呼吸道感染用药”，“消化系统疾病的药物治疗”一章中的“消化性溃疡用药”等，减少对工作中较少使用及与实际脱节的知识的讲解。在教学中重在培养学生的学习思维和自主获取知识能力，让学生在课程学习中养成查阅文献、疾病指南和《内科学》教材等的习惯，做到真正的“授人以渔”。（3）发挥专任教师和临床药师各自的优势，强强联合，服务于课程教学。专任教师学历高、理论基础扎实、教学方法和手段较多，同时了解学生情况，对课程深度和难度把握得比较好；临床药师的临床一线工作经验丰富，实践本领强，掌握当前最新的药物动态，有非常多的实践案例可以用于课堂教学。通过合理分配授课内容，由临床药师讲解其擅长的药学领域相关内容，由专任教师统筹该门课程的内容，控制课程难度，保证教学进度及学生系统掌握本门课程的重点知识，形成具有我院特色的学院专任教师与临床药师合作授课模式。（4）学院教师定期去企业实践，积累实践经验，不断提升理论联系实践能力，更好地服务于教学。（5）授课期间，丰富课程的实训内容，安排学生前往医药相关企业参观学习、短期顶岗实习，为学生创设理论与实践相融合的情境，学生可以亲身体验药学服务对自身知识和技能的要求，对标要求，提升实践能力。

1.3 效果评价

采用课程理论考试和问卷调查两种方式进行教学效果评价。课程理论考试直观反映学生课程学习效果，考试范围涵盖课程所有章节，考试题目由选择题（客观题，60分）和案例分析题（主观题，40分）组成。问卷调查采用不记名调查，主要了解学生课前、课中、课后的学习参与情况，学习内容有趣程度，课堂讲授知识是否易懂，学习兴趣是否浓厚，临床思维能力是否提升及对教学模式是否满意。

1.4 统计学方法

统计实验组及对照组相关数据，应用SPSS软件进行统计分析，考试成绩用（$\bar{x}\pm s$）表示，采用 t 检验，$P<0.05$ 为差异有统计学意义。

2 结果

2.1 考试成绩

结果显示，实验组学生选择题、案例分析题成绩和总成绩均明显优于对照组，差异有统计学意义（$P<0.05$），见表1。

2.2 问卷调查

教学结束后对两组学生发放调查问卷，共发放110份，回收有效问卷110份，有效问卷回收率为100%。结果显示，实验

表 1　两组学生考试成绩比较($\bar{x}\pm s$,分)

组别	选择题	案例分析题	总成绩
对照组	46.5±3.7	29.8±1.9	76.3±4.6
实验组	50.2±4.7*	32.4±4.4*	82.6±6.9*

注:与对照组比较,*$P<0.05$

组与对照组相比,实验组课前自主预习、课中积极参与和课后复习巩固的人数较多,且实验组中大多数学生认为学习内容有趣、课堂讲授的理论知识易懂、学习兴趣浓厚、临床思维能力得到提升以及对教学模式满意,见表 2。

表 2　两组学生教学评价反馈比较 [n(%)]

问卷项目	对照组	实验组
课前自主预习	18(32.7)	41(74.5)
课中积极参与	36(65.5)	50(90.9)
课后复习巩固	16(29.1)	38(69.1)
学习内容有趣	28(50.9)	43(78.2)
课堂讲授的理论知识易懂	31(56.4)	46(83.6)
学习兴趣浓厚	25(45.5)	36(65.5)
临床思维能力得到提升	19(34.5)	49(89.1)
对教学模式满意	27(49.1)	45(81.8)

3　讨论

3.1　传统授课模式在临床药物治疗学教学中应用的不足

传统授课模式中,由学院专任教师授课,主要采用讲授式教学方式,以疾病为纲系统讲授疾病的药物治疗策略,可以快速、直接地把当前的经验性知识传授给学生,但长期采用该方式教学容易造成学生缺乏学习兴趣,学习主动性低,不利于学生实践能力的培养和临床思维能力的提升。

3.2　合作授课模式在临床药物治疗学教学中应用的优势

把合作授课模式引入临床药物治疗学教学中,在提高学生成绩、提升学生自主学习水平、增强学习内容的趣味性和实用性、提升学生对教学模式的满意度等方面均获得了良好的效果。(1)提高学生学习参与度和自主学习水平。传统授课模式多为教师课堂讲课,学生养成了被动学习的习惯。即使教师反复强调课前做好预习、课中积极参与、课后及时复习,也难以长期维持学生的学习参与度。采用合作授课模式后,临床药师授课过程中引入大量临床案例,临床案例生动有趣,为更好地理解案例,学生积极进行课前预习、课中参与、课后巩固,学生自主学习水平大幅度提升。(2)增强学习内容的趣味性和实用性,临床思维能力显著提高。临床常见疾病的治疗方法与治疗药物不断发生变化,“临床指南”更新较快,大部分教材使用多年,与实际工作脱节严重,不利于学生临床思维能力的培养。采用合作授课模式后,专任教师与临床药师共同探讨教学中的重点和难点,保留必备的理论知识,把临床一线案例、疾病指南和临床实际工作的思维方法引入课堂,使学习内容的趣味性和实用性显著增强,学生在耳濡目染中养成了自主查阅文献、疾病指南和《内科学》教材的习惯,进而提升了临床思维能力。(3)学生对教学模式的满意度大幅度提升。本研究中,对照组仅 49.1%的学生对当前教学模式感到满意,日复一日的传统教学模式让学生失去新鲜感。而采用合作授课模式的实验组学生对教学模式的满意度为 81.8%,显著高于对照组,这表明合作授课模式被大部分学生接受且喜爱,值得进一步研究推广。

4　结语

医药类高职院校的药学专业开设临床药物治疗学课程,是基于药学专业学生在以往的培养中重点掌握了药物的概念、理化性质、生产工艺和质量检查等知识,但对于走上工作岗位后更多使用到的药物选用和合理用药等内容存在空白,导致学生在刚毕业进入实际临床工作中存在知识脱节、实践能力不足、无法快速适应工作等情况。临床药物治疗学为药学专业学生提供合理用药知识,为其走上工作岗位开展药学服务打下坚实的基础。与药学专业的其他课程不同,临床药物治疗学更强调知识的实践性和实用性,吸引学生的学习兴趣,以其容易理解的方式把复杂烦琐的药物选用和合理用药相关知识呈现给学生,因此对传统以讲授法为主的教学模式进行改革很有必要。笔者将专任教师与临床药师合作授课创新模式引入临床药物治疗学教学中,收到了不错的成效,可操作性强。当前对于专任教师与临床药师合作授课模式在临床药物治疗学教学中的应用还处于起步阶段,不能完全取代传统的教学模式,我们将进一步探索合作授课模式在临床药物治疗学教学中的深度应用,探讨适宜高职药学专业学生情况的合作授课模式最佳组合。同时也继续拓展合作授课模式的广度,在合作授课模式整体框架下丰富课堂授课方式,在“互联网+”时代,将信息化技术引入教学,可引入微课、慕课、微信等线上平台辅助授课,实现混合式教学;在适当的章节采用案例教学法(CBL)、以问题为基础的教学法(PBL)等启发式教学方法,充分调动学生的学习兴趣和参与热情,使课程教学内容符合岗位知识需求,增强临床药物治疗学课程的实用性和针对性。

参考文献:

[1]钱江华,刘浩,魏芳,等.临床药物治疗学在药学专业人才培养中的重要性探讨[J].基础医学教育,2014,16(9):708-710.

[2]李成林,汪建云,吴云明.提高临床药物治疗学教学效果的探讨[J].基础医学教育,2014,16(9):711-713.

[3]杨帆.临床药物治疗学教学方法探讨[J].基础医学教育,2013,15(6):579-580.

[4]沈杰,贾元威,谢海棠.临床药物治疗学教学现状及存在问题分析[J].教育教学论坛,2018(21):84-85.

[5]童文娟,孙少卫.临床药物治疗学课程教学模式探索[J].卫生职业教育,2021,39(17):99-101.

[6]BAUWENS J,HOURCADE J,FRIEND M.Cooperative teaching:a model for general and special education integration[J].Remedial and Special Education,1989,10(2):17-22.

[7]张静,刘巍.合作办学项目中外教师合作教学新模式研究[J].西南农业大学学报,2012,10(9):86-90.

[8]黄佳乐,金鑫.基于学生视角的大学英语中外籍教师合作授课模式探究[J].海外英语,2018(8):73-75.

[9]郭书法,刘佳佳,汪田田,等.高等医学院校医学专业英语合作教学模式研究[J].成都中医药大学学报(教育科学版),2019,21(2):54-57.

作者简介:万欣(1993—),女,硕士,讲师。研究方向:药学研究、药学教育。

*__通信作者:__梁可(1983—),女,硕士,副教授。研究方向:药学研究、药学教育。▲

基于混合式教学模式的教学实践研究
——以高职实用药物学基础课程为例

万　欣，梁　可*
（惠州卫生职业技术学院，广东　惠州　516000）

摘　要：随着信息技术的快速发展，移动终端作为教育教学的辅助工具，为教育教学的发展带来了新的契机，能够统筹线上线下教学优势的混合式教学模式逐渐受到教育者青睐。高职药学专业的实用药物学基础课程主要研究药物的结构及作用、临床应用、不良反应、用药注意事项等，内容繁杂、理论性强，学生学习兴趣不高，学习较枯燥。传统讲授法教学效果不佳，尝试将混合式教学模式引入教学中，构建融合超星学习通、微课、慕课的线上线下课堂教学，提升教学效果。

关键词：混合式教学　翻转课堂　实用药物学基础
中图分类号：G424.1　　文献标识码：A　　文章编号：1671-1246（2020）06-0068-03

伴随智能手机的普及和“互联网+”技术的飞跃发展，混合式教学模式应运而生，为教育教学改革提供了新思路。混合式教学是指网络平台和课堂面授教学相结合的教学模式[1]。它要求将传统学习方式和网络化学习的优势结合起来，把教师的主导作用和学生的主体地位相统一[2]。混合式教学模式是当前高校认可度较高的教学模式[3]，而如何构建一个成功的混合式学习环境，是目前教育工作者关注和探讨的问题。本文以笔者所授课程实用药物学基础为例，探究如何在课堂教学中运用移动教学App、微课等构建混合式学习环境，以提升学生学习兴趣，提高课堂教学质量，旨在加强学生专业知识与技能，提升学生的就业竞争力。

实用药物学基础是将药理学和药物化学两门课程有机整合而成的一门药学专业核心课程，主要包括药物的结构及作用、临床应用、不良反应、用药注意事项等内容[4]。该门课程为药学专业学生毕业后从事药品生产、药品经营、药品管理相关工作提供根本保障和必备知识。然而，实用药物学基础内容多且杂，理论性强，药物种类繁多，需识记信息量大。基于这些特点，学生对该门课程普遍学习兴趣不高，学习主动性不强。又因该课程是一门新课程，教师对该门课程教学还处于探索阶段，目前仍普遍采用传统面对面讲授法进行教学，教学效果不佳[5]。

1　高职药学专业实用药物学基础课程教学现状

实用药物学基础课程的学习对药学毕业生在药学相关岗位工作中药品说明书阅读、药品分类、药品保养与储存、药品合理使用、药品不良反应监测等起到了至关重要的作用[6]，但目前传统教学中仍存在较多问题。

1.1　学生学习主动性不强

基金项目：惠州卫生职业技术学院“创新强校工程”（2016—2020年）建设规划项目（3.1.74）

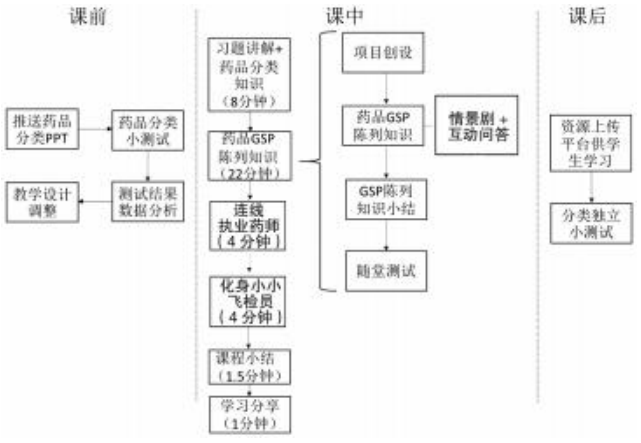

图2　药品GSP陈列教学设计

不再受时间、空间限制。这就要求学生除了正常课堂学习外，还要学会充分利用碎片化时间进行学习，构建属于自己的知识体系[3]。而作为“互联网+”时代的教师应紧跟学生学习模式的转变，不断提高自身信息化教学水平，丰富教学资源，对课程内容进行精心设计。充分利用大数据技术，引入多元化评价体系，并根据学情反馈及时调整教学设计，努力做到因材施教[4]。另外学校也要努力建设“智慧教室”，为智慧课堂教学提供硬件保障，搭设智慧化教学平台。在学校、教师和学生三方共同努力下，通过不断解决智慧课堂教学应用中出现的实际问题，最终探索出适合学生的智慧化课堂教学模式。

参考文献：

[1]刘邦奇. 智慧课堂：“互联网+”时代的课堂变革[N].江苏教育报，2016-09-21.
[2]陈婷.“互联网+教育”背景下智慧课堂教学模式设计与应用研究[D].徐州：江苏师范大学，2017.
[3]何海棠，周华.构建“互联网+”时代学生“碎片化”学习体系的思考[J].赤峰学院学报：自然科学版，2015，31（20）：227-228.
[4]谢礼娴.互联网+时代高职院思政理论课的智慧课堂探析——以蓝墨云班课为例[J].广东水利电力职业技术学院学报，2017，15（3）：52-57.

（*通讯作者：戴胜）

当前实用药物学基础课程多采用传统教学模式，即教师按照教学大纲和教学计划，在规定课时内将知识教授给学生。实用药物学基础课程知识点多，理论性强，理解和识记难度大，学生在学习该门课程中普遍有畏难情绪，学习缺少主动性，学习效率低，识记困难和容易遗忘。

1.2 学生课堂学习容易分神，缺乏师生互动

现在的高职学生生活在网络时代，科技进步、阅读载体的变化和人们求快的心理，带来了碎片化的学习特点。手机电脑已经深入学生学习和生活的方方面面，在课堂中也极易被网络娱乐吸引。学习方式的改变和娱乐诱惑的增加，使学生在课堂上比以往更容易开小差。在中学阶段，学生大多是被动接受知识，处于被动的从属地位，每日机械性听课、做笔记、做练习，逐渐让学生养成了不爱问、不爱答、不爱动的习惯，课堂缺少师生互动，教师不重视学生的学习反馈。

1.3 实践技能不扎实

虽然传统教学中采用了理论教学和实训教学相结合的方式，但由于实训课课时限制，给学生提供的实践动手机会不多，实训教学项目难以深入实际工作的方方面面。实践技能的提升需要不断在实践中积累经验、思考感悟。有限的实训课时及学生对实训课程重要性的忽视导致学生专业技能不扎实，无法满足就业需求。由此可见，实用药物学基础课程教学改革迫在眉睫，应从药学实际岗位工作要求出发，借助多种教学手段联合线上线下教学资源，开展混合式教学，以提高教学效果和促进学生职业成长。

2 基于混合式学习理论的实用药物学基础教学实践

笔者在实用药物学基础课程教学中初步尝试应用混合式教学方法，并研究了教学效果。混合式教学要求将面对面教学与网络教学相结合，以获得最佳学习效果，将线上线下教学相结合以提升教学效果。目前有各种可用于混合式教学的 App，笔者比较后基于操作简便、可满足教学需要及无须付费等优点，选用超星学习通作为主要教学载体。基于超星学习通的混合式教学主要包括以下 3 个阶段。

2.1 课前准备阶段

2.1.1 超星学习通安装及简易介绍 在课程开始前，学生自行在手机或平板电脑等便于携带的移动设备上下载安装超星学习通 App。教师上传超星学习通的操作手册至学生微信群，学生自行熟悉该软件使用方法。教师在超星学习通上建立实用药物学基础课程，在课程中建立与线下班级对应的线上班级，以便开展混合式教学。通过截图方式，将班级二维码发送给对应班级学生，学生通过扫描对应班级二维码进入对应班级，要求学生以实名和学号注册，进入指定班级，便于后期在超星学习通上对学生进行考核。

2.1.2 理论课前准备 课前一周，教师将下一次课程教学资源上传至超星学习通，可以是 PPT、微课、相关动画或时事新闻及案例等，上传内容的学习时间控制在 10 分钟以内。通过这些简短又有趣味性的课前学习内容，可以增加学生对即将授课内容的熟悉程度。教师通过超星学习通可以掌握每个学生的学习时间、学习完成进度，以督促学生养成课前学习习惯，同时可以了解学生学习难点及易错点。学生在超星学习通上反馈课前学习中遇到的难点和困惑，接下来的课堂教学中教师将这些内容作为重点内容进行讲解。

2.1.3 实训课前准备 实训课前，教师将实训课知识点的 PPT 和实训操作相关视频上传超星学习通，要求学生完成实训课前学习。将实训错误操作做成动图，以改错题的方式要求学生找出错误点，加强学生实验规范操作。对因课时限制和场地原因无法安排又与工作密切相关的实训课程，可以与相关企业合作，拍摄实际工作视频，以专题形式上传超星学习通，学生通过观看视频，分小组模拟工作场景等方式提升实操技能。

2.2 课中教学阶段

首先教师让学生在超星学习通上签到，了解学生出勤情况。接下来，可以和学生进行课堂互动，通过使用超星学习通平台组织学生抢答等多种有趣的互动形式，对参与互动的学生给予加分，学期末可直接使用超星学习通计算学生平时成绩，以此促进学生参与课堂互动。课堂互动内容包括对以往学习内容抽查、对即将授课内容的重难点反馈、有趣学习方法的分享以及对学生遇到的重点、难点内容各个击破，对学生普遍理解的知识点适当减少授课内容和时间，对难以理解和容易出错的地方加强讲解。最后，通过随机分组方式，将学生分成 6~8 人一组，以小组形式完成课堂汇报及相关练习，巩固重点、难点，对课堂内容进行总结和升华。在面授中，要用各种方式提高学生课堂参与度，促进学生将知识内化，将手机等移动通信设备充分利用起来，使之为教学所用。

2.3 课后巩固与反馈

课堂教学结束后，超星学习通课程资源库继续对学生开放，并将课堂小组任务也放在对应章节，供学生互相学习，取长补短。不同层次的学生对知识的掌握程度不同，课后的巩固也根据学生情况设置必做任务和选做任务，必做任务适合大部分学生用于巩固提升，选做任务适合学有余力的学生用于深入学习和扩展学习。学生和教师可在课后通过超星学习通继续交流，学生课后发表学习心得和对课程的评价，教师可在线答疑解惑，双方相互促进，提升教学效果。

2.4 教学效果分析

学期末统计学生学习效果，使用混合式教学模式的班级综合成绩优秀的学生占 19%，无成绩不合格学生；而未使用混合式教学模式的同专业同层次班级，综合成绩优秀的学生占 10%，成绩不合格学生占 1.5%。对学生进行教学效果问卷调查发现，采用混合式教学的班级 58%的学生表示课后有通过超星学习通平台自主学习，41%的学生反馈学习有趣味，60%的学生表示课后和教师交流过课程问题；而未采用混合式教学的同专业同层次班级调查显示，仅有 15%的学生课后有自主学习过本课程，25%的学生认为学习有趣味，23%的学生表示课后和教师讨论过课程问题。通过期末学习成绩和问卷调查反馈发现，混合式教学可显著提升学生学习自主性，加深教师对学情的了解，便于师生交流，该教学模式集合线上线下教学优势，提高了药学学生实用药物学基础课程的学习效果。

3 结语

混合式教学模式有效促进了课堂师生互动，为教、学、评等环节带来了便利，较好地调动了学生学习的积极性和主动性，

翻转课堂在高职院校人体解剖学教学中的应用

徐小洁
（江苏省南通卫生高等职业技术学校，江苏 南通 226016）

摘 要 翻转课堂是信息技术高速发展的产物，实现了传统课堂中“知识传授”与“知识内化”两个阶段的颠倒。翻转课堂是以学生为主体、教师为主导的一种新型教学模式，它彻底颠覆了以教师为中心的传统课堂教学模式。对翻转课堂在高职院校人体解剖学教学中的应用进行探究，认为在高职院校人体解剖学教学中合理应用翻转课堂可以提高教学效果，值得推广。

关键词 翻转课堂；人体解剖学；高职院校
中图分类号：G424.1 文献标识码：A 文章编号：1671-1246（2020）06-0070-02

“翻转课堂”一词是2012年由美国科罗拉多州林地公园高中的两名化学教师乔纳森·伯尔曼和亚伦·萨姆斯提出的。他们在2007年将使用屏幕捕捉软件录制PowerPoint演示文稿的视频上传到网上，帮助课堂缺席的学生补习功课，从而开始了翻转课堂的教学实践。但是，翻转课堂在2011年才快速流行起来，这要归功于萨尔曼·罕和他在网上创建的可罕学院。在可罕学院视频教学影片的启发下，许多教师改变了以往的传统教学模式[1]。但翻转课堂在国内外人体解剖学教学中的应用研究很少，在中国高职院校的研究还处于探索阶段，特别是翻转课堂能否显著提高高职院校学生的人体解剖学成绩还存在争议，有待于进一步研究论证。

1 高职院校人体解剖学特点及教学现状

人体解剖学特点：人体解剖学是一门记忆信息量大、枯燥乏味、难懂、实践性强的课程。教学现状：⑴人体解剖学教师资源短缺，学生多、教师少；⑵高职院校的学生大多是初中毕业生，学习动力不足，学习态度不够积极，自律性相对较差，自主学习能力较差，初次踏入医学殿堂，很多学生对尸体充满了恐惧；⑶学校尸源短缺；⑷福尔马林对师生身体健康有损害，降低了人体解剖学教学效率；⑸近年来很多高职院校人体解剖学课时不断压缩，内容多、课时少，课堂时间紧张。

针对目前高职院校人体解剖学特点及教学现状，笔者认为合理应用翻转课堂教学模式可以在某种程度上解决一些教学难题。

2 翻转课堂在高职院校人体解剖学教学中应用的优势、不足与争议

2.1 优势

翻转课堂教学模式可以提高学生的团队合作能力、自主学习能力以及发现问题、思考问题、解决问题能力，可以提高学生学习的积极性以及学习兴趣，增强学生合理安排时间能力，增强学生的评判性思维能力。Raveendranath Veeramani等[2]认为翻转课堂教学模式可以增加师生之间互动的机会，让学生意识到学习是自己的事情，做自己学习的主人。翻转课堂教学中，学生课前学习的教学微视频可选择、可重复、可调控，学生可以根据自己的学习基础、学习时间、学习情况、对知识的理解掌握程度，选择性地进行课前微视频的自主学习[2-3]。教学视频比较精炼，学生在课前自主学习或是师生互动、生生互动都比较有针对性，便于学生针对自身情况查漏补缺，构建知识[4]，这尊重了学生之间的个性化差异，真正做到了因材施教。Sang E等[5]研究发现，大多数学生反映翻转课堂比传统课堂更有趣、互动，合作探究更多，翻转课堂教学模式在课中进行快速小测验可以帮助教师了解学生学习情况，从而在课堂上有针对性地进行讲解。金哨[6]通过研究发现翻转课堂可以培养学生的评判性思维，评判性思维对于将来踏上护理岗位的学生是非常重要的。

翻转课堂教学模式在人体解剖学教学中的应用收到了很好的效果。Todd D Watson[7]调查发现，课前观看人体解剖学教学视频可以缓解学生对尸体的恐惧，被调查学生觉得课前观看教学视频可以增强他们学习人体解剖学的兴趣，更重要的是可以增强他们对尸体解剖的信心。另外，人体解剖学视频可以将2D的解剖断面以3D形式呈现出来，可以更好地理解人体器官的解剖学结构、位置关系等，而且在视频上观看尸体解剖的成本也比较低。课前观看教学视频可以事先让学生掌握解剖操作的基本步骤，使解剖过程有的放矢，从而也降低了解剖实践过程中福尔马林对师生身体健康的损害[8]。

2.2 不足

提升了高职学生的综合职业能力。

参考文献：
[1]李逢庆.混合式教学的理论基础与教学设计[J].现代教育技术，2016，26（9）：18-24.
[2]史冬燕，刘伟.基于超星学习通的植物学混合式教学探究[J].西部素质教育，2019（5）：137-142.
[3]蒋军强，朱晨妍，陆有丽，等.基于移动终端的高交互混合式教学模式初探[J].湖南理工学院学报：自然科学版，2018，31（4）：87-90.
[4]刘芳，罗跃娥，邸丽芝.国家级精品课实用药物学基础课程的设置[J].药学教育，2011，27（2）：24-26.
[5]覃梦岚，刘明研.3种教学方法在药物学基础课程中的应用效果分析[J].卫生职业教育，2019，37（2）：91-92.
[6]姚勇志，江乙，李霏，等.问题设置教学法在药物学基础教学中的应用分析[J].教育观察，2018（16）：119-120.

（*通讯作者 梁可）

十三五”新形态教材
媒体特色教材

临床药物治疗学

CLINICAL PHARMACOTHERAPEUTICS

主　编　支雅军　王　芳　董　俭
副主编　王　硕　闫宇辉

配数字资源
二维码242个

ZHEJIANG UNIVERSITY PRESS
浙江大学出版社

浙江省普通高校“十三五”新形态教材
高等院校数字化融媒体特色教材

临床药物治疗学

主　编　支雅军　王　芳　董　俭
副主编　王　硕　闫宇辉

ZHEJIANG UNIVERSITY PRESS
浙江大学出版社

图书在版编目（CIP）数据

临床药物治疗学 / 支雅军，王芳，董俭主编. —杭州：浙江大学出版社，2021.8
ISBN 978-7-308-21647-0

Ⅰ. ①临… Ⅱ. ①支… ②王… ③董… Ⅲ. ①药物疗法—教材 Ⅳ. ①R453

中国版本图书馆 CIP 数据核字（2021）第 158235 号

临床药物治疗学

主　编　支雅军　王　芳　董　俭
副主编　王　硕　闫宇辉

丛书策划　阮海潮(1020497465@qq.com)
责任编辑　阮海潮
责任校对　王元新
封面设计　周　灵
出版发行　浙江大学出版社
（杭州市天目山路 148 号　邮政编码 310007）
（网址：http://www.zjupress.com）
排　　版　杭州好友排版工作室
印　　刷　绍兴市越生彩印有限公司
开　　本　787mm×1092mm　1/16
印　　张　18.5
字　　数　462 千
版 印 次　2021 年 8 月第 1 版　2021 年 8 月第 1 次印刷
书　　号　ISBN 978-7-308-21647-0
定　　价　65.00 元

《临床药物治疗学》编委会名单

主　编　支雅军　王　芳　董　俭

副主编　王　硕　闫宇辉

编　者　（按姓氏笔画为序）

万　欣（惠州卫生职业技术学院）

王　芳（浙江医药高等专科学校）

王　硕（浙江医药高等专科学校）

王华英（宁波大学附属人民医院）

支雅军（浙江医药高等专科学校）

闫宇辉（江苏食品药品职业技术学院）

李继川（宁波市第一医院）

杨　辉（浙江医药高等专科学校）

吴静怡（浙江医药高等专科学校）

岑丹维（浙江医药高等专科学校）

邹陈君（宁波市康宁医院）

张应忠（宁波市康宁医院）

张聪聪（浙江医药高等专科学校）

邵静萍（浙江医药高等专科学校）

武敏霞（山西药科职业学院）

孟　艳（宁波市医疗中心李惠利医院）

姚晓坤（浙江医药高等专科学校）

袁祖国（宁波大学附属人民医院）

贾　姝(浙江医药高等专科学校)
梅新路(浙江医药高等专科学校)
曹伟娟(浙江医药高等专科学校)
董　俭(宁波市第一医院)
谭学莹(浙江医药高等专科学校)

医药高等职业教育校企双元新形态教材

药学服务综合实务

供药学类、中药学、药品经营与管理专业用

陈育煌　王纯叶　**主编**

中国健康传媒集团
中国医药科技出版社

书网融合教材

医药高等职业教育校企双元新形态教材

药学服务综合实务

（供药学类、中药学、药品经营与管理专业用）

主　编　陈育煌　王纯叶

副主编　安中原　钟小桃　刘燕好　张新忠

编　者　（以姓氏笔画为序）

万　欣（惠州卫生职业技术学院）

王纯叶（惠州市第一妇幼保健院）

申　茹（惠州卫生职业技术学院）

刘燕好（惠州市第一妇幼保健院）

安中原（惠州卫生职业技术学院）

余　巧（惠州卫生职业技术学院）

陈育煌（惠州卫生职业技术学院）

张新忠（惠州卫生职业技术学院）

钟小桃（惠州市第三人民医院）

徐英辉（惠州卫生职业技术学院）

中国健康传媒集团

中国医药科技出版社

内容提要

本教材为“医药高等职业教育校企双元新形态教材”之一，系根据课程标准及岗位任务、结合专业培养目标和本课程的教学目标、内容与任务要求编写而成。全书主要分为理论和实训两篇，理论篇共13章，内容与医院药房及社会药店的工作岗位紧密联系，涵盖药学专业学生所需药学服务的知识与技能，包括认识药学服务、药师在药学服务工作中必备的职业素质、药学信息服务、用药咨询与健康教育、药物相互作用及配伍禁忌、药品不良反应与药源性疾病、特殊人群用药、医院药品调剂的药学服务、社会药店的药学服务、常见疾病的用药指导等内容，贴近药学服务岗位需要，使教学更具针对性。各章除正文外，均配有“案例导入”“知识链接”“知识拓展”“课堂互动”等栏目，以丰富学习内容，强化学生解决问题的能力培养。

本教材主要供全国高职高专院校药学、中药学、药品经营与管理等相关专业教学使用，也可作为临床药师、药学类专业实习生以及其他临床医药工作者学习和培训的参考用书。

图书在版编目（CIP）数据

药学服务综合实务 / 陈育煌，王纯叶主编 . —北京：中国医药科技出版社，2022.12

医药高等职业教育校企双元新形态教材

ISBN 978-7-5214-3639-6

Ⅰ. ①药… Ⅱ. ①陈… ②王… Ⅲ. ①药物学—高等职业教育—教材 Ⅳ. ① R9

中国版本图书馆 CIP 数据核字（2022）第 256821 号

美术编辑 陈君杞

版式设计 南博文化

出版 **中国健康传媒集团** | 中国医药科技出版社

地址 北京市海淀区文慧园北路甲 22 号

邮编 100082

电话 发行：010-62227427 邮购：010-62236938

网址 www. cmstp. com

规格 787 × 1092mm $^{1}/_{16}$

印张 17

字数 352 千字

版次 2022 年 12 月第 1 版

印次 2022 年 12 月第 1 次印刷

印刷 廊坊市海玉印刷有限公司

经销 全国各地新华书店

书号 ISBN 978-7-5214-3639-6

定价 59.00 元

数字化教材编委会

主　编　陈育煌　王纯叶

副主编　安中原　钟小桃　刘燕好　张新忠

编　者　（以姓氏笔画为序）

万　欣（惠州卫生职业技术学院）

王纯叶（惠州市第一妇幼保健院）

申　茹（惠州卫生职业技术学院）

刘燕好（惠州市第一妇幼保健院）

安中原（惠州卫生职业技术学院）

余　巧（惠州卫生职业技术学院）

陈育煌（惠州卫生职业技术学院）

张新忠（惠州卫生职业技术学院）

钟小桃（惠州市第三人民医院）

徐英辉（惠州卫生职业技术学院）

“十四五”普通高等教育规划精品教材
高等医药教材编写委员会专家审定

药事管理与法规

胥彦琪　侯秋苑　唐世锭　主编

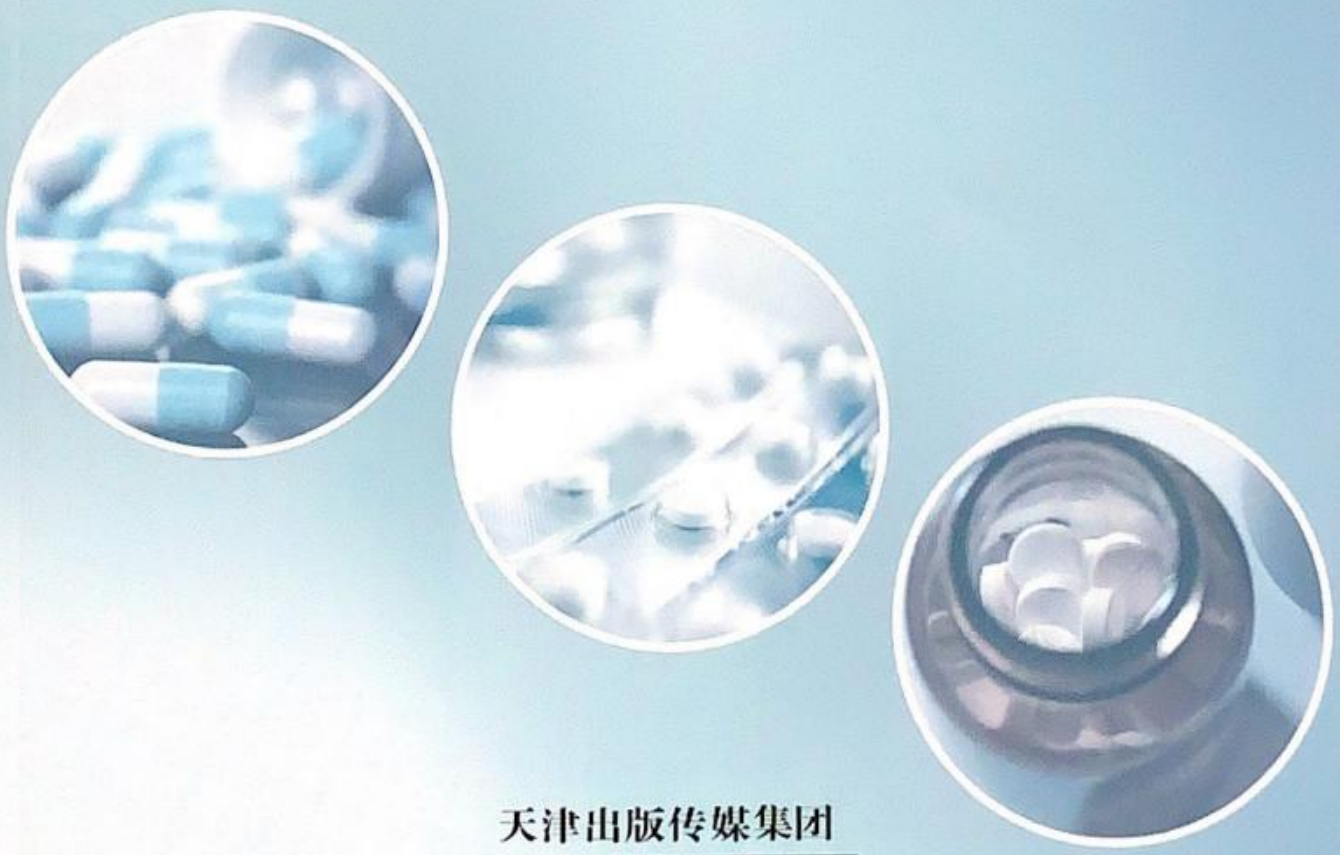

天津出版传媒集团
天津科学技术出版社

“十四五”普通高等教育规划精品教材
高等医药教材编写委员会专家审定

药事管理与法规

胥彦琪　侯秋苑　唐世锭　主编

天津出版传媒集团
天津科学技术出版社

内容提要

本书主要内容包括药事管理与法规概述、药品管理立法、药品监督管理、药学技术人员的管理、药品注册管理、药品生产管理、药品经营管理、医疗机构药事管理、中药管理、特殊管理规定的药品管理、药品信息管理、药品知识产权保护等。

本书可作为医学院校的教学用书，也可作为相关专业人员的参考用书。

图书在版编目（CIP）数据

药事管理与法规 / 胥彦琪，侯秋苑，唐世铿主编
. —天津 ：天津科学技术出版社，2023.6
ISBN 978-7-5742-0944-2

Ⅰ.①药… Ⅱ.①胥… ②侯… ③唐… Ⅲ.①药政管理—职业教育—教材②药事法规—职业教育—教材 Ⅳ.①R95

中国国家版本馆 CIP 数据核字（2023）第 045097 号

药事管理与法规
YAOSHI GUANLI YU FAGUI
责任编辑：孟祥刚
责任印制：赵宇伦
出　版：天津出版传媒集团
　　天津科学技术出版社
地　址：天津市西康路 35 号
邮　编：300051
电　话：（022）23332390
网　址：www.tjkjcbs.com.cn
发　行：新华书店经销
印　刷：三河市恒彩印务有限公司

开本 889×1194　1/16　印张 20　字数 576 000
2023 年 6 月第 1 版第 1 次印刷
定价：69.00 元

PREFACE 前　言

习近平总书记在党的二十大报告中指出：我们要坚持走中国特色社会主义法治道路，建设中国特色社会主义法治体系、建设社会主义法治国家，围绕保障和促进社会公平正义，坚持依法治国、依法执政、依法行政共同推进，坚持法治国家、法治政府、法治社会一体建设，全面推进科学立法、严格执法、公正司法、全民守法，全面推进国家各方面工作法治化。药事管理是保障公民用药安全、有效、经济、合理、方便、及时和生命健康的必要的和有效的手段，对于药品监管，习近平总书记指出：要用“最严谨的标准、最严格的监管、最严厉的处罚、最严肃的问责，确保广大人民群众‘舌尖上的安全’”。

《药事管理与法规》是药学类专业学生的核心必修课程。其主要教学内容包括：药品管理法及药品相关法规；药品管理的体制及机构；药品质量监督管理的基本知识；药品研发、生产、经营、信息管理、价格管理、处方调配、医疗机构药品管理等方面的监督管理要点与方法；特殊药品管理；执业药师管理及药师职业道德与行为准则。通过本门课程的学习，学生能知道药学实践中常用的药事法规和药事活动的基本规律；具备药事管理与法规的基本知识和基本技能；形成自觉执行药事法规的能力；能综合运用药事管理的知识与药事法规的规定，指导药学实践工作，分析解决实际问题。

本教材在编写过程中以反映药事管理的最新进展、提供准确的药事法规信息为总体原则，以2019年8月修订的《中华人民共和国药品管理法》为核心，以保证加强药品管理，保证药品质量，保障公众用药安全和合法权益，保护和促进公众健康为要点，并与执业药师、药学卫生专业技术资格考试内容相衔接。在编写工作中，力求客观、系统的反映国家最新的法规资讯和管理要求，教材内容以国家最新颁布实施的法律、法规、规章及规范性文件为依据，教材中涉及的资料和数据截至2022年12月。力求实现理论知识与实践应用紧密结合，教材中设立了“学习目标”“课堂互动”“知识拓展”等模块，以激发学生学习的积极性、主动性，使学生在掌握理论知识同时，培养学生应用理论分析问题、解决问题的意识和能力。充分挖掘课程思政元素并融合到教材内容中，注重学生职业素质的培养，包括药品质量意识、药品安全意识，严谨务实和精益求精的工作作风与工作态度，高度的责任感、团队合作精神，以及自身可持续发展的学习探索能力。

本教材在编写过程中，得到了各位编委专家的专业支持，在此表示衷心的感谢。同时也向参与本教材审校和提出建议、意见的专家、学者以及编辑表示感谢。

由于教材涉及内容广泛而复杂，虽经编委会反复审校，但教材中仍难免存在不足之处，恳请读者批评指正。

编委会

编委会

主　审　万春艳

主　编　胥彦琪　侯秋苑　唐世锭

副主编　（排名不分先后）

乐志艳　沈静琳　万　欣　孟　佳

刘　珏　朱影影　陈娟娟　李　茜

编　委　（排名不分先后）

万春艳（扬州市职业大学）

胥彦琪（江西医学高等专科学校）

侯秋苑（惠州卫生职业技术学院）

唐世锭（桂林生命与健康职业技术学院）

朱影影（淮南职业技术学院）

程漩格（广东岭南职业技术学院）

乐志艳（江西医学高等专科学校）

万　欣（惠州卫生职业技术学院）

牛学义（鹤壁职业技术学院）

黄建春（广西医科大学）

邓丽芳（桂林生命与健康职业技术学院）

黎德南（桂林生命与健康职业技术学院）

沈静琳（江西医学高等专科学校）

孟　佳（辽宁医药职业学院）

粟　源（桂林生命与健康职业技术学院）

李　茜（云南农业职业技术学院）

滕　云（黑龙江林业职业技术学院）

陈娟娟（湖南环境生物职业技术学院）

张丽红（长春职业技术学院）

刘　珏（华中科技大学附属武汉中心医院）

Redox Biology 56 (2022) 102437

Contents lists available at ScienceDirect

Redox Biology

journal homepage: www.elsevier.com/locate/redox

Phospholipid peroxidation-driven modification of chondrogenic transcription factor mediates alkoxyl radicals-induced impairment of embryonic bone development

Jie Niu [a,b,c,f,1], Xin Wan [a,b,c,g,1], Gui-Yuan Yu [a,b,c,1], Shan Jiang [a,b,c,f,1], Ruo-Nan Yi [a,b,c], Yan-Ping Wu [a,b,c,d,f], Shu-Hua Ouyang [a,b,c,d,f], Lei Liang [a,b,c,d,f], Hiroshi Kurihara [a,b,c,f], Wan-Yang Sun [a,b,c,f], Xiao-Feng Zhu [e], Rong-Hua Zhang [e], Yun-Feng Cao [f,h], Jian-Bo He [a,b,c,d,f,****], Wen-Jun Duan [a,b,c,d,f,***], Yi-Fang Li [a,b,c,f,**], Rong-Rong He [a,b,c,d,f,*]

[a] Guangdong Engineering Research Center of Chinese Medicine & Disease Susceptibility, Jinan University, Guangzhou, 510632, China
[b] International Cooperative Laboratory of Traditional Chinese Medicine Modernization and Innovative Drug Development of Chinese Ministry of Education (MOE), Jinan University, Guangzhou, 510632, China
[c] Guangdong Province Key Laboratory of Pharmacodynamic Constituents of TCM and New Drugs Research, Jinan University, Guangzhou, 510632, China
[d] Integrated Chinese and Western Medicine Department, School of Traditional Chinese Medicine, Jinan University, Guangzhou, 510632, China
[e] Guangdong Provincial Key Laboratory of Traditional Chinese Medicine Informatization, Jinan University, Guangzhou, 510632, China
[f] Joint Laboratory of Dalian Runsheng Kangtai and Jinan University, Jinan University, China
[g] Huizhou Health Sciences Polytechnic, Huizhou, 516025, China
[h] Shanghai Institute for Biomedical and Pharmaceutical Technologies, NHC Key Laboratory of Reproduction Regulation, ShangHai 200032, China

ARTICLE INFO

Keywords:
Lipid peroxidation
Ferroptosis
Alkoxyl radicals
Chondrogenic transcription factor
Embryonic bone development
Chondrogenesis

ABSTRACT

Maternal stress has been associated with poor birth outcomes, including preterm birth, infant mortality, and low birth weight. Bone development disorders in the embryo as a result of maternal stress are believed to be mediated through oxidative stress damage. Various species of free radicals, such as alkoxyl radicals, can be formed through endogenous redox response or exogenous stimuli in the womb and transmitted to embryos. Yet, whether these free radicals lead to abnormal fetal bone development is unclear. Here, we demonstrate prenatal bone growth retardation and ferroptosis-related signals of chondrocytes were induced by classic alkoxyl radical generators. We also show that alkoxyl radicals lead to significant accumulation of oxidized phospholipids in chondrocytes, through the iron-mediated Fenton reaction in embryos. We further demonstrate a role for the lipid peroxidation end product, 4-HNE, which forms adducts with the pivotal chondrogenesis transcription factor SOX9, leading to its degradation, therefore dampening chondrogenesis. Our data define a critical role for phospholipid peroxidation in alkoxyl radicals-evoked abnormal chondrogenesis, and pinpoint it being a precise target for treating oxidative stress-related bone development disorders.

1. Introduction

Prenatal maternal stress is a major concern for fetal and infant health due to its negative consequences in embryonic development [1]. With an estimated birth incidence of 1/10,000 to 1/30,000 [2–4], skeletal dysplasia is a typical developmental disorder and has been implicated in

Abbreviations: 4-HNE, 4-hydroxynonenal; SOX9, SRY-related high-mobility group box 9.

* Corresponding author. Guangdong Engineering Research Center of Chinese Medicine & Disease Susceptibility, Jinan University, Guangzhou, 510632, China.
** Corresponding author. Guangdong Engineering Research Center of Chinese Medicine & Disease Susceptibility, Jinan University, Guangzhou, 510632, China.
*** Corresponding author. Guangdong Engineering Research Center of Chinese Medicine & Disease Susceptibility, Jinan University, Guangzhou, 510632, China.
**** Corresponding author. Guangdong Engineering Research Center of Chinese Medicine & Disease Susceptibility, Jinan University, Guangzhou, 510632, China.
E-mail addresses: hejianbo9@163.com (J.-B. He), duanwj@jnu.edu.cn (W.-J. Duan), liyifang706@jnu.edu.cn (Y.-F. Li), rongronghe@jnu.edu.cn (R.-R. He).
[1] These authors contributed equally.

https://doi.org/10.1016/j.redox.2022.102437
Received 20 July 2022; Accepted 9 August 2022
Available online 20 August 2022

maternal stress [5–9]. By relating with the immature antioxidant system, maternal stress can induce a large amount of free radicals, making the embryos vulnerable to oxidative injury [10,11]. In fact, excessive oxidative injury has been revealed to be an essential pathological factor for maternal stress-provoked bone developmental dysfunction, although the precise mechanisms are enigmatic. Since the discovery of ferroptosis, a type of oxidative cell death, increasing attention has been paid to the pivotal role of phospholipid peroxidation in cell biology and cell pathology [12–14]. The peroxidation of polyunsaturated fatty acids (PUFAs) containing phospholipids (PUFAs-PL) is a free radical-driven chain reaction that can occur in an enzymatic or non-enzymatic manner, comprising of three stages of initiation, propagation, and termination [15,16]. The propagation and amplification of this oxidative reaction largely relies on the accumulation of ferrous iron [17]. The study of ferroptosis opens a new chapter in delineating the pathological mechanisms of oxidative stress-related diseases and greatly contributes to exploiting new targets and therapies [18]. Nevertheless, whether phospholipid peroxidation and ferroptosis are causatively linked to maternal stress-induced bone development defects remain unknown.

During maternal stress, various species of free radicals can be formed through endogenous oxidative stress response and exogenous stimuli, like ionising radiation, ultraviolet radiation, drugs, carcinogenic compounds, and environmental pollutants, among others [19–22]. Of these species, alkoxy radicals play a key role in triggering lipid peroxidation by furnishing PUFA hydroperoxides, which further accelerate the propagation of free radical initiated chain reactions [23]. 2,2′-azobis [2-methylpropionamidine] dihydrochloride (AAPH), a classical generator of alkoxyl radicals, is extensively utilized in oxidative stress-related in *vivo* and in *vitro* studies [24,25], including studies on embryonic development [26–28]. In particular, it is worth noting that AAPH has been shown to initiate the oxidation of PUFAs-PL in cell-free conditions [29,30], whereas the presence of iron further enhances the decomposition of lipid hydroperoxides to a wide variety of secondary oxidation products [29,31]. Based on the above, in the present study, we took advantage of AAPH to obtain insights into the precise mechanism of alkoxyl radicals-induced defective bone development in chicken embryos. Our results unravel the essential role of iron-dependant phospholipid peroxidation in fetal bone development. We further show that these defects are facilitated through 4-hydroxynonenal (4-HNE), which forms adducts with the transcription factor Sry-related high-mobility group box 9 (SOX9), which is pivotal to chondrogenesis. Our findings offer a novel insight on a heretofore undefined role of phospholipid peroxidation and ferroptosis in oxidative stress-related fetal skeletal dysplasia, and provide a potential target for therapeutic intervention.

2. Materials and methods

2.1. Reagents

AAPH was purchased from Wako (Osaka, Japan). Erastin and RSL3 were obtained from Calbiochem (Darmstadt, Germany). Fer-1 and DFO were purchased from Selleck Chemicals (Houston, TX, USA). MTT, Z-vad and Nec-1 were obtained from Sigma-Aldrich (Saint Louis, MO, USA). Primary antibodies against SLC7A11, GPX4, SOX9, Ubiquitin (linkage-specific K48), and 4-HNE were purchased from Abcam (Cambridge, UK). Primary antibodies against DMT1 and TFR1 were obtained from Proteintech Group (Rosemont, IL, USA) and GAPDH antibody was obtained from Fude Co., Ltd. (Hangzhou, China). Goat anti-rabbit IgG-HRP and goat anti-mouse IgG-HRP were purchased from Santa Cruz Biotechnology, Inc. (Dallas,TX, USA). MG132, 3-MA, CHX and 4-HNE were purchased from MedchemExpress (New Jersey, USA).

2.2. Cell culture and chondrogenic differentiation

ATDC5 and SW1353 cells were purchased from RIKEN Cell Bank (Ibaraki, Japan) and cultured in Dulbecco's Modified Eagle Medium (Thermo Fisher Scientific, MA, USA) containing 5% fetal bovine serum (Life Technologies, Carlsbad, CA, USA) at 37 °C in a 5% CO_2 humidified atmosphere.

The medium was replaced with a chondrogenic-induced medium additionally supplemented with 1 × insulin-transferrin-selenium (ITS, Corning, NY, USA) [32,33]. The chondrogenic culture medium was replaced daily. After differentiation for 14 days, ATDC5 cells were washed with phosphate buffer solution (PBS) and fixed with 4% paraformaldehyde solution for 10 min. Subsequently, stained with 1% alcian blue 8GX (Sigma-Aldrich, Saint Louis, MO, USA). Shanghai, China) dissolved in 0.1 M HCl overnight. Cells were washed with PBS twice and photographed.

2.3. MTT assay

MTT cell viability assay was performed as described previously [34]. Briefly, cells were cultured in 96-well plates and exposed to various concentrations of cytotoxic compounds for the indicated time. Next, add 10 μl of the MTT labeling reagent (5 mg/mL) to each well for 4 h. Then, 150 μL of dimethyl sulfoxide was added to each well and shaken gently for 10 min. The absorbance was measured at 570 nm using a SpectraMax M5 microplate reader (Molecular Devices, Sunnyvale, CA).

2.4. The detection of lactate dehydrogenase release

Lactate dehydrogenase (LDH) release assay is a widely accepted method for the quantitative determination of cell viability, which was performed using a cytotoxicity detection kit (Abcam, Cambridge, UK) following the manufacturer's instructions. Absorbance was quantified at 490 nm using a SpectraMax M5 microplate reader (Molecular Devices, Sunnyvale, CA). Cytotoxicity was then calculated according to the following equation: Cytotoxicity (%) = (experimental value–media control)/(positive control–media control) × 100.

2.5. Establishment of oxidative stress model in chicken embryos

(i) *Effect of AAPH on chicken embryos*. Fertilized eggs (South China Agricultural University, Guangzhou, China) were incubated in a humidified incubator (Grumbach, Wentzler, Germany) at 37.5 °C and 68% humidity until they reached the desired developmental stage. Then, a range of dosages of AAPH at 0.25, 0.5, 1.0, 2.0, 4.0, 8.0, and 10.0 μmol/egg or avian saline (control, 0.72% sodium chloride) were injected into the albumen near embryos every other day from embryo development day (EDD) 1.5 to EDD 9.5. The embryos were harvested and their mortality and weight recorded at the desired stages.

(ii) *Effect of ferroptosis induced oxidative stress on bone development.* A range of dosages of RSL3 at 0.1, 1.0, 10.0 nmol/egg were injected into the albumen near embryos every other day from EDD 1.5 to EDD 5.5. The embryos were harvested and assessed for mortality and weight.

(iii) *Effects of ferroptosis inhibitors on chicken embryos.* Chicken embryos were treated with Fer-1 (50 nmol/egg) for 2 h before administering AAPH (0.50 μmol/egg), and the embryos were harvested on EDD17. At the same time, eggs were pre-treated with DFO (200 nmol/egg) for 2 h before AAPH administration (0.50 μmol/egg) and the embryos harvested on EDD7. The embryo weight and tibia length were determined.

2.6. iTRAQ labeling proteomics

The chicken embryo cartilage tissues were ground with liquid nitrogen. Protein quantification was performed using the BCA assay. Approximately 200 μg of each sample were digested with trypsin and tetraethylammonium bromide overnight at 37 °C. The sample was then mixed and identified by two-dimensional LC-MS/MS analysis. The

original MS/MS file data were committed to the ProteinPilot™ Software 5.0.1 for analysis using the Paragon™ algorithm (5.0.1.0, 4874 AB Sciex) against Uniprot chicken database for protein identification. The resulting 5% global fits from FDR corresponding to 95% correct protein identification was used as an initial qualification criterion. For biological replicates or technological replicates, the average fold change induced by treatment relative to the control or AAPH group was defined. Statistically significant variances between AAPH group and control group were determined by the Student's *t*-test (two-tailed or unpaired), and the minimal value among replicates were regarded as the final *p*-value. For protein abundance ratios of AAPH to control measured with iTRAQ, $P < 0.05$ was regarded as the differential protein expression. This research was assisted by the FitGene BioTechnology proteomics platform (http://www.fitgene.com). For bioinformatic analyses, differentially expressed proteins were classified based on annotations from the UniProt knowledge database. Both Gene Ontology (GO) and Kyoto Encyclopedia of Genes and the Genomes (KEGG) pathway enrichment analyses were used to uncover the enriched pathways of significantly altered proteins and to identify their functions.

2.7. Alcian blue and alizarin red staining

To visualize fetal skeleton, chicken embryos were stained with either alcian blue alone or alcian blue and alizarin red dyes as previously described [35]. Briefly, 7-day-old chicken embryos were fixed in 95% ethanol for 24 h. The whole embryos were stained in 0.1% alcian blue (Sigma-Aldrich, Saint Louis, MO, USA) and washed with PBS. The samples were then treated with 1% KOH solution for 36 h, followed by 50%, 75%, and 100% glycerol ordinally until the embryos sank to the bottom.

Similarly, 17-day-old chicken embryos were fixed in 95% ethanol for 24 h, replacing the liquid with fresh 95% ethanol at 12 h. The embryonic skin and hair were peeled. The whole embryos were stained in 0.1% alcian blue for 10 h, treated with 1% KOH solution until transparency is achieved. Lastly, the embryos were stained with saturated alizarin red dye (Solarbio, Beijing, China) solution in 1% KOH for four days. In order to observe the skeleton more clearly, the fat on the surface of chicken embryos was removed. After the above treatment, the whole embryos were photographed. The tibias were photographed using a MVX10 stereomicroscope (Olympus, Allentown, PA, USA) equipped with an OPT-PRO 2007 image acquisition system. The length of the tibia was quantified by IPP 6.0 software.

2.8. Measurement of MDA content, SOD and GPX activities

Malondialdehyde (MDA) content, superoxide dismutase (SOD) and glutathione peroxidase (GPX) activities in the bone tissues on EDD7 or EDD17 were determined using commercially available kits (Nanjing Jiancheng Institute of Biotechnology, Nanjing, China) according to the manufacturer's instructions.

2.9. Determination of GSH and GSSG contents

Levels of reduced glutathione (GSH) and oxidized glutathione (GSSG) were determined by LC-MS using a Dionex Ultimate 3000 HPLC system coupled with a Q-Exactive Hybrid Quadrupole-Orbitrap mass spectrometer (Thermo Fisher Scientific, MA, USA). The cartilage tissues were removed from the embryonic tibia, washed with pre-cooled PBS, and quickly ground with liquid nitrogen. The powders were mixed with 1 mL of extract solution (80% methanol water plus 2 μl of 50 μg/mL glutamate-d5 (Glu-d5)), filtered using a 0.22 μm filter membrane and stored at −20 °C. For in *vitro* samples, cells were collected and resuspended in PBS with 1 mL of extract solution, vortexed for 5 min, then sonicated (5 Hz) for 30 s and centrifuged at 4 °C for 25 min at 14,000 rpm.

The LC/MS conditions are as follows: Waters ACQUITY UPLC BEH Amide column (2.1 mm × 100 mm, 17 μm) with acetonitrile. Solvent A was water containing 5 mM ammonium formate and 0.1% formic acid; solvent B was acetonitrile. The flow rate was 300 μL/min, and the column temperature was 40 °C. The GSH and GSSG content in the samples were calculated using a standard curve, and the ratio of GSH/GSSG in each group was then analyzed.

2.10. Hematoxylin and eosin staining (H&E staining)

Chicken embryos were harvested on EDD7 and EDD17, tibias were separated from the embryos and fixed in 4% paraformaldehyde for 24 h, decalcified completely in 4% methanol for 2 weeks, rinsed under running water for 12 h and embedded using paraffin wax. The embedded tibias were sliced at 4 μm thickness and the vertical sections were stained using H&E. The paraffin sections were photographed using a M8 Digital Microscope and Scanner (PreciPoint GmbH, Freising, Germany).

2.11. Western blot analysis

Cells or bone tissues were collected and lysed in lysis buffer containing proteinase inhibitor (Beyotime Institute of Biotechnology, Shanghai, China) for 30 min on ice. Protein concentrations were measured by the BCA assay kit (Beyotime Institute of Biotechnology, Shanghai, China). Proteins were separated by 10% SDS-PAGE and transferred to nitrocellulose membranes (Amersham Biosciences, Piscataway, NJ, USA). After blocking with 5% dried skimmed milk, the membranes were incubated with indicated primary antibodies at 4 °C overnight. The membranes were then incubated with the appropriate HRP-linked secondary antibody for 2 h at room temperature. Enhanced chemiluminescence (ECL) detection kit (Multi Sciences Biotech Co., Ltd, Beijing, China) was used for visualization of the bands. Band density was quantified using Quantity One Analysis Software (Bio-Rad, Hercules, CA, USA).

2.12. Reverse transcription polymerase chain reaction (RT-PCR) assay

Total RNA was extracted from tissue and cells using Trizol kit (Takara, Kyoto, Japan) according to the manufacturer's instructions. Following reverse transcription, cDNA amplification was performed as previously described [36]. For RT-PCR assay, PCR products were separated on 1% agarose gels (Invitrogen, Carlsbad, CA, USA) and visualized by ethidium bromide staining. The band intensity of ethidium bromide was measured by GelDoc XR system (Bio-Rad Corporation, Hercules, CA, USA) and then quantified with the Quantity one analysis software.

Quantitative real-time polymerase chain reaction assay (qRT-PCR) was performed using SYBR Premix ExTaq II (Promega, Madison,USA) on an ABI 7900 sequence detection system (Thermo Fisher Scientific, MA, USA). Relative mRNA expression was calculated using the $2^{-\Delta\Delta Ct}$ method. *β*-actin was used as an internal control. PCR primers are shown in Supplementary Table 1.

2.13. PI staining and flow cytometry analysis

Cells were seeded in 6-well culture plates. On the day of the experiment, cells were harvested, incubated with propidium iodide (PI, Sigma-Aldrich, Saint Louis, MO, USA) for 20 min, washed three times with PBS and re-suspended in 1 mL PBS. Stained cells were quantified by flow cytometry (BD Biosciences, NJ, USA).

2.14. Measurement of ROS using DCFH-DA

Dichlorofluorescin-diacetate (DCFH-DA) staining is used to measure the total ROS level in cells treated with or without AAPH. After incubation with AAPH, cells were stained with 50 μM DCFH-DA (Sigma-Aldrich, Saint Louis, MO, USA) for 30 min in the dark. Then, cells were

resuspended in PBS and assayed by flow cytometry (BD Biosciences, NJ, USA).

2.15. Measurement of lipid peroxidation using C11-BODIPY 581/591

C11-BODIPY 581/591 staining is used to measure the lipid ROS level in cells treated with or without AAPH. Briefly, cells were seeded in 6-well plates and treated with AAPH for the indicated times. Then, cells were collected and stained with 2 μM C11-BODIPY581/591 (Thermo Fisher Scientific, MA, USA) for 30 min at 37 °C in the dark. Subsequently, cells were collected and measured by flow cytometry (BD Biosciences, NJ, USA). The fluorescence intensity of each group was recorded and the data quantified using Flowjo software.

2.16. Measurement of H_2O_2 using Amplex Red assay

The hydrogen peroxide (H_2O_2) concentration of extracellular medium was measured by the Amplex Red reagent (Thermo Fisher Scientific, MA, USA). The applied substrate (Amplex Red) reacts with H_2O_2 in a horseradish peroxidase catalyzed reaction, producing highly fluorescent resorufin. Fluorescence was measured by a fluorescence plate reader (excitation 535 nm, emission 595 nm).

2.17. Determination of thiol levels

Thiol levels were determined by the total sulfhydryl group assay kit (Solarbio, Beijing, China). The principle is that the reduced sulfhydryl groups react with 5,5′-dithiobis-2-nitrobenzoic acid to produce yellow 2-nitro-5-mercaptobenzoic acid [37]. The product then has a characteristic absorption peak at 412 nm and the amount of free thiol is calculated according to the formula given in the total sulfhydryl group assay kit.

2.18. Fe^{2+} detection by FerroOrange staining

SW1353 cells were seeded in six-well plates or confocal dishes at a density of 1×10^5 cells/mL. Cells were then incubated with the Fe^{2+} binding fluorescent probe FerroOrange (1 μM, Ex: 543 nm, Em: 580 nm) (Dojindo, Japan) for 30 min at 37 °C under 5% CO_2 atmosphere. The culture medium was removed and the cells washed three times with PBS before flow cytometry or observation under a laser scanning confocal microscope (LSM, Zeiss, Germany).

2.19. Measurement of iron levels

Iron levels were measured by an iron assay kit (Abcam, Cambridge, UK) according to the manufacturer's instructions. Cells were collected, homogenized in 10× volume of iron assay buffer on ice and centrifuged (14,000×*g*, 10 min) at 4 °C. The supernatant was collected and 5 μl iron reducer was added to each sample and incubated at 37 °C for 30 min. Next, add 100 μl iron probe and incubate for 60 min at 37 °C protected from light. Absorbance was analyzed at 593 nm using a microplate reader (Thermo Fisher Scientific, MA, USA).

2.20. Co-immunoprecipitation (CO-IP) assay

SW1353 cells were seeded into a 10 cm dish and processed as indicated. Cells were lysed in RIPA lysis buffer (Beyotime Institute of Biotechnology, Shanghai, China) containing 1 mM PMSF (Beyotime Institute of Biotechnology, Shanghai, China) and protease inhibitor (Abcam, Cambridge, UK) on ice for 30 min. After centrifugation at 12,000×*g* for 10 min, the supernatant was incubated with indicated primary antibodies overnight. Next, protein A/G beads (Santa Cruz Biotechnology, Dallas,TX, USA) were added to the lysates and the incubation continued on a rotating table for 3-4 h. The beads were washed five times with RIPA lysis buffer, centrifuged at 2500 rpm for 1 min, and loading buffer was added to each sample. Finally, beads were boiled for 5 min at 95 °C.

2.21. Preparation of phospholipids and LC-MS/MS-based phospholipidomics analysis

Preparation and analysis of phospholipids in the chondrocytes were performed as previously described [18]. Dionex UltiMate 3000 DGLC standard system (Thermo Fisher Scientific, MA, USA) was employed to separate phospholipids with an HPLC column (C30 reverse phase column; 2.1 mm × 25 cm, 2.6 μm,Thermo Fisher Scientific, MA, USA). Solvent A was isopropanol: hexane: water (57:43:1); solvent B was isopropanol: hexane: water (57:43:8) containing 10 mM ammonium formate as mobile-phase modifiers. The gradient was as follows: 0-20 min, 10-32% solvent B; 20-30 min, 32-70% solvent B; 30-32 min, 70-100% solvent B; 32-58 min, hold at 100% solvent B; 58-60 min, 100-10% solvent B; 60-75 min, hold at 10% solvent B for equilibration. The flow rate was 200 μL/min, and the column temperature was 40 °C.

Phospholipids were detected on a Q Exactive mass spectrometer (Thermo Fisher Scientific, MA, USA), and then analyzed by Compound Discoverer 2.0 (Thermo Fisher Scientific, MA, USA) with an in-house generated analysis workflow. The species of phospholipid were identified and filtered by retention time.

2.22. Confocal microscopy

Cells were fixed with 4% paraformaldehyde for 10 min at room temperature. After washing with PBS, cells were permeabilized with 0.1% Triton-X for 10 min, blocked with 0.5% BSA for 1 h and incubated with the anti-SOX9 (1:200) and anti-4HNE (1:200) primary antibodies overnight at 4 °C. Cells were washed again and incubated with Alexa-Flour 555 and 488 secondary antibodies (1:400) at room temperature for 1 h. DAPI nuclear staining was done at room temperature for 10 min. The samples were examined using a confocal laser scanning microscope (LSM 880 with AiryScan, Carl Zeiss).

2.23. CHX-chase analysis

SOX9 protein degradation was assayed by CHX-chase analysis. SW1353 cells were pre-incubated with or without 4-HNE. Subsequently, 100 μM CHX was added to inhibit protein synthesis. Cells were collected at 0, 1, 2, 4, 6, and 8 h after CHX treatment as previously described.

2.24. Statistical analysis

All data were analyzed and processed using GraphPad Prism 8.3 software. The data were expressed as mean ± SD. The statistical significance of multiple groups was evaluated using one-way analysis of variance (ANOVA) followed by Dunnett's multiple comparison test. The difference between the two groups was tested by the Student's *t*-test. Non-linear regression was used to estimate the IC_{50} value. $P < 0.05$ was considered to be statistically significant.

3. Results

3.1. Alkoxyl radicals exposure retard embryonic skeleton development

We established a chronic oxidative stress model in chicken embryos by injecting AAPH, a generator of alkoxyl radicals, into the albumen on embryo development day (EDD) 1.5. This treatment was given to embryos every other day for a total of five times (Fig. 1A). On EDD17, a dramatic elevation of mortality was observed in AAPH treated embryos (Fig. 1B), which corresponded with a decrease in embryo weight (Fig. 1C) and retardation in the growth of embryonic limbs (Fig. 1D). To determine whether limb deformity has already occurred during endochondral bone formation, cartilage from EDD7 embryos was stained.

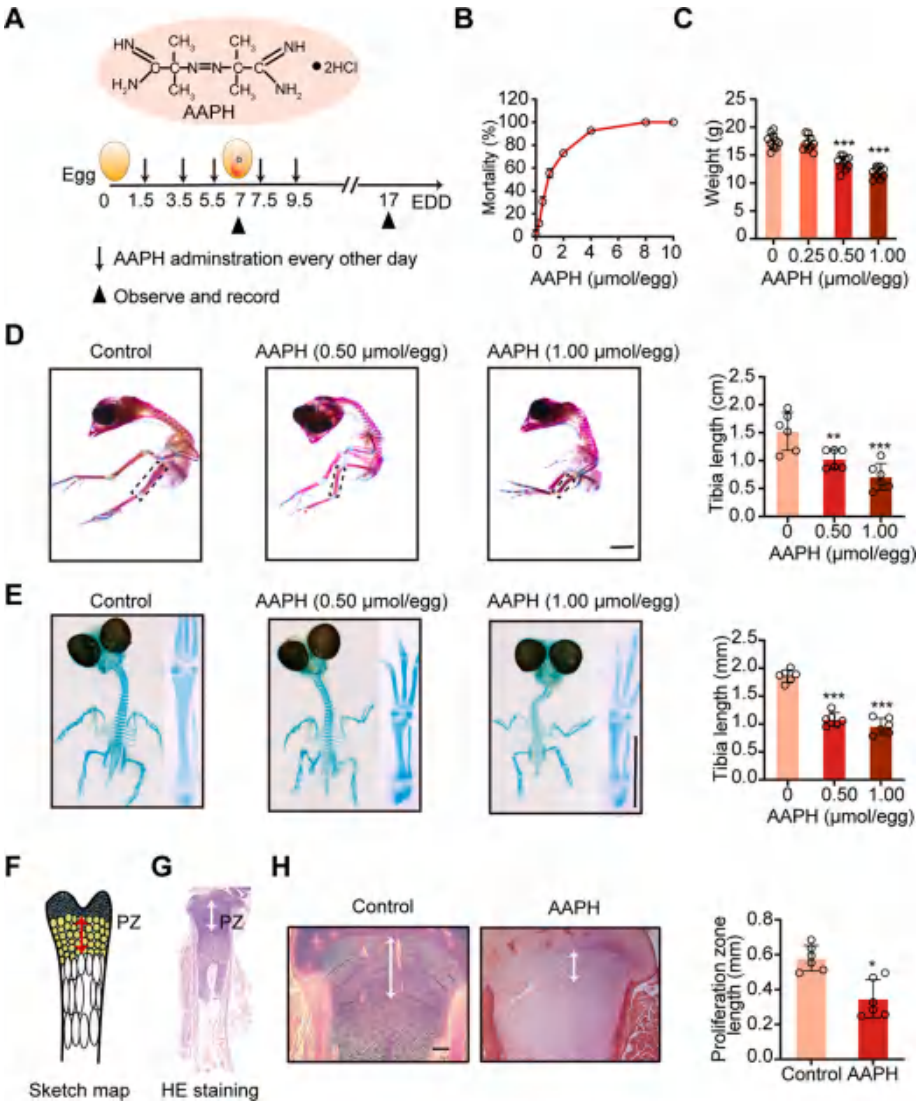

Fig. 1. Alkoxyl radicals exposure restrict embryonic limb growth. (A) Schematic diagram establishing a chronic oxidative injury model in chicken embryos by injecting alkoxyl radicals generator AAPH into the albumen of eggs. The first day of incubation is considered as the initiation day of embryonic development and is termed as embryo development day (EDD). (B) The mortality and (C) body weight of chicken embryos were measured on EDD17. (D) Representative images of alcian blue and alizarin red-stained tibia and the quantification of tibia length of EDD17 embryos. Scale bar, 1 cm. (E) Representative images of the alcian blue-stained tibia and the quantification of tibia length of EDD7 embryos. The whole embryos and tibias were photographed. Scale bar, 1 mm. (F) The schematic diagram of the growth plate subregions. PZ indicates proliferative zone. (G) H&E staining of tibial growth plate. (H) H&E staining of the tibial PZ mapping the white double-head arrows on EDD17. Scale bar, 200 μm. Quantification of tibial proliferation zone is shown in the right panel. AAPH, 0.50 μmol/egg. Data are represented as mean ± SD. Comparisons between groups were made using one-way ANOVA (C–E) and Student's *t*-test (H). $^{*}P < 0.05$, $^{**}P < 0.01$, $^{***}P < 0.001$ vs the Control group. (For interpretation of the references to colour in this figure legend, the reader is referred to the Web version of this article.)

Consistent with the results at EDD17, embryos at EDD7 also presented shorter limbs in the AAPH treatment group (Fig. 1E).

Endochondral ossification is a critical step for initial limb development in the fetus. The growth plate, which plays an important role in endochondral bone formation [38], can be divided into stagnant zone, proliferation zone (PZ), hypertrophic zone and calcified zone (Fig. 1F). H&E staining performed on paraffin sections of the tibial growth plates (Fig. 1G) showed that the structure of PZ was destroyed and the length of PZ shortened in the AAPH treatment group (Fig. 1H). Collectively, the above results illustrate that alkoxyl radicals-induced oxidative stress induces abnormal chondrogenic development, thereby impeding embryonic bone growth.

3.2. *Ferroptosis is implicated in alkoxyl radicals-induced chondrogenic development defects*

To identify the molecular mechanism involved in oxidative stress-induced aberrant chondrogenesis, iTRAQ-labeling proteomics analysis was performed in cartilaginous tissues from control and AAPH-treated chicken embryos (Fig. 2A). In total, 1534 credible proteins were identified (with confidence≥95%), of which 449 proteins were found to be significantly regulated in the AAPH group versus the control group. Of these, sixteen proteins were upregulated and two proteins were downregulated (Fig. 2B). Furthermore, gene set enrichment analysis (GSEA) revealed that the differentially expressed genes were enriched in iron-ion-binding pathways (Fig. 2C). KEGG analysis indicated that the assembled signaling included metabolic pathways, ferroptosis pathways, arachidonic acid metabolism, regulation of actin cytoskeleton, etc. (Fig. 2D and E). The key differentially expressed proteins involved in ferroptosis (Fig. 2F) were further confirmed by western blot analysis of the bone tissues of these embryos. Results showed that embryos exposed to AAPH had elevated expression of DMT1 and TFR1 and dramatically reduced levels of GPX4 and SLC7A11 (Fig. 2G). Additionally, AAPH treatment was also seen to boost the production of MDA, and the depletion of GSH (Fig. 2H and I), and remarkably reduce GPX and SOD activities (Fig. 2J and K) in the bone tissues. Furthermore, ferroptosis inducer RSL3 was administrated to chicken embryos and results showed that RSL3 at doses between 1.0 and 10.0 nmol/egg notably increased embryo mortality (Figure 2L) and decreased embryo weight (Figure 2M). Alcian blue staining demonstrated that RSL3 treatment remarkably hindered the growth of embryonic limbs (Figure 2N). These data offered proof underscoring the essential role of ferroptosis in oxidative stress-induced bone development disorder.

In line with chicken embryos, AAPH at a dose of 1.00 mM, which showed little impact on cell viability (Fig. 3A), remarkably repressed ITS-induced chondrogenesis in ATDC5 cells (Fig. 3B). A similar trend was also observed in the treatment of the ferroptosis inducer Erastin (Fig. 3C). Both AAPH and Erastin-caused mortality of ATDC5 cells was

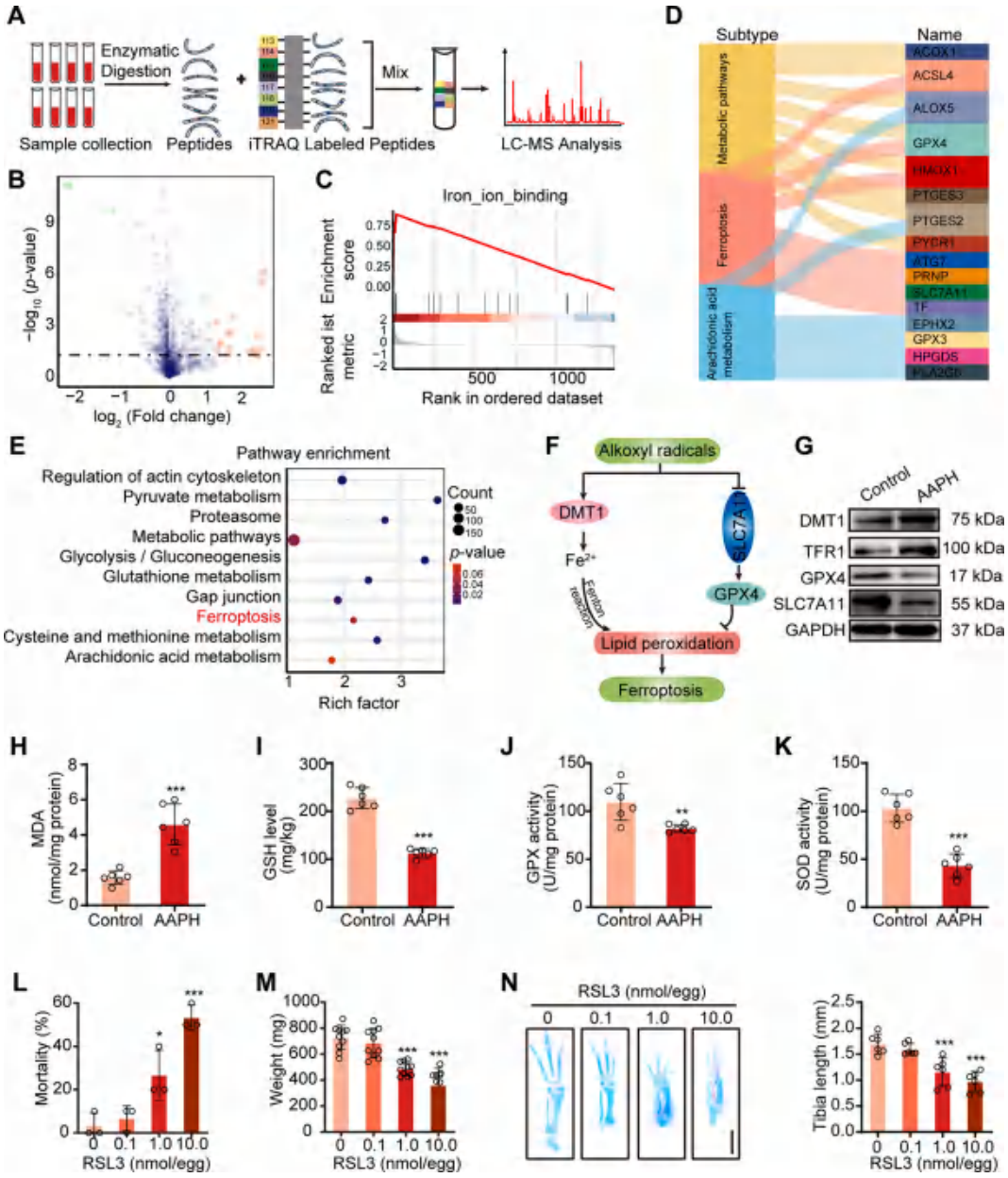

Fig. 2. Ferroptosis is involved in alkoxyl radicals-induced bone development dysfunction. (A) Schematic diagram of iTRAQ labeling proteomic approach. (B) Volcano plot showing differentially expressed proteins in chicken embryo between the control group and AAPH group. Low expression is depicted in green, while high expression is depicted in red. AAPH, 0.50 μmol/egg. (C) Enrichment score of the iron-ion-binding pathway analyzed by GSEA based on the iTRAQ labeling proteomic datasets. (D) Sankey diagram showing the classifications of proteins based on Kyoto Encyclopedia of Genes and Genomes (KEGG) database. (E) KEGG pathway enrichment analyses. The y-axis represents the main pathways. (F) Cartoon depicting the mechanism of alkoxyl radicals-induced ferroptosis. (G) Immunoblotting analysis was performed to detect the expression of ferroptosis-related proteins. AAPH, 0.50 μmol/egg. (H–K) Effects of AAPH on the contents of MDA (H) and GSH (I), and the activities of GPX (J) and SOD (K) were measured on EDD17. AAPH, 0.50 μmol/egg. (L) The mortality and (M) body weight of chicken embryos were measured after treated with various concentrations of RSL3 on EDD7, respectively. (N) Representative images of alcian blue-stained tibia of RSL3-treated embryos. Scale bar, 1 mm. Histograms represent the quantification of tibia length of EDD7 embryos. Data are represented as mean ± SD. Comparisons between groups were made using one-way ANOVA (L–N) and Student's *t*-test (H–K).*$P < 0.05$, **$P < 0.01$, ***$P < 0.001$ vs the Control group. (For interpretation of the references to colour in this figure legend, the reader is referred to the Web version of this article.)

reversed by ferroptosis inhibitors, but not by the apoptosis inhibitor Z-VAD-FMK, and the necroptosis inhibitor Nec-1 partially protects against cell mortality caused by AAPH (Fig. 3D and E). In SW1353 cells, AAPH and RSL3 caused the release of LDH (Fig. 3F and G), and inhibited cell viability in a dose-dependent manner (Fig. 3H and I), while Fer-1 and DFO attenuated cell death (Fig. 3J). A time-dependent analysis by DCFH-DA, C11-BODIPY and Amplex Red staining, respectively, indicated that the levels of total ROS, lipid ROS and H_2O_2 were increasingly elevated in chondrogenic SW1353 cells upon AAPH treatment (Figs. S1A–S1C). Moreover, AAPH significantly reduced the content of sulfhydryl groups (Fig. S1D), and diminished the GSH/GSSG ratio (Figs. S1E and S1F). Altogether, these results illustrate that alkoxyl radicals impede the osteogenesis process to prohibit embryonic limb bone growth.

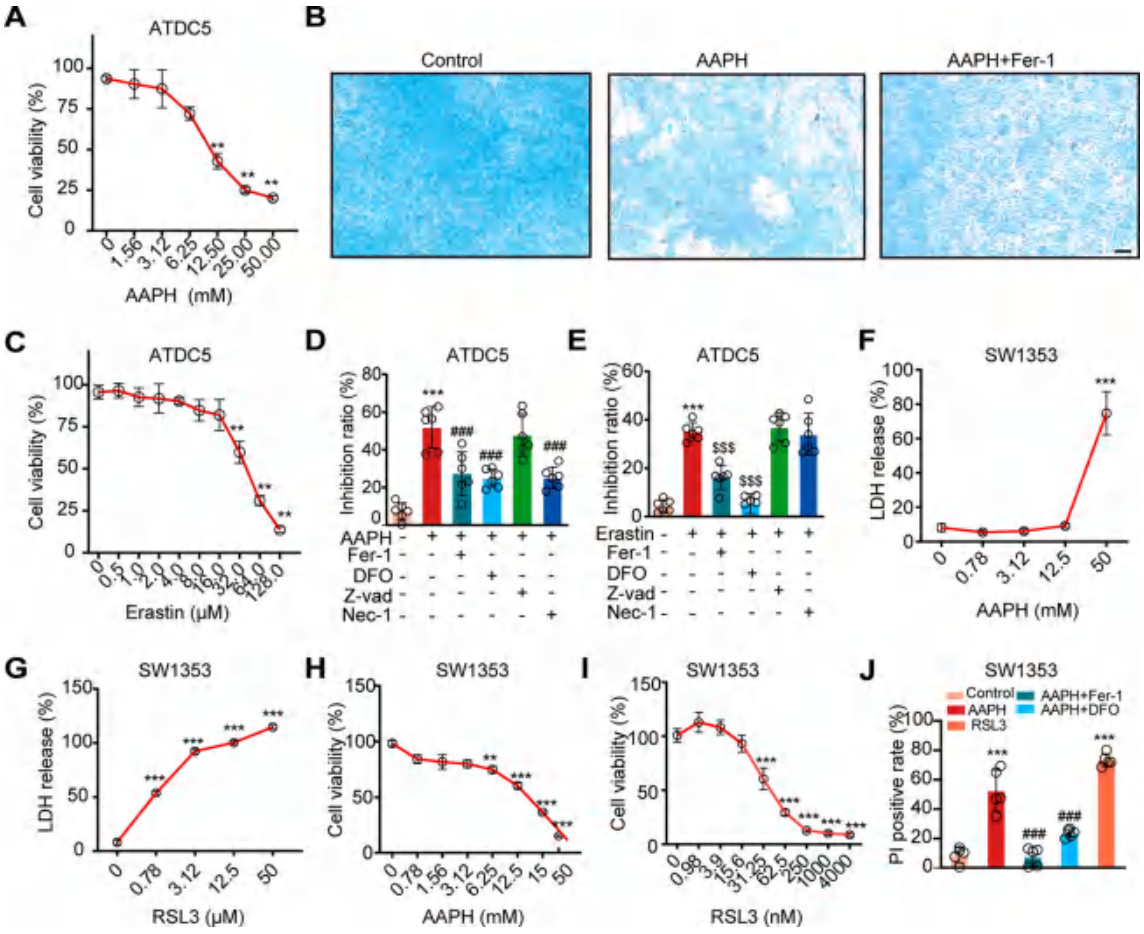

Fig. 3. Alkoxyl radicals induce ferroptosis in ATDC5 and SW1353 chondrocytes. (A) ATDC5 cells were incubated with various concentrations of AAPH for 24 h. Cell viability was determined by MTT assay. (B) The representative images of ATDC5 cells stained by alcian blue. Scale bar, 50 μm. AAPH, 1.00 mM; Fer-1, 4.00 μM. (C) ATDC5 cells were incubated with various concentrations of Erastin for 24 h. Cell viability was determined by MTT assay. (D–E) ATDC5 cells were treated with AAPH, Erastin (a ferroptosis inducer), Fer-1 and DFO (ferroptosis inhibitors), Z-vad (an apoptosis inhibitor), and Nec-1 (a necroptosis inhibitor), then cell viability were measured by MTT. AAPH, 12.50 mM; Erastin, 32.00 μM; Fer-1, 4.00 μM; DFO, 8.00 μM; Z-vad, 25.00 μM; Nec-1, 25.00 μM. (F–G) SW1353 cells were treated with different concentrations of AAPH and RSL3 for 24 h, and cytotoxicity were evaluated by LDH assay. (H–I) Cell viability of AAPH and RSL3 in SW1353 cells were determined by MTT assay. (J) Cell death was determined by PI staining coupled with flow cytometry in SW1353 cells. AAPH, 20 mM; RSL3, 60 nM; DFO, 200 μM; Fer-1, 5 μM. Data are represented as mean ± SD. Comparisons between groups were made using one-way ANOVA. $^{**}P < 0.01$, $^{***}P < 0.001$ vs the Control group. $^{\#\#\#}P < 0.001$ vs the AAPH-treated group; $^{\$\$\$}P < 0.001$ vs the Erastin-treated group. (For interpretation of the references to colour in this figure legend, the reader is referred to the Web version of this article.)

3.3. Ferroptosis inhibitors rescue alkoxyl radicals-induced chondrogenic developmental defects

To affirm the role of ferroptosis in abnormal bone development, Fer-1 and DFO, two classic ferroptosis inhibitors, were used *in vivo*. As expected, Fer-1 significantly rescued AAPH-induced mortality (Fig. 4A) and weight loss of chicken embryos on EDD17 (Fig. 4B). AAPH-impeded growth of the tibia was also attenuated by Fer-1 (Fig. 4C and D). H&E staining showed that Fer-1 treatment notably rescued the shrinkage of tibial PZ in the developing bones (Fig. 4E and F). A similar trend was also observed in chicken embryos treated with the ferroptosis inhibitor DFO. In line with EDD17, EDD7 embryos also showed increased mortality and weight loss after AAPH exposure, which were significantly rescued by DFO (Fig. 4G and H). Moreover, DFO treatment also significantly alleviated the shortening of the tibia caused by AAPH (Fig. 4I and J).

Next, the effect of ferroptosis inhibition on alkoxyl radicals-initiated redox imbalance was examined in chicken embryos. The studies revealed that Fer-1 and DFO dramatically abrogated AAPH-caused accumulation of MDA (Figs. S2A and S3A), depletion of GSH (Figs. S2B and S3B), attenuation of GPX (Figs. S2C and S3C) and SOD activities (Figs. S2D and S3D). Consistent with the results described above, Fer-1 and DFO restored expressions of DMT1, TFR1, GPX4 and SLC7A11 disturbed by AAPH exposure (Figs. S2E–2H, Figs. S3E and S3F). A similar expression pattern of ferroptosis-related proteins, including DMT1, TFR1, SLC7A11 and GPX4, was also seen in AAPH-exposed ATDC5 cells and SW1353 cells (Figs. S2I and S3G), which were arrested by ferroptosis inhibitors (Figs. S2I and S2J, Figs. S3G and S3H). Overall, these data support a concept linking ferroptosis to alkoxyl radicals-induced bone developmental disorders.

3.4. Exposure to alkoxyl radicals trigger iron overload in chondrocytes

Iron is required for Fenton reaction-propagating phospholipid peroxidation [39]. DMT1 and TFR1 are two major iron transporters that contribute to iron metabolism in cells [40–42]. The expression patterns of DMT1 and TFR1 observed from the ITAQ assay (Fig. 2A) and western blot analysis (Fig. 2G) implied the involvement of iron in alkoxyl radicals-disturbed chondrogenesis. Therefore, we examined changes of intracellular iron by flow cytometry and iron assay kit in chondrogenic cells. High Fe^{2+} levels were observed in AAPH/RSL3-treated cells, which were abolished by Fer-1 and DFO administration (Fig. 5A-C).To further understand the role of iron in chondrogenesis, siRNA based reduction in

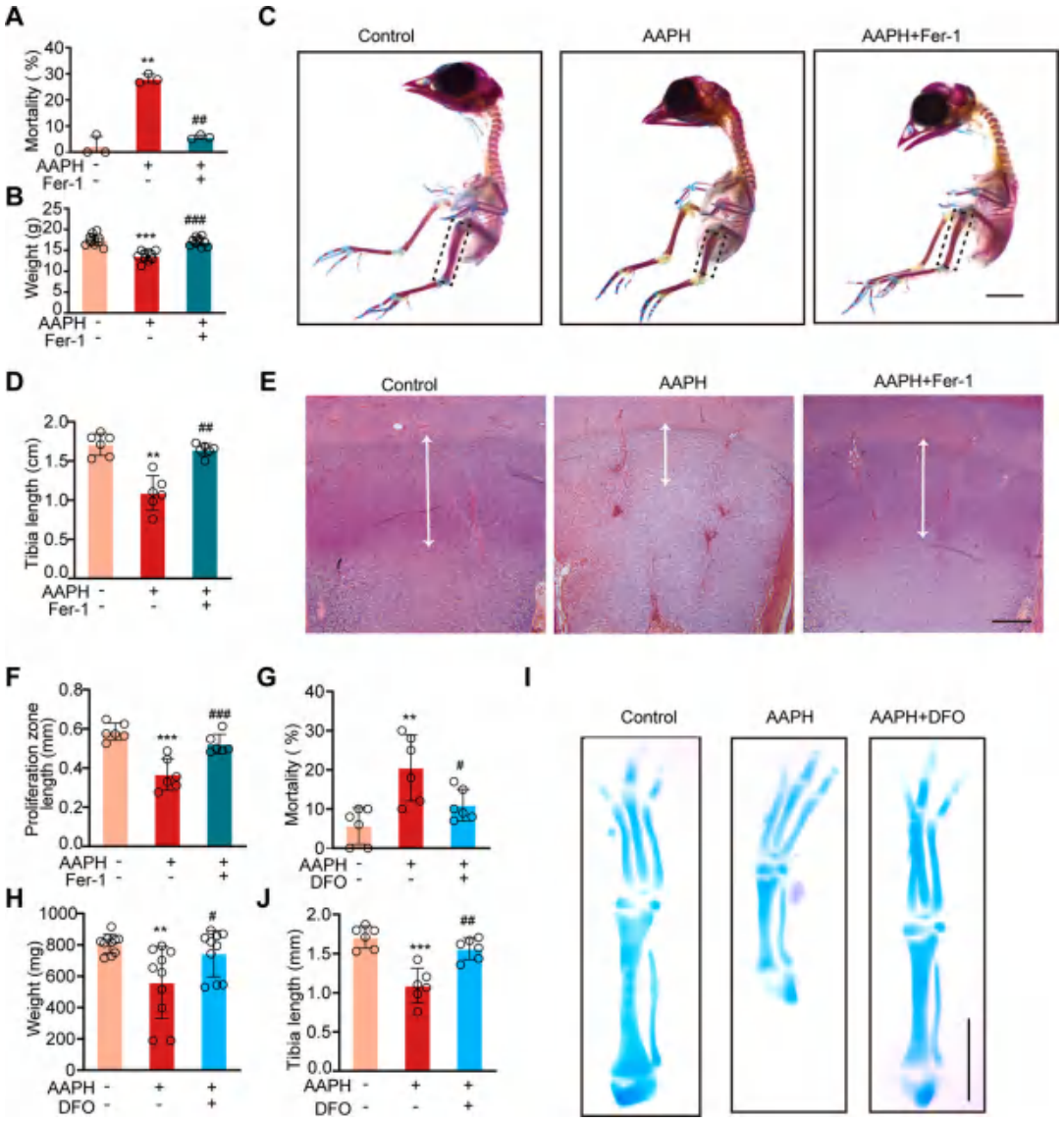

Fig. 4. Inhibition of ferroptosis rescues alkoxyl radicals-induced bone growth retardation. (A) The mortality and (B) body weight of chicken embryos were measured on EDD17. AAPH, 0.50 μmol/egg; Fer-1, 50 nmol/egg. (C) Representative images of chicken embryos stained with alcian blue and alizarin red on EDD17. The embryos were treated with Fer-1 (50 nmol/egg) and AAPH (0.50 μmol/egg). Scale bar, 1 cm. (D) Quantification of tibia length of EDD17 embryos. (E–F) The tibial paraffin sections were stained by H&E staining. The regions surrounded by white dashed lines were PZ in the growth plate, photographed by a microscope. Scale bar, 200 μm. (G) Mortality and (H) body weight of chicken embryos were measured on EDD7. AAPH, 0.50 μmol/egg; DFO, 200 nmol/egg. (I–J) Representative images and quantification of chicken embryos stained by alcian blue on EDD7. The embryos were treated with DFO (200 nmol/egg) and AAPH (0.50 μmol/egg). Scale bar, 1 mm. Data are represented as mean ± SD. Comparisons between groups were made using one-way ANOVA.$^{**}P < 0.01$ and $^{***}P < 0.001$ vs the Control group. $^{\#}P < 0.05$, $^{\#\#}P < 0.01$ and $^{\#\#\#}P < 0.001$ vs the AAPH-treated group. (For interpretation of the references to colour in this figure legend, the reader is referred to the Web version of this article.)

cellular DMT1 was achieved (Fig. 5D). It was determined that loss of DMT1 reversed AAPH triggered suppression of osteogenesis-related genes *BMP6*, *COL2A1* and *ACAN* (Fig. 5E). Taken together, these *in vitro* findings provide support for a critical role for iron overload in oxidative stress-disturbed embryonic osteogenesis.

3.5. Accumulation of oxidized phospholipids (OxPLs) in alkoxyl radicals-exposed chondrocytes dampens chondrogenesis

Since oxidation of PUFA at the bis-allylic position of phospholipid is a driving factor for peroxidation and ferroptosis, we measured the level of lipid peroxidation by C11-BODIPY staining. The results shown in Fig. 6A demonstrate that AAPH or Erastin treatment leads to accumulation of lipid peroxidation products in cells, which were inhibited by Fer-1 treatment. Redox lipidomics analysis by LC-MS/MS identified five major classes of OxPLs, including phosphatidyl ethanolamine (PE), phosphatidylcholine (PC), phosphatidylserine (PS), phosphatidylglycerol (PG) and phosphatidylinositol (PI) (Fig. 6B). Notably, the AAPH-treated group displayed distinct patterns with more lipid peroxidation compared with the control group (Fig. 6C). A large number of mono-oxygenated and di-oxygenated phospholipid species were increased in the AAPH-treated group (Fig. 6D and E), for example, SAPE-OOH (PE (38:4)+2O). To determine whether SAPE-OOH could directly contribute to the observed effects on bone development, ATDC5 cells were treated with exogenous SAPE-OOH. Consistent with AAPH treatment, incubating cells with SAPE-OOH was found to inhibit *Bmp6*, *Co12a1,* and *Acan* genes, which were associated with bone development (Fig. 6F). These data define the accumulation of OxPLs in alkoxyl radicals-exposed chondrocytes, which suppresses the chondrogenesis process.

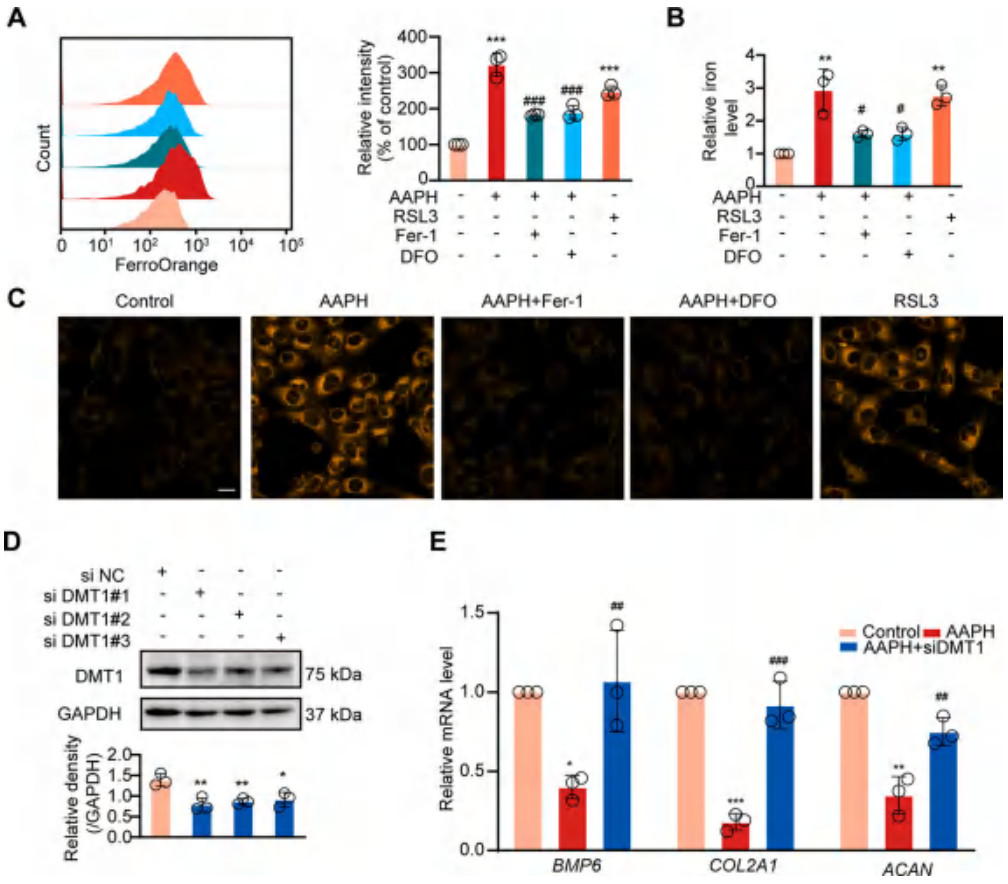

Fig. 5. Alkoxyl radicals trigger iron overload in chondrocytes. (A) Levels of intracellular iron were detected by flow cytometry after incubating with Fe^{2+} ions fluorescent probe FerroOrange in SW1353 cells subjected to different treatments. AAPH, 15 mM; RSL3, 30 nM; DFO, 200 μM; Fer-1, 5 μM. (B) Levels of intracellular iron were detected by iron assay kit in SW1353 cells subjected to different treatments. (C) Representative confocal microscopy images of FerroOrange staining in SW1353 cells. Scale bar, 20 μm. (D) The verification of DMT1 knockdown with siDMT1 in SW1353 cells. (E) Relative mRNA levels of *BMP6*, *COL2A1* and *ACAN* in SW1353 cells were determined after transfected with siDMT1. Data are represented as mean ± SD. Comparisons between groups were made using one-way ANOVA. $^{*}P < 0.05$, $^{**}P < 0.01$ and $^{***}P < 0.001$ vs the Control group. $^{\#}P < 0.05$, $^{\#\#}P < 0.01$ and $^{\#\#\#}P < 0.001$ vs the AAPH-treated group.

3.6. 4-HNE modification drives ubiquitin-dependant degradation of SOX9

The transcription factor SOX9 is a key regulator of chondrogenesis [43–45]. When delineating AAPH-induced alteration of chondrogenesis-related pathways, we determined that SOX9 protein levels, rather than mRNA levels, were altered by AAPH treatment (Fig. 7A and B) in chicken embryos and chondrogenic cells (Figs. S4A–S4C). Meanwhile, AAPH substantially perturbed chondrogenesis-related genes, including *Bmp6*, *Co12a1* and *Acan,* which were rescued by DFO treatment (Fig. 7C). Moreover, Fer-1 and DFO treatment abrogated AAPH-induced down-regulation of SOX9 protein (Figs. S4B and S4C), thus normalizing the expressions of *BMP6*, *COL2A1* and *ACAN* in SW1353 cells (Fig. S4D).

4-HNE, an end product of lipid peroxidation, has important electrophilic properties and is able to react with a variety of proteins to form HNE-protein adducts. HNE-protein adducts formation is known to affect the fate of these modified proteins by altering their activities or inducing degradation [46]. In this study, we noticed that 4-HNE-conjugated protein level was considerably increased after AAPH treatment (Fig. 7D). Given this intriguing fact, we proposed whether the decrease of SOX9 at protein level was correlative with 4-HNE modification. To prove this hypothesis, we performed Co-IP assay to determine the interaction between SOX9 and 4-HNE in SW1353 cells, and results indicated that AAPH exposure led to an enhanced level of SOX9 bound to 4-HNE (Fig. 7E). Immunofluorescence staining further confirmed the co-localization of 4-HNE and SOX9 (Fig. 7F). As expected, knockdown of DMT1 by siRNA weakened the conjugation of SOX9 with 4-HNE (Fig. 7G).

Next, a CHX chase experiment was designed to understand 4-HNE modification-induced SOX9 degradation. These experiments revealed that while degradation of SOX9 protein level was dramatically promoted following exogenous 4-HNE treatment (Fig. 7H), the proteasome inhibitor MG132 inhibited AAPH-triggered decline in SOX9 protein levels, while the autophagy inhibitor 3-MA had little effect (Fig. 7I). These data prompted analysis of the ubiquitin-dependant degradation pathways. SW1353 cells were co-transfected with ubiquitin and SOX9 plasmids. AAPH treatment in these cells was seen to promote K48 ubiquitination of SOX9, which was reversed by knockdown of DMT1 (Fig. 7J and K). Altogether, these data suggest that the lipid peroxidation end product 4-HNE commands ubiquitin-proteasomal degradation of SOX9 via protein modification in chondrocytes.

4. Discussion

Oxidative stress has long been deemed as a detrimental factor for embryonic bone developmental disorders [47,48]. Increasing studies have reported that fetal bone is extremely sensitive to environmental influences in pregnancy, during which adverse exposures such as oxidative stress will reduce the weight and growth rate of newborns, thereby increasing the risk of skeletal disorders [7,49,50]. although the precise mechanism has been elusive. Almeida et al. found that the levels of lipid peroxidation and expression of lipoxygenases increased in the murine skeleton with age, which correlated with loss of bone mineral mass [51]. Mutation of GPX4, a phospholipid hydroperoxidase, has also been reported to cause Sedaghatian-type spondylometaphyseal dysplasia [52]. Clinical studies have shown that preterm birth, low birth weight, growth restriction and developmental malformations are associated with lipid peroxidation in the fetus [49,53]. At birth, preterm infants have been reported to have higher levels of lipid peroxidation than full-term infants, as revealed by higher plasma MDA and presence of lipid peroxides [54,55]. These observations suggest that accumulation of lipid peroxides is a risk for preterm birth.

Alkoxyl radicals, which can be endogenously produced in large quantities are known to be important for ferroptosis [18,56–58]. In the

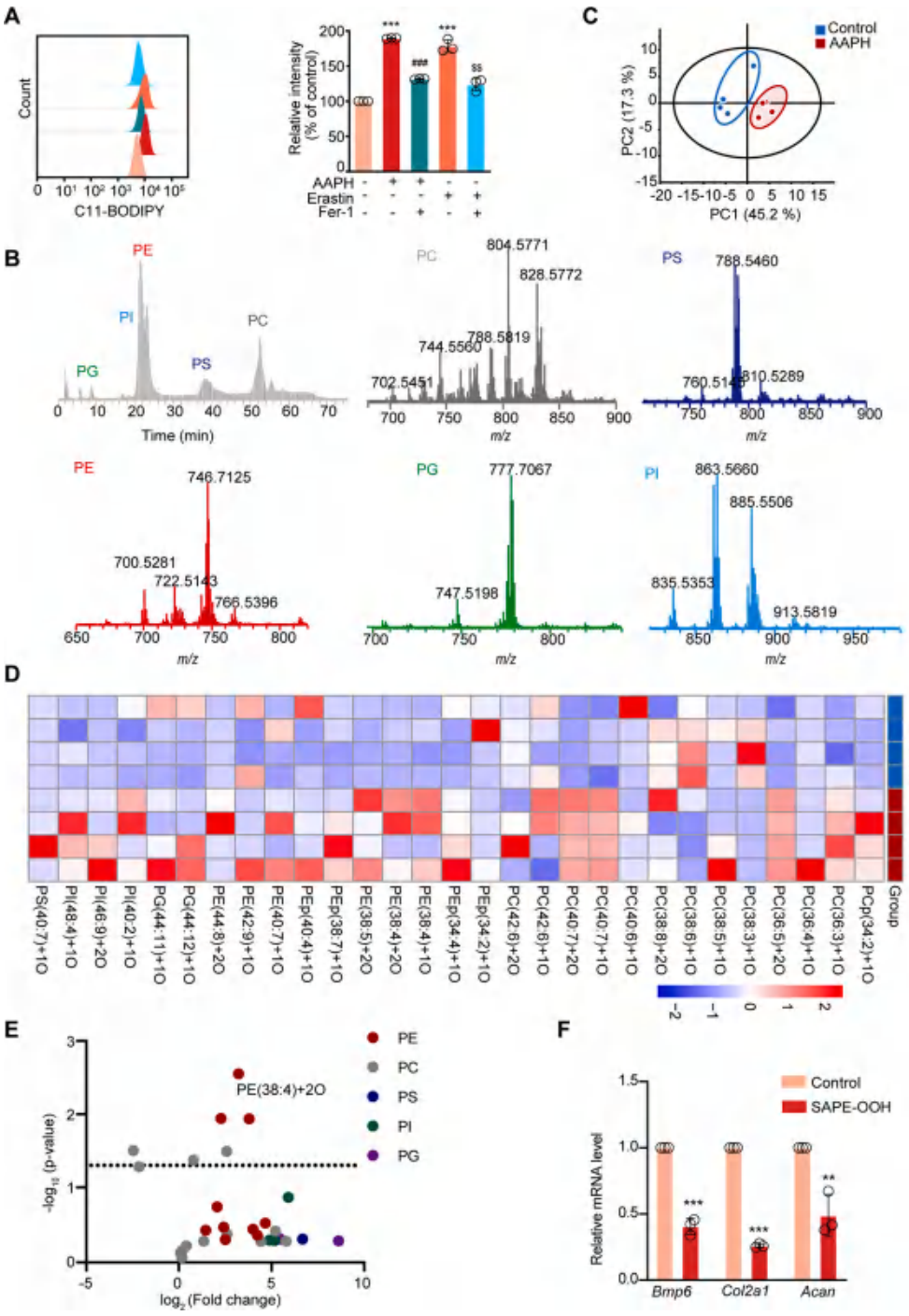

Fig. 6. Oxidized phospholipids accumulates in alkoxyl radicals-treated chondrocytes and suppress bone development. (A) Lipid peroxidation level was detected by flow cytometry after incubating with C11-BODIPY in ATDC5 cells. (B) Normal phase LC/MS chromatogram (grey) and mass spectra of PLs in ATDC5 cells. (C) OxPLs in chondrocytes were extracted and analyzed by principal component analysis, and the 2D score plots display repertoires of control and AAPH-treated embryos. Each point represents a sample, and ellipses represent 95% confidence regions (n = 4). (D–E) Heat map and Volcano plot showing differentially expressed OxPLs between control group and AAPH group. Each dot represents one class of phospholipids and the fold change was set to >2.0. (F) Expressions of chondrogenesis-related genes were measured by qRT-PCR. ATDC5 cells were treated with SAPE-OOH (2 μM). Data are presented as mean ± SD. Comparisons between groups were made using one-way ANOVA (A) and Student's *t*-test (F). $^{**}P < 0.01$, $^{***}P < 0.001$ vs the Control group. $^{\#\#\#}P < 0.001$ vs the AAPH-treated group. $^{\$\$}P < 0.01$ vs the Erastin-treated group.

present study, by utilizing AAPH, it was revealed that alkoxyl radicals impede bone development by inducing chondrocyte ferroptosis. To our knowledge, this study provides the first evidence demonstrating a negative role for ferroptosis in embryonic bone development.

The propagation of lipid peroxidation ascribes to iron-dependant Fenton reactions and lipoxygenases-catalyzed oxidation [59,60]. Inhibiting iron accumulation inhibits accumulation of lipid peroxides [61,62] and prevents ferroptotic cell death [63]. In the present study, expression analysis of iron transporters (TFR1 and DMT1), FerroOrange staining, iron chelator, and siRNA gene knockdown, were used to demonstrate that iron accumulation is central to alkoxyl radicals mediated disturbance in chondrogenesis. These findings are in line with a previous report showing that iron overload resulting from upregulation of iron transporters, resulted in changes in bone microarchitecture and bone loss [64]. Yamada et al. used a cell-free system to show that while AAPH autoxidation resulted in an excessive accumulation of lipid hydroperoxides, iron and other metal ions further promoted the transformation of lipid hydroperoxides to many secondary oxidative products, thus amplifying lipid peroxidation [29]. These observations are in harmony with the collaborative mode of alkoxyl radicals and iron identified in our study.

We further determined that oxidative stress negatively affects embryonic bone development via 4-HNE dependent conjugation of the transcription factor SOX9, a master regulator in the osteogenesis process. This explosive burst of phospholipid peroxidation products produces a large amount of 4-HNE [65,66], which promotes carbonylation

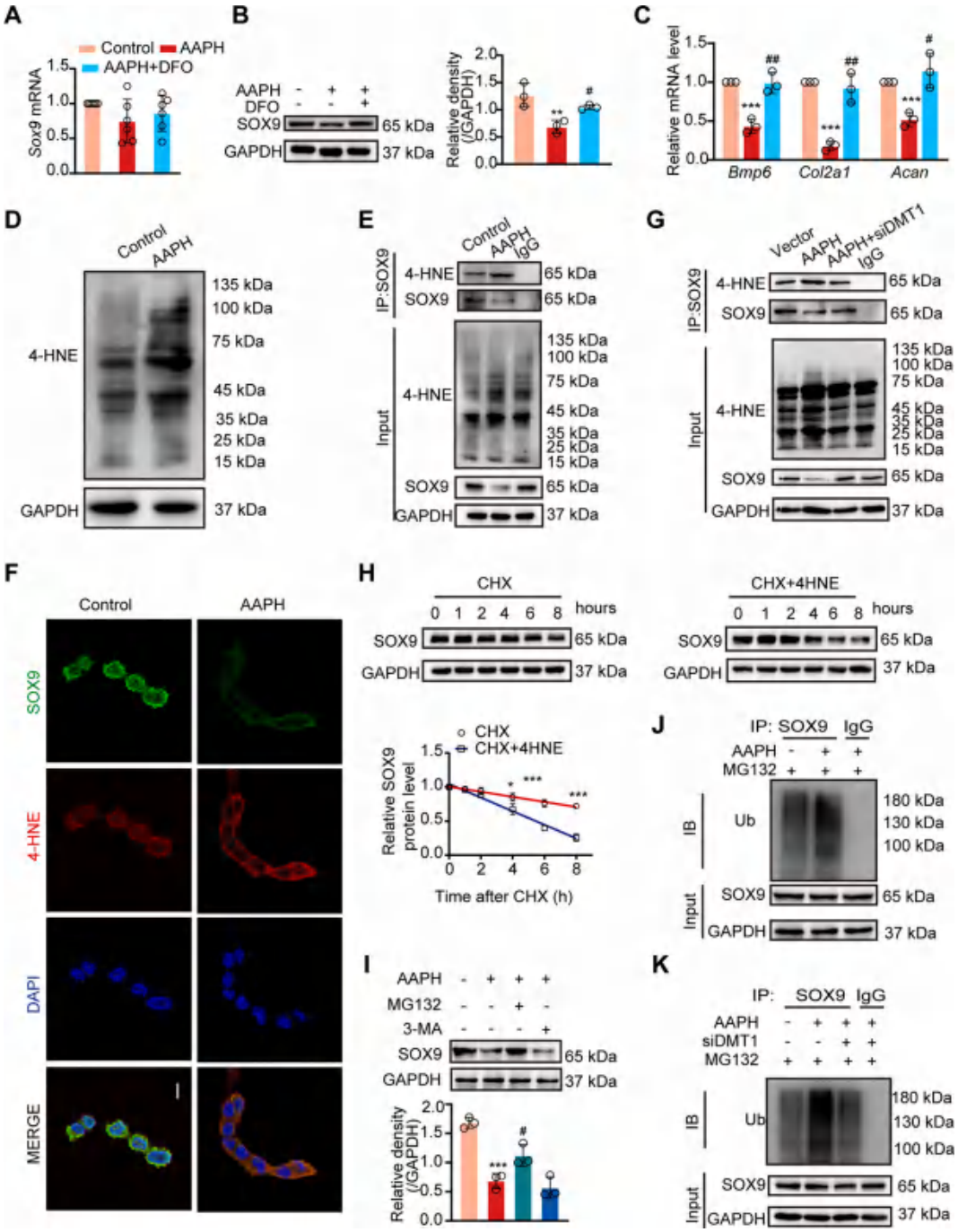

Fig. 7. AAPH induces 4-HNE modification of SOX9 and promotes its ubiquitin-proteasomal degradation. (A) Relative mRNA level of *Sox9* in chicken embryos. (B) Immunoblotting analysis was performed to detect the level of SOX9 protein after treated with DFO and AAPH in chicken embryos. (C) Expressions of chondrogenesis-related genes were measured by qRT-PCR in chicken embryos treated with DFO and AAPH. (D) Protein expression of 4-HNE was visualized by immunoblotting in SW1353 cells after treatment with AAPH (15 mM). (E) CO-IP assay determined the level of SOX9 conjuncted with 4-HNE in SW1353 cells. (F) Representative confocal images showing the colocalization of SOX9 (green) and 4-HNE (red). Scale bars, 20 μm. (G) CO-IP assay determined the level of SOX9 conjuncted with 4-HNE in siDMT1-treated SW1353 cells. (H) Turnover of SOX9 by CHX chase assay in SW1353 cells with or without 4-HNE. CHX, 100 μM; 4-HNE, 10 μM. (I) Effects of MG132 (10 μM) or 3-MA (20 μM) on the AAPH-induced level of SOX9 protein. The diagram showed quantitative analysis of SOX9 protein levels. (J–K) Ubiquitination of SOX9 was assessed by immunoblotting in SW1353 cells (J) and siDMT1-treated SW1353 cells (K). Data are represented as mean ± SD. Comparisons between groups were made using one-way ANOVA (A–C) and Student's *t*-test (H). $^{*}P < 0.05$, $^{**}P < 0.01$ and $^{***}P < 0.001$ vs the Control group. $^{\#}P < 0.05$ and $^{\#\#}P < 0.01$ vs the AAPH-treated group. (For interpretation of the references to colour in this figure legend, the reader is referred to the Web version of this article.)

of SOX9, leading to its ubiquitin-dependant degradation. Loss of SOX9 eventually impedes transduction of signaling guiding osteogenesis, thereby impacting normal bone development.

5. Conclusions

In the present study, we characterize an essential role of ferroptosis in dysplasia in embryonic bone development by establishing an oxidative injury model in chicken embryos and chondrocytes. Alkoxyl

radicals give rise to the accumulation of lipid peroxidation by a synergic mechanism involving the initiation of auto-oxidative reaction and iron-mediated amplification. The lipid peroxidation end product 4-HNE triggered SOX9 modification, which leads to its ubiquitin-mediated degradation in chondrocytes. Our findings show that ferroptosis is switched on by oxidative stress, which leads to dysfunction in embryonic bone development. These findings provide support for use of anti-ferroptosis agents in treating oxidative stress dependent defects in bone development.

Author contributions

R. R. He, Y.F. Li, and H Kurihara conceived and designed the research. J Niu, X Wan, G.Y. Yu, S Jiang, R.N. Yi, Y.P. Wu, and S·H Ouyang performed the experiments. J Niu, L Liang, X Wan, and W.Y. Sun contributed to the acquisition and analysis of the data. J Niu and W.J. Duan prepared figures, tables and the manuscript. Y.F. Cao, X.F. Zhu, and R.H. Zhang partly advised the research. Y.F. Cao supported the LC-MS platform. R.R. He, Y.F. Li, W.J. Duan, and J.B. R.R. He and Y.F. Li revised and approved the manuscript. All of the authors have approved the final manuscript.

Availability of data and materials

The datasets used to support the findings of this study are available from the corresponding author upon request.

Declaration of competing interest

The authors declare no conflicts of interest.

Data availability

Data will be made available on request.

Acknowledgments

This study was partly supported by National Key Research and Development Program of China (grant number 2018YFC2002500), Natural Science Foundation of China (grant number 82004012, 82125038, 81873209, 81973718 and 81903821), Natural Science Foundation of Guangdong (2019A1515010909, 2021A1515011297, 2021B1515120023), the Local Innovative and Research Teams Project of Guangdong Pearl River Talents Program (grant number 2017BT01Y036), and the Innovation Team Project of Guangdong Provincial Department of Education (2020KCXTD003) and GDUPS (2019). The authors (Rong-Rong He and Yi-Fang Li) also gratefully acknowledge the support of K.C. Wong Education Foundation.

Appendix A. Supplementary data

Supplementary data to this article can be found online at https://doi.org/10.1016/j.redox.2022.102437.

References

[1] T.P. Fleming, A.J. Watkins, M.A. Velazquez, J.C. Mathers, A.M. Prentice, J. Stephenson, M. Barker, R. Saffery, C.S. Yajnik, J.J. Eckert, et al., Origins of lifetime health around the time of conception: causes and consequences, Lancet (London, England) 391 (10132) (2018) 1842–1852.
[2] J. Hoover-Fong, C.I. Scott, M.C. Jones, Health supervision for people with achondroplasia, Pediatrics 145 (6) (2020).
[3] R. Savarirayan, L. Tofts, M. Irving, W. Wilcox, C.A. Bacino, J. Hoover-Fong, R. Ullot Font, P. Harmatz, F. Rutsch, M.B. Bober, et al., Once-daily, subcutaneous vosoritide therapy in children with achondroplasia: a randomised, double-blind, phase 3, placebo-controlled, multicentre trial, Lancet (London, England) 396 (10252) (2020) 684–692.
[4] F. Zhou, J. Mei, X. Han, H. Li, S. Yang, M. Wang, L. Chu, H. Qiao, T. Tang, Kinsenoside attenuates osteoarthritis by repolarizing macrophages through inactivating NF-κB/MAPK signaling and protecting chondrocytes, Acta Pharm. Sin. B 9 (5) (2019) 973–985.
[5] T. Kimura, K. Hino, T. Kono, A. Takano, N. Nitta, N. Ushio, S. Hino, R. Takase, M. Kudo, Y. Daigo, et al., Maternal undernutrition during early pregnancy inhibits postnatal growth of the tibia in the female offspring of rats by alteration of chondrogenesis, Gen. Comp. Endocrinol. 260 (2018) 58–66.
[6] A. Wang, Z.K. Zsengellér, J.L. Hecht, R. Buccafusca, S.D. Burke, A. Rajakumar, E. Weingart, P.B. Yu, S. Salahuddin, S.A. Karumanchi, Excess placental secreted frizzled-related protein 1 in maternal smokers impairs fetal growth, J. Clin. Invest. 125 (11) (2015) 4021–4025.
[7] M.E. Snow, K. Keiver, Prenatal ethanol exposure disrupts the histological stages of fetal bone development, Bone 41 (2) (2007) 181–187.
[8] H.L. Zhu, X.T. Shi, X.F. Xu, G.X. Zhou, Y.W. Xiong, S.J. Yi, W.B. Liu, L.M. Dai, X. L. Cao, D.X. Xu, et al., Melatonin protects against environmental stress-induced fetal growth restriction via suppressing ROS-mediated GCN2/ATF4/BNIP3-dependent mitophagy in placental trophoblasts, Redox Biol. 40 (2021), 101854.
[9] M. Hedegaard, T.B. Henriksen, S. Sabroe, N.J. Secher, Psychological distress in pregnancy and preterm delivery, Br. Med. J. 307 (6898) (1993) 234–239.
[10] T. Kimura, K. Hino, T. Kono, A. Takano, N. Nitta, N. Ushio, S. Hino, R. Takase, M. Kudo, Y. Daigo, et al., Maternal undernutrition during early pregnancy inhibits postnatal growth of the tibia in the female offspring of rats by alteration of chondrogenesis, Gen. Comp. Endocrinol. 260 (2018) 58–66.
[11] T.E. Tipple, N. Ambalavanan, Oxygen toxicity in the neonate: thinking beyond the balance, Clin. Perinatol. 46 (3) (2019) 435–447.
[12] X. Jiang, B.R. Stockwell, M. Conrad, Ferroptosis: mechanisms, biology and role in disease, Nat. Rev. Mol. Cell Biol. 22 (4) (2021) 266–282.
[13] H.F. Yan, T. Zou, Q.Z. Tuo, S. Xu, H. Li, A.A. Belaidi, P. Lei, Ferroptosis: mechanisms and links with diseases, Signal Transduct. Targeted Ther. 6 (1) (2021) 49.
[14] C. Espinós, M.I. Galindo, M.A. García-Gimeno, J.S. Ibáñez-Cabellos, D. Martínez-Rubio, J.M. Millán, R. Rodrigo, P. Sanz, M. Seco-Cervera, T. Sevilla, et al., Oxidative stress, a crossroad between rare diseases and neurodegeneration, Antioxidants 9 (4) (2020).
[15] D. Liang, A.M. Minikes, X. Jiang, Ferroptosis at the intersection of lipid metabolism and cellular signaling, Mol. Cell 82 (12) (2022) 2215–2227.
[16] H. Bayır, T.S. Anthonymuthu, Y.Y. Tyurina, S.J. Patel, A.A. Amoscato, A. M. Lamade, Q. Yang, G.K. Vladimirov, C.C. Philpott, V.E. Kagan, Achieving life through death: redox biology of lipid peroxidation in ferroptosis, Cell chemical biology 27 (4) (2020) 387–408.
[17] Z. Cheng, Y. Li, What is responsible for the initiating chemistry of iron-mediated lipid peroxidation: an update, Chem. Rev. 107 (3) (2007) 748–766.
[18] W.Y. Sun, V.A. Tyurin, K. Mikulska-Ruminska, I.H. Shrivastava, T. S. Anthonymuthu, Y.J. Zhai, M.H. Pan, H.B. Gong, D.H. Lu, J. Sun, et al., Phospholipase iPLA(2)β averts ferroptosis by eliminating a redox lipid death signal, Nat. Chem. Biol. 17 (4) (2021) 465–476.
[19] K.H. Al-Gubory, Environmental pollutants and lifestyle factors induce oxidative stress and poor prenatal development, Reprod. Biomed. Online 29 (1) (2014) 17–31.
[20] S. Sreetharan, L. Stoa, M.E. Cybulski, D.E. Jones, A.H. Lee, A.V. Kulesza, S. Tharmalingam, D.R. Boreham, T.C. Tai, J.Y. Wilson, Cardiovascular and growth outcomes of C57Bl/6J mice offspring exposed to maternal stress and ionizing radiation during pregnancy, Int. J. Radiat. Biol. 95 (8) (2019) 1085–1093.
[21] M.M. Shivananjappa, Muralidhara, Differential oxidative stress induction and lethality of rat embryos after maternal exposure to t-butyl hydroperoxide during postimplantation period, Drug Chem. Toxicol. 36 (2) (2013) 209–216.
[22] Y.W. Xiong, H.L. Zhu, Y. Nan, X.L. Cao, X.T. Shi, S.J. Yi, Y.J. Feng, C. Zhang, L. Gao, Y.H. Chen, et al., Maternal cadmium exposure during late pregnancy causes fetal growth restriction via inhibiting placental progesterone synthesis, Ecotoxicol. Environ. Saf. 187 (2020), 109879.
[23] G. Miotto, M. Rossetto, M.L. Di Paolo, L. Orian, R. Venerando, A. Roveri, A. M. Vučković, V. Bosello Travain, M. Zaccarin, L. Zennaro, et al., Insight into the mechanism of ferroptosis inhibition by ferrostatin-1, Redox Biol. 28 (2020), 101328.
[24] V. Barygina, M. Becatti, T. Lotti, S. Moretti, N. Taddei, C. Fiorillo, ROS-challenged keratinocytes as a new model for oxidative stress-mediated skin diseases, J. Cell. Biochem. 120 (1) (2019) 28–36.
[25] Y.F. Li, S.H. Ouyang, L.F. Tu, X. Wang, W.L. Yuan, G.E. Wang, Y.P. Wu, W.J. Duan, H.M. Yu, Z.Z. Fang, et al., Caffeine protects skin from oxidative stress-induced senescence through the activation of autophagy, Theranostics 8 (20) (2018) 5713–5730.
[26] R.R. He, Y. Li, X.D. Li, R.N. Yi, X.Y. Wang, B. Tsoi, K.K. Lee, K. Abe, X. Yang, H. Kurihara, A new oxidative stress model, 2,2-azobis(2-amidinopropane) dihydrochloride induces cardiovascular damages in chicken embryo, PLoS One 8 (3) (2013), e57732.
[27] Y. Li, X.Y. Wang, Z.L. Zhang, X. Cheng, X.D. Li, M. Chuai, K.K. Lee, H. Kurihara, X. Yang, Excess ROS induced by AAPH causes myocardial hypertrophy in the developing chick embryo, Int. J. Cardiol. 176 (1) (2014) 62–73.
[28] T. Wu, G.Y. Yu, J. Xiao, C. Yan, H. Kurihara, Y.F. Li, K.F. So, R.R. He, Fostering efficacy and toxicity evaluation of traditional Chinese medicine and natural products: chick embryo as a high throughput model bridging in vitro and in vivo studies, Pharmacol. Res. 133 (2018) 21–34.
[29] Y. Matsuoka, M. Takahashi, Y. Sugiura, Y. Izumi, K. Nishiyama, M. Nishida, M. Suematsu, T. Bamba, K.I. Yamada, Structural library and visualization of endogenously oxidized phosphatidylcholines using mass spectrometry-based techniques, Nat. Commun. 12 (1) (2021) 6339.

[30] S. Xin, C. Mueller, S. Pfeiffer, V.A.N. Kraft, J. Merl-Pham, X. Bao, R. Feederle, X. Jin, S.M. Hauck, P. Schmitt-Kopplin, et al., MS4A15 drives ferroptosis resistance through calcium-restricted lipid remodeling, Cell Death Differ. 29 (3) (2022) 670–686.
[31] Y. Matsuoka, Y. Izumi, M. Takahashi, T. Bamba, K.I. Yamada, Method for structural determination of lipid-derived radicals, Anal. Chem. 92 (10) (2020) 6993–7002.
[32] I. Kurakazu, Y. Akasaki, M. Hayashida, H. Tsushima, N. Goto, T. Sueishi, M. Toya, M. Kuwahara, K. Okazaki, T. Duffy, et al., FOXO1 transcription factor regulates chondrogenic differentiation through transforming growth factor β1 signaling, J. Biol. Chem. 294 (46) (2019) 17555–17569.
[33] X. Dong, X. Xu, C. Yang, Y. Luo, Y. Wu, J. Wang, USP7 regulates the proliferation and differentiation of ATDC5 cells through the Sox9-PTHrP-PTH1R axis, Bone 143 (2021), 115714.
[34] T.O. Vu, P.T. Tran, W. Seo, J.H. Lee, B.S. Min, J.A. Kim, Triterpenoids from Celastrus orbiculatus Thunb. inhibit RANKL-induced osteoclast formation and bone resorption via c-Fos signaling, J. Nat. Med. 75 (1) (2021) 56–65.
[35] S. Gabner, P. Böck, D. Fink, M. Glösmann, S. Handschuh, The visible skeleton 2.0: phenotyping of cartilage and bone in fixed vertebrate embryos and foetuses based on X-ray microCT, Development 147 (11) (2020).
[36] D. Fang, L.Y. Kong, J. Cai, S. Li, X.D. Liu, J.S. Han, G.G. Xing, Interleukin-6-mediated functional upregulation of TRPV1 receptors in dorsal root ganglion neurons through the activation of JAK/PI3K signaling pathway: roles in the development of bone cancer pain in a rat model, Pain 156 (6) (2015) 1124–1144.
[37] S. Radbakhsh, S. Ganjali, S.A. Moallem, P.C. Guest, A. Sahebkar, Antioxidant effects of trehalose in an experimental model of type 2 diabetes, Adv. Exp. Med. Biol. 1328 (2021) 473–480.
[38] M. Hoshino, K. Kaneko, Y. Miyamoto, K. Yoshimura, D. Suzuki, T. Akaike, T. Sawa, T. Ida, S. Fujii, H. Ihara, et al., 8-Nitro-cGMP promotes bone growth through expansion of growth plate cartilage, Free Radic. Biol. Med. 110 (2017) 63–71.
[39] Y.J. He, X.Y. Liu, L. Xing, X. Wan, X. Chang, H.L. Jiang, Fenton reaction-independent ferroptosis therapy via glutathione and iron redox couple sequentially triggered lipid peroxide generator, Biomaterials 241 (2020), 119911.
[40] G. Gao, J. Li, Y. Zhang, Y.Z. Chang, Cellular iron metabolism and regulation, Adv. Exp. Med. Biol. 1173 (2019) 21–32.
[41] H. Feng, K. Schorpp, J. Jin, C.E. Yozwiak, B.G. Hoffstrom, A.M. Decker, P. Rajbhandari, M.E. Stokes, H.G. Bender, J.M. Csuka, et al., Transferrin receptor is a specific ferroptosis marker, Cell Rep. 30 (10) (2020) 3411–3423, e3417.
[42] S. Wang, X. He, Q. Wu, L. Jiang, L. Chen, Y. Yu, P. Zhang, X. Huang, J. Wang, Z. Ju, et al., Transferrin receptor 1-mediated iron uptake plays an essential role in hematopoiesis, Haematologica 105 (8) (2020) 2071–2082.
[43] N. van Gastel, S. Stegen, G. Eelen, S. Schoors, A. Carlier, V.W. Daniëls, N. Baryawno, D. Przybylski, M. Depypere, P.J. Stiers, et al., Lipid availability determines fate of skeletal progenitor cells via SOX9, Nature 579 (7797) (2020) 111–117.
[44] V. Lefebvre, M. Angelozzi, A. Haseeb, SOX9 in cartilage development and disease, Curr. Opin. Cell Biol. 61 (2019) 39–47.
[45] H. Song, K.H. Park, Regulation and function of SOX9 during cartilage development and regeneration, Semin. Cancer Biol. 67 (Pt 1) (2020) 12–23.
[46] C.L. Hawkins, M.J. Davies, Detection, identification, and quantification of oxidative protein modifications, J. Biol. Chem. 294 (51) (2019) 19683–19708.
[47] X. Zhu, C. Xi, B. Thomas, B.S. Pace, Loss of NRF2 function exacerbates the pathophysiology of sickle cell disease in a transgenic mouse model, Blood 131 (5) (2018) 558–562.
[48] Y. Yao, Q. Liu, I. Adrianto, X. Wu, J. Glassbrook, N. Khalasawi, C. Yin, Q. Yi, Z. Dong, F. Geissmann, et al., Histone deacetylase 3 controls lung alveolar macrophage development and homeostasis, Nat. Commun. 11 (1) (2020) 3822.
[49] M.R. Prater, C.L. Laudermilch, C. Liang, S.D. Holladay, Placental oxidative stress alters expression of murine osteogenic genes and impairs fetal skeletal formation, Placenta 29 (9) (2008) 802–808.
[50] A.L. Ponsonby, C. Symeonides, R. Saffery, J.F. Mueller, M. O'Hely, P.D. Sly, N. Wardrop, A. Pezic, T. Mansell, F. Collier, et al., Prenatal phthalate exposure, oxidative stress-related genetic vulnerability and early life neurodevelopment: a birth cohort study, Neurotoxicology 80 (2020) 20–28.
[51] R.L. Jilka, M. Almeida, E. Ambrogini, L. Han, P.K. Roberson, R.S. Weinstein, S. C. Manolagas, Decreased oxidative stress and greater bone anabolism in the aged, when compared to the young, murine skeleton with parathyroid hormone administration, Aging Cell 9 (5) (2010) 851–867.
[52] A.C. Smith, A.J. Mears, R. Bunker, A. Ahmed, M. MacKenzie, J. A. Schwartzentruber, C.L. Beaulieu, E. Ferretti, J. Majewski, D.E. Bulman, et al., Mutations in the enzyme glutathione peroxidase 4 cause Sedaghatian-type spondylometaphyseal dysplasia, J. Med. Genet. 51 (7) (2014) 470–474.
[53] G.S. Abd El-Aziz, M.M. El-Fark, H.A. Saleh, The prenatal toxic effect of methylmercury on the development of the appendicular skeleton of rat fetuses and the protective role of vitamin E, Anat. Rec. 295 (6) (2012) 939–949. Hoboken, NJ : 2007.
[54] K. Katti, K.R. Ayasolla, T. Iurcotta, D. Potak, C. Codipilly, B. Weinberger, Lipid peroxidation products as predictors of oxidant-mediated disease in preterm infants, J. Matern. Fetal Neonatal Med. (2021) 1–6.
[55] I. Torres-Cuevas, A. Parra-Llorca, A. Sánchez-Illana, A. Nuñez-Ramiro, J. Kuligowski, C. Cháfer-Pericás, M. Cernada, J. Escobar, M. Vento, Oxygen and oxidative stress in the perinatal period, Redox Biol. 12 (2017) 674–681.
[56] X. Chen, C. Yu, R. Kang, G. Kroemer, D. Tang, Cellular degradation systems in ferroptosis, Cell Death Differ. 28 (4) (2021) 1135–1148.
[57] T.S. Anthonymuthu, Y.Y. Tyurina, W.Y. Sun, K. Mikulska-Ruminska, I. H. Shrivastava, V.A. Tyurin, F.B. Cinemre, H.H. Dar, A.P. VanDemark, T. R. Holman, et al., Resolving the paradox of ferroptotic cell death: ferrostatin-1 binds to 15LOX/PEBP1 complex, suppresses generation of peroxidized ETE-PE, and protects against ferroptosis, Redox Biol. 38 (2021), 101744.
[58] Y. Liu, Z. Song, Y. Liu, X. Ma, W. Wang, Y. Ke, Y. Xu, D. Yu, H. Liu, Identification of ferroptosis as a novel mechanism for antitumor activity of natural product derivative a2 in gastric cancer, Acta Pharm. Sin. B 11 (6) (2021) 1513–1525.
[59] J. Liu, R. Kang, D. Tang, Signaling pathways and defense mechanisms of ferroptosis, FEBS J. 6 (2021) 1–13.
[60] N. Kong, X. Chen, J. Feng, T. Duan, S. Liu, X. Sun, P. Chen, T. Pan, L. Yan, T. Jin, et al., Baicalin induces ferroptosis in bladder cancer cells by downregulating FTH1, Acta Pharm. Sin. B 11 (12) (2021) 4045–4054.
[61] J. Wan, H. Ren, J. Wang, Iron toxicity, lipid peroxidation and ferroptosis after intracerebral haemorrhage, Stroke and vascular neurology 4 (2) (2019) 93–95.
[62] N. Yamada, T. Karasawa, H. Kimura, S. Watanabe, T. Komada, R. Kamata, A. Sampilvanjil, J. Ito, K. Nakagawa, H. Kuwata, et al., Ferroptosis driven by radical oxidation of n-6 polyunsaturated fatty acids mediates acetaminophen-induced acute liver failure, Cell Death Dis. 11 (2) (2020) 144.
[63] D. Tang, X. Chen, R. Kang, G. Kroemer, Ferroptosis: molecular mechanisms and health implications, Cell Res. 31 (2) (2021) 107–125.
[64] J. Tsay, Z. Yang, F.P. Ross, S. Cunningham-Rundles, H. Lin, R. Coleman, P. Mayer-Kuckuk, S.B. Doty, R.W. Grady, P.J. Giardina, et al., Bone loss caused by iron overload in a murine model: importance of oxidative stress, Blood 116 (14) (2010) 2582–2589.
[65] M.W. Park, H.W. Cha, J. Kim, J.H. Kim, H. Yang, S. Yoon, N. Boonpraman, S.S. Yi, I.D. Yoo, J.S. Moon, NOX4 promotes ferroptosis of astrocytes by oxidative stress-induced lipid peroxidation via the impairment of mitochondrial metabolism in Alzheimer's diseases, Redox Biol. 41 (2021), 101947.
[66] H. Zhong, H. Yin, Role of lipid peroxidation derived 4-hydroxynonenal (4-HNE) in cancer: focusing on mitochondria, Redox Biol. 4 (2015) 193–199.

Bioorganic Chemistry 131 (2023) 106316

Contents lists available at ScienceDirect

Bioorganic Chemistry

journal homepage: www.elsevier.com/locate/bioorg

Discovery and structural optimization of 3-*O*-*β*-Chacotriosyl betulonic acid saponins as potent fusion inhibitors of Omicron virus infections

Mingjian Liu [a,1], Jinshen Wang [b,1], Xin Wan [c,1], Baixi Li [a], Mingming Guan [a], Xiaoyun Ning [a], Xiaojie Hu [a], Sumei Li [d,*], Shuwen Liu [b,e,*], Gaopeng Song [a,*]

[a] Key Laboratory for Biobased Materials and Energy of Ministry of Education, College of Materials and Energy, South China Agricultural University, Guangzhou 510642, China
[b] Guangdong Provincial Key Laboratory of New Drug Screening, School of Pharmaceutical Sciences, Southern Medical University, Guangzhou, 510515, China
[c] Huizhou Health Sciences Polytechnic, Huizhou 516025, China
[d] Department of Human anatomy, School of Medicine, Jinan University, Guangzhou 510632, China
[e] State Key Laboratory of Organ Failure Research, Guangdong Provincial Institute of Nephrology, Southern Medical University, Guangzhou 510515, China

ARTICLE INFO

Keywords:
Betulonic acid derivatives
Omicron
Membrane fusion
Structure–activity relationships

ABSTRACT

The recent global Omicron epidemics underscore the great need for the development of small molecule therapeutics with appropriate mechanisms. The trimeric spike protein (S) of SARS-CoV-2 plays a pivotal role in mediating viral entry into host cells. We continued our efforts to develop small-molecule SARS-CoV-2 entry inhibitors. In this work, two sets of BA derivatives were designed and synthesized based on the hit **BA-1** that was identified as a novel SARS-CoV-2 entry inhibitor. Compound **BA-4**, the most potent one, showed broad inhibitory activities against pOmicron and other pseudotyped variants with EC_{50} values ranging 2.73 to 5.19 μM. Moreover, pSARS-CoV-2 assay, SPR analysis, Co-IP assay and the cell–cell fusion assay coupled with docking and mutagenesis studies revealed that **BA-4** could stabilize S in the pre-fusion step to interfere with the membrane fusion, thereby displaying promising inhibition against Omicron entry.

1. Introduction

The severe acute respiratory syndrome coronavirus 2 (SARS-CoV-2) that leads to the coronavirus disease 2019 (COVID-19), has rapidly spread around the world, devastating consequences for the health sector and the economy since the late December of 2019 [1,2]. Currently, the public become more aware of the devastation caused by the emerging variants and mutations of SARS-CoV-2, as exampled by Omicron variant, which is posing a great challenge to public health and safety globally [3–5]. As of September 2022, there have been>610 million confirmed cases and 6.5 million deaths worldwide despite a ring vaccination program with the FDA-approved BNT162b2 and others, underlining the urgency for developing effective antiviral agents to prevent these lethal infections. Remdesivir [6], a RdRp inhibitor, was approved by the United States Food and Drug Administration (FDA) in May 2020 for the treatment of severe COVID-19 patients. In December 2021, a nucleoside analog molnupiravir that was originally used for influenza, was also approved by FDA [7]. The third drug approved by FDA is paxlovid, which was found to reduce the risk of hospitalization and death by 89 % in the Phase 2/3 EPIC-HR study [8]. In addition, other small-molecule drugs targeting the replication cycle of SARS-CoV-2 are currently being developed in clinic [9,10]. For example, small-molecule inhibitors GC373 and GC376 can effectively inhibit the enzymatic activity of 3CLpro by covalent modification with the amino acid residue Cys145 of the catalytic site to display potent inhibitory potency coupled with low toxicity, which represent potential candidate drugs for the treatment of COVID-19 [11].

SARS-CoV-2 is a new member of single-stranded RNA and enveloped *β*-coronaviruses family, of which infection process starts from the viral entry into host cells. Evidence has shown that the spike protein (S) of SARS-CoV-2 is a “Type I” viral transmembrane glycoprotein, which plays a vital role in viral entry [12,13]. The S protein consists of two

* Corresponding authors at: Department of Human anatomy, School of Medicine, Jinan University, Guangzhou, 510632, China (S. Li); Guangdong Provincial Key Laboratory of New Drug Screening, School of Pharmaceutical Sciences, Southern Medical University, Guangzhou, 510515, China (S. Liu); Key Laboratory for Biobased Materials and Energy of Ministry of Education, College of Materials and Energy, South China Agricultural University, Guangzhou, 510642, China (G. Song).
E-mail addresses: lisumei1234@163.com (S. Li), liusw@smu.edu.cn (S. Liu), songgp1021@scau.edu.cn (G. Song).
[1] These authors contributed equally to this work.

https://doi.org/10.1016/j.bioorg.2022.106316
Received 7 October 2022; Received in revised form 7 November 2022; Accepted 5 December 2022
Available online 8 December 2022

subunits, namely S1 and S2, of which the former can recognize and bind to human angiotensin-converting enzyme 2 (ACE2) receptor of host cells through RBD domain and the latter is responsible for regulating S-mediated viral/cell membrane fusion [14,15]. Structurally, S2 subunit is composed of fusion peptide (FP), heptapeptide repeat 1 (HR1), heptapeptide repeat 2 (HR2), transmembrane domain (TM), and cytoplasmic domain (CP) [16]. After SARS-CoV-2 S1 binds to ACE2, the S protein needs to be activated by cellular proteases to permit insertion of FP into the host membrane, the anchoring process. Subsequently, the HR1 and HR2 regions of the trimeric viral transmembrane protein interact to form a six-helix bundle, which pulls the viral and cellular membranes together and mediates fusion, thereby leading to the release of the viral genome into the cytoplasm [17]. All these steps, attachment to the cellular receptors, conformational changes of S1/S2, FP insertion, rearrangement, and 6HB formation, are critical for SARS-CoV-2 infection and more importantly, the S2 subunit sequence is more conservative than the S1 subunit sequence [18]. Collectively, the SARS-CoV-2 S2 subunit mediates viral fusion and entry, which represents the main target for the development of neutralizing antibodies, and small-molecule fusion inhibitors.

So far, multiple potential SARS-CoV-2 fusion inhibitors have been identified, which showed good antiviral activities in *vivo/vitro*, as exampled by HR-derived peptides EK1 and its analogs [19], niclosamide [20], bergamottin (**1**, Fig. 1A) [3], clofazimine [21], and other natural products such as angeloylgomisin O (**2**, Fig. 1A), schisandrin B (**3**, Fig. 1A) [22]. For example, EK1 and its analogs have been shown to target the HR1 or HR2 domain to interact with virus-cell fusion, thereby exhibiting potent inhibition against SARS-CoV-2 and its variants in vivo [19]. Zhou and co-workers reported that bergamottin could act at multiple stages of the SARS-CoV-2 life cycle to reduce viral entry into cells by both blocking the S-mediated membrane fusion stage and inhibiting the expression of ACE2 [3]. Angeloylgomisin O and schisandrin B that were extracted from Schisandra chinensis, a plant used to treat hepatitis, were found to exhibit strong inhibitory effects on membrane fusion and show more potent antiviral activity against SARS-CoV-2 than remdesivir [22]. In addition, our group has previously conducted multiple high-throughput screens of various small-molecule libraries to identify salvianolic acid C (Sal-C, **4**, Fig. 1A) [23] and estradiol (**5**, Fig. 1A) [24] as potential anti-SARS-CoV-2 agents, which could inhibit SARS-CoV-2 infection *in vitro* by blocking the formation of six-helix bundle core of S to block S-mediated membrane fusion. However, only a few SARS-CoV-2 fusion inhibitors have advanced to clinical trials up to now.

Betulinic acid (BA, **6**, Fig. 1B), a naturally occurring pentacyclic triterpene, represents a promising structure type for a wide variety of agents with good antiviral use against HIV, influenza virus, HSV and others [25–27]. For example, the BA core is present in bevirimat, an HIV maturation inhibitor, which has undergone phase 2 clinical evaluation. Interestingly, BA was found to possess anti-SARS-CoV activity in the μM range *in vitro* and in particular, betulonic acid (**7**, Fig. 1B), an oxidized analog at C-3 position of BA, exhibited improved anti-SARS-CoV potency with an EC_{50} of 0.63 μM [28]. Recently, a class of BA derivatives with a 1, 2, 3-triazolo-fused BA structure have been shown to be potent inhibitors of HCoV-229E nsp15 replication by Naesens and co-workers [29]. Encouraged by these results, we decided to investigate if BA and its derivatives will also have anti-SARS-CoV-2 activity *in vitro*.

Here, we report identification of a class of SARS-CoV-2 fusion inhibitors with a 3-*O*-*β*-chacotriosyl BA structure based on the hit **BA-1**. We describe their hit-to-lead modification, structure–activity relationship (SAR), and the mechanistic findings, giving rise to the lead compound **BA-4** that can directly target S protein as a novel Omicron fusion inhibitor. These biological data consisted well with the binding model that we obtained by the lead compound **BA-4** docking in the Omicron S protein structure, which was supported by site-specific mutation. We demonstrate that the interface in Omicron S where the lead **BA-4** binds, can be as a potential target for developing Omicron and other SARS-CoV-2 fusion inhibitors.

2. Results and discussion

2.1. Chemical synthesis

Compound **BA-1** was prepared according to our previous procedure [34]. The synthetic routes for title compounds **BA-3** – **BA-16** and amide analogs **BA-N-1** as well as **BA-N-2** were illustrated in Scheme 1. Esterification of BA with benzyl bromide in the presence of potassium carbonate afforded the known intermediate **8** [35]. 3*β*-acetoxylup-20 (29)-ene-3, 28-diol **9** [36] was obtained from the commercially available betulin following literature procedures. The TfOH catalyzed coupling reaction between **9** and benzyl 2, 2, 2-trichloroacetimidate furnished benzyl-substituted ether **10**, which then went through the hydrolysis reaction under basic conditions (LiOH) to yield the intermediate **11**.

With glycosyl acceptor **8** or **11** as well as the known the glycosyl donor 2, 3, 4, 6-tetra-*O*-benzoyl-*D*-glucopyranosyl trichloroacetimidate **12** [30] in hand, TMSOTf-catalyzed glycosylations were performed to provide compound **13** or **14**, followed by the hydrolysis reaction under basic conditions (CH_3ONa in MeOH) to yield 3-*O*-*β*-glucopyranoside **15** or **16**, respectively. Subsequently, the pivaloyl (Piv) group could be selectively installed at the 3, 6-OHs of the *β*-glucopyranosyl residues in **15** or **16** at a controlled low temperature to afford **17** or **18**, respectively.

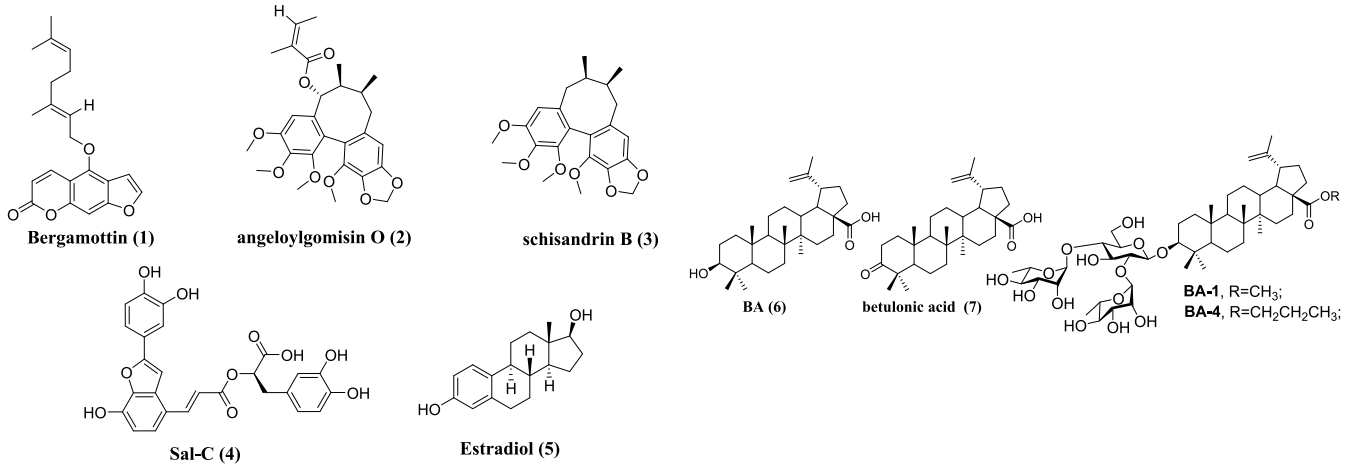

Fig. 1. A. Chemical structures of representative small-molecule SARS-CoV-2 fusion inhibitors **1**–**5** Fig. 1**B.** Chemical structures of betulinic acid **6**, betulonic acid **7**, the hit compound **BA-1** and the lead compound **BA-4.**

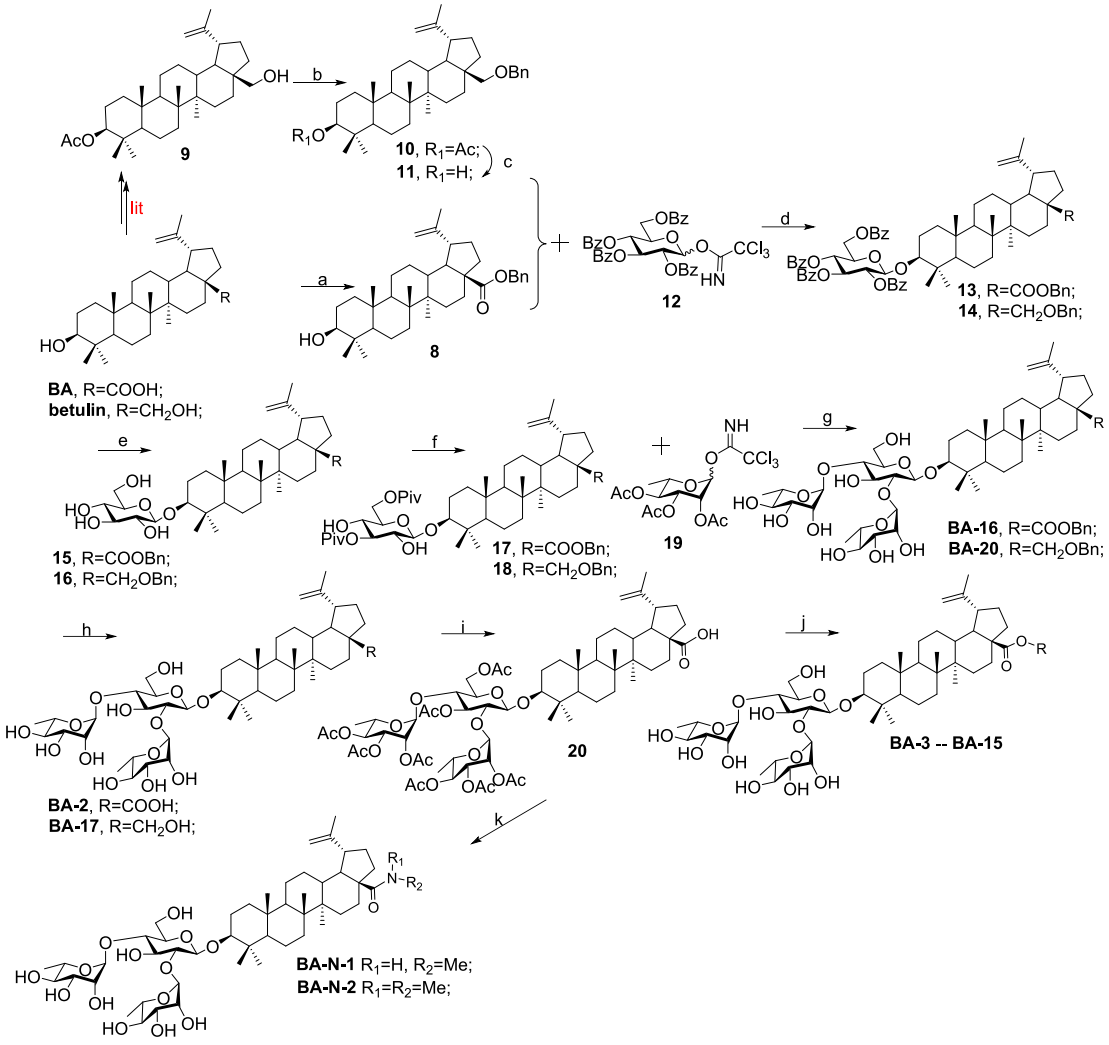

Scheme 1. Reagents and conditions: (a) BnBr, K_2CO_3, DMF; (b) benzyl 2, 2, 2-trichloroacetimidate, TfOH, CH_2Cl_2; (c) LiOH, THF-MeOH-H_2O; (d) TMSOTf, 4 Å Ms, CH_2Cl_2; (e) CH_3ONa, MeOH; (f) PivCl, CH_2Cl_2; (g) (i) TMSOTf, 4 Å Ms, CH_2Cl_2; (ii) NaOH, MeOH-THF-H_2O; (h) 10 % Pd/C, H_2, MeOH-THF; (i) (i) Ac_2O, DMAP, pyridine; (j) (i) various bromide alkanes, K_2CO_3, DMF; (ii) CH_3ONa, MeOH; (k) (i) $(COCl)_2$, CH_2Cl_2 (ii) $R_1R_2N\bullet HCl$, Et_3N, CH_2Cl_2; (iii) CH_3ONa, CH_3OH.

With the glycosyl donor 2, 3, 4-tri-*O*-acetyl-L-rhamnopyranosyl trichloroacetimidate **19** [30] and acceptor **17** or **18**, the glycosylation reaction was then performed under TMSOTf activation to provide crude trisaccharides, followed by sodium hydroxide (NaOH)-mediated deprotection to give the title compound **BA-16** or **BA-20**, respectively. Using 10 % Pd/C as a catalyst, hydrogenolysis of the benzyl group in **BA-16** or **BA-20** was carried out smoothly to provide the title saponin **BA-2** or **BA-17**, respectively. Then the intermediate **20** was obtained from **BA-**

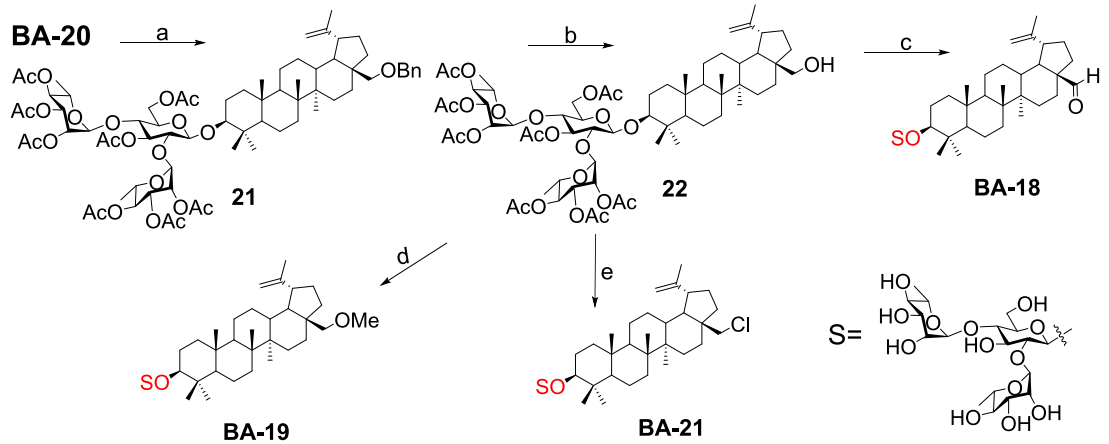

Scheme 2. Reagents and conditions: (a) Ac_2O, DMAP, pyridine; (b) 10 % Pd/C, H_2, MeOH-THF; (c) (i) PCC, CH_2Cl_2; (ii) CH_3ONa, MeOH; (d) (i) CH_3I, Ag_2O, ACN; (ii) CH_3ONa, MeOH; (e) (i) $SOCl_2$, CH_2Cl_2; (ii) CH_3ONa, MeOH.

2 through a direct acetylation reaction with acetic anhydride, which served as the coupling partner for subsequent diversifications, respectively. Under the basic conditions, the corresponding alkyl residues were incorporated at the C-28 position of BA in **20**, followed by removing all the acetyl groups using the similar method as **15** and **16** to afford the subseries **BA-3** – **BA-15** (Table 2), with different hydrophobic substituents at the C-28 position of BA core. On the other hand, **20** was treated with oxalyl chloride to furnish 28-acyl chloride, which was then condensed with appropriate amines, followed by removal of all the Ac groups with MeONa to give the corresponding target saponins **BA-N-1** and **BA-N-2**, respectively.

The following attempts were made to decorate the hydroxymethylene moiety at the C-17 position of **BA-17** to expand our chemical diversity. As depicted in Scheme 2, treatment of **BA-20** with acetic anhydride as did **20** gave rise to **21**, followed by hydrogenolysis of the benzyl group in **21** over palladium/carbon to yield the important intermediate **22**, which served as the starting partner for subsequent diversifications, respectively. On the one hand, **BA-17** was converted to the corresponding aldehyde **BA-18** by reaction of **22** with the freshly prepared PCC reagent, which then undergo hydrolysis reaction with CH_3ONa similarly as compounds **15** and **16**. On the other hand, nucleophilic substitution of **22** with methyl iodide, followed by CH_3ONa-mediated deprotection of all Ac groups gave rise to **BA-19**. In addition, by treating with thionyl chloride, compound **22** was readily converted into chlorides, of which all the Ac groups were then hydrolyzed using CH_3ONa to afford the title saponin **BA-21**.

2.2. Hit discovery

Previous screening efforts focused on human CoVs (SARS-CoV, HCoV-229E) and consequently revealed these BA-based molecules with potential could inhibit SARS-CoV-2 or other variants in the SARS-CoV-2 family. Since the chacotrioside moiety, a 2, 4-branched trisaccharide residue, has been characterized as an antiviral-privileged fragment [30,31], we supposed that introducing this moiety into BA might enhance the potency of pharmacologically active molecules. Thus, we decided to fuse this unique fragment to BA at the C-3 position, giving rise to the saponin **BA-1** (Fig. 1B). Initial attempts to confirm the inhibitory effects of BA and **BA-1** on infectious SARS-CoV-2 virus (wuhan-HU-1 variant) were made in a BSL-3 facility, wherein we determined their EC_{50} values against authentic SARS-CoV-2 in Vero-E6 cells using a full-time treatment model. Encouragingly, **BA-1** proved to be a highly effective SARS-CoV-2 inhibitor with an EC_{50} value of 0.51 μM, which did not exhibit cytotoxicity against Vero E6, even at a concentration of 50 μM (Fig. 2A). This data demonstrated that **BA-1** might interfere only slightly with the growth of Vero E6 cells and could inhibit specifically SARS-CoV-2 in cell cultures. In contrast to **BA-1**, the starting compound BA was virtually inactive (Table 1), implying that the privileged

Table 1
anti-SARS-CoV-2 and inhibitory activities against 3CL of BA and **BA-1**.

Compound	Anti-SARS-CoV-2 EC_{50}[a] (μM)	inhibition rate against 3CL (%)[b]		
		100	50	25
BA	>20	72.2	51.4	30.2
BA-1	0.51 ± 0.19	31.3	22.6	18.5
Ebselen	0.08 ± 0.01	98.5	97.6	96.2

[a] The samples were examined in Vero-E6 cells in triplicate. Vero-E6 cells were incubated with test compounds and SARS-CoV-2 (wuhan-HU-1 variant), and the concentration of test compound resulting in 50 % cell protection was reported as the EC_{50}. Values are the mean of three experiments, presented as the mean ± standard deviation (SD). [b]Inhibitory rate against 3CL based on the FRET assay. Data are expressed as the mean ± SD of three experiments.

β-chacotriosyl moiety is critical for the anti-SARS-CoV-2 activity. Briefly, these results suggested that the 3-*O*-*β*-chacotriosyl betulonic acid methyl ester **BA-1** possessed excellent efficiency against SARS-CoV-2 and promising safety, which should be identified as a hit for further development.

Due to its pivotal role in the SARS-CoV-2 life cycle that is involved in the viral maturation process to cleave the virus-encoded polyproteins, the 3CL protease has become a key target for discovery of anti-SARS-CoV-2 agents. It has been confirmed that BA possessed moderate inhibitory effects on SARS 3CL protease activity with an IC_{50} value of 10 μM [28]. SARS 3CL and SARS-CoV-2 3CL are structurally similar members of the human CoV family, sharing high homology and similarity in sequences, structures, and functions [32]. Thus, in parallel, these two compounds were also evaluated for inhibition of SARS-CoV-2 3CL protease activity based on a quenched fluorescence energy transfer (FRET) method where Ebselen was used as a positive control. As expected, BA displayed an acceptable enzyme inhibitory effect, especially at a high concentration 100 μM (Table 1). In contrast, **BA-1** only exhibited weak inhibitory ability with a 31.3 % inhibition rate at 100 μM, consistent with a low equilibrium dissociation constant (K_D) value of 46.3 μM (Fig. 2B) on the basis of a surface plasmon resonance (SPR) analysis, suggesting that **BA-1** inhibited replication of SARS-CoV-2 through a different mechanism or pathway from BA and the positive control Ebselen. Collectively, these results demonstrate that **BA-1** has a potent anti-SARS-CoV-2 activity with a high selectivity index in cell culture models but its antiviral potency is independent of inhibition toward 3CL protease.

2.3. Target identification

Evidence from several reports has illustrated that BA derivatives could effectively interfere with the fusion of the incoming virus to the host cell membrane to block HIV/H5N1/SARS and other viral entry into

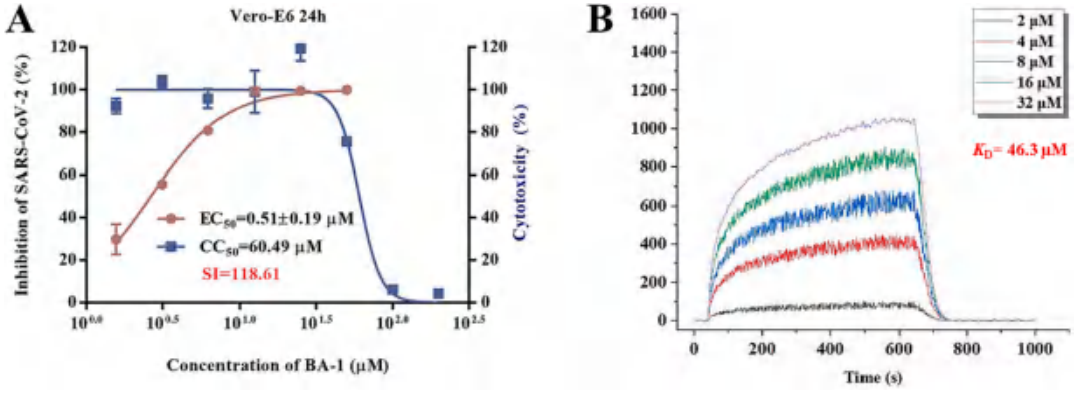

Fig. 2. (A) Evaluation on cytotoxicity of **BA-1** and inhibitory activity against authentic SARS-CoV-2 virus (wuhan-HU-1 variant) infection in Vero-E6 cells. (B) SPR analysis of the interaction between **BA-1** with SARS-CoV-2 3CL.

Table 2
Inhibitory activities of saponins **BA-1**-**BA-16** against infection of 293 T-ACE2 cells by pSARS-CoV-2.

Compound	R	EC_{50} [a] (μM)	CC_{50} [b](μM)	SI[c]
BA-1	CH_3	4.64 ± 0.52	40.88 ± 0.25	8.81
BA-2	OH	> 20.00	NT	NT
BA-3	Et	3.70 ± 0.72	36.12 ± 1.05	9.76
BA-4	*n*-propyl	3.12 ± 0.40	39.13 ± 0.73	12.54
BA-5	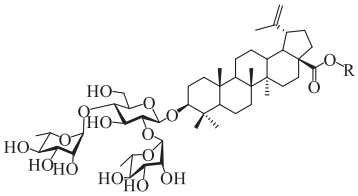	6.42 ± 0.20	76.49 ± 1.23	11.91
BA-6	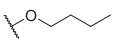	5.37 ± 0.37	24.36 ± 0.33	4.54
BA-7	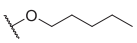	5.54 ± 0.81	16.39 ± 0.19	2.96
BA-8	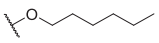	6.05 ± 0.38	47.25 ± 0.63	7.81
BA-9		> 20.00	NT	NT
BA-10		7.67 ± 0.31	51.81 ± 1.35	6.75
BA-11	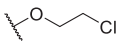	9.03 ± 0.56	46.12 ± 0.31	5.11
BA-12	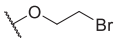	> 20.00	NT	NT
BA-13	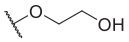	8.61 ± 0.47	36.21 ± 0.75	4.21
BA-14	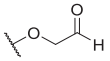	8.23 ± 0.55	84.62 ± 0.76	10.28
BA-15		15.90 ± 0.82	75.52 ± 1.63	4.75
BA-16	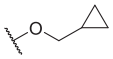	3.13 ± 0.42	12.79 ± 0.25	4.09
Sal-C	/	4.06 ± 0.51	>100.00	>24.63

[a] The samples were examined in 293 T-ACE2 cells in triplicate. 293 T-ACE2 cells were incubated with test compounds and pSARS-CoV-2, and the concentration of test compound resulting in 50 % cell protection was reported as the EC_{50}. Values are the mean of three experiments, presented as the mean ± standard deviation (SD). [b]50% cellular cytotoxicity concentration (CC_{50}). [c]SI: selectivity index as CC_{50}/EC_{50}.

test cells in the low micromolar range [28,33]. Considering the similarity between the viral fusion proteins such as gp41/HIV-1, HA2/H5N1, GP/EBOV and S2 of SARS-CoV-2, all of which play key roles in virus-induced membrane fusion, we speculated that a further anti-SARS-CoV-2 mechanism of **BA-1** might be the blocking of SARS-CoV-2 entry by inhibiting the membrane fusion, thereby disrupting viral entry into the host cells. To confirm our hypothesis, **BA-1** was firstly evaluated in a luciferase-expressing pseudovirus encoding SARS-CoV-2 S protein (pSARS-CoV-2) inhibition assay, which allowed for direct comparison of S protein function with a common lentiviral core and reporter [23]. Notably, we found that **BA-1** exhibited the similar capability in effectively inhibiting pSARS-CoV-2 as the positive control Sal-C, a small-molecule SARS-CoV-2 entry inhibitor previously shown to bind S directly [23], and the inhibitory effect was concentration-dependent with an EC_{50} value of 4.64 μM (Fig. 3A). It was interesting that **BA-1** displayed not only negligible inhibition toward VSV-G pseudovirus (Fig. 3A) but also marginal cytotoxicity against 293 T-ACE2 cells (HEK293T cells overexpressing human angiotensin-converting enzyme 2) within the effective concentration range (Fig. 3B). These results highlighted that **BA-1** could exert inhibitory activity against SARS-CoV-2 entry by targeting the S protein and the similarity in the potency of **BA-1** between the pseudovirus and infectious virus assays supported the validity of the S/HIV-based anti-SARS-CoV-2 assay used in 293 T-ACE2 cells.

Having identified S as the potential target, we then utilized the cell–cell fusion assay mediated by SARS-CoV-2 S protein to explore whether **BA-1** had any effect on the viral membrane fusion, the critical step for entry of SARS-CoV-2 viruses into host cells for initiation of virus infection. As shown in Fig. 3C, **BA-1** was identified to potently interfere with the membrane fusion of S-overexpressed-HEK293T and Vero-E6 cells in a marked dose-dependent manner at 24 h, demonstrating that its antiviral potency apparently involved action on SARS-CoV-2 S-mediated membrane fusion. Taken together, **BA-1** represents a novel SARS-CoV-2 fusion inhibitor, which was selected as a promising structure for further research and optimization.

2.4. Proposed binding mode of hit to the spike protein

In view of SARS-CoV-2 S as the important target and the membrane fusion interaction between virus and host cells as the critical interruption event, we performed blind docking calculations based on the X-ray crystal structures of SARS-CoV-2 S (PDB code: 6VXX) to investigate the potential binding site. A proposed binding mode of **BA-1** was established (Fig. 4), which indicated that **BA-1** could occupy well a cavity between the S1 and S2 subunits at the entrance to a large tunnel that links with equivalent tunnels from the other monomers of the trimer at the threefold axis. As shown in Fig. 4, at the upper region of the cavity, the hydrophilic chacotriosyl residue of **BA-1** made multiple stable hydrogen bonds with the backbone of residues Thr961, Leu303, Arg765, and Lys964 to result in increased interaction with S, further supporting the proposition that that the trisaccharide moiety was vital to improve antiviral activity. Hydrophobic pentacyclic triterpenoid skeleton of **BA-**

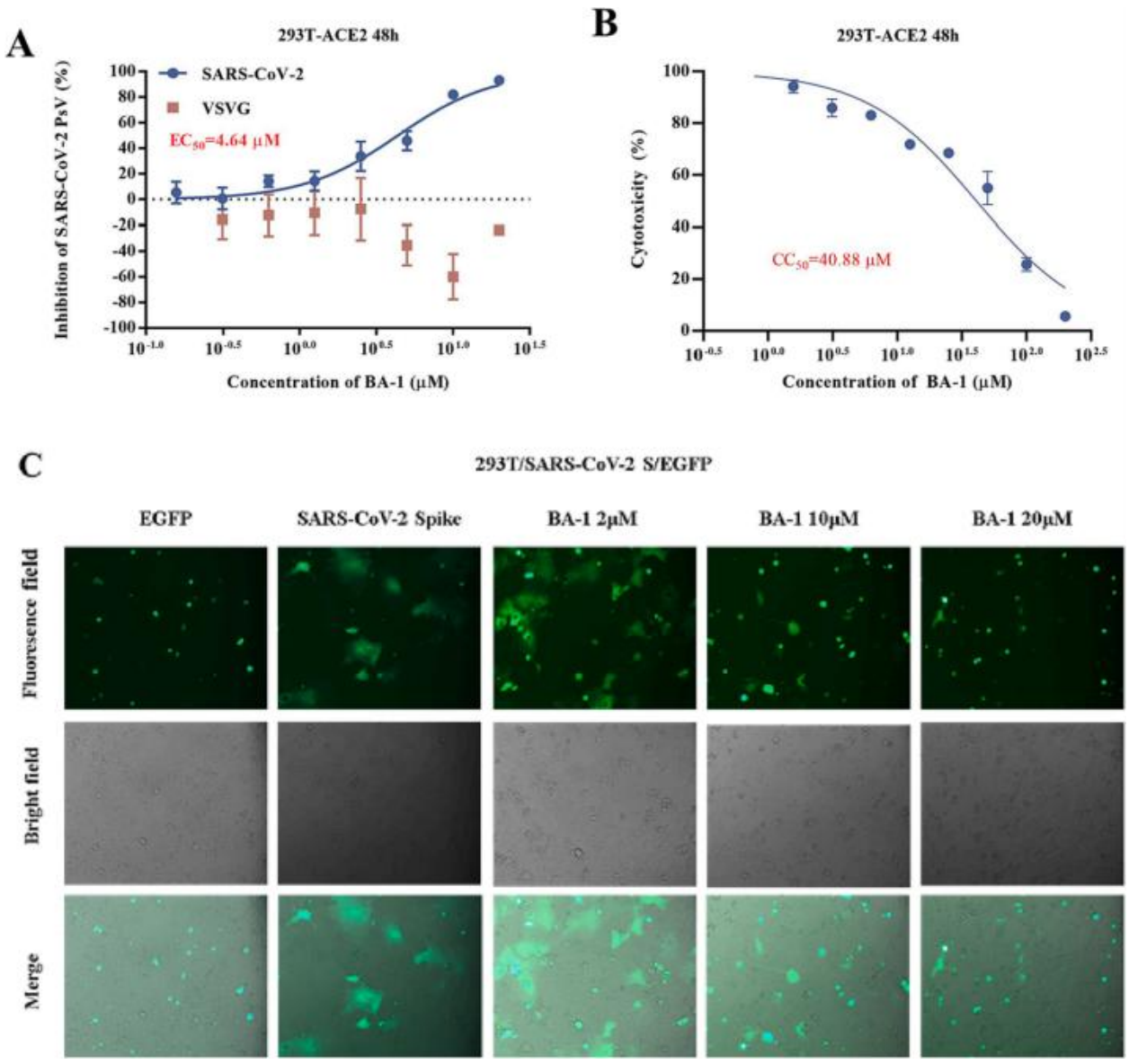

Fig. 3. (A) Dose-response curves and EC_{50} of **BA-1** on inhibiting the entry of SARS-CoV-2 PsV and VSV-G in 293 T-ACE2 cells. (B) Evaluation on cytotoxicity of **BA-1** in 293 T. (C) **BA-1** inhibited pSARS-CoV-2 infection by dose-dependent blocking of S-mediated membrane fusion.

1 occupied a large lipophilic region located in the middle of the cavity, creating a tight hydrophobic interaction with the side chain of Val772 to maintain the active conformation of **BA-1**.

To further confirm the above binding mode, we conducted the single amino acid mutagenesis of pSARS-CoV-2 S to understand the molecular basis of fusion inhibition by the hit **BA-1**. As indicated by the preliminary mutagenesis studies (Fig. 5), the pSARS-CoV-2 N764A/R765A/Q957A/K964 A mutations resulted in a significant loss of potency toward **BA-1** in dose-dependent fashion relative to WT S. In short, the docking result, supported by the mutagenesis studies, led us to propose a potential SARS-CoV-2-S binding pose of **BA-1**, which reflected some characteristics that could guide subsequent structural modification and optimization.

2.5. Design of novel SARS-CoV-2 fusion inhibitors

The proposed mode analysis indicated that the hit **BA-1** fitted well in the binding region, where important hydrogen-bond networks were observed between the chacotriosyl moiety and the cavity. However, there was still some space for further modification to fit better in the binding site. On the basis of the proposed mode, we identified a hydrophobic region under the aglycone core that is formed by D663, P665, V772, D775 and K776 residues. As depicted in Fig. 4, the C-17 position of **BA-1** seemed well positioned to extend into this pocket but there is no chemical structure that can form stable interactions with this region. We reasoned that this cavity could be presumably occupied by an alternative bulky group like an ethyl ester substituent or another type of linear/ring structure to yield better intermolecular interactions to improve potency. Here, our strategy was to enhance antiviral activity by extending from the 17-position of the aglycone BA to fill the bottom area of the binding cavity. At the other side of the molecule, the *β*-chacotriosyl fragment moiety probably needs to be kept since it forms multiple hydrogen bonds with S protein. It is noteworthy that most of the pocket residues are conserved, which highlights the relevance of this S interface pocket for new SARS-CoV-2 fusion inhibitors design. Briefly, we attempted to improve potency further by increasing steric bulk to more completely occupy this area of the binding pocket and derive additional hydrophobic contacts, which resulted in a set of 3-*O*-*β*-chacotriosyl BA derivatives.

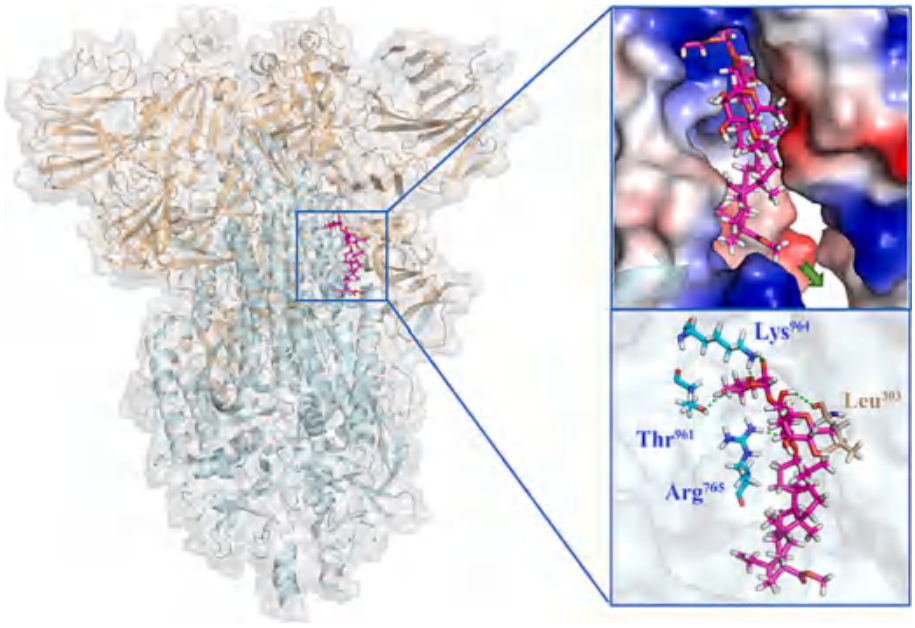

Fig. 4. Molecular docking of **BA-1** to spike protein (PDB: 6VXX). S1 subunit, S2 subunit, and **BA-1** were shown as orange ribbon, blue ribbon, magenta sticks, respectively. Green dashes in the interaction plot indicating hydrogen bond. (For interpretation of the references to colour in this figure legend, the reader is referred to the web version of this article.)

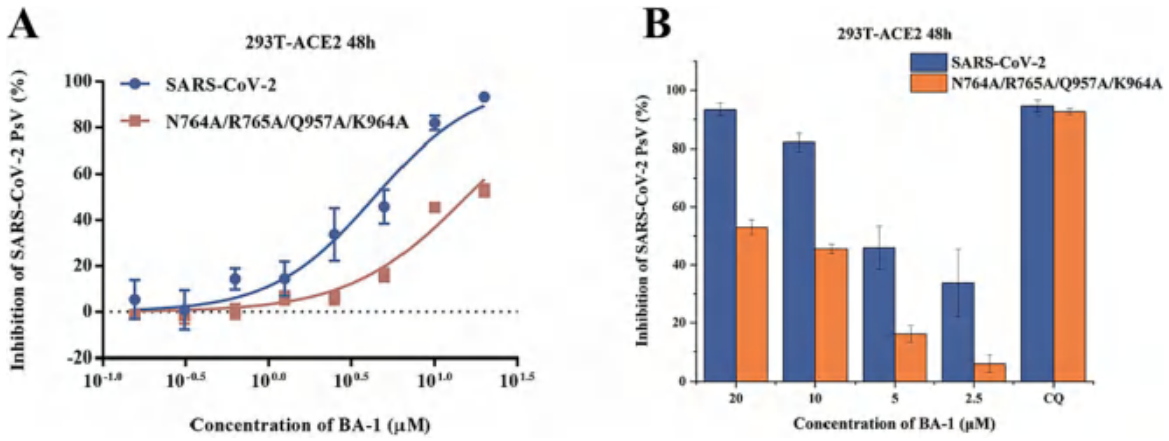

Fig. 5. (A) Inhibitions of **BA-1** against SARS-CoV-2 PsV and its mutants infections in 293 T-ACE2 cells, including N764A/R765A/Q957A/K964A. (B) Antiviral efficacy of **BA-1** against SARS-CoV-2 PsV mutants caused by site-directed mutation, including N764A/R765A/Q957A/K964A.

2.6. Sars of the BA saponins modified at 28-position

We focused our SAR campaign on investigating the alkyl groups at the C-28 position of BA, to a lesser extent, the linker at the C-17 position. Initially, we changed the ester moiety at the C-17 position of **BA-1** into amide moiety as its bioisosteric surrogates (compound **BA-N-1** and **BA-N-2**) to investigate their influence on biological activity. Unexpectedly, **BA-N-1** and **BA-N-2** showed significantly reduced inhibition against pSARS-CoV-2 entry relative to **BA-1** (Figure S1), presumably due to unfavorable conformation. For example, **BA-N-1** and **BA-N-2** only exhibited about 50 % inhibition rate against pSARS-CoV-2 at high concentration 20 μM. Thus, further amide modifications incorporated at the 17-position of BA were not pursued and we turned attention to the ester linker in this study. To identify novel and potent SARS-CoV-2 entry inhibitors, we performed a screen of the above two series of 3-*O*-*β*-chacotriosyl BA derivatives **BA-2**–**BA-16** based on the established pseudovirus model of SARS-CoV-2 (S/HIV) under low level containment (biosafety level 2) while VSVG/HIV pseudoviral transduction was used as a specificity control to exclude inhibitory effect on post-entry for HIV infection. As shown in Table 2, the variety of structural modifications described herein, especially the incorporation of bulky alkyl or aryl substituents, furnished compounds either almost equipotent or more potent against pSARS-CoV-2 virus while no effects on VSVG (Figure S2). Among these analogs, the 28-*n*-propyl-substituted analogue **BA-4** showed the strongest inhibition toward pSARS-CoV-2 virus coupled with the highest selectivity index (SI = 12.54).

To continue probing interactions with the potential binding pocket, our initial efforts were made by changing the length, size or type of the fragments linked by ester group at the C-28 position of BA to fine-tune the hydrophobicity effects on the antiviral activities, exampled by the analogs **BA-2**–**BA-16**. As illustrated in Table 2, the free carboxylic acid **BA-2** exhibited a significant decrease in potency against pSARS-CoV-2 relative to **BA-1** (EC_{50} > 20.00 μM), probably due to limited membrane permeability. Careful examination on the chemical structure of **BA-2** revealed that the carboxylic acid moiety may be responsible for its inferior cellular activities, which is known to negatively impact cell

membrane permeability. However, ethyl ester **BA-3** displayed a slight increased potency (EC_{50} = 3.63 μM) compared to **BA-1**. These findings reveal that the substitutions at the C-28 position of BA may play an important role in the drug-target interactions and appropriate C-28 substitutions are helpful in improving the antiviral potency, especially against SARS-CoV-2 virus. Based on the docking analysis, we inferred that this cavity could accomodate an alternative larger substituent than ethyl group and further chemical optimization at the side chain of **BA-1** probably led to more potent entry inhibitors. This hypothesis gave rise to analogs **BA-4**–**BA-8** (Table 2) with improved (**BA-4** vs **BA-1**) or maintained inhibitory activities. Notably, augmenting the length and hydrophobicity of R substituent with *n*-propyl group (**BA-4**) led to 1.5-fold enhanced inhibitory activity (EC_{50} = 3.12 μM) **BA-1**, rendering compound **BA-4** as the most potent candidate against pSARS-CoV-2 entry identified in the preliminary SAR optimization attempt. The improvement in potency may be attributed to the fact that the *n*-propyl group (**BA-4**) can occupy the binding pocket more because of its bigger bulk than methyl group to enhance the intermolecular hydrogen and hydrophobic interactions with SARS-CoV-2 S (see Fig. 9B). However, an increase in the length (**BA-5**, **BA-6** and **BA-7**) or volume (**BA-8**) of the hydrophobic side chain via the inclusion of a *n*-butyl, *n*-pentyl, *n*-hexyl or isopropyl moiety at the 28-position of BA did not lead to more active compounds but coupled with different effects on cytotoxicity against 293 T-ACE2 cells. For example, the replacement of methyl moiety with *n*-butyl group (**BA-5**) or isopropyl residue (**BA-8**) resulted in a slight drop in antiviral potency while there was concomitant decrease in cytotoxicity against 293 T-ACE2 cells. In contrast to compound **BA-5**, the replacement by longer *n*-pentyl (**BA-6**) or *n*-hexyl (**BA-7**) presented a 1.7- to 2.5-fold increased toxic while keeping similar anti-SARS-CoV-2 activities. These data suggest that the side chain length at the C-28 position of BA is a critical component of both antiviral activity and selectivity index for this chemotype. In additional to these linear alkyl residues, the substitution of the methyl group in **BA-1** with ring structures such as a cyclohexyl moiety generated **BA-9**, and surprisingly, the activity observed in pseudoviruses was entirely lost against pSARS-CoV-2 (Table 2). This data revealed that the volume size of R subsite was limited and this moiety was intolerant to cyclic alkyl chains. Collectively, these results demonstrated that a hydrophobic alkyl side chain with a length between 1 and 4 atoms at the position 28 of BA is optimal for inhibition against SARS-CoV-2 entry, which seems to accept a short and linear structure.

The encouraging antiviral profiles of compounds with small linear alkyl substituents, exampled by **BA-3** and **BA-4** prompted an examination of introduction of functional groups into the preferred ethyl or *n*-propyl substituent to form additional potential interactions, exampled by the analogs **BA-10**–**BA-16** (Table 2). With the exception of 2′- hydroxyl derivative **BA-12**, these analogs exhibited comparable or slightly reduced antiviral activity compared to **BA-4**, as a result, their potency was still potent enough to emphasize the significance of the modification of side chains attached to C-28 position of BA. Among this set of derivatives, chlorine derivative **BA-10** was more active than the corresponding bromine derivative **BA-11** though 2.4-fold decreased potency relative to **BA-4**. However, insertion of a hydroxyl group into ethyl moiety (**BA-12**) led to a total loss of potency, of while oxidic product **BA-13** could maintain comparable potency to **BA-1**, supporting the need for the general high hydrophobicity required for the side scaffold at the C-28 position of BA. To weaken cytotoxic activity, we incorporated in our chemical optimization campaign modifications to the preferred **BA-4** based on the conformational constraints strategy, anticipated to enhance selectivity index. As shown in Table 2, the incorporation of a rigid carbon–carbon double bond (**BA-14**) led to a 2.6-fold reduced potency coupled with remarkably decreased cytotoxicity compared to **BA-4**, thereby displaying a similar SI as **BA-4** but superior to **BA-1**. This result implied that the unsaturated fragment was tolerated on the alkyl side chain region in this set of SARS-CoV-2 entry inhibitors. In contrast to compound **BA-14**, the cyclized derivative **BA-15** suffered a significant 4.9-fold loss of inhibition against pSARS-CoV-2 probably due to steric clashes with S protein, though it displayed reduced cytotoxicity as did **BA-14**. To address this gap, we hypothesized that it was better to incorporate the cyclized aromatic group through a flexible linker at the C-28 position of BA to form additional interaction with S protein. As expected, benzyl ester (**BA-16**) demonstrated comparable potency to **BA-4** against pSARS-CoV-2 (EC_{50} = 3.13 μM) while showing increased cytotoxicity. As seen in Fig. S3A, the docking model demonstrated that the introduced benzyl moiety was extended to the inside of hydrophobic pockets and formed tight Van der Waals interactions with Pro665 and Val772 residues, and thus made a good functional ligand–protein interaction. In short, these results again emphasize the importance of the property, type, and size of the R substituent at the C-28 position of BA for exhibiting inhibition against pSARS-CoV-2.

2.7. Sars of the betulin derivatives

For better orientation of the tail region of **BA-1** into the new hydrophobic pocket, we then shifted our focus onto the more flexible ether linker moiety at the 17-position of of BA. Firstly, we proceed to investigate the effect of the 17-COOH of BA on the anti-SARS-CoV-2 activity through reduction of the carboxyl group. As depicted in Table 3, the betulin saponin **BA-17** displayed no potencies in cellular assays as did the unsubstituted acid analogue **BA-2**, supporting the highly hydrophobic nature of the potential new SARS-CoV-2-S binding site. Interestingly, further optimization for potencies through oxidation of hydroxyl group at the 28 position of **BA-17** was achieved in betulinicaldehyde saponin **BA-18** with an EC_{50} value of 5.12 μM, which indicated the requirement of the hydrophobic properties at the 17 position of the aglycone skeleton to maintain highly potent inhibitory activity against pSARS-CoV-2. The observation prompted us to examine the potential of more hydrophobic modification around the hydroxyl group in betulin at the 28 positon. Therefore, a small set of 3-*O*-*β*-chacotriosyl betulin derivatives **BA-19** – **BA-21** differing only in the substituent at the 17 position were picked for the preliminary SARs study. Although a bit less potent than the ester analogue **BA-1**, methyl ether of OH (**BA-19**) induced a markedly increase in inhibitory activity relative to **BA-17**, again highlighting that the enhancement of potency appeared to be correlated to the lipophilicity of the substituents at the 17 position. Interestingly, the introduction of benzyl group at the 28-position of **BA-17** yielded compound **BA-20** with moderate potency, which was 4.81-fold less active than its benzyl ester analogue **BA-16**. As seen in Fig. S3B, reduction of carbonyl group to methylene resulted in more flexible conformation of side chain linked at the 28 position, which would not stabilize the BA skeleton orientation and make the head chacotriosyl moiety shift toward the inside of the binding cavity, thus failing to form hydrogen bond with the critical residue Lys964. Since the hydrophobic interaction between the side chain and the new hydrophobic pocket was critical for increased potency of these SARS-CoV-2 entry inhibitors, we attempted to enhance the hydrophobic interaction by replacing hydroxyl group at the 28 position of **BA-17** with one chlorine atom to produce **BA-21**. Surprisingly, **BA-21** presented a substantial increase in SARS-CoV-2 entry inhibitory potency though it exhibited poor SI because of high toxic. One possible reason for the increased antiviral activity of **BA-21** was that the incorporation of chlorine atom into the end of the side chain at the 28 position led to a greater binding interaction energy with the active pocket in the S protein, as illustrated in Fig. S3C. This result reinforced the importance of the chlorine atom as a versatile design element for lead optimization while needing to balance between the potency and cytotoxicity.

Taken together, through our SARs effort, we discovered that the introduction of hydrophobic side chain at the 17 position of the aglycone BA was favorable to enhance anti-SARS-CoV-2 activities as a result of increased interaction with S. In the present SARs study, the type of linker at the 17 position of the aglycone may affect the preferential binding conformation between saponins and the S protein, which in turn affects

Table 3
Inhibitory activities of saponins **BA-17**-**BA-21** against infection of 293 T-ACE2 cells by pSARS-CoV-2.

Compound	R	EC_{50}[a] (μM)	CC_{50}[b](μM)	SI[c]
BA-17	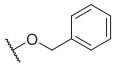	>20.00	NT	NT
BA-18	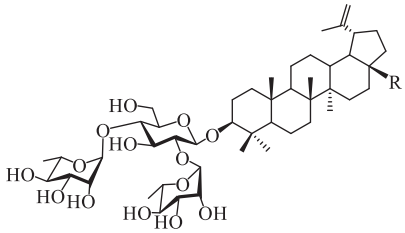	5.12 ± 0.31	29.86 ± 0.22	5.83
BA-19	CH_2OH	11.38 ± 1.41	34.18 ± 0.93	3.01
BA-20	CHO	15.07 ± 1.05	96.20 ± 1.88	6.38
BA-21	CH_2OCH_3	3.53 ± 0.18	15.01 ± 0.24	4.25
Sal-C	/	4.06 ± 0.51	>100.00	>24.63

[a] The samples were examined in 293 T-ACE2 cells in triplicate. 293 T-ACE2 cells were incubated with test compounds and pSARS-CoV-2, and the concentration of test compound resulting in 50 % cell protection was reported as the EC_{50}. Values are the mean of three experiments, presented as the mean ± standard deviation (SD). [b]50% cellular cytotoxicity concentration (CC_{50}). [c]SI: selectivity index as CC_{50}/EC_{50}.

inhibitory potency toward pSARS-CoV-2. Similarly, the intensity of the hydrogen bond between the chacotriosyl residue and the binding pocket as well as hydrophobic interaction formed by the aglycone with S may also change due to the introduction of the different substituent group at the 28 position, which will lead to changes in compound activity. In addition, the potency change was probably attributed to various factors including the length, volume and type of the substituent group at the 28 position, not just the hydrophobic properties. In general, the substitution of short and small-volume hydrophobic groups did improve the inhibitory effects of these saponins. Among them, **BA-4** stood out with the most potent antiviral activity *in vitro* and best selectivity index, rendering compound **BA-4** as the lead compound against SARS-CoV-2 entry identified in the SARs optimization attempt.

2.8. Broad inhibitory activities against Omicron and other variants

More recently, the emerged Omicron and Delta variants that bear multiple mutations in their S proteins have exhibited increased adaptability and transmissibility. The good potencies of representative compounds **BA-1** and **BA-4** against pSARS-CoV-2 prompted us to examine the inhibitory activity of these two saponins against emerging variants such as Omicron, Delta, and other variants with N501Y, D614G, E484K, or P681H single mutation in their S proteins, respectively. As shown in Table 4, the broad antiviral effects of **BA-1** and **BA-4** against these SARS-CoV-2 pseudoviruses containing multiple mutations in S protein were observed in micromole levels, implying that these newly developed BA saponins are broad-spectrum anti-SARS-CoV-2 agents that can block the S-mediated SARS-CoV-2 entry process. Notably, saponins **BA-1** and **BA-4** demonstrated comparable potency against Omicron pseudovirus to pSARS-CoV-2 with EC_{50}s of 7.04 μM and 4.66 μM, which was in good agreement with the SARs. Briefly, broad and appreciable inhibition of viral entry for all pSARS-CoV-2 variants tested, along with good selectivity index, highlights the lead compound **BA-4** as a potential antiviral candidate for the treatment of Omicron infections.

Table 4
Inhibitory activities of **BA-1** and **BA-4** against Omicron pseudovirus and other variants.

varians compds	EC_{50}[a](μM)					
	Omicron	Delta	N501Y	D614G	E484K	P681H
BA-1	7.04 ± 0.35	8.79 ± 0.22	5.84 ± 0.60	7.70 ± 0.41	8.41 ± 0.63	9.62 ± 0.50
BA-4	4.66 ± 0.52	4.25 ± 0.37	2.73 ± 0.31	3.01 ± 0.25	4.75 ± 0.58	5.19 ± 0.86

[a] The samples were examined in 293 T-ACE2 cells in triplicate. 293 T-ACE2 cells were incubated with test compounds and pSARS-CoV-2, and the concentration of test compound resulting in 50 % cell protection was reported as the EC_{50}.

2.9. Validation of Omicron s binding

Given the robust activity of the lead compound **BA-4** against Omicron, we used this virus to reveal its mechanism of action and appreciate how its anti-SARS-CoV-2 was. To explore whether the findings in the present SARS-CoV-2 study could be extended to Omicron, a similar VSV-based Omicron S protein-bearing pseudovirus (pv) was firstly used to assess the efficacy of **BA-4** on virus entry. As shown in Fig. 6A, **BA-4** exhibited a dose-dependent inhibition of Omicron pv infection while no inhibition was observed on VSV-G pseudoviral transduction. Moreover, it was found that **BA-4** showed strong binding affinity to S of Omicron variant with a K_D value of 0.36 μM based on a SPR assay (Fig. 6B), demonstrating that **BA-4** could directly target the Omicron S protein to block virus entry into hose cells.

2.10. *BA-4* could mediate membrane fusion of viral entry

Omicron entry into host cells can divided into two major steps: virus attachment to host cell receptor and virus-cell membrane fusion. As the lead compound **BA-4** could inhibit Omicron entry into hose cells by targeting S, we further dissected which steps were blocked by **BA-4**. As shown in Fig. 7A, **BA-4** displayed little effect on the interaction of Omicron S1 subunit with its ACE2 receptor based on a Co-Immunoprecipitation (Co-IP) assay, the critical step for recognition and attachment of Omicron to host cells for initiation of virus infection, suggesting that **BA-4** may be acting during Omicron S2 mediated fusion stage. Notably, **BA-4** was able to interfere with the membrane fusion of A549 cells mediated by Omicron S in a concentration-dependent fashion (as seen in Fig. 7B), supporting our hypothesis. Interestingly, we found that **BA-4** bound strongly to the Omicron S2 subunit, displaying a potent dose-dependent response, with a much higher K_D value of 85.2 pM (Fig. 7C) relative to S; no specific binding to Omicron S1 subunit was

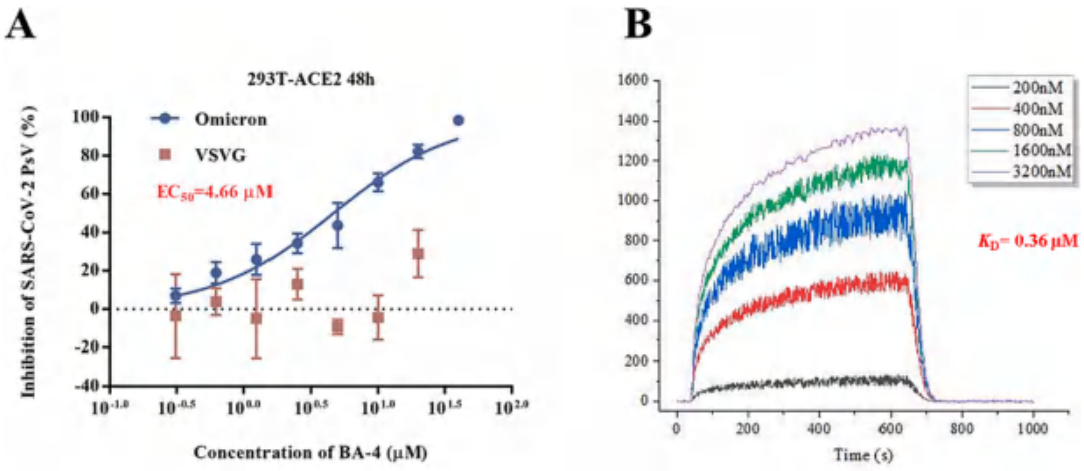

Fig. 6. (A) Dose-response curves and EC_{50} of **BA-4** on inhibiting the entry of Omicron and VSV-G in 293 T-ACE2 cells. (B) SPR analysis of the interaction between **BA-4** with Omicron S-trimer.

found for **BA-4** in the parallel experiment (Fig. 7D). Taken together, these results revealed that the lead compound **BA-4** had a specific affinity to S2, and thus interfered with the viral and cell membrane fusion, by which Omicron entry into host cells could be blocked.

2.11. BA-4 could target the prefusion state during viral-host fusion

Receptor engagement by RBD will induce conformation change of Omicron S2 subunit from the pre-fusion state to a post-fusion trimer-of-hairpins conformation to result in viral membrane fusion, where the 6-HB structure formed by HR1 and HR2 regions in the S2 subunit has been identified as a critical element of the trimer-of-hairpins [18]. For a better understanding of possible mechanism during the fusion of Omicron with cellular membranes treated by **BA-4**, we determined the biophysical change of 6-HB by using circular-dichroism (CD) spectroscopy as described before [23]. Unlike Sal-C that can target the 6-HB of SARS-CoV-2 (Figure S4), **BA-4** had negligible effect on inhibiting viral 6-HB formation (Fig. 8), demonstrating that **BA-4** exerted potent inhibitory effect on Omicron-cell membrane fusion by the different action mechanism from Sal-C. Based on these data, we speculated that a further anti-Omicron mechanism of **BA-4** might be the maintaining S protein in the pre-fusion step during the fusion of virus particle into host cells to inhibit Omicron entry.

To investigate the potential binding mode of our new compounds, selected **BA-4** was docked into Omicron S (PDB code: 7TF8) that is physically blocked in the pre-fusion state. As depicted in Fig. 9A, at the head region, stable hydrogen bonds between the *β*-chacotriosyl moiety and Lys964, Thr761, Arg765, Thr302, Glu309 as well as Leu303 are formed to create a critical interaction with the Omicron S protein, which is conducive to stabilizing the pre-fusion state of S to prevent its conformational rearrangements. In the center of the binding pocket, BA aglycone makes multiple Van der Waals interactions with Arg765, Val772, Pro665 and Ile312 residues, which is helpful in maintaining the active conformation of **BA-4**. In the underpart region, the *n*-propyl side chain at the 28 position of BA forms additional hydrophobic contacts with Lys310, validating that extension of methyl side chain in **BA-1** is contributing positively to binding with S. Consistent well with this result, **BA-4** adopts the similar binding mode with SARS-CoV-2 S (Fig. 9B), suggesting that there is a general similarity between the structure of the SARS-CoV-2 S binding pocket and that of other variants bearing S mutants. While a hydrophobic interaction between Lys310 in the binding cacity and the *n*-propyl residue appears to be weakened, both chacotriosyl moiety and BA skeleton of **BA-4** are able to be involved in multiple similar interactions with Lys964, Leu303, and other residues in this corresponding hydrophobic pocket as that with Omicron S. Thus, we hypothesize that the observed broad inhibition against pSARS-CoV-2 Omicron and other variants maybe results from the similar binding mode in this region with corresponding S protein. Taken together, the high conservation of residues located in this binding cavity among different SARS-CoV-2 strains, makes this cavity an ideal target for designing novel SARS-CoV-2 fusion inhibitors that can disrupt the the viral and cell membrane fusion to display broad antiviral activities.

2.12. Site-specific mutation of Omicron-S supports s binding as blocking inhibition of viral entry

Based on the CD spectroscopy and docking analysis, the potential mechanism of antiviral activity of the lead compound **BA-4** against SARS-CoV-2 is more intriguing as **BA-4**-binding site is physically blocked in the Omicron-S prefusion state. We next used the single amino acid mutagenesis of pOmicron S to confirm our hypothesis, where the representative residues K964 and R765 in the fusion loop of conserved S2 subunit were evaluated. When compared to WT Omicron, pOmicron S mutant K964A caused a right shift and an over 2.5-fold loss of potency in response to **BA-4** (Fig. 10A). Similarly, the pOmicron S mutant R765A showed only a modest right shift of the dose–response curve, possibly due to weaker hydrogen bond between R765 and S relative to K964 as seen in Fig. 9A. Furthermore, the similar trend of the response to **BA-1** in the pOmicron S mutant K964A or R765A was observed (Fig. 10B). The SARs and docking, supported by the mutagenesis studies, confirmed the binding of **BA-4** to the site near the key residue K964 in the binding cavity between the attachment (S1) and fusion (S2) subunits.

*2.13. Compound **BA-4** exhibited promising liver microsomes, intestinal S9-UDPGA and stability in mouse plasma*

Given that the lead compound **BA-4** displayed braod and promising anti-SARS-CoV-2 activities *in vitro*, we further evaluated the stability of **BA-4** *in vitro* metabolic stability in mouse liver, mouse intestinal S9-UDPGA and in mouse plasma, respectively. First, we evaluated the metabolic stability of **BA-4** in a mouse liver microsomes assay while propafenone with moderate metabolic stability was used as the control compound. As depicted in Table 5, compound **BA-4** displayed acceptable metabolic stability with a half-life value of 16.1 min in mouse liver microsomes, which was superior to 6.8 min of propafenone. Meanwhile, **BA-4** also exhibited reasonable clearance rates with the intrinsic clearance (CL) value of 59.3 μL/min/mg, which was 4-fold lowe than that of propafenone in the same assay (CL = 201.6 μL/min/mg). In addition, the stability of **BA-4** in mouse intestinal S9-UDPGA was also evaluated where clozapine was tested for comparison. Notably, **35** showed

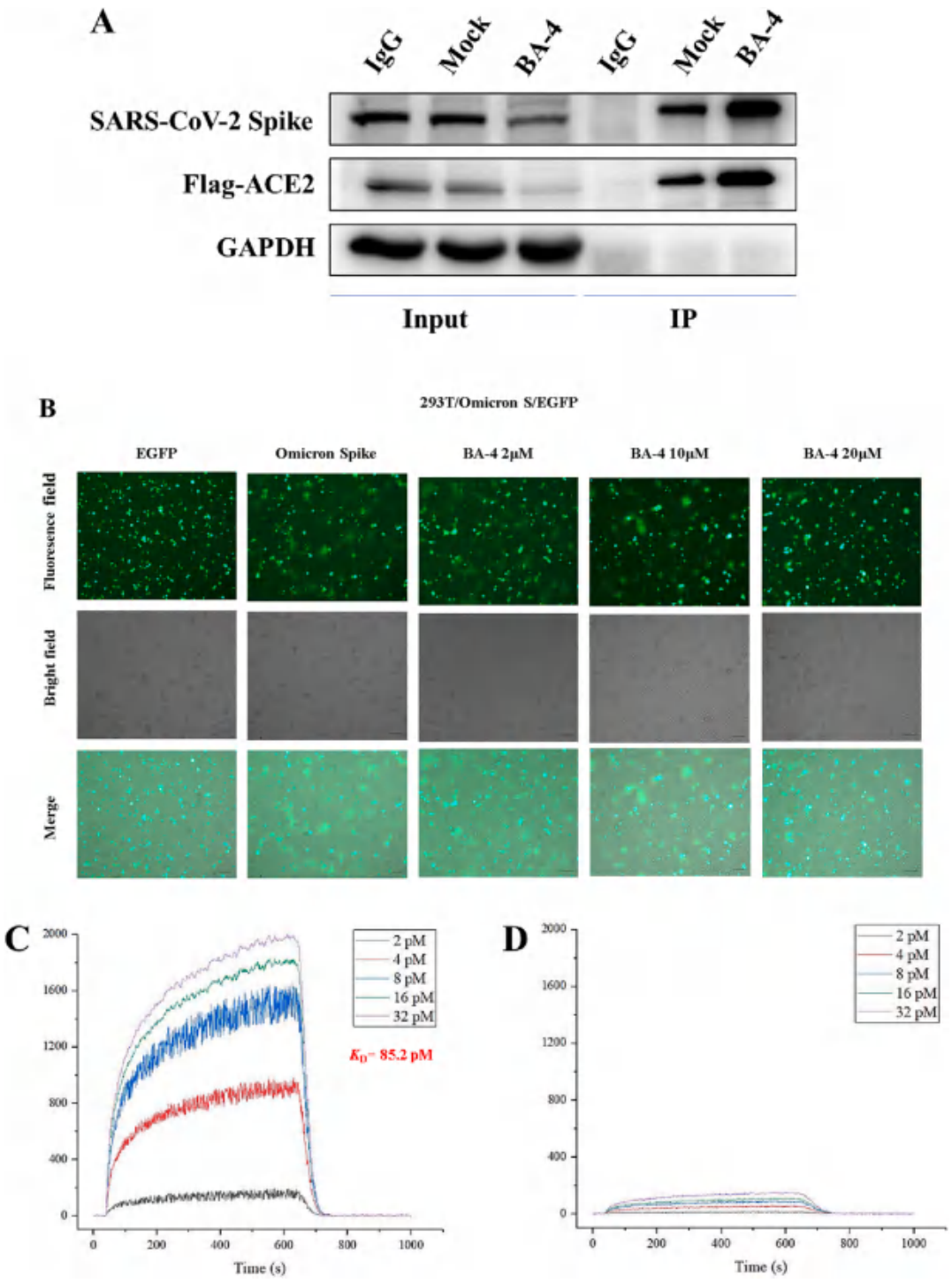

Fig. 7. (A) With addition of **BA-4** (20 uM), Co-IP assays showed no affection of the binding of SARS-CoV-2 S protein and ACE2 (anti-Flag). (B) **BA-4** inhibited SARS-CoV-2 Omicron mutant infection via blocking Omicron protein-mediated membrane fusion. (C) SPR analysis of the interaction between **BA-4** with Omicron S2. (D) SPR analysis of the interaction between **BA-4** with Omicron S1.

promising stability in mouse intestinal S9-UDPGA with higher half-life values of 77.8 min and lower CL value of 14.1 μL/min/mg compared to that of microsomal stability, though was inferior to those of clozapine.

Then we examined the stability of **BA-4** in mouse plasma using propantheline bromide as a reference. As shown in Table 6, **BA-4** exhibited moderate stability in mouse plasma, displaying an approximately 50 % compound retention after 120 min incubation, which was superior to that of the reference propantheline bromide. Collectively, these results reveal that the lead compound **BA-4** possesses acceptable metabolic stability in mouse liver microsomes and stability in mouse plasma as well as reasonable S9-UDPGA, which meets the basic requirements of ADMET.

3. Conclusions

This study presented here discovered a hit compound **BA-1** that showed good inhibition against infectious and pseudotyped SARS-CoV-2 virus by directly targeting the S protein. Based on the structure **BA-1**,

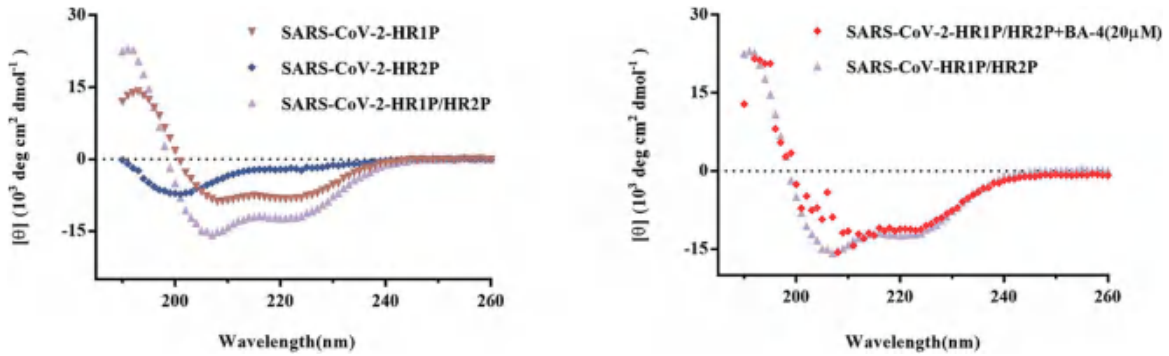

Fig. 8. The CD curve of the SARS-CoV Omicron HR1P/HR2P complex (purple) shows a characteristic α-helix spectrum with a minimum at 208 or 222 nm. The secondary structure of 6-HB in the HR1P/HR2P mixture was unaffected by the addition of **BA-4** (20 μM), as shown by the purple and red models. (For interpretation of the references to colour in this figure legend, the reader is referred to the web version of this article.)

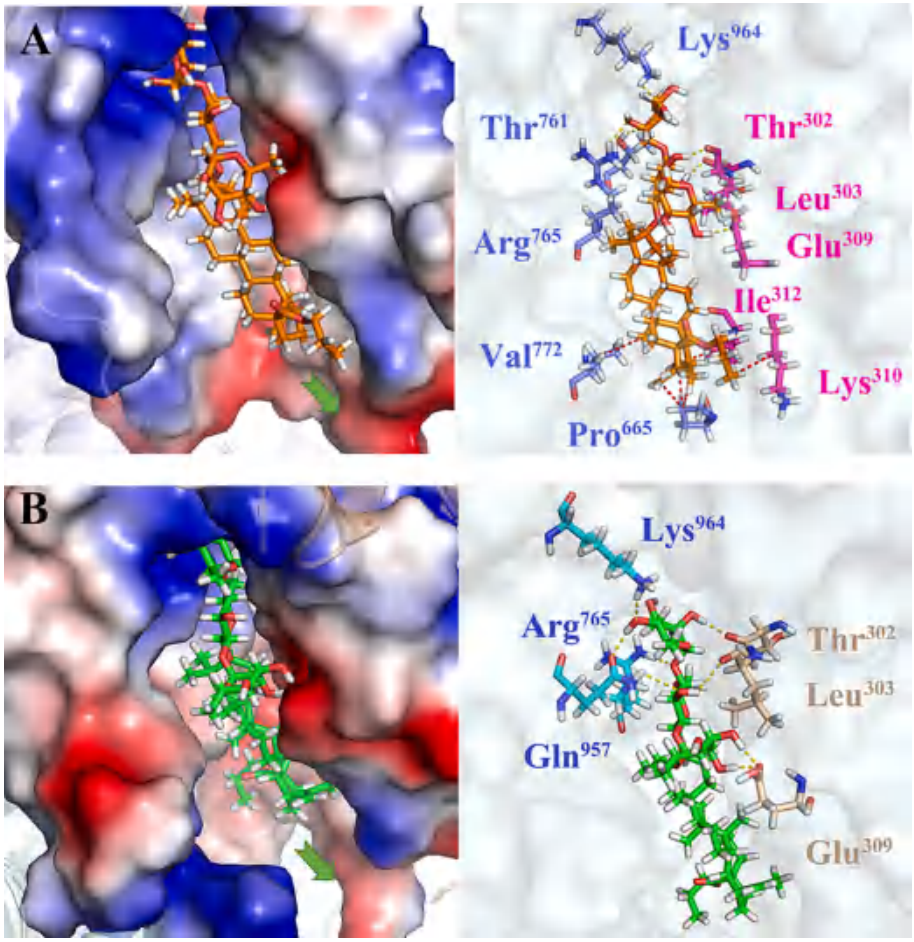

Fig. 9. (A) Molecular docking of **BA-4** to Omicron spike protein (PDB: 7TF8). S1 subunit, S2 subunit, and **BA-4** were shown as magenta ribbon, purple ribbon, orange sticks, respectively. Yellow dashes in the interaction plot indicating hydrogen bond. Red dashes in the interaction plot indicating hydrophobic interaction. (B) Molecular docking of **BA-4** to spike protein (PDB: 6VXX). S1 subunit, S2 subunit, and **BA-4** were shown as orange ribbon, blue ribbon, green sticks, respectively. Yellow dashes in the interaction plot indicating hydrogen bond. (For interpretation of the references to colour in this figure legend, the reader is referred to the web version of this article.)

rational drug design and subsequent chemical optimization resulted in the development of the lead compound **BA-4**, as a novel Omicron fusion inhibitor. Utilizing the SPR assay, CD spectroscopy, docking and mutagenesis studies, we confirmed that the anti-Omicron mechanism of **BA-4** was through directly binding to the S protein, which was capable of stabilizing S in the pre-fusion step to block Omicron entry into host cells. Moreover, the lead compound **BA-4** was found to have a broad-spectrum entry inhibition against all SARS-CoV-2 variants tested and display favorable SI values. Overall, **BA-4** represents a novel and potent Omicron fusion inhibitor and justifies further development as a potential candidate for treatment of SARS-CoV-2 infections.

4. Experimental

4.1. Chemistry

Solvents were purified in a conventional manner. Thin layer chromatography (TLC) was performed on precoated E. Merck silica gel 60 F254 plates. Flash column chromatography was performed on silica gel (200–300 mesh, Qingdao, China). ^{1}H NMR and ^{13}C NMR spectra were taken on a JEOL JNM-ECP 600 spectrometer with tetramethylsilane as an internal standard, and chemical shifts are recorded in ppm values. Mass spectra were recorded on a Q-TOF Global mass spectrometer.

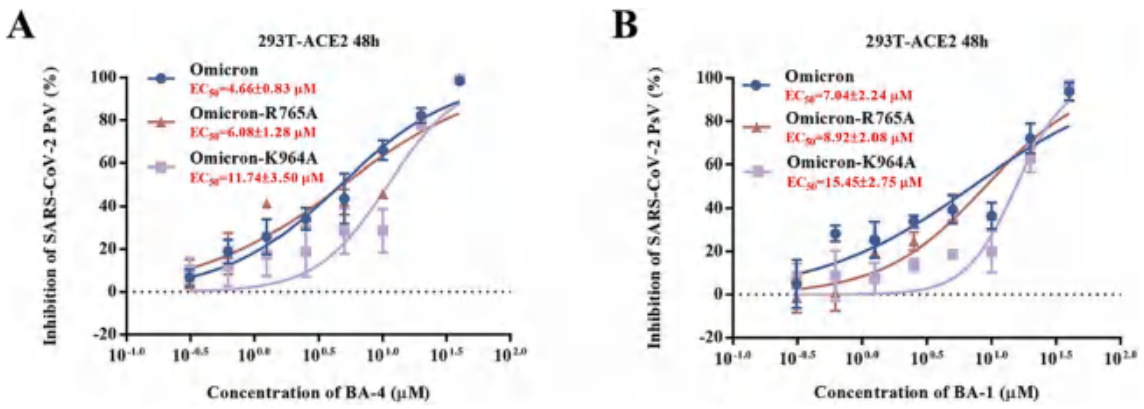

Fig. 10. (A) Inhibitions of **BA-4** against SARS-CoV-2 PsV mutants caused by site-directed mutation, including R765A, K964A. (B) Inhibitions of **BA-1** against SARS-CoV-2 PsV mutants caused by site-directed mutation, including R765A, K964A.

Table 5
Metabolic stability in the presence of mouse liver microsomes and stability in the intestinal S9-UDPGA of **BA-4.**

compd	mouse liver microsomes		mouse S9-UDPGA	
	$T_{1/2}$[a] (min)	$CL^{b}_{int(mic)}$ (μL/min/mg)	$T_{1/2}$[a] (min)	CL_{int}(*in vitro*)[b] (μL/min/mg)
BA-4	16.1	59.3	77.8	14.1
propafenone	6.8	201.6	/	/
clozapine	/	/	>145	<6.8

[a] $T_{1/2}$ is the half-life and $CL_{int\ (mic)}$ is the intrinsic clearance. [b]$CL_{int\ (mic)}$ = 0.693/half-life/mg microsome protein per milliliter.

Table 6
Stability of compound **BA-4** in mouse plasma.

incubation time (min)	**BA-4** remained mouse plasma (%)	Propantheline bromide remained mouse plasma (%)
0	100	100
30	73.6	45.5
60	61.3	18.2
90	53.4	10.3
120	47.5	2.0

4.1.1. 28-(Benzyloxy)-3β-acetoxy-lup-20 (29)-ene-3-ol (10)

To a solution of **9** (3.00 g, 6.19 mmol), benzyl 2, 2, 2-trichloroacetimidate (3.42 g, 13.62 mmol) and 4 Å molecular sieves in dry CH_2Cl_2 (50 mL) was added TfOH (0.14 g, 0.93 mmol) at −10 ℃ under N_2 atmosphere. The reaction mixture was kept at −10 °C for 2 h and warmed to room temperature for 1 h. After the reaction was complete detected by TLC, triethylamine was added to quench the reaction. The mixture was filtered and the filtrate was concentrated under reduced pressure. The residue was purified by silica gel column chromatography (petroleum-ether-EtOAc-CH_2Cl_2, 30:1:1) to yield **10** (3.16 g, 89 %) as a white solid. ^{1}H NMR (600 MHz, $CDCl_3$): δ 7.45–7.20 (m, 5H, Ar-H), 4.64 (s, 1H, C = CH_2-1), 4.56 (s, 2H, Ar-CH_2), 4.48 (s, 1H, C = CH_2-2), 3.51 (d, 1H, J = 8.9 Hz), 3.09 (d, 1H, J = 8.9 Hz), 2.35 (td, 1H, J = 10.6, 5.6 Hz), 2.03 (s, 3H, $COCH_3$), 1.66 (s, 3H, CH_3), 0.94 (s, 6H, 2 × CH_3), 0.84 (s, 9H, 3 × CH_3), 0.79 (d, 1H, J = 9.5 Hz, H-5); ^{13}C NMR (151 MHz, $CDCl_3$): δ 171.14, 150.85 (C-20), 139.13, 128.43 (two), 127.67 (two), 127.56, 109.64 (C-29), 81.07, 73.50, 68.15, 55.47, 50.38, 48.94, 48.10, 47.38, 42.71, 40.96, 38.47, 37.91, 37.54, 37.16, 34.98, 34.21, 30.10, 30.05, 28.07, 27.22, 25.25, 23.81, 21.44, 20.94, 19.18, 18.31, 16.62, 16.27, 15.89, 14.86. HRMS (ESI) *m/z*: calcd for $C_{39}H_{59}O_3$ $[M + H]^+$, 575.4464; found, 575.4478.

4.1.2. 28-(Benzyloxy)-3β-hydroxy-lup-20 (29)-ene-3-ol (11)

To a solution of **10** (3.16 g, 5.50 mmol) and LiOH (2.87 g, 0.12 mmol) in THF-MeOH-H_2O (90 mL) and then the reaction mixture was stirred at 50 ℃ for 12 h. After the reaction was complete detected by TLC, 1 M HCl was added to adjust pH = 7. The mixture was concentrated *in vacuo*. The residue was dissolved in EtOAc (150 mL), then extracted with water (3 × 50 mL) and brine (3 × 50 mL). The combined organic layer was concentrated under vacuum after drying over Na_2SO_4. The resulting crude was then purified by column chromatography (CH_2Cl_2-MeOH, 30:1) to give **11** (2.1 g, 72 %) as a white solid. ^{1}H NMR (600 MHz, $CDCl_3$): δ 7.37–7.31 (m, 5H, Ar-H), 4.64 (s, 1H, C = CH_2-1), 4.55 (s, 2H, Ar-CH_2), 4.48 (s, 1H, C = CH_2-2), 3.51 (d, 1H, J = 8.9 Hz), 3.09 (d, 1H, J = 8.9 Hz), 2.35 (td, 1H, J = 10.7, 5.6 Hz), 1.66 (s, 3H, CH_3), 0.96, 0.94, 0.84, 0.79, 0.75 (each s, each 3H, CH_3), 0.66 (d, 1H, J = 9.4 Hz, H-5); ^{13}C NMR (151 MHz, $CDCl_3$): δ 150.85 (C-20), 139.11, 128.43 (two), 127.67 (two), 127.56, 109.61 (C-29), 79.07, 73.50, 68.14, 55.38, 50.47, 48.96, 48.07, 47.38, 42.71, 40.94, 38.97, 38.79, 37.55, 37.24, 34.98, 34.28, 30.11, 30.06, 28.11, 27.50, 27.23, 25.29, 20.92, 19.20, 18.43, 16.20, 15.89, 15.49, 14.89. HRMS (MALDI) *m/z*: calcd for $C_{37}H_{56}O_2Na$ $[M + Na]^+$, 555.4178; found, 555.4192.

4.1.3. General procedure for 13 and 14

To a solution of **8** or **11** (1 eq), 2, 3, 4, 6-tetra-*O*-benzoyl-*D*-glucopyranosyl trichloroacetimidate **12** (1.5 eq) and 4 Å molecular sieves in dry CH_2Cl_2 (30 mL) was added TMSOTf (0.15 eq) at −5 ℃ under N_2 atmosphere. The reaction mixture was kept at −5 °C for 0.5 h and then warmed to room temperature for 1 h. After the reaction was complete detected by TLC, the reaction was quenched with trimethylamine. The mixture was filtered and the filtrate was concentrated under vacuum. Then the residue was purified by silica gel column chromatography (petroleumether-EtOAc-CH_2Cl_2, 8:1:1) to produce **13** or **14** as a white solid, respectively.

4.1.3.1. Benzyl-3β-O-(2, 3, 4, 6-tetra-O-benzoyl-β-d-glucopyranosyl)-lup-20 (29)-ene-28-oic acid (13). Compound **13** was obtained as a white solid. ^{1}H NMR (600 MHz, $CDCl_3$): δ 7.95–7.65 (m, 15H, Ar-H), 7.46–7.09 (m, 10*H*, Ar-H), 5.77 (t, 1H, J = 9.7 Hz, H-3′), 5.45 (t, 1H, J = 9.5 Hz, H-4′), 5.00 (d, 1H, J = 12.2 Hz, Ar-CH_2-1), 4.95 (d, 1H, J = 12.3 Hz, Ar-CH_2-2), 4.72 (s, 1H, C = CH_2-1), 4.70 (s, 1H, C = CH_2-2), 4.64–4.59 (m, 1H, H-1′), 4.51–4.48 (m, 1H, H-2′), 4.46 (dd, 1H, J = 11.9, 3.4 Hz, H-6′-1), 4.40 (dd, 1H, J = 11.9, 6.6 Hz, H-6′-2), 4.06–3.96 (m, 1H, H-5′), 2.92 (dd, 1H, J = 11.7, 4.5 Hz, H-3), 2.13 (d, 1H, J = 12.4 Hz), 1.57, 0.77, 0.59, 0.56, 0.52, 0.47 (each s, each 3H, CH_3), 0.40 (d, 1H, J = 9.7 Hz, H-5); ^{13}C NMR (151 MHz, $CDCl_3$): δ 175.85 (C-28), 166.12, 165.96, 165.40, 165.11, 150.69 (C-20), 136.53, 133.56, 133.32, 133.18, 130.16, 129.93 (two), 129.84 (four), 129.82 (three), 129.74, 129.66, 129.47, 128.91, 128.85, 128.58 (three), 128.52 (two), 128.47 (three), 128.37 (two), 128.34 (three), 128.16 (two), 109.64 (C-29), 103.31 (C-1′), 90.81, 73.05, 72.22, 72.05, 70.37, 65.83, 63.52, 56.62,

55.65, 50.61, 49.52, 46.97, 42.41, 40.68, 38.93, 38.67, 38.23, 37.03, 36.86, 34.30, 32.19, 30.71, 29.60, 27.58, 26.06, 25.63, 20.92, 19.60, 18.12, 16.11, 16.06, 15.87, 14.69. HRMS (ESI) *m/z*: calcd for $C_{71}H_{81}O_{12}$ $[M + H]^+$, 1125.5728; found, 1125.5750.

4.1.3.2. 28-(Benzyloxy)-3β-O-(2, 3, 4, 6-tetra-O-benzoyl-β-d-glucopyranosyl)-lup-20 (29)-ene-3-ol (14). Compound **14** was obtained as a white solid. ^{1}H NMR (600 MHz, $CDCl_3$): δ 8.05–7.80 (m, 10*H*, Ar-H), 7.56–7.22 (m, 15H, Ar-H), 5.91 (t, 1H, J = 9.9, H-3′), 5.56 (t, 1H, J = 10.1 Hz, H-4′), 4.86 (s, 1H, C = CH_2-1), 4.84 (s, 1H, C = CH_2-2), 4.68–4.63 (m, 1H, H-1′), 4.62–4.56 (m, 3H, H-2′, Ar-CH_2), 4.58–4.49 (m, 1H, H-6′-1), 4.50–4.42 (m, 1H, H-6′-2), 4.19–4.10 (m, 1H, H-5′), 3.49 (d, 2H, J = 8.9 Hz, C-CH_2), 3.07 (dd, 1H, J = 11.2, 6.6 Hz, H-3), 2.40–2.31 (m, 1H), 1.69, 0.90, 0.78, 0.72, 0.67, 0.61 (each s, each 3H, CH_3), 0.54 (d, 1H, J = 10.1 Hz, H-5); ^{13}C NMR (151 MHz, $CDCl_3$): δ 166.05, 165.90, 165.34, 165.06, 150.76 (C-20), 138.98, 133.48, 133.24, 133.10, 133.08, 129.87 (two), 129.78 (four), 129.75 (three), 129.71, 129.44, 128.88, 128.82, 128.45 (two), 128.38 (three), 128.32 (four), 127.56 (three), 127.47, 109.49 (C-29), 103.26 (C-1′), 90.70, 73.40, 73.01, 72.19, 72.01, 70.33, 68.02, 63.46, 55.54, 50.36, 48.86, 47.92, 47.28, 42.56, 40.80, 38.87, 38.59, 37.41, 36.76, 34.89, 34.12, 30.01, 27.52, 27.09, 25.99, 25.21, 20.79, 19.20, 18.06, 15.98 (two), 15.74, 14.72. HRMS (ESI) *m/z*: calcd for $C_{71}H_{81}O_{11}$ $[M + H]^+$, 1111.5935; found, 1111.5947.

4.1.4. Benzyl 3β-O-(D-glucopyranosyl)-lup-20 (29)-ene-28-oic acid (15)

To a stirred solution of compound **13** (12.11 g, 10.7 mmol) in CH_2Cl_2 (60 mL) and MeOH (60 mL), CH_3ONa was added until pH = 10. Stirring was continued overnight at room temperature. Then, the mixture was neutralized with Dowex 50 × 8 (H^+) resin until pH = 7, filtered and then evaporated to remove excess solvent under vacuum. The residue was purified by silica gel column chromatography (CH_2Cl_2-MeOH, 10:1) to give **15** (7.05 g, 92 %) as a white solid. ^{1}H NMR (600 MHz, CD_3OD): δ 7.42–7.29 (m, 5H, Ar-H), 5.16 (d, 1H, J = 12.1 Hz, Ar-CH_2-1), 5.08 (d, 1H, J = 12.1 Hz, Ar-CH_2-2), 4.70 (s, 1H, C = CH_2-1), 4.59 (s, 1H, C = CH_2-2), 4.30 (d, 1H, J = 7.8 Hz, H-1′), 3.90 (s, 1H), 3.83 (dd, 1H, J = 11.9, 2.3 Hz, H-6′-1), 3.67 (dd, 1H, J = 11.9, 5.2 Hz, H-6′-2), 3.38–3.27 (m, 1H, H-5), 3.19–3.09 (m, 1H), 3.07–2.96 (m, 1H, H-3), 2.28–2.21 (m, 2H), 1.68, 1.02, 0.97, 0.83, 0.82, 0.74 (each s, each 3H, CH_3), 0.71 (d, 1H, J = 9.7 Hz, H-5); ^{13}C NMR (151 MHz, CD_3OD): δ 177.06 (C-28), 151.67 (C-20), 137.90, 129.61 (two), 129.54 (two), 129.23, 110.40 (C-29), 106.73 (C-1′), 90.73, 78.18, 77.58, 75.57, 71.50, 66.80, 62.71, 57.77, 57.09, 51.90, 50.60, 48.44, 43.49, 41.88, 40.25, 39.55, 38.00, 37.88, 35.53, 33.13, 31.62, 30.69, 28.43, 27.64, 27.61, 27.16, 26.82, 22.06, 19.65, 19.26, 16.86, 16.62, 15.22. HRMS (ESI) *m/z*: calcd for $C_{43}H_{65}O_8$ $[M + H]^+$, 709.4679; found, 709.4691.

4.1.5. 28-(Benzyloxy)-3β-O-(d-glucopyranosyl)-lup-20 (29)-ene-3-ol (16)

Compound **16** was obtained from **14** as a white solid using the similar method as **15**. ^{1}H NMR (600 MHz, CD_3OD): δ 7.32–7.00 (m, 5H, Ar-H), 4.60 (s, 1H, C = CH_2-1), 4.50 (s, 1H, C = CH_2-2), 4.34 (dd, 1H, J = 12.3, 6.8 Hz, H-6′-1), 4.24 (d, 1H, J = 7.7 Hz, H-1′), 3.90–3.72 (m, 1H, H-6′-2), 3.67–3.40 (m, 2H), 3.21–3.04 (m, 6H), 1.92 (s, 2H), 1.60 (s, 3H, CH_3), 0.97 (s, 6H, 2 × CH_3), 0.76 (s, 9H, 3 × CH_3), 0.65 (d, 1H, J = 10.0 Hz, H-5); ^{13}C NMR (151 MHz, CD_3OD): δ 150.38 (C-20), 138.82, 128.04 (two), 127.60 (two), 127.57, 108.98 (C-29), 105.36 (C-1′), 89.38, 76.86, 76.23, 74.25, 72.97, 70.19, 67.69, 67.53, 61.40, 55.68, 50.38, 48.74, 42.33, 40.69, 38.90, 38.62, 37.43, 36.61, 34.07, 33.92, 29.83, 29.66, 27.10, 26.91, 25.82, 25.17, 20.62, 17.93, 15.53, 15.48, 15.22, 14.02. HRMS (MALDI) *m/z*: calcd for $C_{43}H_{66}O_7Na$ $[M + Na]^+$, 717.4706; found, 717.4732.

4.1.6. General procedure for 17 and 18

To a stirred solution of **15** or **16** (1.00 mmol) in 30 mL of dry pyridine and CH_2Cl_2 (*V*: *V* = 1: 1), PivCl (5.00 mmol) was added slowly to the mixture at −15 ℃ under argon atmosphere. Stirring was continued for 12 h at that temperature and then the reaction was quenched with CH_3OH. Excess solvent was removed *in vacuo*. The residue was extracted with dichloromethane and washed with saturated $NaHCO_3$ solution and brine. The organic layer was dried over Na_2SO_4 and concentrated under vacuum to furnish a crude product that was further purified by column chromatography (petroleumether-EtOAc-CH_2Cl_2, 8:1:1) to produce **17** or **18**, respectively.

4.1.6.1. Benzyl-3β-O-(3, 6-di-O-pivaloyl-β-d-glucopyranosyl)-lup-20 (29)-ene-28-oic acid (17). Compound **17** was obtained in 84 % yield as white solid. ^{1}H NMR (600 MHz, $CDCl_3$): δ 7.39–7.28 (m, 5H, Ar-H), 5.14 (d, 1H, J = 12.3 Hz, Ar-CH_2-1), 5.08 (d, 1H, J = 12.3 Hz, Ar-CH_2-2), 4.91–4.81 (m, 1H), 4.72 (s, 1H, C = CH_2-1), 4.60 (s, 1H, C = CH_2-2), 4.45 (dd, 1H, J = 11.8, 2.2 Hz, H-6′-1), 4.39 (d, 1H, J = 7.8 Hz, H-1′), 4.18 (dd, 1H, J = 12.0, 7.2 Hz, H-6′-2), 3.62–3.50 (m, 1H, H-5′), 3.45 (t, 1H, J = 9.4 Hz), 3.12 (dd, 1H, J = 11.9, 4.5 Hz), 3.03 (dd, 1H, J = 10.9, 4.4 Hz, H-3), 2.27 (d, 2H, J = 12.3 Hz), 1.68 (s, 3H, CH_3), 1.24 (s, 9H, C$(CH_3)_3$), 1.20 (s, 9H, C$(CH_3)_3$), 0.96, 0.93, 0.79, 0.78, 0.74 (each s, each 3H, CH_3), 0.66 (d, 1H, J = 9.2 Hz, H-5); ^{13}C NMR (151 MHz, $CDCl_3$): δ 180.42, 178.72 (C-28), 175.92, 150.78 (C-20), 136.57, 128.61 (two), 128.36 (two), 128.18, 109.67 (C-29), 104.84 (C-1′), 90.54, 78.07, 74.21, 72.76, 70.26, 65.86, 63.93, 56.67, 55.72, 50.61, 49.55, 47.04, 42.47, 40.76, 39.17, 38.70, 38.26, 36.99, 34.34, 32.21, 30.72, 29.66, 28.29, 27.20 (two), 26.06, 25.65, 20.98, 19.54, 18.27, 16.59, 16.21, 15.94, 14.74. HRMS (ESI) *m/z*: calcd for $C_{53}H_{81}O_{10}$ $[M + H]^+$, 877.5830; found, 877.5862.

4.1.6.2. 28-(Benzyloxy)-3β-O-(3, 6-di-O-pivaloyl-β-d-glucopyranosyl)-lup-20 (29)-ene-3-ol (18). Compound **18** was obtained as a white solid. ^{1}H NMR (600 MHz, $CDCl_3$): δ 7.41–7.18 (m, 5H, Ar-H), 4.89–4.87 (m, 1H), 4.65 (d, 1H, J = 2.5 Hz), 4.61–4.52 (m, 2H, C = CH_2), 4.47 (d, 1H, J = 6.1 Hz), 4.47–4.41 (m, 1H), 4.40 (d, 1H, J = 7.8 Hz, H-1′), 4.18 (dd, 1H, J = 11.8, 7.2 Hz, H-6′-1), 3.62–3.40 (m, 4H), 3.17–3.06 (m, 1H, H-3), 2.39 (d, 1H, J = 12.9 Hz), 1.67 (s, 3H, CH_3), 1.24 (s, 9H, C$(CH_3)_3$), 1.20 (s, 9H, C$(CH_3)_3$), 0.97, 0.93, 0.83 (each s, each 3H, CH_3), 0.80 (s, 6H, 2 × CH_3), 0.67 (d, 1H, J = 10.0 Hz, H-5); ^{13}C NMR (151 MHz, $CDCl_3$): δ 180.29, 178.62, 150.83 (C-20), 138.99, 128.33 (two), 127.56 (two), 127.47, 109.47 (C-29), 104.73 (C-1′), 90.38, 77.95, 74.12, 73.39, 72.70, 70.14, 68.01, 63.83, 55.56, 50.32, 48.86, 47.96, 47.29, 42.58, 40.84, 39.07 (two), 38.84, 38.57, 37.42, 36.85, 34.12, 29.99, 28.18, 27.17 (four), 27.10 (five), 25.95, 25.19, 20.81, 19.14, 18.18, 16.48, 16.04, 15.78, 14.73. HRMS (ESI) *m/z*: calcd for $C_{53}H_{83}O_9$ $[M + H]^+$, 863.6037; found, 863.6051.

4.1.7. General procedure for BA-16 and BA-20

To a mixture of **17** or **18** (1.0 mmol) and 4 Å molecular sieves in dried CH_2Cl_2 (20 mL) at −40 °C under argon was added TMSOTf (0.20 mmol), followed by a solution of the 2, 3, 4-tri-*O*-acetyl-L-rhamnopyranosyl trichloroacetimidate **19** (5.00 mmol) in dry CH_2Cl_2 (5 mL). After stirring at − 40 °C for 3 h, the reaction mixture was warmed to 0 °C and stirred for 5 h under argon. After the reaction was complete detected by TLC, the reaction was quenched with Et_3N. The solid was filtered, and the filtrate was concentrated in reduced pressure and then purified by column chromatography (petroleum ether-EtOAc, 1:1) to afford the crude trisaccharide product. Subsequently, to a stirred solution of this crude product in 20 mL THF and CH_3OH (*V*:*V* = 1:1), 4 M NaOH (10 mL) was added. After stirred at 45 °C for 10 h, 1 M HCl was added to adjust pH = 7. The resulting precipitate was filtered off and washed with CH_3OH, and then concentrated under vacuum. The obtained crude product was further purified by column chromatography, eluting with CH_2Cl_2/CH_3OH mixtures, with gradient from 8:1 to 4:1, to furnish the target compound **BA-16** or **BA-20**, respectively.

4.1.7.1. Benzyl-3β-O-[2, 4-di-O-(α-l-rhamnopyranosyl)-β-d-glucopyranosyl]-lup-20 (29)-ene-28-oic acid (BA-16). Compound **BA-16** was obtained as a white powder. ^{1}H NMR (600 MHz, CD_3OD): δ 7.42–7.30 (m, 5H, Ar-H), 5.35 (d, 1H, J = 1.7 Hz, Rha-H-1), 5.17 (d, 1H, J = 12.1 Hz, Ar-CH_2-1), 5.09 (d, 1H, J = 12.1 Hz, Ar-CH_2-2), 4.82 (d, 1H, J = 1.1 Hz, Rha-H-1), 4.70 (s, 1H, C = CH_2-1), 4.60 (s, 1H, C = CH_2-2), 4.41 (d, 1H, J = 7.7 Hz, H-1′), 4.11 (s, 1H), 4.03–3.93 (m, 2H), 3.92–3.90 (m, 2H), 3.90–3.79 (m, 1H, H-5′), 3.75 (dd, 1H, J = 9.6, 3.4 Hz, Rha-H-3), 3.68 (d, 1H, J = 3.7 Hz), 3.63 (dd, 1H, J = 9.6, 3.2 Hz, Rha-H-3), 3.57–3.53 (m, 2H), 3.48–3.33 (m, 2H), 3.34–3.25 (m, 2H), 3.12 (dd, 1H, J = 11.7, 4.4 Hz, H-3), 3.05–2.96 (m, 1H), 2.29–2.35 (m, 1H), 1.68 (s, 3H, CH_3), 1.27 (d, 3H, J = 6.2 Hz, Rha-H-6), 1.21 (d, 3H, J = 6.2 Hz, Rha-H-6), 1.02 (s, 3H, CH_3), 0.97 (s, 3H, CH_3), 0.83 (s, 6H, 2 × CH_3), 0.74 (s, 3H, CH_3), 0.70 (d, 1H, J = 9.8 Hz, H-5); ^{13}C NMR (151 MHz, CD_3OD): δ 177.16 (C-28), 151.71 (C-20), 137.88, 130.21, 129.93, 129.61 (two), 129.55 (two), 129.25, 110.37 (C-29), 105.48 (C-1′), 103.02 (Rha-C-1), 101.98 (Rha-C-1), 90.40, 80.29, 79.19, 78.10, 76.40, 73.91, 73.66, 72.41, 72.10, 71.97, 70.72, 69.99, 66.83, 61.94, 57.80, 57.39, 51.96, 50.62, 47.81, 43.49, 41.89, 40.32, 39.58, 38.01, 37.87, 35.53, 33.12, 31.62, 30.68, 28.39, 27.35, 26.85, 22.05, 19.61, 19.24, 18.03, 17.90, 16.99, 16.92, 16.59, 15.18. HRMS (ESI) *m/z*: calcd for $C_{55}H_{84}O_{16}Na$ $[M + Na]^+$, 1023.5657; found, 1023.5623.

4.1.7.2. 28-(Benzyloxy)-3β-O-[2, 4-di-O-(α-l-rhamnopyranosyl)-β-d-glucopyranosyl]-lup-20 (29)-ene-3-ol (BA-20). Compound **BA-20** was obtained as a white powder. ^{1}H NMR (600 MHz, CD_3OD): δ 7.39–7.21 (m, 5H, Ar-H), 5.37 (d, J = 1.7 Hz, 1H, Rha-H-1), 4.86 (d, 1H, J = 1.1 Hz, Rha-H-1), 4.72 (s, 1H, C = CH_2-1), 4.66 (s, 1H, C = CH_2-2), 4.58 (d, 2H, J = 12.5 Hz, Ar-CH_2), 4.43 (d, 1H, J = 7.9 Hz, H-1′), 4.40 (d, 1H, J = 2.3 Hz), 4.01–3.93 (m, 2H), 3.95–3.87 (m, 1H, H-5′), 3.84 (t, 1H, J = 9.4 Hz, Rha-H-4), 3.76 (dd, 1H, J = 9.7, 3.5 Hz, Rha-H-3), 3.66 (dd, 1H, J = 9.7, 3.6 Hz, Rha-H-3), 3.66–3.58 (m, 3H), 3.60–3.48 (m, 3H), 3.48–3.35 (m, 3H), 3.15–3.09 (m, 1H, H-3), 2.45–2.33 (m, 2H), 1.98 (s, 1H), 1.67 (s, 3H, CH_3), 1.26 (d, 3H, J = 6.3 Hz, Rha-H-6), 1.21 (d, 3H, J = 6.2 Hz, Rha-H-6), 1.02 (s, 3H, CH_3), 0.96 (s, 3H, CH_3), 0.83 (s, 6H, 2 × CH_3), 0.82 (s, 3H, CH_3), 0.70 (d, 1H, J = 9.5 Hz, H-5); ^{13}C NMR (151 MHz, CD_3OD): δ 150.40 (C-20), 138.78, 128.03 (two), 127.66 (two), 127.31, 108.92 (C-29), 104.10 (C-1′), 101.60 (Rha-C-1), 100.55 (Rha-C-1), 94.36, 89.03, 78.91, 77.83, 76.72, 75.03, 72.92, 72.83, 72.53, 72.29, 71.05, 70.74, 70.62, 69.33, 68.61, 67.82, 67.43, 60.56, 55.95, 50.43, 42.29, 40.67, 38.96, 38.89, 37.42, 36.59, 34.51, 34.02, 29.75, 29.60, 27.02, 26.87, 25.98, 25.16, 20.57, 18.07, 17.88, 16.75, 16.65, 16.53, 15.63, 15.50, 15.11, 13.93. HRMS (MALDI) *m/z*: calcd for $C_{55}H_{86}O_{15}Na$ $[M + Na]^+$, 1009.5864; found, 1009.5882.

4.1.8. General procedure for BA-2 and BA-17

To a stirred solution of **BA-16** or **BA-20** (1.00 mmol) in 20 mL of dry methanol and tetrahydrofuran (*V*: *V* = 1:1), 10 % Pd/C (100 mg) was added at r.t. under argon atmosphere. Then the solution was stirred at room temperature for 12 h under hydrogen atmosphere. The mixture was filtered and concentrated under reduced pressure. The resultant crude material was purified by column chromatography (CH_2Cl_2-CH_3OH, 5:1) to afford the title compound **BA-2** or **BA-17** as a white solid, respectively.

4.1.8.1. 3β-O-[2, 4-Di-O-(α-l-Rhamnopyranosyl)-β-d-glucopyranosyl]-lup-20 (29)-ene-28-oic acid (BA-2). Saponin **BA-2** was obtained as a white powder. ^{1}H NMR (600 MHz, CD_3OD): δ 5.38 (s, 1H, Rha-H-1), 4.86 (d, 1H, J = 1.1 Hz, Rha-H-1), 4.70 (s, 1H, C = CH_2-1), 4.59 (s, 1H, C = CH_2-2), 4.42 (d, 1H, J = 7.6 Hz, H-1′), 4.03–3.96 (m, 2H), 3.98–3.85 (m, 1H, H-5′), 3.79 (t, 1H, J = 10.0 Hz, Rha-H-4), 3.67–3.63 (m, 2H), 3.57 (t, 1H, J = 9.8 Hz, Rha-H-4), 3.48–3.37 (m, 1H), 3.35–3.32 (m, 2H), 3.23–3.19 (m, 4H), 3.14 (dd, 1H, J = 11.5, 4.2 Hz, H-3), 3.05–3.03 (m, 1H), 2.23 (d, 1H, J = 12.0 Hz), 1.69 (s, 3H, CH_3), 1.27 (d, 3H, J = 6.2 Hz, Rha-H-6), 1.21 (d, 3H, J = 6.0 Hz, Rha-H-6), 1.03, 1.00, 0.96, 0.86, 0.83 (each s, each 3H, CH_3), 0.76–0.70 (m, 1H, H-5); ^{13}C NMR (151 MHz, CD_3OD): δ 172.73 (C-28), 151.99 (C-20), 110.19 (C-29), 105.48 (C-1′), 102.81 (Rha-C-1), 101.77 (Rha-C-1), 90.38, 80.07, 79.13, 78.02, 76.38, 74.16, 73.84, 73.63, 73.02, 72.40 (two), 72.07, 71.97, 70.58, 69.89, 69.09, 61.83, 57.53, 57.38, 51.98, 50.37, 43.53, 41.90, 40.32 (two), 39.55, 38.01 (two), 35.57, 31.68, 30.83, 28.37, 27.36, 26.86, 22.07, 19.57, 19.26, 18.01, 17.90, 16.98, 16.93, 16.68, 15.15. HRMS (ESI) *m/z*: calcd for $C_{48}H_{77}O_{16}$ $[M + H]^+$, 909.5290; found, 909.5277.

4.1.8.2. 3β-O-[2, 4-Di-O-(α-l-Rhamnopyranosyl)-β-d-glucopyranosyl]-lup-20 (29)-ene-3, 28-diol (BA-17). Compound **BA-17** was obtained as a white powder. ^{1}H NMR (600 MHz, CD_3OD): δ 5.16 (s, 1H, Rha-H-1), 4.81 (s, 1H, Rha-H-1), 4.47 (s, 1H, C = CH_2-1), 4.35 (s, 1H, C = CH_2-2), 4.20 (d, 1H, J = 7.7 Hz, H-1′), 3.83–3.64 (m, 5H), 3.56 (t, 1H, J = 8.8 Hz), 3.47–3.40 (m, 4H), 3.36 (t, 1H, J = 8.5 Hz), 3.23–3.20 (m, 2H), 3.09 (s, 2H, C-CH_2), 2.89–2.83 (m, 1H, H-3), 2.20 (d, 1H, J = 11.5 Hz), 1.46 (s, 3H, CH_3), 1.05 (d, 3H, J = 6.2 Hz, Rha-H-6), 1.00 (d, 3H, J = 6.0 Hz, Rha-H-6), 0.85, 0.81, 0.78, 0.65, 0.62 (each s, each 3H, CH_3), 0.59–0.48 (m, 1H, H-5); ^{13}C NMR (151 MHz, CD_3OD): δ 151.81 (C-20), 110.27 (C-29), 105.45 (C-1′), 102.77 (Rha-C-1), 101.74 (Rha-C-1), 90.39, 80.16, 79.24, 77.98, 76.39, 73.65, 72.41, 72.12, 71.99, 70.57, 69.90, 61.89, 60.32, 57.33, 51.83, 50.00, 43.94, 43.76, 42.16, 42.12, 40.32 (two), 38.64, 37.97, 35.45, 34.98, 30.78, 30.33, 28.38, 27.35, 26.58, 23.45, 22.63, 21.99, 19.39, 19.26, 17.99, 17.88, 16.98, 16.85, 16.53, 15.25, 9.09, 7.84. HRMS (MALDI) *m/z*: calcd for $C_{48}H_{79}O_{15}$ $[M + H]^+$, 895.5497; found, 895.5473.

4.1.9. General procedure for 20 and 21

Compound **BA-2** or **BA-20** (1.0 mmol) was dissolved in 20 mL of dry pyridine, Ac_2O (16.0 mmol) and DMAP (0.8 mmol) were added at 0 ℃. The reaction mixture was warmed to 60 ℃ and stirred for 24 h under N_2 atmosphere. After excess solvent was removed *in vacuo*, the crude product was extracted with ethyl acetate, which was then washed with 1 M HCl, saturated $NaHCO_3$ solution and brine. The organic layer was dried over Na_2SO_4 and concentrated *in vacuo* to provide a crude residue. The residue was further purified by column chromatography (petroleumether-EtOAc-CH_2Cl_2, 3:1:1) to yield **20** or **21**, respectively.

4.1.9.1. 3β-O-[2, 4-Di-O-(2, 3, 4-tri-O-Acetyl-α-l-rhamnopyranosyl)-β-(3, 6-di-O-acetyl)-d-glucopyranosyl]-lup-20(29)-ene-28-oic acid (20). Compound **20** was obtained as a white powder. ^{1}H NMR (600 MHz, $CDCl_3$): δ 5.28–5.20 (m, 3H), 5.17 (dd, 1H, J = 10.2, 3.2 Hz, Rha-H-3), 5.10 (dd, 1H, J = 3.5, 1.8 Hz, Rha-H-2), 5.05–5.01 (m, 4H), 4.80 (d, 1H, J = 1.7 Hz, Rha-H-1), 4.74 (s, 1H, C = CH_2-1), 4.62 (s, 1H, C = CH_2-2), 4.53 (d, 1H, J = 7.7 Hz, H-1′), 4.46 (dd, 1H, J = 12.4, 2.1 Hz, H-6′-1), 4.27 (dd, 1H, J = 13.4, 5.3 Hz, H-6′-2), 4.25–4.17 (m, 1H, H-5′), 3.91–3.81 (m, 2H), 3.76 (t, 1H, J = 9.3 Hz, Rha-H-4), 3.71–3.58 (m, 3H), 3.14–3.12 (m, 1H), 3.05–2.94 (m, 1H, H-3), 2.27 (d, 1H, J = 12.5 Hz), 2.14, 2.13, 2.11, 2.10, 2.04, 2.01, 1.99, 1.97 (each s, each 3H, each CH_3CO), 1.70 (s, 3H, CH_3), 1.17 (d, 3H, J = 6.2 Hz, Rha-H-6), 1.15 (d, 3H, J = 6.2 Hz, Rha-H-6), 1.01, 0.98, 0.92, 0.82, 0.78 (each s, each 3H, CH_3), 0.71 (d, 1H, J = 10.3 Hz, H-5); ^{13}C NMR (151 MHz, $CDCl_3$): δ 181.96, 170.76, 170.37, 170.27, 170.22 (C-28), 170.14 (two), 169.81, 150.48 (C-20), 109.85 (C-29), 103.83 (C-1′), 99.58 (Rha-C-1), 97.03 (Rha-C-1), 90.15, 78.05, 77.48, 77.16, 75.59, 75.43, 72.17, 71.20, 70.59, 70.00, 69.80, 68.69, 68.58, 68.00, 66.75, 62.31, 56.44, 56.07, 50.57, 49.27, 46.98, 42.51, 40.77, 39.24, 39.20, 38.45, 36.99, 34.35, 32.23, 30.65, 29.74, 27.80, 26.23, 25.54, 21.60, 21.07, 21.01, 20.97, 20.94 (three), 20.86, 20.81, 19.45, 18.25, 17.34, 17.24, 16.34, 16.13, 16.02, 14.75. HRMS (ESI) *m/z*: calcd for $C_{64}H_{95}O_{24}$ $[M + H]^+$, 1247.6213; found, 1247.6235.

4.1.9.2. 28-(Benzyloxy)-3β-O-[2, 4-Di-O-(2, 3, 4-tri-O-Acetyl-α-l-rhamnopyranosyl)-β-(3, 6-di-O-acetyl)-d-glucopyranosyl]-lup-20 (29)-ene-3-ol (21). Compound **21** was obtained as a white powder. ^{1}H NMR (600 MHz, $CDCl_3$): δ 7.37–7.23 (m, 5H, Ar-H), 5.49–5.30 (m, 3H), 5.26 (dd,

1H, $J = 9.7$, 3.4 Hz, Rha-H-3), 5.15–5.01 (m, 2H), 4.84 (s, 1H, Rha-H-1), 4.65 (s, 1H, Rha-H-1), 4.56 (s, 1H, C = CH_2-1), 4.48 (s, 1H, C = CH_2-2), 4.42 (d, 1H, $J = 8.1$ Hz, H-1′), 4.34–4.17 (m, 3H), 4.08 (dd, 1H, $J = 9.8$, 7.0 Hz, H-2′), 3.99 (d, 1H, $J = 2.5$ Hz), 3.73 (t, 1H, $J = 9.5$ Hz, Rha-H-4), 3.61 (t, 1H, $J = 9.1$ Hz, Rha-H-4), 3.54–3.40 (m, 3H), 3.09 (d, 2H, $J = 9.1$ Hz), 2.40–2.32 (m, 1H), 2.18–1.94 (m, 24H, 8 × CH_3CO), 1.67 (s, 3H, CH_3), 1.27 (d, 3H, $J = 6.4$ Hz, Rha-H-6), 1.19 (d, 3H, $J = 6.3$ Hz, Rha-H-6), 1.05 (s, 3H, CH_3), 0.94 (s, 3H, CH_3), 0.83 (s, 3H, CH_3), 0.81 (s, 6H, 2 × CH_3), 0.70 (d, 1H, $J = 9.5$ Hz, H-5); ^{13}C NMR (151 MHz, $CDCl_3$): δ 171.93 (C-28), 170.20, 170.12 (two), 170.10 (two), 170.00 (two), 169.78, 149.64 (C-20), 140.06, 128.45, 127.69, 127.58, 118.61 (C-29), 104.07 (C-1′), 99.31 (Rha-C-1), 97.63 (Rha-C-1), 85.23, 83.18, 73.99, 71.64, 70.09, 69.45, 69.23, 68.12, 67.33, 65.05, 57.77, 56.60, 54.34, 53.95 (three), 51.52, 50.15, 48.71, 46.99, 45.85, 42.58, 42.15, 42.00, 41.39, 40.82, 39.10, 38.70, 38.22, 36.30, 33.53, 33.14, 30.14, 27.94, 27.52, 25.75, 25.25, 21.62, 21.14 (two), 20.99 (two), 20.91 (three), 17.86, 16.11, 14.78. HRMS (ESI) *m/z*: calcd for $C_{71}H_{103}O_{23}$ $[M + H]^+$, 1323.6890; found, 1323.6898.

4.1.10. General procedure for BA-3 – BA-15

To a solution of **BA-2** (1.00 mmol) in DMF (20 mL) was added K_2CO_3 (5 mmol) at 30 °C under N_2 atmosphere. After stirring at 30 °C for 2 h, the corresponding halogenated hydrocarbon (3.00 mmol) was added. Stirring was continued overnight at that temperature. After the mixture was evaporated to remove excess solvent under reduced pressure, the residue was dissolved in EtOAc (100 mL), then extracted with water (3 × 50 mL) and brine (3 × 50 mL). The combined organic layer was concentrated *in vacuo* after drying over Na_2SO_4. Then, the residue was re-dissolved in MeOH (10 mL) and CH_2Cl_2 (10 mL), CH_3ONa was added until pH = 10. After the reaction mixture was stirred at r.t. for 5 h, Dowex 50 × 8 (H^+) resin was added until pH = 7. The reaction mixture was filtered and concentrated under vacuum. The residue was purified by silica gel column chromatography (CH_2Cl_2-MeOH, 6:1) to give title saponins **BA-3–BA-15**.

4.1.10.1. Ethyl-3β-O-[2, 4-di-O-(α-l-rhamnopyranosyl)-β-d-glucopyranosyl]-lup-20 (29)-ene-28-oic acid (BA-3). Similarly, **BA-3** was prepared as a white solid in 82 % yield for two steps; ^{1}H NMR (600 MHz, CD_3OD): δ 5.37 (d, 1H, $J = 1.7$ Hz, Rha-H-1), 4.82 (s, 1H, Rha-H-1), 4.74 (s, 1H, C = CH_2-1), 4.62 (s, 1H, C = CH_2-2), 4.43 (d, 1H, $J = 7.7$ Hz, H-1′), 4.24–4.07 (m, 2H), 4.03–3.96 (m, 2H), 3.92 (dd, 1H, $J = 9.5$, 3.2 Hz, Rha-H-3), 3.86 (dd, 1H, $J = 3.3$, 1.8 Hz, Rha-H-2), 3.81 (dd, 1H, $J = 12.1$, 2.0 Hz, H-6′-1), 3.76 (dd, 1H, $J = 9.6$, 3.4 Hz, Rha-H-3), 3.70–3.68 (m, 1H), 3.66 (dd, 1H, $J = 3.4$, 1.7 Hz), 3.66–3.60 (m, 1H), 3.58–3.56 (m, 1H), 3.52–3.34 (m, 2H), 3.34–3.29 (m, 2H), 3.15 (dd, 1H, $J = 11.7$, 4.4 Hz, H-3), 2.26 (d, 1H, $J = 8.2$ Hz), 1.71 (s, 3H, CH_3), 1.28 (s, 3H, CH_3), 1.27 (d, 3H, $J = 6.3$ Hz, Rha-H-6), 1.22 (d, 3H, $J = 6.1$ Hz, Rha-H-6), 1.05, 1.02, 0.96, 0.88, 0.85 (each s, each 3H, CH_3), 0.75 (d, 1H, $J = 9.8$ Hz, H-5); ^{13}C NMR (151 MHz, CD_3OD): δ 177.58 (C-28), 151.78 (C-20), 110.34 (C-29), 105.49 (C-1′), 103.03 (Rha-C-1), 101.99 (Rha-C-1), 90.40, 80.30, 79.20, 78.11, 76.42, 73.91, 73.67, 72.41, 72.11, 71.97, 70.73, 69.99, 61.95, 61.02, 57.72, 57.43, 52.00, 50.57, 43.52, 41.97, 40.34 (two), 39.64, 38.05, 37.95, 36.97, 35.57, 33.14, 31.66, 30.75, 28.40, 27.36, 26.88, 22.09, 19.62, 19.27, 18.02, 17.90, 16.99, 16.93, 16.64, 15.21, 14.71 (two). HRMS (ESI) *m/z*: calcd for $C_{50}H_{82}O_{16}Na$ $[M + Na]^+$, 961.5501; found, 961.5423.

4.1.10.2. n-Propyl-3β-O-[2, 4-di-O-(α-l-rhamnopyranosyl)-β-d-glucopyranosyl]-lup-20 (29)-ene-28-oic acid (BA-4). Similarly, **BA-4** was prepared as a white solid in 80 % yield for two steps; ^{1}H NMR (600 MHz, CD_3OD): δ 5.38 (s, 1H, Rha-H-1), 4.85 (d, 1H, $J = 1.2$ Hz, Rha-H-1), 4.73 (s, 1H, C = CH_2-1), 4.63 (s, 1H, C = CH_2-2), 4.44 (d, 1H, $J = 7.7$ Hz, H-1′), 4.14–4.00 (m, 2H), 4.03–3.95 (m, 2H), 3.92 (dd, 1H, $J = 9.6$, 3.3 Hz, Rha-H-3), 3.88–3.78 (m, 1H), 3.76 (dd, 1H, $J = 9.5$, 3.3 Hz, Rha-H-3), 3.66 (t, 1H, $J = 10.6$ Hz, Rha-H-4), 3.58 (t, 1H, $J = 8.1$ Hz), 3.50–3.38 (m, 3H), 3.38–3.29 (m, 3H), 3.15 (dd, 1H, $J = 11.7$, 4.4 Hz, H-3), 3.10–2.98 (m, 1H), 2.28 (d, 1H, $J = 10.3$ Hz), 1.72 (s, 3H, CH_3), 1.50–1.35 (m, 2H, CH_2), 1.28 (d, 3H, $J = 6.2$ Hz, Rha-H-6), 1.23 (d, 3H, $J = 6.2$ Hz, Rha-H-6), 1.05, 1.03, 1.01, 0.96, 0.89, 0.86 (each s, each 3H, CH_3), 0.75 (d, 1H, $J = 9.9$ Hz, H-5); ^{13}C NMR (151 MHz, CD_3OD): δ 177.69 (C-28), 151.75 (C-20), 110.36 (C-29), 105.50 (C-1′), 103.02 (Rha-C-1), 102.00 (Rha-C-1), 90.40, 80.29, 79.21, 78.11, 76.42, 73.91, 73.67, 72.41, 72.10, 71.96, 70.73, 69.99, 66.78, 61.95, 57.89, 57.43, 51.99, 50.59, 43.54, 41.97, 40.34 (two), 39.70, 38.05, 36.97, 35.58, 33.21, 31.68, 30.79, 28.41, 27.36, 26.88, 23.20 (two), 22.10, 19.63, 19.28, 18.03 (two), 17.90 (two), 16.99, 16.94, 16.67, 15.24. HRMS (ESI) *m/z*: calcd for $C_{51}H_{84}O_{16}Na$ $[M + Na]^+$, 975.5557; found, 975.5582.

4.1.10.3. n-Butyl-3β-O-[2, 4-di-O-(α-l-rhamnopyranosyl)-β-d-glucopyranosyl]-lup-20 (29)-ene-28-oic acid (BA-5). Similarly, **BA-5** was prepared as a white solid in 78 % yield for two steps; ^{1}H NMR (600 MHz, CD_3OD): δ 5.36 (s, 1H, Rha-H-1), 4.86 (d, 1H, $J = 1.1$ Hz, Rha-H-1), 4.72 (s, 1H, C = CH_2-1), 4.61 (s, 1H, C = CH_2-2), 4.42 (d, 1H, $J = 7.7$ Hz, H-1′), 4.17–4.02 (m, 2H), 4.01–3.93 (m, 2H), 3.91 (dd, 1H, $J = 9.5$, 7.7 Hz, H-2′), 3.87–3.77 (m, 1H), 3.75 (dd, 1H, $J = 9.6$, 3.4 Hz, Rha-H-3), 3.71–3.59 (m, 2H), 3.57 (t, 1H, $J = 9.0$ Hz, Rha-H-4), 3.48–3.34 (m, 3H), 3.33–3.30 (m, 2H), 3.14 (dd, 1H, $J = 11.6$, 4.3 Hz, H-3), 3.10–2.98 (m, 1H), 1.95 (d, 1H, $J = 9.7$ Hz), 1.70 (s, 3H, CH_3), 1.46–1.43 (m, 4H), 1.27 (d, 3H, $J = 6.2$ Hz, Rha-H-6), 1.21 (d, 3H, $J = 6.1$ Hz, Rha-H-6), 1.03, 1.01 (each s, each 3H, CH_3), 0.97 (t, 3H, $J = 7.4$ Hz, CH_3), 0.94, 0.87, 0.84 (each s, each 3H, CH_3), 0.74 (d, 1H, $J = 9.3$ Hz, H-5); ^{13}C NMR (151 MHz, CD_3OD): δ 177.72 (C-28), 151.76 (C-20), 110.34 (C-29), 105.48 (C-1′), 103.04 (Rha-C-1), 101.99 (Rha-C-1), 90.39, 80.34, 79.21, 78.12, 76.41, 73.91, 73.67, 72.41, 72.11, 71.98, 70.73, 69.99, 64.84, 61.95, 57.89, 57.41, 51.99, 50.59, 43.54, 41.97, 40.34 (two), 39.73, 38.04, 38.00, 35.58, 33.20, 31.96 (two), 31.68, 30.79, 28.39, 27.36, 26.88, 22.09, 20.43 (two), 19.59, 19.26, 18.02, 17.90, 16.99, 16.92, 16.68, 15.20, 14.04. HRMS (ESI) *m/z*: calcd for $C_{52}H_{87}O_{16}$ $[M + H]^+$, 967.5994; found, 967.6018.

4.1.10.4. n-Pentyl-3β-O-[2, 4-di-O-(α-l-rhamnopyranosyl)-β-d-glucopyranosyl]-lup-20 (29)-ene-28-oic acid (BA-6). Similarly, **BA-6** was prepared as a white solid in 76 % yield for two steps; ^{1}H NMR (600 MHz, CD_3OD): δ 5.38 (d, 1H, $J = 1.7$ Hz, Rha-H-1), 4.83 (d, 1H, $J = 1.2$ Hz, Rha-H-1), 4.73 (s, 1H, C = CH_2-1), 4.63 (s, 1H, C = CH_2-2), 4.44 (d, 1H, $J = 7.7$ Hz, H-1′), 4.19–4.03 (m, 2H), 4.03–3.95 (m, 2H), 3.94–3.92 (m, 1H), 3.86 (dd, 1H, $J = 3.2$, 1.8 Hz, Rha-H-2), 3.82 (dd, 1H, $J = 12.0$, 2.0 Hz, H-6′-1), 3.76 (dd, 1H, $J = 9.6$, 3.4 Hz, Rha-H-3), 3.72–3.63 (m, 2H), 3.64 (dd, 1H, $J = 3.4$, 1.1 Hz, Rha-H-2), 3.58 (t, 1H, $J = 9.0$ Hz, Rha-H-4), 3.50–3.38 (m, 2H), 3.35–3.30 (m, 2H), 3.16 (dd, 1H, $J = 11.7$, 4.2 Hz, H-3), 3.10–2.98 (m, 2H), 2.27 (d, 1H, $J = 9.4$ Hz), 1.72 (s, 3H, CH_3), 1.47–1.38 (m, 6H), 1.29 (d, 3H, $J = 6.2$ Hz, Rha-H-6), 1.23 (d, 3H, $J = 6.2$ Hz, Rha-H-6), 1.05, 1.03, 0.96, 0.96, 0.88, 0.86 (each s, each 3H, CH_3), 0.76 (d, 1H, $J = 9.9$ Hz, H-5); ^{13}C NMR (151 MHz, CD_3OD): δ 177.77 (C-28), 151.78 (C-20), 110.35 (C-29), 105.49 (C-1′), 103.05 (Rha-C-1), 102.00 (Rha-C-1), 90.38, 80.34, 79.21, 78.13, 76.42, 73.92, 73.68, 72.43, 72.11, 71.99, 70.74, 69.99, 65.13, 61.96, 57.91, 57.41, 51.98, 50.58, 49.85, 43.55, 41.98, 40.34, 39.76, 38.05, 35.59, 33.23, 31.70, 30.79, 29.59 (three), 28.39, 27.36, 26.88, 23.36 (two), 22.09, 19.60, 19.27, 18.02, 17.90, 16.99, 16.92, 16.72, 15.19, 14.43 (two). HRMS (ESI) *m/z*: calcd for $C_{53}H_{89}O_{16}$ $[M + H]^+$, 981.6151; found, 981.6183.

4.1.10.5. n-Hexyl-3β-O-[2, 4-di-O-(α-l-rhamnopyranosyl)-β-d-glucopyranosyl]-lup-20 (29)-ene-28-oic acid (BA-7). Similarly, **BA-7** was prepared as a white solid in 75 % yield for two steps; ^{1}H NMR (600 MHz, CD_3OD): δ 5.38 (d, 1H, $J = 1.1$ Hz, Rha-H-1), 4.85 (d, 1H, $J = 1.1$ Hz, Rha-H-1), 4.73 (s, 1H, C = CH_2-1), 4.63 (s, 1H, C = CH_2-2), 4.44 (d, 1H, $J = 7.7$ Hz, H-1′), 4.19–4.03 (m, 2H), 4.03–3.95 (m, 2H), 3.93 (dd, 1H, $J = 9.5$, 7.3 Hz, H-2′), 3.86 (dd, 1H, $J = 3.2$, 1.8 Hz, Rha-H-2), 3.82 (dd,

1H, J = 12.0, 2.0 Hz, H-6′-1), 3.76 (dd, 1H, J = 9.6, 3.4 Hz, Rha-H-3), 3.72–3.63 (m, 2H), 3.64 (d, 1H, J = 3.4 Hz, Rha-H-2), 3.58 (t, 1H, J = 9.0 Hz, Rha-H-4), 3.50–3.38 (m, 2H), 3.33 (brs, 1H), 3.16 (dd, 1H, J = 11.7, 4.2 Hz, H-3), 3.10–2.98 (m, 1H), 2.27 (d, 1H, J = 9.4 Hz), 1.72 (s, 3H, CH_3), 1.47–1.38 (m, 8H), 1.29 (d, 3H, J = 6.2 Hz, Rha-H-6), 1.23 (d, 3H, J = 6.2 Hz, Rha-H-6), 1.05, 1.03, 0.96, 0.96, 0.88, 0.86 (each s, each 3H, CH_3), 0.76 (d, 1H, J = 9.9 Hz, H-5); ^{13}C NMR (151 MHz, CD_3OD): δ 177.80 (C-28), 151.79 (C-20), 110.36 (C-29), 105.50 (C-1′), 103.06 (Rha-C-1), 102.01 (Rha-C-1), 90.39, 80.36, 79.22, 78.14, 76.44, 73.93, 73.68, 72.43, 72.12, 71.99, 70.75, 70.00, 65.15, 61.97, 57.92, 57.42, 51.98, 50.59, 43.55, 41.99, 40.35, 40.31, 39.78, 38.05, 35.59, 33.25, 32.57, 31.71, 30.82, 29.87, 28.40, 27.37, 27.07, 26.88, 23.73 (two), 22.10, 19.60, 19.27, 18.02, 17.90, 16.99, 16.92, 16.73, 15.20, 14.40. HRMS (ESI) *m/z*: calcd for $C_{54}H_{91}O_{16}$ $[M + H]^+$, 995.6307; found, 995.6335.

4.1.10.6. Isopropyl-3β-O-[2, 4-di-O-(α-l-rhamnopyranosyl)-β-d-glucopyranosyl]-lup-20 (29)-ene-28-oic acid (BA-8). Similarly, **BA-8** was prepared as a white solid in 78 % yield for two steps; ^{1}H NMR (600 MHz, CD_3OD): δ 5.36 (s, 1H, Rha-H-1), 4.82 (d, 1H, J = 1.1 Hz, Rha-H-1), 5.06–4.94 (m, 1H), 4.72 (s, 1H, C = CH_2-1), 4.61 (s, 1H, C = CH_2-2), 4.42 (d, 1H, J = 7.7 Hz, H-1′), 4.03–3.95 (m, 2H), 3.91 (dd, 1H, J = 9.5, 7.2 Hz, H-2′), 3.84 (m, 1H), 3.80 (d, 1H, J = 10.9 Hz), 3.75 (dd, 1H, J = 9.6, 3.4 Hz, Rha-H-3), 3.71–3.59 (m, 2H), 3.57 (t, 1H, J = 9.7 Hz, Rha-H-4), 3.48–3.34 (m, 2H), 3.32–3.30 (m, 2H), 3.14 (dd, 1H, J = 11.5, 4.2 Hz, H-3), 3.07–2.97 (m, 1H), 2.24 (d, 1H, J = 8.5 Hz), 1.70 (s, 3H, CH_3), 1.28–1.25 (m, 6H), 1.25 (d, 3H, J = 6.2 Hz, Rha-H-6), 1.21 (d, 3H, J = 6.2 Hz, Rha-H-6), 1.03, 1.01, 0.95, 0.87, 0.84 (each s, each 3H, CH_3), 0.74 (d, 1H, J = 9.6 Hz, H-5); ^{13}C NMR (151 MHz, CD_3OD): δ 177.14 (C-28), 151.82 (C-20), 110.31 (C-29), 105.48 (C-1′), 103.02 (Rha-C-1), 101.99 (Rha-C-1), 90.39, 80.31, 79.21, 78.11, 76.41, 73.90, 73.66, 72.41, 72.10, 71.97, 70.72, 69.98, 68.36, 61.95, 57.67, 57.42, 51.99, 50.51, 43.53, 42.01, 40.34 (two), 39.69, 38.04 (two), 35.56, 33.14, 31.70, 30.72, 28.40, 27.36, 26.90, 22.11 (three), 22.05 (two), 19.62, 19.26, 18.02, 17.90, 16.98, 16.93, 16.70, 15.20. HRMS (ESI) *m/z*: calcd for $C_{51}H_{85}O_{16}$ $[M + H]^+$, 953.5838; found, 953.5852.

4.1.10.7. Cyclohexyl-3β-O-[2, 4-di-O-(α-l-rhamnopyranosyl)-β-d-glucopyranosyl]-lup-20 (29)-ene-28-oic acid (BA-9). Similarly, **BA-9** was prepared as a white solid in 73 % yield for two steps; ^{1}H NMR (400 MHz, CD_3OD): δ 5.34 (s, 1H, Rha-H-1), 4.85 (d, 1H, J = 1.2 Hz, Rha-H-1), 4.68 (s, 1H, C = CH_2-1), 4.56 (s, 1H, C = CH_2-2), 4.40 (d, 1H, J = 7.7 Hz, H-1′), 3.98–3.95 (m, 2H), 3.92–3.69 (m, 3H), 3.68–3.46 (m, 3H), 3.46–3.32 (m, 2H), 3.12 (d, 1H, J = 9.6 Hz, H-3), 2.70–2.66 (m, 10*H*, cyclohexanol-H), 2.22 (d, 1H, J = 12.8 Hz), 1.67 (s, 3H, CH_3), 1.24 (d, 3H, J = 6.3 Hz, Rha-H-6), 1.18 (d, 3H, J = 6.1 Hz, Rha-H-6), 1.00, 0.98, 0.94, 0.83, 0.81 (each s, each 3H, CH_3), 0.71 (d, 1H, J = 9.9 Hz, H-5); ^{13}C NMR (101 MHz, CD_3OD): δ 170.73 (C-28), 152.26 (C-20), 110.12 (C-29), 105.46 (C-1′), 102.97 (Rha-C-1), 101.96 (Rha-C-1), 90.40, 80.22, 79.19, 78.08, 76.40, 73.90, 73.67, 72.41, 72.08 (two), 71.98, 70.70, 69.98, 61.91, 57.40, 52.01, 50.42, 43.56, 41.93, 40.32 (two), 39.57, 38.03, 35.60, 35.38 (two), 31.73, 30.86, 28.38, 27.35, 26.90, 22.09, 19.57, 19.26, 18.01 (two), 17.91 (two), 16.97 (two), 16.90 (two), 16.73, 15.13. HRMS (ESI) *m/z*: calcd for $C_{54}H_{89}O_{16}$ $[M + H]^+$, 993.6151; found, 993.6175.

4.1.10.8. 2′-Chloroethyl-3β-O-[2, 4-di-O-(α-l-rhamnopyranosyl)-β-d-glucopyranosyl]-lup-20 (29)-ene-28-oic acid (BA-10). Similarly, **BA-10** was prepared as a white solid in 74 % yield for two steps; ^{1}H NMR (600 MHz, CD_3OD): δ 5.38 (s, 1H, Rha-H-1), 4.82 (d, 1H, J = 1.2 Hz, Rha-H-1), 4.75 (s, 1H, C = CH_2-1), 4.63 (s, 1H, C = CH_2-2), 4.44 (d, 1H, J = 7.9 Hz, H-1′), 4.40–4.32 (m, 2H), 3.97–3.95 (m, 2H), 3.82–3.80 (m, 3H), 3.72–3.51 (m, 2H), 3.44–3.41 (m, 2H), 3.16 (d, 1H, J = 10.7 Hz, H-3), 2.29 (d, 1H, J = 10.1 Hz, H-13), 1.73 (s, 3H, CH_3), 1.29 (d, 3H, J = 6.0 Hz, Rha-H-6), 1.23 (d, 3H, J = 6.0 Hz, Rha-H-6), 1.05, 1.04, 0.97, 0.89, 0.86 (each s, each 3H, CH_3), 0.76 (d, 1H, J = 9.3 Hz, H-5; ^{13}C NMR (151 MHz, CD_3OD): δ 177.21 (C-28), 151.74 (C-20), 110.38 (C-29), 105.50 (C-1′), 103.06 (Rha-C-1), 102.01 (Rha-C-1), 90.41, 80.35, 79.21, 78.14, 76.44, 73.93, 73.68, 72.43, 72.12 (two), 71.99, 70.75, 70.00, 65.09, 61.97, 57.98, 57.43, 52.00, 50.63, 43.54, 43.26, 42.00, 40.35 (two), 39.72, 38.05, 35.58, 33.08, 31.63, 30.82, 28.40, 27.38, 26.88, 19.60, 19.27, 18.02 (two), 17.91, 16.99 (two), 16.94 (two), 16.65, 15.21. HRMS (ESI) *m/z*: calcd for $C_{50}H_{82}O_{16}Cl$ $[M + H]^+$, 973.5291; found, 973.5317.

4.1.10.9. 2′-Bromoethyl 3β-O-[2, 4-di-O-(α-l-rhamnopyranosyl)-β-d-glucopyranosyl]-lup-20 (29)-ene-28-oic acid (BA-11). Similarly, **BA-11** was prepared as a white solid in 70 % yield for two steps; ^{1}H NMR (600 MHz, CD_3OD): δ 5.34 (d, 1H, J = 1.8 Hz, Rha-H-1), 4.83 (s, 1H, Rha-H-1), 4.70 (s, 1H, C = CH_2-1), 4.58 (s, 1H, C = CH_2-2), 4.40 (d, 1H, J = 7.7 Hz, H-1′), 4.16–4.08 (m, 2H), 3.99–3.91 (m, 2H), 3.89 (dd, 1H, J = 9.6, 7.4 Hz, H-2′), 3.83–3.81 (m, 1H), 3.78 (dd, 1H, J = 12.0, 2.0 Hz, H-6′-1), 3.72 (dd, 1H, J = 9.7, 3.1 Hz, Rha-H-3), 3.64 (dd, 1H, J = 13.0, 5.6 Hz, H-6′-2), 3.63–3.56 (m, 2H), 3.59–3.49 (m, 1H), 3.46–3.34 (m, 2H), 3.32–3.27 (m, 2H), 3.16–3.07 (m, 1H, H-3), 3.03–2.93 (m, 1H), 2.27 (d, 1H, J = 12.8 Hz), 1.67 (s, 3H, CH_3), 1.24 (d, 3H, J = 6.2 Hz, Rha-H-6), 1.19 (d, 3H, J = 6.1 Hz, Rha-H-6), 1.01, 0.98, 0.92, 0.84, 0.81 (each s, each 3H, CH_3), 0.71 (d, 1H, J = 9.6 Hz, H-5); ^{13}C NMR (151 MHz, CD_3OD): δ 177.62 (C-28), 151.83 (C-20), 110.42 (C-29), 105.46 (C-1′), 103.02 (Rha-C-1), 101.97 (Rha-C-1), 90.37, 80.32, 79.20, 78.11, 76.40, 73.90, 73.67, 72.41, 72.10 (two), 71.98, 70.71, 69.97, 66.33, 61.12, 57.88, 57.40, 51.99, 49.85, 43.52, 41.95 (two), 40.32 (two), 39.57, 38.03 (two), 33.04, 30.72, 28.37, 27.35, 26.86, 22.05, 19.57, 19.25, 18.00 (two), 17.90 (two), 16.97 (two), 16.89 (two), 16.59, 15.16. HRMS (ESI) *m/z*: calcd for $C_{50}H_{82}O_{16}Br$ $[M + H]^+$, 1017.4786; found, 1017.4803.

4.1.10.10. 2′-Hydroxylethyl-3β-O-[2, 4-di-O-(α-l-rhamnopyranosyl)-β-d-glucopyranosyl]-lup-20 (29)-ene-28-oic acid (BA-12). Similarly, **BA-12** was prepared as a white solid in 70 % yield for two steps; ^{1}H NMR (600 MHz, CD_3OD): δ 5.37 (s, 1H, Rha-H-1), 4.82 (d, 1H, J = 1.1 Hz, Rha-H-1), 4.73 (s, 1H, C = CH_2-1), 4.61 (s, 1H, C = CH_2-2), 4.42 (d, 1H, J = 7.7 Hz, H-1′), 4.16–4.14 (m, 2H), 3.97–3.95 (m, 2H), 3.87–3.71 (m, 3H), 3.66–3.64 (m, 1H), 3.57 (t, 1H, J = 8.7 Hz), 3.47–3.35 (m, 2H), 3.34–3.32 (m, 3H), 3.19–3.11 (m, 1H, H-3), 3.02–3.00 (m, 2H), 2.31 (d, 1H, J = 11.9 Hz), 1.71 (s, 3H, CH_3), 1.27 (d, 3H, J = 6.0 Hz, Rha-H-6), 1.22 (d, 3H, J = 6.1 Hz, Rha-H-6), 1.04, 1.01, 0.95, 0.87, 0.84 (each s, each 3H, CH_3), 0.73 (d, 1H, J = 9.7 Hz, H-5); ^{13}C NMR (151 MHz, CD_3OD): δ 178.06 (C-28), 151.73 (C-20), 110.36 (C-29), 105.48, 105.30 (C-1′), 103.02 (Rha-C-1), 101.97 (Rha-C-1), 90.37, 80.30, 79.17, 78.12, 76.41, 73.91, 73.67, 72.41, 72.11 (two), 71.98, 70.72, 69.97, 61.94, 57.86, 57.41, 56.45, 51.97, 51.84, 50.62, 43.50, 41.90, 40.33 (two), 39.63, 38.04, 37.86, 35.55, 33.13, 31.62, 30.80, 28.40, 27.36, 26.84, 22.06, 19.60, 19.27, 18.03, 17.91, 16.99, 16.92, 16.59, 15.21. HRMS (ESI) *m/z*: calcd for $C_{50}H_{83}O_{17}$ $[M + H]^+$, 955.5630; found, 955.5658.

4.1.10.11. 2′-Oxopethyl-3β-O-[2, 4-di-O-(α-l-rhamnopyranosyl)-β-d-glucopyranosyl]-lup-20 (29)-ene-28-oic acid (BA-13). Similarly, **BA-13** was prepared as a white solid in 65 % yield for two steps; ^{1}H NMR (500 MHz, CD_3OD): δ 9.60 (s, 1H, CHO), 5.33 (s, 1H, Rha-H-1), 4.87 (d, 1H, J = 1.1 Hz, Rha-H-1), 4.82 (brs, 2H), 4.68 (s, 1H, C = CH_2-1), 4.57 (s, 1H, C = CH_2-2), 4.38 (d, 1H, J = 7.8 Hz, H-1′), 3.92–3.87 (m, 3H), 3.74 (dd, 1H, J = 9.6, 7.5 Hz, H-2′), 3.63–3.61 (m, 4H), 3.53 (t, 1H, J = 9.2 Hz, Rha-H-4), 3.42–3.33 (m, 1H), 3.28–3.26 (m, 2H), 3.20–3.14 (m, 3H), 3.12–3.10 (m, 1H, H-3), 3.01–2.91 (m, 2H), 2.19 (d, 1H, J = 11.3 Hz), 1.66 (s, 3H, CH_3), 1.23 (d, 3H, J = 6.0 Hz, Rha-H-6), 1.17 (d, 3H, J = 6.0 Hz, Rha-H-6), 0.99, 0.97, 0.90, 0.83, 0.80 (each s, each 3H, CH_3), 0.70 (d, 1H, J = 9.4 Hz, H-5); ^{13}C NMR (151 MHz, CD_3OD): δ 207.02, 178.08 (C-28), 151.72 (C-20), 110.38 (C-129), 105.49 (C-1′), 103.00 (Rha-C-1), 101.98 (Rha-C-1), 90.39, 80.23, 79.17, 78.10, 76.41, 73.89, 73.65, 72.40, 72.08 (two), 71.96, 70.70, 69.98, 61.91, 57.85, 57.40, 51.96, 51.86, 50.61,

43.49, 41.89, 40.33 (two), 39.62, 38.03 (two), 37.86, 35.54, 33.12, 31.60, 30.79, 28.39, 27.35, 26.82, 22.06, 19.59, 19.26, 18.03 (two), 17.91 (two), 16.99, 16.93, 16.58, 15.21. HRMS (ESI) *m/z*: calcd for $C_{50}H_{81}O_{17}$ $[M + H]^+$, 953.5474; found, 953.5496.

4.1.10.12. Allyl-3β-O-[2, 4-di-O-(α-l-rhamnopyranosyl)-β-d-glucopyranosyl]-lup-20 (29)-ene-28-oic acid (BA-14). Similarly, **BA-14** was prepared as a white solid in 68 % yield for two steps; ^{1}H NMR (600 MHz, CD_3OD): δ 6.04–5.90 (m, 1H), 5.38 (s, 1H, Rha-H-1), 5.35 (d, 1H, J = 11.7 Hz), 5.25 (d, 1H, J = 10.4 Hz), 4.85 (s, 1H, Rha-H-1), 4.73 (s, 1H, C = CH_2-1), 4.61 (s, 1H, C = CH_2-2), 4.58 (d, 2H, J = 8.2 Hz), 4.43 (d, 1H, J = 7.7 Hz, H-1′), 4.03–3.94 (m, 2H), 3.92 (dd, 1H, J = 9.5, 7.2 Hz, H-2′), 3.88–3.77 (m, 2H), 3.75 (dd, 1H, J = 9.6, 3.3 Hz, Rha-H-3), 3.71–3.60 (m, 2H), 3.62–3.53 (m, 1H), 3.49–3.35 (m, 3H), 3.33–3.31 (m, 1H), 3.15 (dd, 1H, J = 11.3, 4.1 Hz, H-3), 3.02–3.00 (m, 1H), 2.89–2.87 (m, 1H), 2.27 (d, 1H, J = 9.4 Hz), 1.71 (s, 3H, CH_3), 1.28 (d, 3H, J = 6.1 Hz, Rha-H-6), 1.22 (d, 3H, J = 6.2 Hz, Rha-H-6), 1.04, 1.02, 0.94, 0.87, 0.85 (each s, each 3H, CH_3), 0.74 (d, 1H, J = 9.5 Hz, H-5); ^{13}C NMR (151 MHz, CD_3OD): δ 177.18 (C-28), 151.78 (C-20), 61.97, 57.91, 57.42, 52.01, 50.64, 43.53, 42.00, 40.35, 39.66, 38.05, 37.92, 36.97, 35.56, 35.38 (two), 33.13, 31.62, 30.77, 28.38, 27.37, 26.86, 22.07, 19.55, 19.26, 18.01, 17.90, 16.98, 16.89, 16.64, 15.14. HRMS (ESI) *m/z*: calcd for $C_{51}H_{83}O_{16}$ $[M + H]^+$, 951.5681; found, 951.5703.

4.1.10.13. Cyclopropylmethyl-3β-O-[2, 4-di-O-(α-l-rhamnopyranosyl)-β-d-glucopyranosyl]-lup-20 (29)-ene-28-oic acid (BA-15). Similarly, **BA-15** was prepared as a white solid in 70 % yield for two steps; ^{1}H NMR (600 MHz, CD_3OD): δ 5.37 (s, 1H, Rha-H-1), 4.82 (s, 1H, Rha-H-1), 4.74 (s, 1H, C = CH_2-1), 4.62 (s, 1H, C = CH_2-2), 4.43 (d, 1H, J = 7.7 Hz, H-1′), 4.04–3.94 (m, 4H), 3.91 (dd, 1H, J = 9.6, 7.2 Hz, H-2′), 3.90–3.78 (m, 1H), 3.76 (dd, 1H, J = 9.6, 3.4 Hz, Rha-H-3), 3.72–3.60 (m, 3H), 3.58 (t, 1H, J = 8.4 Hz), 3.48–3.35 (m, 3H), 3.33–3.31 (m, 2H), 3.15 (dd, 1H, J = 11.4, 4.3 Hz, H-3), 3.10–2.99 (m, 2H), 2.29 (d, 1H, J = 10.1 Hz), 1.71 (s, 3H, CH_3), 1.28 (d, 3H, J = 6.2 Hz, Rha-H-6), 1.22 (d, 3H, J = 6.2 Hz, Rha-H-6), 1.04, 1.02, 0.96, 0.88, 0.85 (each s, each 3H, CH_3), 0.75 (d, 1H, J = 9.7 Hz, H-5), 0.58 (q, 2H, J = 7.7 Hz), 0.32 (q, 2H, J = 7.5 Hz); ^{13}C NMR (151 MHz, CD_3OD): δ 177.72 (C-28), 151.81 (C-20), 110.34 (C-29), 105.50 (C-1′), 103.04 (Rha-C-1), 102.00 (Rha-C-1), 90.40, 80.31, 79.21, 78.12, 76.42, 73.91, 73.67, 72.42, 72.11 (two), 71.98, 70.73, 69.99, 69.68, 61.95, 57.87, 57.43, 52.00, 50.60, 43.56, 41.97, 40.35 (two), 39.71, 38.05, 35.60, 33.21, 31.70, 30.78, 28.41, 27.37, 26.90, 22.12, 19.63, 19.28, 18.03 (two), 17.90 (two), 16.99 (two), 16.94 (two), 16.73, 15.24, 10.99. HRMS (ESI) *m/z*: calcd for $C_{52}H_{85}O_{16}$ $[M + H]^+$, 965.5838; found, 965.5856.

*4.1.11 General procedure for **BA-N-1** and **BA-N-2**.* To a solution of compound **20** (1.0 mmol) in 10 mL dried CH_2Cl_2 was added oxalyl chloride (1 mL) under argon. Then the mixture was stirred at room temperature for 12 h and concentrated to dryness *in vacuo*. To a dried CH_2Cl_2 (10 mL) solution of methylamine hydrochloride or dimethylamine hydrochloride (2.0 mmol) was added to the crude acid chloride. The reaction mixturewas was stirred at r.t. for 3 h under argon and then concentratedunder reduced pressure. The obtained residue was redissolved in 2:1 MeOH/CH_2Cl_2 (15 mL) and then NaOMe was added until pH = 10. After stirred at r.t. for 3 h, the solution was neutralized with Dowex 50 × 8 (H^+) resin until pH = 7, filtered and concentrated *in vacuo*. Then the residue was purified by silica gel column chromatography (CH_2Cl_2-MeOH, 6:1) to yield compounds **BA-N-1** and **BA-N-2**, respectively.

4.1.11. N-{β-O-[2, 4-Di-O-(α-l-rhamnopyranosyl)-β-Dglucopyranosyl]-lup-20 (29)-ene-28-oyl}-methylamine (BA-N-1)

BA-N-1 was prepared as a white solid in 85 % yield for three steps. ^{1}H NMR (600 MHz, CD_3OD): δ 5.37 (s, 1H, Rha-H-1), 4.83 (s, 1H, Rha-H-1), 4.71 (s, 1H, C = CH_2-1), 4.59 (s, 1H, C = CH_2-2), 4.43 (d, 1H, J = 7.4 Hz, H-1′), 3.94–3.90 (m, 3H), 3.83 (d, 1H, J = 12.0 Hz), 3.76 (t, 1H, J = 11.2 Hz), 3.71–3.52 (m, 3H), 3.45–3.36 (m, 3H), 2.70 (s, 3H, NH-CH_3), 2.57–2.55 (m, 1H), 2.11 (d, 1H, J = 12.2 Hz), 1.69 (s, 3H, CH_3), 1.25–1.19 (m, 6H, 2 × Rha-H-6), 1.03, 1.00, 0.96, 0.87, 0.84 (each s, each 3H, CH_3), 0.78–0.70 (m, 1H, H-5); ^{13}C NMR (151 MHz, CD_3OD): δ 179.75 (C-28), 152.37 (C-20), 109.93 (C-29), 105.45 (C-1′), 103.04 (Rha-C-1), 101.94 (Rha-C-1), 90.34, 80.34, 79.13, 78.17, 76.42, 73.93, 73.70, 72.44, 72.11 (two), 72.03, 70.74, 69.96, 61.92, 57.43, 56.94, 52.09, 51.43, 48.17, 43.48, 41.97, 40.33 (two), 39.34, 38.97, 38.05, 35.59, 34.13, 31.93, 30.54, 28.39, 27.38, 26.98, 26.42, 22.14, 19.63, 19.27, 18.04, 17.96, 16.99, 16.91, 16.72, 15.09. HRMS (ESI) *m/z*: calcd for $C_{49}H_{81}O_{15}NNa$ $[M + Na]^+$, 946.5498; found, 946.5447.

4.1.12. N-{β-O-[2, 4-di-O-(α-l-rhamnopyranosyl)-β-Dglucopyranosyl]-lup-20(29)-ene-28-oyl}-dimethylamine (BA-N-2)

BA-N-2 was prepared as a white solid in 82 % yield for three steps; ^{1}H NMR (600 MHz, CD_3OD): δ 5.37 (s, 1H, Rha-H-1), 4.81 (s, 1H, Rha-H-1), 4.70 (s, 1H, C = CH_2-1), 4.58 (s, 1H, C = CH_2-2), 4.43 (d, 1H, J = 7.7 Hz, H-1′), 4.00–3.95 (m, 3H), 3.92 (dd, 1H, J = 9.5, 6.8 Hz, H-2′), 3.87–3.78 (m, 3H), 3.75 (dd, 1H, J = 9.5, 3.4 Hz, Rha-H-3), 3.70–3.62 (m, 2H), 3.57–3.55 (m, 1H), 3.47–3.35 (m, 2H), 3.2 (s, 6H, 2 × NCH_3), 3.07–2.95 (m, 1H, H-3), 2.34 (d, 1H, J = 13.4 Hz), 1.70 (s, 3H, CH_3), 1.27 (d, 3H, J = 6.2 Hz, Rha-H-6), 1.21 (d, 3H, J = 6.1 Hz, Rha-H-6), 1.03, 1.00, 0.95, 0.87, 0.84 (each s, each 3H, CH_3), 0.74 (s, 1H, H-5); ^{13}C NMR (151 MHz, CD_3OD): δ 177.13 (C-28), 152.63 (C-20), 109.83 (C-29), 105.47 (C-1′), 103.09 (Rha-C-1), 101.98 (Rha-C-1), 90.40, 80.44, 79.19, 78.19, 76.44, 73.94, 73.70, 72.45, 72.13, 72.03, 70.76, 70.00, 61.96, 57.51, 56.09, 53.92, 52.28, 47.49, 43.03, 41.94, 40.36, 38.49, 38.08, 36.83, 35.62, 32.92, 32.44, 31.02, 28.37, 27.38, 27.03, 22.34, 19.75, 19.29, 18.01, 17.91, 17.48, 17.29, 17.10, 16.98, 16.68, 15.10. HRMS (ESI) *m/z*: calcd for $C_{50}H_{83}O_{15}NNa$ $[M + Na]^+$, 960.5660; found, 960.5691.

4.1.13. 3β-O-[2, 4-Di-O-(2, 3, 4-tri-O-Acetyl-α-l-rhamnopyranosyl)-β-(3, 6-di-O-acetyl)-d-glucopyranosyl]-lup-20 (29)-ene-3, 28-diol (22)

Compound **21** (360 mg, 0.27 mmol) dissolved in THF (5 mL) and MeOH (5 mL), and 10 % Pd/C (40 mg) was added to the solution. The reaction mixture was stirred under atmospheric pressure hydrogen at r.t. for 1 h. After Pd/C was filtered off, the mixture was concentrated under vacuum to give a crude residue, which was purified by column chromatography (petroleumether-EtOAc-CH_2Cl_2, 2:1:1) to obtain **22** (302 mg, 90 %) as a white powder. ^{1}H NMR (600 MHz, $CDCl_3$): δ 5.52–5.21 (m, 2H), 5.11–5.07 (m, 3H), 4.86 (s, 1H, C = CH_2-1), 4.82 (s, 1H, C = CH_2-2), 4.69–4.67 (m, 1H), 4.58 (d, 1H, J = 7.9 Hz, H-1′), 4.42 (t, 1H, J = 9.7 Hz, Rha-H-4), 4.36–4.16 (m, 3H), 4.16–3.88 (m, 4H), 3.73 (t, 1H, J = 9.2 Hz, H-4′), 3.61 (t, 1H, J = 8.8 Hz, Rha-H-4), 3.55–3.43 (m, 2H, C-CH_2), 3.31 (d, 1H, J = 10.6 Hz), 3.18–3.05 (m, 1H, H-3), 2.15, 2.12, 2.12, 2.06, 2.04, 2.00, 1.99, 1.95 (each s, each 3H, each CH_3CO), 1.67 (s, 3H, CH_3), 1.24 (d, 3H, J = 6.3 Hz, CH_3), 1.17 (d, 3H, J = 6.3 Hz, CH_3), 1.04 (s, 6H, 2 × CH_3), 1.00 (s, 3H, CH_3), 0.81 (s, 6H, 2 × CH_3), 0.75 (d, 1H, J = 7.0 Hz, H-5); ^{13}C NMR (151 MHz, $CDCl_3$): δ 170.27, 170.13 (three), 170.09 (three), 169.82, 150.01 (C-20), 111.18 (C-29), 104.02 (C-1′), 99.14 (Rha-C-1), 97.36 (Rha-C-1), 90.28, 82.28, 76.33, 75.63, 75.56, 75.42, 71.67, 71.22, 70.70, 70.02, 69.73, 69.62, 69.28, 69.11, 68.71, 68.21, 66.66, 62.66, 60.42, 56.05, 50.44, 48.92, 47.88, 42.81, 41.08, 39.26, 36.94, 34.26, 34.08, 29.35, 28.28, 27.84, 26.99, 26.29, 25.88, 23.02, 22.58, 21.06, 20.92 (three), 20.88 (three), 20.84 (three), 20.76 (two), 18.29, 17.49 (two), 17.42 (two), 16.24 (two), 16.23, 14.89, 14.80. HRMS (ESI) *m/z*: calcd for $C_{64}H_{97}O_{23}$ $[M + H]^+$, 1233.6421; found, 1233.6443.

4.1.14. 3β-O-[2, 4-Di-O-(α-l-Rhamnopyranosyl)-β-d-glucopyranosyl]-lup-20 (30)-en-28-al (BA-18)

To a solution of **21** (0.20 g, 0.16 mmol, 1.0 eq) in CH_2Cl_2-MeOH (20 mL, *V*: *V* = 1: 1) and was added PCC (0.10 g, 0.41 mmol) at 0 ℃ under argon. After the mixture was stirred at r.t. for 4 h, the reaction mixture was filtered and the filtrate was concentrated under vacuum. The residue was dissolved in EtOAc (60 mL), then extracted with water (3 × 30

mL) and brine (3 × 30 mL). The organic phase was concentrated under reduced pressure. The residue was re-dissolved in MeOH (10 mL) and CH_2Cl_2 (10 mL), CH_3ONa was added until pH = 10. The reaction mixture was stirred at r.t. until the reaction was complete detected by TLC. Then, the mixture was neutralized with Dowex 50 × 8 (H^+) resin until pH = 7. The reaction mixture was filtered and evaporated to remove excess solvent under vacuum. The residue was purified by silica gel column chromatography (CH_2Cl_2-MeOH, 5:1) to produce **BA-18** (0.13 g, 84 % for two steps). ^{1}H NMR (600 MHz, CD_3OD): δ 9.58 (s, 1H, CHO), 5.29 (s, 1H, Rha-H-1), 4.89 (s, 1H, Rha-H-1), 4.56 (s, 2H, C = CH_2), 4.35 (d, 1H, J = 7.7 Hz, H-1′), 3.87 (m, 2H), 3.79–3.63 (m, 1H), 3.62–3.44 (m, 3H), 3.42–3.29 (m, 3H), 3.25–3.23 (m, 3H), 3.12–3.00 (m, 1H, H-3), 2.86–2.73 (m, 2H), 2.03–1.80 (m, 1H), 1.64 (s, 3H, CH_3), 1.17 (m, 6H, 2 × Rha-H-6), 1.00–0.67 (m, 15H, 5 × CH_3); ^{13}C NMR (151 MHz, CD_3OD): δ 207.06 (CHO), 149.80 (C-20), 110.21 (C-29),104.09 (C-1′), 101.65 (Rha-C-1), 100.62 (Rha-C-1), 89.04, 78.95, 77.84, 76.74, 75.05, 72.54, 72.30, 71.04, 70.73, 70.61, 69.35, 68.63, 60.58, 59.13, 56.53, 56.00, 50.64, 42.50, 42.28, 42.17, 40.66, 40.55, 38.95, 38.69, 36.66, 34.20, 29.43, 26.99, 25.98, 20.68, 19.76, 18.19, 17.86, 16.63, 16.52, 15.61, 15.51, 15.26, 15.09, 13.75, 13.68, 13.30. HRMS (ESI) *m/z*: calcd for $C_{49}H_{81}O_{15}$ $[M + H]^+$, 909.5575; found, 909.5593.

4.1.15. 28-(Methoxy)-3β-O-[2, 4-di-O-(α-l-Rhamnopyranosyl)-β-d-glucopyranosyl]-lup-20 (29)-ene-3-al (BA-19)

To a solution of **21** (0.20 g, 0.16 mmol) in ACN (10 mL) was added Ag_2O (0.19 g, 0.81 mmol). After stirring for 20 min, CH_3I (0.12 g, 0.81 mmol) was added quickly while the mixture was at 60 ℃ under argon atmosphere. Stirring was continued overnight at that temperature. Then the mixture was cooled to room temperature, filtered and the filtrate was concentrated under vacuum. The residue was dissolved in EtOAc (100 mL), then extracted with water (3 × 50 mL) and brine (3 × 50 mL). The organic phase was concentrated under vacuum. Then, the residue was re-dissolved in MeOH (10 mL) and CH_2Cl_2 (10 mL), CH_3ONa was added until pH = 10. After the reaction mixture was stirred at r.t. for 5 h, Dowex 50 × 8 (H^+) resin was added until pH = 7. The reaction mixture was filtered and concentrated under vacuum. The residue was purified by silica gel column chromatography (CH_2Cl_2-MeOH, 6:1) to afford **BA-19** (0.12 g, 83 % for two steps). ^{1}H NMR (600 MHz, CD_3OD): δ 5.39 (s, 1H, Rha-H-1), 4.85 (d, 1H, J = 1.7 Hz, Rha-H-1), 4.72 (s, 1H, C = CH_2-1), 4.60 (s, 1H, C = CH_2-2), 4.44 (d, 1H, J = 7.7 Hz, H-1′), 3.99 (dd, 1H, J = 3.5, 1.7 Hz, Rha-H-2), 3.93 (dd, 1H, J = 9.5, 7.4 Hz, H-2′), 3.86 (dd, 1H, J = 3.3, 1.9 Hz, Rha-H-2), 3.86–3.78 (m, 1H), 3.77 (dd, 1H, J = 9.7, 3.5 Hz, Rha-H-3), 3.67 (dd, 1H, J = 9.7, 3.8 Hz, Rha-H-3), 3.58 (t, 1H, J = 9.3 Hz, Rha-H-3), 3.50–3.38 (m, 3H), 3.36–3.30 (m, 4H), 3.20–3.11 (m, 2H), 2.49–2.45 (m, 1H), 1.71 (s, 3H, CH_3), 1.29 (d, 3H, J = 6.2 Hz, Rha-H-6), 1.23 (d, 3H, J = 6.3 Hz, Rha-H-6), 1.10, 1.06, 1.03, 0.90, 0.87 (each s, each 3H, CH_3), 0.76 (d, 1H, J = 9.8 Hz, H-5); ^{13}C NMR (151 MHz, CD_3OD): δ 151.77 (C-20), 110.33 (C-29), 105.49 (C-1′), 103.05 (Rha-C-1), 102.00 (Rha-C-1), 90.39, 80.36, 79.21, 78.14, 76.43, 73.93, 73.68, 72.43, 72.12, 72.00, 70.75, 70.00, 61.96, 59.88, 57.38, 51.87, 50.13, 48.41, 43.78, 42.15, 40.35, 40.29, 38.88, 38.01, 35.77, 35.47, 31.07, 30.99, 30.77, 28.40, 28.35, 27.37, 26.59, 22.00, 19.42, 19.28, 18.02, 17.90, 17.00, 16.90, 16.58, 15.33. HRMS (MALDI) *m/z*: calcd for $C_{49}H_{82}O_{15}Na$ $[M + Na]^+$, 933.5551; found, 933.5573.

4.1.16. 28-Chloro-3β-O-[2, 4-di-O-(α-l-Rhamnopyranosyl)-β-d-glucopyranosyl]-lup-20 (29)-ene-3-al (BA-21)

To a solution of **21** (0.20 g, 0.16 mmol, 1.0 eq) in dry CH_2Cl_2 (10 mL) was added $SOCl_2$ (18 μL, 0.21 mmol) at 0 ℃ under N_2 atmosphere. After the mixture was stirred at r.t. for 12 h, the reaction was quenched with $NaHCO_3$ at 0 ℃. Then, the reaction mixture was concentrated under vacuum. The residue was dissolved in EtOAc (60 mL), then extracted with water and brine, dried over Na_2SO_4, and concentrated in reduced pressure. The obtained crude product was re-dissolved in MeOH (10 mL) and CH_2Cl_2 (10 mL), CH_3ONa was added until pH = 10. The reactant was then held at 30 °C until TLC indicated the reaction was complete. Dowex 50 × 8 (H +) resin was added until pH = 7. Removal of the precipitate by filtration provided a yellowish solution, which was concentrated under vacuum. The residue was purified by silica gel column chromatography (CH_2Cl_2-MeOH, 6:1) to yield **BA-21** (0.11 g, 76 % for two steps). ^{1}H NMR (600 MHz, CD_3OD): δ 5.38 (s, 1H, Rha-H-1), 4.85 (s, 1H, Rha-H-1), 4.70 (s, 1H, C = CH_2-1), 4.63 (s, 1H, C = CH_2-2), 4.45 (d, 1H, J = 7.7 Hz, H-1′), 4.04–3.95 (m, 2H), 3.93 (dd, 1H, J = 9.5, 7.4 Hz, H-2′), 3.89–3.78 (m, 2H), 3.77 (dd, 1H, J = 9.6, 3.4 Hz, Rha-H-3), 3.73–3.59 (m, 2H), 3.55–3.56 (m, 1H), 3.53–3.43 (m, 2H), 3.47–3.36 (m, 2H), 3.34–3.31 (m, 2H), 3.18 (dd, 1H, J = 11.7, 4.6 Hz, H-3), 3.03–3.01 (m, 1H), 2.90–2.88 (m, 1H), 2.04–1.94 (m, 1H), 1.32–1.30 (m, 2H), 1.23 (d, 3H, J = 6.2 Hz, Rha-H-6), 1.05 (d, 3H, J = 6.2 Hz, Rha-H-6), 0.98, 0.94, 0.92, 0.87, 0.85 (each s, each 3H, CH_3), 0.75 (d, 1H, J = 9.7 Hz, H-5); ^{13}C NMR (151 MHz, CD_3OD): δ 150.19 (C-20), 108.89 (C-29), 104.25 (C-1′), 101.01 (Rha-C-1), 100.45 (Rha-C-1), 88.45, 87.20, 77.39, 76.90, 75.68, 72.39, 71.19, 71.09, 70.74, 70.62, 69.20, 69.17, 68.55, 60.59, 55.97, 50.93, 46.63, 41.37, 40.72, 39.16, 38.97, 36.94, 36.53, 36.37, 36.27, 34.72, 34.21, 33.90, 33.16, 29.27, 27.68, 26.46, 26.43, 26.36, 26.31, 24.71, 21.25, 18.32 (two), 18.10, 16.89, 16.44, 15.86, 13.75, 11.84. HRMS (MALDI) *m/z*: calcd for $C_{48}H_{79}O_{14}ClNa$ $M + Na]^+$, 937.5056; found, 937.5072.

4.2. Biology assay

4.2.1. Cell lines and plasmids

HEK-293 T (Human, embryonic kidney) and Vero-E6 (African green monkey, kidney) cells were cultured in Dulbecco's Modified Eagle Medium (Gibco) supplemented with 10 % fetal bovine serum (Capricorn Scientific) and 1 % penicillin (100 units/mL) /streptomycin (100 μg/mL) (Gibco, USA). 293 T-ACE2 (293 T cells stably expressing human ACE2) were constructed by our laboratory and cultivated under the same conditions as above.

Plasmid pcDNA3.1-SARS-CoV-2-Sipke and pAAV-IRES-GFP-SARS-CoV-2-Sipke were given by the laboratory of Professor Shibo Jiang. Plasmid pAAV-IRES-EGFP was purchased from Hedgehogbio Science and Technology ltd. Expression plasmids for full-length vesicular stomatitis virus (VSV) glycoprotein (VSV-G) and pNL4-3.Luc.R-E- plasmids were obtained from Addgene (Cambridge, MA). Based on Plasmid pcDNA3.1-SARS-CoV-2 Spike, its mutants N501Y, D614G and Delta were all retained in our laboratory. Plasmid pcDNA3.1-SARS-CoV-2-Omicron and its 2 mutant plasmids were constructed by our laboratory. In brief, primers containing mutant sites were designed to amplify the specified DNA fragments with pcDNA3.1-SARS-CoV-2-Omicron as a template. The product obtained by PCR in the previous step was subjected to homologous recombination according to the manufacturer's instructions (Vazyme, China). The recombinant plasmids were used to transform stabl3 and inoculated in culture plates containing the corresponding resistance. After incubation in 37 ℃ for 12–16 h, single colonies on plates were selected and sequenced. Mutation sites and corresponding primers were shown in followed table [30]:

765-*Foward*	GCTTCTGCACCCAGCTGAAGGCAGCCCTGACCGGCATCGCCGTGG
765-*Reverse*	CTTCAGCTGGGTGCAGAAGCTGCC
964-*Foward*	CCAGGCCCTGAACACCCTGGTGGCGCAGCTGTCCAGCAAGTTCGG
964-*Reverse*	CACCAGGGTGTTCAGGGCCTGG
Circ-*Foward*	GCGTGAAGCTGCACTACACCGGCGGCACCGAGACATCTCAGG
Circ-*Reverse*	GGCTAGCACGGAAGCGACCAGCATC

4.2.2. Pseudotyped SARS-CoV-2 infection assay

HEK293T cells were seeded in 6-well plates and cultured overnight at 37 °C. 1 μg pNL4-3.Luc.R-E-plasmid and 0.5 μg pcDNA3.1-SARS-CoV-2-S plasmid were transfected into 293 T cells, and the supernatant virus liquid was collected after culturing at 37 °C for 48 h. 293 T-ACE2 cells were seeded in 96-well cell plates one day before infection. The concentration gradient drug and SARS-CoV-2 pseudovirus were mixed for

30 min at room temperature, and then added to the cells for 48 h of infection. Cells were lysed and luciferase activities were quantified by Luciferase assay system (Promega, USA) [30].

4.2.3. Cytotoxicity assay

Cells were seeded in a 96-well plate at a density of $1*10^4$ cells/well, and cultured at 37 °C overnight. After 48 h of concentration gradient administration, 20 μL of MTT working solution (5 mg/mL) was added to each well, and cultured at 37 °C for 4 h. After discarding the culture supernatant, 150 μL of DMSO was added to each well, and the absorbance at 570 nm was measured by a microplate reader after sufficient shaking to dissolve. According to the measured OD value, the survival rate of cells under the action of the corresponding concentration of drugs compared with the control group was calculated, respectively [31].

4.2.4. Authentic SARS-CoV-2 inhibition assay

Authentic SARS-CoV-2 inhibition assay was performed by Wuhan institute of virology, Chinese academy of sciences. Vero-E6 cells were seeded in a 48-well plate at a cell density of 3*105 cells/well and cultured overnight at 37 °C, 5 % CO_2. SARS-CoV-2 virus dilution (MOI = 0.05) and serially diluted drugs were pre-incubated at 37 °C for 1 h to infect cells. After that, the supernatant of the infectious material was fully removed and 200 μL of complete medium was added to each well to continue the culture. After 24 h, 150 μL of cell culture supernatant was collected and viral RNA was extracted with an RNA extraction kit (Takara, Japan). The reverse transcribed product was determined by qRT-PCR for viral copy number in the supernatant (Takara TB Green® Premix Ex Taq™ II, Japan) [31].

4.2.5. Co-immunoprecipitation and western blotting

HEK-293 T cells were seeded in six-well plates at a density of $4*10^5$ cells/well one day in advance. 2 ug plasmids pcDNA3.1-ACE2-Flag and 2 ug pcDNA3.1-SARS-Omicron were co-transfected into each well and drugs were added in at the same time. After 48 h, total cell protein was extracted and incubated with protein A Sepharose bound by anti-labeled antibody or mouse IgG. The protein samples were separated by polyacrylamide gel electrophoresis after 12–16 h incubation with the antibody and were transferred to nitrocellulose membranes (Roche, Germany). SARS-Omicron and ACE2 were detected by anti-SARS-CoV-S (Sinol biological Inc., China) and anti-Flag (Sigma, USA) with mouse anti-goat-horseradish peroxidase (HRP) (Fude biological Technology Co., ltd., China) as the secondary antibody [31].

4.2.6. Cell-cell fusion assays

HEK-293 T cells were seeded in 6-well plates at a density of $4*10^5$/well and cultured overnight. After transfection with pAAV-IRES-GFP-SARS-CoV-2-S plasmid expressing both SARS-CoV-2-S protein and green fluorescent protein GFP or pAAV-IRES-GFP vector plasmid, the cells were cultured at 37 °C for 48 h. Target cells Vero-E6 were seeded in 96-well plates at a density of $1*10^4$ cells/well 6 h before cell fusion experiments. 293 T/SARS-CoV-2-S/EGFP or 293 T/EGFP effector cells were incubated with the concentration gradient drug for 30 min and then added to the target cells. After 24 h, three random fields were imaged by inverted fluorescence microscope (Zeiss, Germany) [19].

4.2.7. Surface plasmon resonance (SPR) measurement

Compound **BEA-1**, or **BEA-4** was fixed on the chip by photo-crosslinking, then recombinant SARS-CoV-2 S-trimer protein (DRA 47, Novoprotein Inc. Shanghai) at indicated concentrations was injected sequentially into the chamber in buffer PBST (0.1 % Tween 20, pH 7.4). The interaction of S-trimer with **BEA-1**, or **BEA-4** fixed was detected by PlexArrayTM HT SPRi (Seattle, US). The reaction temperature was controlled at 4 ℃, binding time was 600 s, disassociation time was 360 s, flow rate was 0.5 μL/s. The chip was regenerated with Glycine Hydrochloride (pH 2.0). The data of interaction signals was retrieved and analyzed with PlexeraDE software [30].

4.2.8. Circular dichroism (CD) spectroscopy

CD spectra were recorded on a Chirascan plus ACD (Applied Photophysics ltd, England). HR1P and HR2P were dissolved in buffer (0.1 M KCl, 0.05 M KH_2PO_4, pH 7.2) at a final concentration of 10 μM. Briefly, HR1P was incubated with PBS or **BA-4** (20 μM) at 25 ℃ for 30 min, followed by addition of HR2P (10 μM). After further incubation at 25 ℃ for 30 min, the CD wave scans were measured from 190 to 260 nm at 4 ℃ with the bandwidth of 2 nm and the step size of 1 nm [18,19].

4.2.9. Molecular docking

A molecular docking study was performed using Discovery Studio 3.0. The 3D crystal structure of SARS-CoV-2 spike glycoprotein was downloaded from RCSB Protein Date Bank (https://www.rcsb.org) using PDB IDs of 6VXX or 7TF8, water and glycosyl molecules removed by manual. The protein and the ligand were prepared by minimization with CHARMM force field. Then the binding site of the protein was defined and prepared for docking by using Define Site (From Receptor Cavities) protocol. Molecular docking results were carried out using CDOCKER protocol without constraint and ranked by -CDOCKER_ENERGY [37].

4.2.10. Plasma stability, microsomal stability and intestinal S9-UDPGA stability

Plasma stability was determined as following steps [38]: (1) prepare a 10 mM DMSO stock of **BA-4**. (2) Dilute the 10 mM stock to 1 μM with mouse plasma. (3) Transfer 50 μL plasma into a new tube and stop reaction using 250 μL acetonitrile. (4) Incubate the plasma sample in a water bath at 37 °C. (5) Stop reaction at 10, 30, 60, and 90 min, respectively. (6) Measure the compound concentration by LC-MS/MS; microsomal stability was determined using 10 μM **BA-4** to incubate with mouse microsomes (0.5 mg/mL) for 5 min at 37 °C in phosphate buffer (100 mM, pH = 7.4) before 1 mM NADPH was added to start the reaction. Then, the cold acetonitrile was utilized to precipitate the protein. Lastly, the samples were centrifuged for further analysis by LC-MS/MS; the experimental procedures of mouse intestinal S9-UDPGA were similar as previously reported [39].

Declaration of Competing Interest

The authors declare that they have no known competing financial interests or personal relationships that could have appeared to influence the work reported in this paper.

Data availability

No data was used for the research described in the article.

Acknowledgments

This work was supported by the National Natural Science Foundation of China (82073722 to G.S. and 82130101 to S.L.), Guangdong Basic and Applied Basic Research Foundation (2022A1515010016) to G.S., the Major scientific and technological projects of Guangdong Province (2019B020202002) and Chinese Academy of Traditional Chinese Medicine (ZZ13-035-02, 2019XZZX-LG04) to S. L; Youth Innovative Talents Project from the Department of Education of Guangdong Province (2022KQNCX245) to X. W; and Science and Technology Program of Huizhou (2022CZ010192) to X. W.

Appendix A. Supplementary data

Supplementary data to this article can be found online at https://doi.org/10.1016/j.bioorg.2022.106316.

References

[1] J. Bedford, D. Enria, J. Giesecke, D.L. Heymann, C. Ihekweazu, G. Kobinger, H. C. Lane, Z. Memish, M.D. Oh, A.A. Sall, A. Schuchat, K. Ungchusak, L.H. Wieler, COVID-19: towards controlling of a pandemic, Lancet 395 (2020) 1015–1018.

[2] B. Hu, H. Guo, P. Zhou, Z.L. Shi, Characteristics of SARSCoV-2 and COVID-19, Nat. Rev. Microbiol. 19 (2021) 141–154.

[3] M.M. Zhou, Y. Liu, J.Y. Cao, S.Q. Dong, Y.X. Hou, Y. Yu, Q.Y. Zhang, Y.L. Zhang, X. Y. Jia, B. Zhang, G.F. Xiao, G. Li, W. Wang, Bergamottin, a bioactive component of bergamot, inhibits SARS-CoV-2 infection in golden Syrian hamsters, Antivir. Res. 204 (2022), 105365.

[4] M. Hoffmann, N. Krüger, S. Schulz, A. Cossmann, C. Rocha, A. Kempf, I. Nehlmeier, L. Graichen, A.S. Moldenhauer, M.S. Winkler, M. Lier, A. Dopfer-Jablonka, H. M. Jäck, G.M.N. Behrens, S. Pöhlmann, The Omicron variant is highly resistant against antibody-mediated neutralization: Implications for control of the COVID-19 pandemic, Cell 185 (2022) 447–456.

[5] Y. Fan, X. Li, L. Zhang, S. Wan, L. Zhang, F. Zhou, SARS-CoV-2 Omicron variant: recent progress and future perspectives, Signal. Transduct. Target. Ther. 7 (2022) 141.

[6] S. Kundu, D. Sarkar, Synthetic attempts towards eminent anti-viral candidates of SARS-CoV, Mini. Rev. Med. Chem. 22 (2022) 232–247.

[7] A. Jayk Bernal, M.M. Gomes da Silva, D.B. Musungaie, E. Kovalchuk, A. Gonzalez, V. Delos Reyes, A. Martín-Quirós, Y. Caraco, A. Williams-Diaz, M.L. Brown, J. Du, A. Pedley, C. Assaid, J. Strizki, J.A. Grobler, H.H. Shamsuddin, R. Tipping, H. Wan, A. Paschke, J.R. Butterton, M.G. Johnson, C. De Anda, MOVe-OUT study group. Molnupiravir for oral treatment of Covid-19 in nonhospitalized patients, N. Engl. J. Med. 386 (2022) 509–520.

[8] R. Najjar-Debbiny, N. Gronich, G. Weber, J. Khoury, M. Amar, N. Stein, L. H. Goldstein, W. Saliba, Effectiveness of paxlovid in reducing severe COVID-19 and mortality in high risk patients, Clin. Infect. Dis. (2022) ciac443.

[9] N. Drayman, J.K. DeMarco, K.A. Jones, S.A. Azizi, H.M. Froggatt, K. Tan, N. I. Maltseva, S. Chen, V. Nicolaescu, S. Dvorkin, K. Furlong, R.S. Kathayat, M. R. Firpo, V. Mastrodomenico, E.A. Bruce, M.M. Schmidt, R. Jedrzejczak, M.Á. Muñoz-Alía, B. Schuster, V. Nair, K.Y. Han, A. O'Brien, A. Tomatsidou, B. Meyer, M. Vignuzzi, D. Missiakas, J.W. Botten, C.B. Brooke, H. Lee, S.C. Baker, B.C. Mounce, N.S. Heaton, W.E. Severson, K.E. Palmer, B.C. Dickinson, A. Joachimiak, G. Randall, S. Tay, Masitinib is a broad coronavirus 3CL inhibitor that blocks replication of SARS-CoV-2, Science 373 (2021) 931–936.

[10] H.Z. Tan, Y.M. Hu, P. Jadhav, B. Tan, J. Wang, Progress and challenges in targeting the SARS-CoV-2 papain-like protease, J. Med. Chem. 65 (2022) 7561–7580.

[11] W. Vuong, M.B. Khan, C. Fischer, E. Arutyunova, T. Lamer, J. Shields, H.A. Saffran, R.T. McKay, M.J. van Belkum, M.A. Joyce, H.S. Young, D.L. Tyrrell, J.C. Vederas, M.J. Lemieux, Feline coronavirus drug inhibits the main protease of SARS-CoV-2 and blocks virus replication, Nat. Commun. 11 (2020) 4282.

[12] L.Y ang, R.J. Pei, H. Li, X.N. Ma, Y. Zhou, F.H. Zhu, P.L. He, W. Tang, Y.C. Zhang, J. Xiong, S.Q. Xiao, X.K. Tong, B. Zhang, J.P. Zuo,, Identification of SARS-CoV-2 entry inhibitors among already approved drugs, Acta Pharmacol. Sin. 42 (2021) 1347–1353.

[13] S. Yu, X. Zheng, B. Zhou, J. Li, M. Chen, R. Deng, G. Wong, D. Lavillette, G. Meng, SARS-CoV-2 spike engagement of ACE2 primes S2' site cleavage and fusion initiation, Proc. Natl. Acad. Sci. U. S. A. 119 (2022) e2111199119.

[14] M. Gur, E. Taka, S.Z. Yilmaz, C. Kilinc, U. Aktas, M. Golcuk, Conformational transition of SARS-CoV-2 spike glycoprotein between its closed and open states, J. Chem. Phys. 153 (2020) 75101.

[15] L. Braga, H. Ali, I. Secco, E. Chiavacci, G. Neves, D. Goldhill, R. Penn, J. M. Jimenez-Guardeño, A.M. Ortega-Prieto, R. Bussani, A. Cannatà, G. Rizzari, C. Collesi, E. Schneider, D. Arosio, A.M. Shah, W.S. Barclay, M.H. Malim, J. Burrone, M. Giacca, Drugs that inhibit TMEM16 proteins block SARS-CoV-2 spike-induced syncytia, Nature 594 (2021) 88–93.

[16] D. Schütz, Y.B. Ruiz-Blanco, J. Münch, F. Kirchhoff, E. Sanchez-Garcia, J.A. Müller, Peptide and peptide-based inhibitors of SARS-CoV-2 entry, Adv. Drug. Deliv. Rev. 167 (2020) 47–65.

[17] J. Shang, Y. Wan, C. Luo, G. Ye, Q. Geng, A. Auerbach, F. Li, Cell entry mechanisms of SARS-CoV-2, Proc. Natl. Acad. Sci. 117 (2020) 11727–11734.

[18] S. Xia, M.Q. Liu, C. Wang, W. Xu, Q.S. Lan, S.L. Feng, F.F. Qi, L.L. Bao, L.Y. Du, S. W. Liu, C. Qin, F. Sun, Z.L. Shi, Y. Zhu, S.B. Jiang, L. Lu, Inhibition of SARS-CoV-2 (previously 2019-nCoV) infection by a highly potent pan-coronavirus fusion inhibitor targeting its spike protein that harbors a high capacity to mediate membrane fusion, Cell Res. 30 (2020) 343–355.

[19] S. Xia, Q.S. Lan, Y. Zhu, C. Wang, W. Xu, Y.T. Li, L.J. Wang, F. Jiao, J. Zhou, C. Hua, Q. Wang, X. Cai, Y. Wu, J. Gao, H. Liu, G. Sun, J. Münch, F. Kirchhoff, Z. H. Yuan, H. Yo, F. Xie, S.B. Sun, L.L. Jiang, Structural and functional basis for pan-CoV fusion inhibitors against SARS-CoV-2 and its variants with preclinical evaluation, Signal. Transduct. Target. Ther. 6 (2021) 288.

[20] S. Drożdżal, J. Rosik, K. Lechowicz, F. Machaj, B. Szostak, J. Przybyciński, S. Lorzadeh, K. Kotfis, S. Ghavami, M.J. Łos, An update on drugs with therapeutic potential for SARS-CoV-2 (COVID-19) treatment, Drug Resist. Updat. 59 (2021), 100794.

[21] S.F. Yuan, X. Yin, X.Z. Meng, J.F. Chan, Z.W. Ye, L. Riva, L. Pache, C.C. Chan, P. M. Lai, C.C. Chan, V.K. Poon, A.C. Lee, N. Matsunaga, Y. Pu, C.K. Yuen, J. Cao, R. Liang, K. Tang, L. Sheng, Y.S. Du, W. Xu, C.Y. Lau, K.Y. Sit, W.K. Au, R.M. Wang, Y.Y. Zhang, Y.D. Tang, T.M. Clausen, J. Pihl, J. Oh, K.H. Sze, A.J. Zhang, H. Chu, K. H. Kok, D. Wang, X.H. Cai, J.D. Esko, I.F. Hung, R.A. Li, H. Chen, H. Sun, D.Y. Jin, R. Sun, S.K. Chanda, K.Y. Yuen, Clofazimine broadly inhibits coronaviruses including SARS-CoV-2, Nature 593 (2021) 418–423.

[22] J.Y. Cao, Y. Liu, M.M. Zhou, S.Q. Dong, Y.X. Hou, X.Y. Jia, X.H. Lan, Y.L. Zhang, J. Guo, G.F. Xiao, W. Wang, Screening of botanical drugs against SARS-CoV-2 entry reveals novel therapeutic agents to treat COVID-19, Viruses 14 (2022) 353.

[23] C. Yang, X.Y. Pan, X.F. Xu, C. Cheng, Y. Huang, L. Li, S.B. Jiang, W. Xu, G.F. Xiao, S.W. Liu, Salvianolic acid C potently inhibits SARS-CoV-2 infection by blocking the formation of six-helix bundle core of spike protein, Signal. Transduct. Target. Ther. 5 (2020) 220.

[24] C. Yang, X.Y. Pan, Y. Huang, C. Cheng, X.F. Xu, Y. Wu, Y.X. Xu, W.J. Shang, X. G. Niu, Y.H. Wan, Z.F. Li, R. Zhang, S.W. Liu, G.F. Xiao, W. Xu, Drug repurposing of itraconazole and estradiol benzoate against COVID-19 by blocking SARS-CoV-2 spike protein-mediated membrane fusion, Adv Ther (Weinh). 4 (2021) 2000224.

[25] J. Wang, W.H. Wei, X.F. Zhang, S.Q. Cao, B.T. Hu, Y. Ye, M. Jiang, T.Q. Wang, J. P. Zuo, S.J. He, C.H. Yang, Synthesis and biological evaluation of C-17-amino-substituted pyrazole-fused betulinic acid derivatives as novel agents for osteoarthritis treatment, J. Med. Chem. 64 (2021) 13676–13692.

[26] H. Wang, R.Y. Xu, Y.Y. Shi, L.L. Si, P.X. Jiao, Z.B. Fan, X. Han, X.Y. Wu, X.S. Zhou, F. Yu, Y.M. Zhang, L. Zhang, L.R. Zhang, D.M. Zhou, S.L. Xiao, Design, synthesis and biological evaluation of novel L-ascorbic acid-conjugated pentacyclic triterpene derivatives as potential influenza virus entry inhibitors, Eur. J. Med. Chem. 110 (2016) 376–388.

[27] R.J. Visalli, H. Ziobrowski, K.R. Badri, J.J. He, X.G. Zhang, S.R. Arumugam, H. Zhao, Ionic derivatives of betulinic acid exhibit antiviral activity against herpes simplex virus type-2 (HSV-2), but not HIV-1 reverse transcriptase, Bioorg. Med. Chem. Lett. 25 (2015) 3168–3171.

[28] C.C. Wen, Y.H. Kuo, J.T. Jan, P.H. Liang, S.Y. Wang, H.G. Liu, C.K. Lee, S.T. Chang, C.J. Kuo, S.S. Lee, C.C. Hou, P.W. Hsiao, S.C. Chien, L.F. Shyur, N.S. Yang, Specific plant terpenoids and lignoids possess potent antiviral activities against severe acute respiratory syndrome coronavirus, J. Med. Chem. 50 (2007) 4087–4095.

[29] A. Stevaert, B. Krasniqi, B. Van Loy, T. Nguyen, J. Thomas, J. Vandeput, D. Jochmans, V. Thiel, R. Dijkman, W. Dehaen, A. Voet, L. Naesens, Betulonic acid derivatives interfering with human coronavirus 229E replication via the nsp15 endoribonuclease, J. Med. Chem. 64 (2021) 5632–5644.

[30] H. Li, C. Cheng, S.S. Shi, Y. Wu, Y.F. Gao, Z.H. Liu, M.J. Liu, Z.D. Li, L.J. Huo, X. Y. Pan, S.W. Liu, G.P. Song, Identification, optimization, and biological evaluation of 3-*O*-*β*-chacotriosyl ursolic acid derivatives as novel SARS-CoV-2 entry inhibitors by targeting the prefusion state of spike protein, Eur. J. Med. Chem. 238 (2022), 114426.

[31] H. Li, C. Cheng, S.M. Li, Y. Wu, Z.H. Liu, M.J. Liu, J.X. Chen, Q.Y. Zhong, X. S. Zhang, S.W. Liu, G.P. Song, Discovery and structural optimization of 3-*O*-*β*-chacotriosyl oleanane-type triterpenoids as potent entry inhibitors of SARS-CoV-2 virus infections, Eur. J. Med. Chem. 215 (2021), 113242.

[32] W.H. Dai, B. Zhang, X.M. Jiang, H.X. Su, J. Li, Y. Zhao, X. Xie, Z.M. Jin, J.J. Peng, F.J. Liu, C.P. Li, Y. Li, F. Bai, H.F. Wang, X. Cheng, X.B. Cen, S.L. Hu, X.N. Yang, J. Wang, X. Liu, G.F. Xiao, H.L. Jiang, Z.H. Rao, L.K. Zhang, Y.C. Xu, H.T. Yang, H. Liu, Structure-based design of antiviral drug candidates targeting the SARS-CoV-2 main protease, Science 368 (2020) 1331–1335.

[33] L.L. Si, K. Meng, Z.Y. Tian, J.Q. Sun, H.Q. Li, Z.W. Zhang, V. Soloveva, H.W. Li, G. Fu, Q. Xia, S.L. Xiao, L.H. Zhang, D.M. Zhou, Triterpenoids manipulate a broad range of virus-host fusion via wrapping the HR2 domain prevalent in viral envelopes, Sci Adv. 4 (2018) eaau8408.

[34] G.P. Song, X.T. Shen, S.M. Li, Y.B. Li, Y.P. Liu, Y.S. Zheng, R.H. Lin, J.H. Fan, H.M. Ye,W. Liu,, Structure-activity relationships of 3-*O*-β-chacotriosyl ursolic acid derivatives as novel H5N1 entry inhibitors, Eur. J. Med. Chem. 93 (2015) 431–442.

[35] R.K. Wolfram, L. Heller, R. Csuk, Targeting mitochondria: esters of rhodamine B with triterpenoids are mitocanic triggers of apoptosis, Eur. J. Med. Chem. 152 (2018) 21–30.

[36] B. Brandes, S. Hoenke, L. Fischer, R. Csuk, Design, synthesis and cytotoxicity of BODIPY FL labelled triterpenoids, Eur. J. Med. Chem. 185 (2020), 111858.

[37] Z.H. Liu, S.Y. Gu, X. Zhu, M.J. Lu, Z.Q. Cao, P.S. Qiu, S.M. Li, S.W. Liu, G.P. Song, Discovery and optimization of new 6, 7-dihydroxy-1, 2, 3, 4-tetrahydroisoquinoline derivatives as potent influenza virus PA_N inhibitors, Eur. J. Med. Chem. 227 (2022), 113929.

[38] L. Wang, J.S. Jiang, L.X. Zhang, Q.Y. Zhang, J.R. Zhou, L. Li, X.L. Xu, Q.D. You, Discovery and optimization of small molecules targeting the protein-protein interaction of heat shock protein 90 (Hsp90) and cell division cycle 37 as orally active inhibitors for the treatment of colorectal cancer, J. Med. Chem. 63 (2020) 1281–1297.

[39] W.M. Kazmierski, B. Xia, J. Miller, M. De la Rosa, D. Favre, R.M. Dunham, Y. Washio, Z. Zhu, F. Wang, M. Mebrahtu, H. Deng, J. Basilla, L. Wang, G. Evindar, L. Fan, A. Olszewski, N. Prabhu, C. Davie, J.A. Messer, V. Samano, DNA-Encoded library technology-based discovery, lead optimization, and prodrug strategy toward structurally unique indoleamine 2,3-dioxygenase-1 (IDO1) inhibitors, J. Med. Chem. 63 (2020) 3552–3562.

磷酸氯喹与洛匹那韦利托那韦治疗新型冠状病毒肺炎的疗效和安全性对比研究Δ

廖世雄[1*]，李楚云[1]，刘燕好[2]（1. 惠州市中心人民医院药学部，广东 惠州 516001；2. 惠州市第一妇幼保健院药剂科，广东 惠州 516001）

中图分类号 R978.7 文献标志码 A 文章编号 1672－2124(2020)11－1340－04
DOI 10.14009/j.issn.1672-2124.2020.11.015

摘 要 目的：比较磷酸氯喹与洛匹那韦利托那韦分别用于新型冠状病毒肺炎（COVID-19）的疗效和安全性，为临床治疗提供用药参考。方法：抽取2020年1—2月惠州市中心人民医院30例确诊COVID-19出院病例（男性19例，女性11例；年龄19～78岁），根据治疗方法的不同，分为研究组（15例，使用磷酸氯喹0.5 g，口服，1日2次）和对照组（15例，使用洛匹那韦利托那韦0.5 g，口服，1日2次），比较两组患者的疗效、不良反应发生情况。结果：研究组患者平均体温恢复正常时间为（2.0±0.3）d，对照组为（3.3±0.6）d，两组的差异有统计学意义（$P<0.05$）；研究组患者平均呼吸道标本病毒核酸转阴性时间为治疗后（3.6±0.4）d，对照组为治疗后（14.0±0.7）d，两组的差异有统计学意义（$P<0.05$）。研究组患者不良反应发生率为6.7%（1/15），对照组为66.7%（10/15），两组的差异有统计学意义（$P<0.05$）。结论：磷酸氯喹在改善COVID-19患者的临床症状和加快病毒清除方面优于洛匹那韦利托那韦，且不良反应发生率低。

关键词 新型冠状病毒肺炎；磷酸氯喹；洛匹那韦利托那韦

Comparison of Efficacy and Safety of Chloroquine Phosphate and Lopinavir/Ritonavir in the Treatment of Patients with COVID-19Δ

LIAO Shixiong[1], LI Chuyun[1], LIU Yanhao[2] (1. Dept. of Pharmacy, Huizhou Central People's Hospital, Guangdong Huizhou 516001, China; 2. Dept. of Pharmacy, the First Maternal and Child Health Hospital of Huizhou, Guangdong Huizhou 516001, China)

ABSTRACT OBJECTIVE: To compare the efficacy and safety of chloroquine phosphate and lopinavir/ritonavir in the treatment of patients with COVID-19, so as to provide reference for the clinical treatment. METHODS: Thirty confirmed COVID-19 discharged patients (19 males and 11 females, aged from 19 to 78 years) were collected from Huizhou Central People's Hospital from Jan. to Feb. 2020. According to different treatment methods, patients were divided into the study group (15 patients, treated with chloroquine 0.5 g, orally, twice a day) and the control group (15 patients, treated with lopinavir/ritonavir 0.5 g, orally, twice a day). The efficacy and adverse drug reactions of two groups were compared. RESULTS: The average body temperature of the patients in the study group returned to normal time was (2.0±0.3) d and that in the control group was (3.3±0.6) d, the difference was statistically significant ($P<0.05$). The average nucleic acid negative time of respiratory virus specimens in the study group was (3.6±0.4) d after treatment, while that in the control group was (14.0±0.7) d after treatment, with statistically significant difference ($P<0.05$). The incidence of adverse drug reactions was 6.7% (1/15) in the study group and 66.7% (10/15) in the control group, the difference was statistically significant ($P<0.05$). CONCLUSIONS: The effect of chloroquine phosphate is superior to lopinavir/ritonavir in improving clinical symptoms and accelerating virus clearance in COVID-19 patients, with the lower incidence of adverse drug reactions.

KEYWORDS COVID-19; Chloroquine phosphate; Lopinavir/Ritonavir

新型冠状病毒肺炎（COVID-19）由于疫情防控情势十分严峻，但是目前尚无特效药物。本研究通过信息系统抽取了2020年1—2月共30例COVID-19确诊患者病历，回顾性对比磷酸氯喹和洛匹那韦利托那韦在COVID-19治疗中的疗效和安全性，为临床医师和药师提供用药参考。

Δ 基金项目：惠州市科技专项（No. 2020SC0709009）

* 主管药师。研究方向：临床药学。E-mail：676234318@163.com

1 资料与方法

1.1 资料来源

抽取2020年1—2月惠州市中心人民医院30例确诊COVID-19的出院病例。纳入标准：患者年龄≥18岁；根据国家卫生健康委发布的《新型冠状病毒感染的肺炎诊疗方案（试行第四版）》[1]，诊断为COVID-19普通型。排除标准：年龄＜18岁；根据国家卫生健康委发布的《新型冠状病毒肺炎

诊疗方案(试行第四版)》,未确诊及诊断为 COVID-19 轻型、重型和危重型患者。根据治疗方法的不同,分为研究组(15 例)和对照组(15 例)。两组患者基本情况比较见表 1,结果显示,两组患者性别构成、年龄、体重、疾病分型和基础疾病等情况相似,具有可比性。本研究对已出院病例进行回顾性研究,该项目通过医院伦理委员会伦理审查批准。

表 1 两组患者用药前基本情况比较

Tab 1 Comparison of basic conditions before medication between two groups

组别	病例数	性别/例		年龄/($\bar{x}\pm s$,岁)	体重/($\bar{x}\pm s$,kg)	疾病分型/例			基础疾病/例
		男性	女性			轻型	普通型	重型	
研究组	15	9	6	46±3.5	63±8.2	0	15	0	2
对照组	15	8	7	47±3.7	64±8.7	0	15	0	2

1.2 方法

根据《新型冠状病毒感染的肺炎诊疗方案(试行第四版)》推荐剂量,研究组患者使用磷酸氯喹 0.5 g,口服,1 日 2 次,平均用药时间 7.4 d;对照组患者使用洛匹那韦利托那韦 0.5 g,口服,1 日 2 次,平均用药时间 12.4 d。

1.3 观察指标

观察两组患者治疗前后体温、血常规白细胞计数(WBC)、C 反应蛋白(CRP)、降钙素原(PCT)及血气分析等指标的变化。

1.4 解除隔离和出院标准

根据《新型冠状病毒感染的肺炎诊疗方案(试行第四版)》,体温恢复正常 >3 d、呼吸道症状明显好转,连续 2 次呼吸道病原核酸检测阴性(采样时间间隔至少 1 d),可解除隔离出院或根据病情转至相应科室治疗其他疾病,以此计算临床有效率。

1.5 统计学方法

本研究采用 SPSS 11.5 统计软件,计数资料采用率(%)表示,进行 χ^2 检验;计量资料采用均数±标准差($\bar{x}\pm s$)表示,进行 t 检验;$P<0.05$ 为差异有统计学意义。

2 结果

2.1 两组患者抗病毒治疗前相关炎症指标比较

抗病毒治疗前相关炎症指标包括体温、WBC、CRP、PCT 及氧合指数 PaO_2/FiO_2,两组患者上述指标水平比较,差异无统计学意义($P>0.05$),见表 2。

表 2 两组患者抗病毒治疗前相关炎症指标比较($\bar{x}\pm s$)

Tab 2 Comparison of related inflammation indicators between two groups before antiviral treatment($\bar{x}\pm s$)

组别	体温/℃	WBC/$\times10^9$/L	CRP/(mg/L)	PCT/(μg/L)	(PaO_2/FiO_2)/mm Hg
研究组($n=15$)	37.6±0.5	4.8±2.1	21±13	0.12±0.026	393±23
对照组($n=15$)	37.4±0.3	4.6±1.9	22±14	0.14±0.016	394±20
t	0.72	0.93	2.14	0.12	5.43
P	>0.05	>0.05	>0.05	>0.05	>0.05

注:1 mm Hg=0.133 kPa

Note:1 mm Hg=0.133 kPa

2.2 两组患者抗病毒治疗后相关炎症指标比较

抗病毒治疗后相关炎症指标包括体温、WBC、CRP、PCT 及氧合指数 PaO_2/FiO_2,两组患者上述指标水平比较,差异无统计学意义($P>0.05$),见表 3。

2.3 两组患者临床疗效比较

两组患者均在治疗后第 6、8 日进行鼻咽拭子核酸检测,核酸转阴性时间、体温恢复正常(体温 <37.3 ℃)时间比较,差异有统计学意义($P<0.05$),见表 4。

表 3 两组患者抗病毒治疗后相关炎症指标比较($\bar{x}\pm s$)

Tab 3 Comparison of related inflammation indicators between two groups after antiviral treatment($\bar{x}\pm s$)

组别	时间	体温/℃	WBC/$\times10^9$/L	CRP/(mg/L)	PCT/(μg/L)	(PaO_2/FiO_2)/mm Hg
研究组($n=15$)	第 2 日	37.3±0.6	5.8±2.5	31±12	0.11±0.036	392±41
	第 4 日	37.1±0.7	7.7±6.5	23±11	0.09±0.043	395±38
	第 6 日	36.9±0.3	8.2±3.1	16±9	0.11±0.021	401±37
	第 8 日	36.4±0.4	8.6±2.1	14±7	0.08±0.17	420±35
	第 10 日	36.5±0.6	8.2±2.5	15±9	0.07±0.02	453±32
对照组($n=15$)	第 2 日	37.6±0.6	6.2±2.6	30±11	0.10±0.036	394±25
	第 4 日	37.4±0.9	6.8±2.4	25±15	0.10±0.043	401±42
	第 6 日	37.2±0.8	6.9±3.1	20±9	0.09±0.021	402±57
	第 8 日	37.0±0.3	6.4.±2.2	17±5	0.11±0.17	435±36
	第 10 日	36.5±0.4	6.3±1.7	13±4	0.09±0.09	445±42

表 4 两组患者临床疗效比较($\bar{x}\pm s$,d)

Tab 4 Comparison of clinical efficacy between two groups($\bar{x}\pm s$,d)

组别	核酸转阴性时间	体温恢复正常时间
研究组($n=15$)	3.6±0.4	2.0±0.3
对照组($n=15$)	14.0±0.7	3.3±0.6
t	2.24	0.58
P	<0.05	<0.05

2.4 两组患者不良反应发生率比较

通过药品说明书、用药时间与出现不良反应的时间,排除了其他药品导致的不良反应,因此,纳入本研究的药品不良反应均为氯喹或洛匹那韦利托那韦的不良反应。研究组不良反应发生率为 6.7%(1/15),对照组为 66.7%(10/15),两组比较,差异有统计学意义($P<0.05$)。两组患者常见不良反应如恶心、纳差和腹泻的发生率比较,差异有统计学意义($P<0.05$),两组患者均未发生呕吐、头晕、头痛、视网膜病和神经病变等不良反应,见表 5。

表 5 两组患者不良反应发生率比较[%(例)]

Tab 5 Comparison of incidence of adverse drug reactions between two groups [%(cases)]

组别	纳差	恶心	腹泻	合计
研究组($n=15$)	6.7(1)	0(0)	0(0)	6.7(1)
对照组($n=15$)	20.0(3)	40.0(6)	6.7(1)	66.7(10)
χ^2	5.37	4.69	3.83	4.98
P	<0.05	<0.05	<0.05	<0.05

3 讨论

3.1 COVID-19 流行病学

冠状病毒属是一类具有包膜的单股正链 RNA 病毒[2]。自从严重急性呼吸综合征(severe acute respiratory syndrome,SARS)和中东呼吸综合征(Middle East respi-ratory syndrome,

MERS) 暴发以来，冠状病毒从动物传播到人类的可能性已经得到证实[3-4]。除了严重急性呼吸综合征冠状病毒 2 型(severe acute respiratory syndrome coronavirus 2，SARS-CoV-2)外，已知 6 种人类冠状病毒(human coronavirus，HCoV)能导致呼吸道感染，其中严重急性呼吸综合征冠状病毒(severe acute respiratory syndrome coronavirus，SARS-CoV)和中东呼吸综合征冠状病毒(Middle East respiratory syndrome coronavirus，MERS-CoV)属于高致病性病毒，目前临床上尚未有针对以上 7 种 HCoV 的特效药物[5]。

3.2 抗病毒治疗药物

目前尚无针对 SARS-CoV-2 的特效抗病毒药，因此，尽快寻找针对 SARS-CoV-2 的有效药物，对于控制患者病情和治疗极为重要。已有文献报道，SARS-CoV-2 与 SARS-CoV 的基因组序列高度同源，引起的病毒性肺炎在临床症状方面也与 SARS 有一些相似之处[6]。洛匹那韦/利托那韦虽然没有 SARS-CoV-2 的体外研究数据，但该药在 SARS 和 MERS 的体内外都积累了较充足的研究证据[7-8]。根据既往治疗 SARS 和 MERS 的经验和相关基础及临床研究推测，洛匹那韦/利托那韦可能对治疗 COVID-19 具有一定的疗效[9]。既往研究结果显示，氯喹可以改变内吞体的 pH，对通过内吞体途径侵入细胞的病毒感染具有显著的抑制作用，如博尔纳病病毒[10]、禽白血病病毒[11]、寨卡病毒[12]等。氯喹能改变人类免疫缺陷病毒(human immunodeficiency virus，HIV) 1 gp120 包膜的糖基化模式，抑制 $CD4^+$ T 细胞内 HIV 的复制[13]。另外，动物实验结果证明，应用氯喹能有效抑制 H5N1 禽流感病毒在鼠肺中的自噬作用，减轻肺泡上皮损伤[14]。据相关文献报道，氯喹能阻断寨卡病毒诱导的自噬现象，从而抑制病毒复制，并且在小鼠实验中，氯喹能切断寨卡病毒自母胎途径的垂直感染[15]。

3.3 治疗效果

住院治疗期间，两组普通型患者均未发展为重症。研究组中 6 例患者有低热，使用氯喹后体温恢复正常的平均时间为 2.0 d；对照组中 9 例患者有低热，使用洛匹那韦/利托那韦后体温恢复正常的平均时间为 3.3 d，两组比较，差异有统计学意义($P<0.05$)。研究组患者呼吸道标本病毒核酸检测转阴性时间为 3.6 d，而对照组患者呼吸道标本病毒核酸检测转阴性时间为治疗后 14.0 d，两组比较，差异有统计学意义($P<0.05$)。但因本研究样本量较小，抗病毒治疗是否在疾病治疗中发挥了重要的作用尚待进一步评估。

3.4 主要不良反应

在治疗过程中，研究组 1 例(占 6.7%)患者发生不良反应，表现为纳差，与药品说明书描述一致。而对照组 10 例(占 66.7%)患者发生不良反应，其中以恶心、腹泻等消化道症状为多见，与陈军等[16]的报道一致。两组患者不良反应发生率的差异有统计学意义($P<0.05$)。所有发生不良反应的患者经停药或给予对症支持后好转。

4 结论

目前，尚无治疗 COVID-19 的有效抗病毒药。本研究结果显示，研究组治疗方案在改善患者临床症状(如体温恢复正常)和加快病毒清除方面优于对照组，研究组治疗方案的不良反应发生率低于对照组，这可能与药物剂量或疗程有关。本研究尚存在一些不足之处：首先，由于各种原因，未采用空白对照，即不服用任何抗病毒药进行对比分析，无法进行更为准确的抗病毒效果评价。其次，并未每日采集咽拭子，也未能对病原核酸进行定量检测，因此，无法准确判断呼吸道标本的病原转阴时间和药物的抗病毒效果。虽然本研究纳入样本较小，影响因素较多，但在目前有限的临床经验中，仍有较高的临床价值，值得进一步深入研究。

参考文献

[1] 国家卫生健康委办公厅，国家中医药管理局办公室. 关于印发新型冠状病毒感染的肺炎诊疗方案(试行第四版)的通知[S]. 国卫办医函(2020)77 号. 2020-01-27.

[2] Fung TS，Liu DX. Human Coronavirus：Host-Pathogen Interaction[J]. Annu Rev Microbiol，2019，73：529-557.

[3] Cui J，Li F，Shi ZL. Origin and evolution of pathogenic coronaviruses[J]. Nat Rev Microbiol，2019，17(3)：181-192.

[4] Cauchemez S，Van Kerkhove MD，Riley S，et al. Transmission scenarios for Middle East Respiratory Syndrome Coronavirus(MERS-CoV) and how to tell them apart[J]. Euro Surveill，2013，18(24)：20503.

[5] 广东省科技厅及广东省卫生健康委磷酸氯喹治疗新冠状病毒肺炎多中心协作组. 磷酸氯喹治疗新型冠状病毒肺炎的专家共识[J]. 中华结核和呼吸杂志，2020，43(3)：185-188.

[6] Zhou P，Yang XL，Wang XG，et al. Discovery of a novel coronavirus associated with the recent pneumonia outbreak in humans and its potential bat origin[J/OL]. [2020-01-23](2020-03-27). https://www.biorxiv.org/content/10.1101/2020.01.22.914952v2.

(下转第 1346 页)

(上接第 1339 页)

[6] 国家药典委员会. 中华人民共和国药典：一部[S]. 2020 年版. 北京：中国医药科技出版社，2020：279，178，290，317.

[7] 杨明，刘小彬，黄庆德. 附子甘草配伍减毒增效机理探析[J]. 时珍国医国药，2003，14(4)：197-198.

[8] 王晓梅，李云鹤. 观察中药各类毒性成分的中毒机制及其炮制减毒原理[J]. 中国实用医药，2016，11(14)：265-266.

[9] 国家药典委员会. 中华人民共和国药典：四部[S]. 2020 年版. 北京：中国医药科技出版社，2020：31-32.

[10] 李芸，苗小楼，刘峰林，等. 一种高乌头的解毒炮制工艺：中国，CN104491035A[P]. 2015-04-08.

[11] 洪玉梅，王维皓，王智民，等. 甘草制吴茱萸炮制研究[J]. 中国中药杂志，2008，33(8)：884-888.

[12] 侯士果，谷学新，王书妍，等. HPLC 测定洋金花中东莨菪碱和阿托品的含量[J]. 中国中药杂志，2006，31(13)：1065-1066.

[13] 李红红，陈朋朋，付传香，等. HPLC 法同步测定洋金花中东莨菪碱和莨菪碱的含量[J]. 安徽化工，2018，44(5)：92-94.

[14] 吐鲁洪·卡地尔，李建梅，希尔艾力·吐尔逊. 曼陀罗子维吾尔医不同炮制方法及含量变化的研究[J]. 中医药导报，2017，23(17)：48-50.

(收稿日期：2020-07-20)

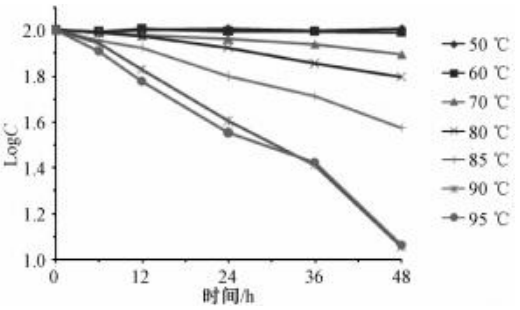

图 4　温度和时间对复方替硝唑溶液中替硝唑含量的影响

Fig 4　Effects of temperature and time on the contents of tinidazole in compound tinidazole solution

的研究结果发现，替硝唑溶液在 pH 为 4.0 ~ 5.5 范围内最稳定，当 pH > 6.5，则降解明显加快。因此，推测该协同作用是醋酸氯己定引起溶液 pH 改变所致。

《中华人民共和国药典》[2] 凡例中规定，热水温度指 70 ~ 80 ℃。经验证，替硝唑和醋酸氯己定的溶解度分别为 4.7 和 12.8 mg/ml(25 ℃) 。实际生产过程中，替硝唑和醋酸氯己定在初步溶解阶段，其浓度远远高于本研究所用的溶液浓度，且生产量大、冷却时间长，因此，工艺中采用热水助溶对替硝唑含量的影响更大。鉴于醋酸氯己定对替硝唑的降解具有协同作用，在复方替硝唑溶液配制过程中，结合实际工作，建议替硝唑在60 ℃以下单独溶解，减少降解产物的生成。

参考文献

[1] 中央军委后勤保障部卫生局. 中国人民解放军医疗机构制剂规范(第一册) [S] . 2015 年版. 北京: 人民军医出版社，2016: 230-231.

[2] 国家药典委员会. 中华人民共和国药典: 二部 [S] . 2015 年版. 北京: 中国医药科技出版社，2015: 1257/1543，Ⅹ Ⅲ.

[3] 湛建国，程泽能. 复方替硝唑含漱剂的研制 [J] . 中国药学杂志，1997，32(2) : 94-96.

[4] 刘音贝，杨世林. 药物制剂稳定性影响因素分析 [J] . 医药前沿，2019，9(14) : 232-233.

[5] 崔福德. 药剂学 [M] . 6 版. 北京: 人民卫生出版社，2007: 293-313.

[6] 邹振鸿，文九芳，胡萍. 替硝唑葡萄糖注射液中替硝唑的稳定性预测 [J] . 湖北省卫生职工医学院学报，2001，14(2) : 50-51.

[7] 鄢海燕，孟凡强. 复方替硝唑含漱剂中替硝唑的稳定性预测 [J] . 世界医学杂志，2001，5(8) : 85-86.

[8] 王远，高梦洁，李伟，等. 经典恒温法考察苍桂颗粒的有效期 [J] . 新疆中医药，2019，37(2) : 37-39.

[9] 王金梅，姚辰，李昌勤，等. 经典恒温法预测红花的有效期 [J] . 天然产物研究与开发，2017，29(2) : 273-277，283.

[10] 缑慧君，杨滢，任杰，等. 大黄素、大黄酚标准溶液有效期的研究 [J] . 中国中药杂志，2018，43(24) : 4892-4899.

[11] 王金梅，姚辰，李昌勤，等. 中药女贞子的质量稳定性研究 [J] . 中国药学杂志，2017，52(1) : 31-35.

[12] 胡军，毕海林，杨敬，等. 番泻叶中番泻苷 A、B 的稳定性探究 [J] . 中国兽医杂志，2018，54(6) : 121-124.

[13] 高磊，贾燕花，王晓青，等. RP-HPLC 同时测定复方替硝唑溶液中替硝唑和醋酸氯己定的含量 [J] . 河北医药，2015，37(2) : 290-291.

[14] 陈建明，邓莉，王秀鑫，等. 药物有效期预测及稳定性影响因素实验设计 [J] . 药学实践杂志，2010，28(1) : 7-10.

[15] 涂家生，武志昂，赵安虎. 替硝唑溶液稳定性的研究 [J] . 中国药科大学学报，1996，27(9) : 525-527.

[16] 翟灵妍，董俊，苟宏莉，等. 替硝唑葡萄糖注射液制备工艺研究 [J] . 现代医药卫生，2014，30(11) : 1624-1626.

[17] 王丽华，张雪梅，周峰. 影响替硝唑氯化钠注射液有关物质升高的因素及控制措施 [J] . 药学研究，2014，33(6) : 367-368.

[18] 贾飞，李珏. 探讨替硝唑及其注射液有关物质中杂质的控制 [J] . 中国药品标准，2009，10(5) : 341-342.

[19] 高兴浩，牟会举. 0.05% 醋酸氯己定溶液化学稳定性的考察 [J] . 中国医药导报，2008，5(9) : 38-39.

[20] 陈立. 葡萄糖酸氯己定含漱液的制备、含量测定及效期观察 [J] . 海峡药学，2016，28(5) : 14-15.

(收稿日期: 2020-06-18)

(上接第 1342 页)

[7] Chen F，Chan KH，Jiang Y，et al. In vitro susceptibility of 10 clinical isolates of SARS coronavirus to selected antiviral compounds [J] . J Clin Virol，2004，31(1) : 69-75.

[8] Wu CY，Jan JT，Ma SH，et al. Small molecules targeting severe acute respiratory syndrome human coronavirus [J] . Proc Natl Acad Sci U S A，2004，101(27) : 10012-10017.

[9] Chu CM，Cheng VC，Hung IF，et al. Role of lopinavir/ritonavir in the treatment of SARS: initial virological and clinical findings [J] . Thorax，2004，59(3) : 252-256.

[10] Gonzalez-Dunia D，Cubitt B，de la Torre JC . Mechanism of borna disease virus entry into cells [J] . J Virol，1998，72(1) : 783-788.

[11] Diaz-Griffero F，Hoschander SA ，Brojatsch J. Endocytosis is a critical step in entry of subgroup B avian leukosis viruses [J] . J Virol，2002，76(24) : 12866-12876.

[12] Delvecchio R，Higa LM，Pezzuto P，et al. Chloroquine，an Endocytosis Blocking Agent，Inhibits Zika Virus Infection in Different Cell Models [J] . Viruses，2016，8(12) : 322.

[13] Naarding MA，Baan E，Pollakis G，et al. Effect of chloroquine on reducing HIV-1 replicationin vitroand the DC-SIGN mediated transfer of virus to CD4 + T-lymphocytes [J] . Retrovirology，2007，4: 6.

[14] Yan Y，Zou Z，Sun Y，et al. Anti-malaria drug chloroquine is highly effective in treating avian influenza A H5N1 virus infection in an animal model [J] . Cell Res，2013，23(2) : 300-302.

[15] Zhang S，Yi C，Li C，et al. Chloroquine inhibits endosomal viral RNA release and autophagy-dependent viral replication and effectively prevents maternal to fetal transmission of Zika virus [J] . Antiviral Res，2019，169: 104547.

[16] 陈军，凌云，席秀红，等. 洛匹那韦利托那韦和阿比多尔用于治疗新型冠状病毒肺炎的有效性研究 [J] . 中华传染病杂志，2020，38(2) : 86-89.

(收稿日期: 2020-03-27)

万古霉素血药谷浓度的影响因素及临床药师干预对治疗效果的影响

廖世雄[1*] 刘燕好[2]

【摘要】目的 通过分析影响万古霉素血药谷浓度的主要因素，探讨临床药师干预对治疗效果的影响，提高万古霉素的临床治疗效果。**方法** 选取 2020 年 12 月至 2021 年 11 月在惠州市中心人民医院接受万古霉素血药谷浓度监测的 458 例患者作为研究对象，采用多元 Logistic 回归分析的统计方法，寻找并确定影响万古霉素血药谷浓度的主要因素。将血药谷浓度不达标（＜10 mg/L 或＞20 mg/L）的万古霉素患者 192 例剔除因各种原因未复测血药谷浓度患者 20 例后随机分为对照组与观察组，每组 86 例。对照组监测血药谷浓度后，临床药师未给予个体化用药建议，临床药师给予观察组患者一对一个体化用药建议，对临床药师干预效果进行分析。**结果** 多元 Logistic 回归模型分析结果显示，患者年龄、体重指数（BMI）、肌酐清除率（CrCl）、中重度外周水肿是万古霉素血药谷浓度的主要影响因素（P＜0.05）。对照组血药谷浓度达标率、患者短期（30 d）病死率及不良反应发生率分别为 32.56%、22.09%及 20.93%，观察组分别为 77.91%、4.65%及 9.30%，差异有统计学意义（P＜0.05）。**结论** 患者年龄、中重度外周水肿、CrCl、BMI 是万古霉素血药谷浓度的主要影响因素。因此，临床药师应根据以上主要影响因素，加强万古霉素血药谷浓度的干预，以提高药物治疗效果和降低不良反应发生率。

【关键词】万古霉素；血药谷浓度；影响因素；临床药师干预
【中图分类号】R978.1 **【文献标识码】**A

Analysis of the Influencing Factors of Vancomycin Plasma Concentration and the Influence of Clinical Pharmacists' Intervention on the Therapeutic Effect

LIAO Shi-Xiong[1*], *LIU Yan-Hao*[2]

1. *Pharmacy Department of Huizhou Central People's Hospital, Huizhou 516001, China;* 2. *Pharmacy Department of Huizhou first maternal and child health hospital, Huizhou 516001, China*

【Abstract】Objective By analyzing the main factors affecting the blood concentration of vancomycin,the influence of clinical pharmacist intervention on the therapeutic effect was discussed to improve the clinical therapeutic effect of vancomycin. **Methods** 458 patients who received the monitoring of vancomycin blood valley concentration in Huizhou Central People's Hospital from December 2020 to November 2021 were selected as the research objects, and the statistical method of multiple logistic regression analysis was used to find and determine the main factors affecting vancomycin blood valley concentration. 192 cases of vancomycin medical records whose blood drug valley concentration was not up to the standard (＜10 mg/L or ＞20 mg/L), 20 cases of patients whose blood drug valley concentration was not re measured due to various reasons were excluded, and the remaining 172 cases were randomly divided into the control group and the observation group, with 86 cases in each group. After monitoring the blood drug trough concentration in the control group, the clinical pharmacist did not give individualized drug recommendations. The clinical pharmacist in the observation group gave one-to-one individualized drug recommendations, with 86 cases in each group, to analyze the intervention effect of the clinical pharmacist. **Results** The results of multiple logistic regression model analysis showed that the patient's age, body mass index (BMI), CrCl and moderate to severe peripheral edema were the main influencing factors of vancomycin blood concentration (P＜0.05). In the control group, the rate of reaching the standard of blood grain concentration, the short-term (30 day) mortality and the incidence of adverse reactions were 32.56%, 22.09% and 20.93%, respectively,

DOI：10.12010/j.issn.1673-5846.2022.12.021
基金项目：惠州市科技计划项目（2022CZ010115）
作者单位：1.惠州市中心人民医院药学部，广东惠州 516001；2.惠州市第一妇幼保健院药剂科，广东惠州 516001
*通信作者：廖世雄，E-mail：676234318@163.com

while in the observation group, they were 77.91%, 4.65% and 9.30%, respectively, with a statistically significant differencet ($P<0.05$). **Conclusion** Patient age, Moderate to severe peripheral edema, CrCl and BMI were the main influencing factors of vancomycin plasma trough concentration. Therefore, clinical pharmacists should strengthen the intervention of vancomycin blood trough concentration based on the above main influencing factors to improve the drug treatment effect and reduce the occurrence of adverse reactions.

【Key words】 Vancomycin; Blood concentration; Related factors; Clinical pharmacist intervention

万古霉素是治疗耐甲氧西林金黄色葡萄球菌（MRSA）的一线药物[1]。万古霉素存在较大的个体差异，而万古霉素血药谷浓度与临床治疗效果和不良反应发生密切相关。因此，建议对万古霉素进行血药谷浓度监测[2]。目前，指南推荐对于有感染 MRSA 证据的感染性心内膜炎、急/慢性骨髓炎、细菌性脑膜炎等，万古霉素稳定谷浓度应控制在 15～20 mg/L，对于普通成人患者应维持浓度＞10 mg/L，以减少万古霉素耐药的发生[3]。但临床研究发现，即使严格按照肾小球滤过率推荐使用万古霉素，仍常出现血药谷浓度不达标的情况[4]。本研究就万古霉素血药谷浓度的影响因素及临床药师干预对治疗效果的影响进行分析。现报道如下。

1 资料与方法

1.1 一般资料

通过病历系统，选取 2020 年 12 月至 2021 年 11 月惠州市中心人民医院出院患者中，收集使用万古霉素并进行血药谷浓度检测的 458 例患者的病例资料进行汇总分析。

纳入标准：1）患者年龄≥18 岁；2）静脉滴注万古霉素，严格按稳态血药谷浓度要求（第 5 次给药前 30 min 采血）检测万古霉素血药谷浓度。排除标准：1）年龄＜18 岁；2）静脉滴注万古霉素少于 4 次未达到稳态血药谷浓度、检测为峰浓度、无法收集到完整资料的病例。

1.2 方法

根据患者病历资料、用药资料、实验室检查等，收集患者的性别、年龄、体重、临床诊断、万古霉素给药方法、血药谷浓度检测时间及次数、血肌酐值、白蛋白、液体出入量等资料。

本研究采用注射用盐酸万古霉素（浙江医药股份有限公司，国药准字 H20033365，规格：0.5 g（50 万 U）/支），采用 ELITechGroup B.V.公司生产的型号为 Viva-E 全自动生化分析仪，医疗器械注册编号：国食药监械（进）字 2014 第 2404372 号。试剂为 Siemens Healthcare Diagnostics Inc 生产的万古霉素检测试剂（酶放大免疫测定法），产品编号：4W018UL。

将血药谷浓度不达标（＜10 mg/L 或＞20 mg/L）的万古霉素患者 192 例剔除因各种原因未复测血药谷浓度患者 20 例后随机分为对照组与观察组，每组 86 例。专科临床药师将对观察组进行一对一个体化用药干预，临床药师查阅患者临床资料，根据《国家抗微生物治疗指南》第 2 版[5]和《热病》第 48 版[6]，针对患者的性别、年龄、体重、肾小球滤过率等资料给予个性化给药建议，通过血药谷浓度检测报告单或临床会诊方式，对万古霉素给药剂量进行干预，并对临床疗效及药物不良反应进行汇总分析。

1.3 统计学分析

采用 SPSS 20.0 统计软件进行数据分析，计量资料以 $\bar{x}\pm s$ 表示，组间比较采用 F 检验，计数资料以百分率表示，组间比较采用 χ^2 检验，采用多元 Logistic 回归分析的统计方法分析影响万古霉素血药谷浓度的因素，$P<0.05$ 为差异有统计学意义。

2 结果

2.1 患者临床资料

分布不同血药谷浓度范围的万古霉素患者性别、年龄和体重差异无统计学意义（$P>0.05$）。见表 1。

表 1 使用万古霉素患者的基本情况

谷浓度(mg/L)	例数	男	年龄(岁,$\bar{x}\pm s$)	体重(kg,$\bar{x}\pm s$)
＜10	122	52	53.11±17.04	64.21±9.34
10～20	183	126	55.25±19.02	65.73±12.23
＞20	153	47	57.32±22.45	63.98±13.74
F 值		2.51	3.68	3.47
P 值		0.162	0.678	0.286

2.2 万古霉素血药谷浓度分布情况

458 例患者万古霉素血药谷浓度分布情况，仅有

183 例次（39.96%）万古霉素血药谷浓度达标（10～20 mg/L），达标比例较低；122 例（26.64%）万古霉素血药谷浓度＜10 mg/L；153 例（33.41%）万古霉素血药谷浓度＞20 mg/L。见表 2。

表 2 万古霉素血药谷浓度分布情况

谷浓度(mg/L)	例次	比例(%)	均值(mg/L,$\bar{x}\pm s$)	最低(mg/L)	最高(mg/L)
＜10	122	26.64	6.23±2.34	2.00	9.90
10～20	183	39.96	15.25±4.62	10.00	20.00
＞20	153	33.41	28.21±10.36	20.01	50.00
总计	458	100.00	19.35±9.98	2.00	50.00

2.3 不同肾功能患者万古霉素血药谷浓度比较

不同肾功能患者万古霉素血药谷浓度比较差异有统计学意义（P＜0.05）。与肌酐清除率（CrCl）＞90 ml/min 组相比，CrCl 50～90 ml/min 和 CrCl 10～50 ml/min 组万古霉素平均血药谷浓度水平显著升高，而 CrCl＜10 ml/min 组与 CrCl＞90 ml/min 组差异无统计学意义（P＞0.05）。见表 3。

表 3 不同肾功能患者万古霉素血药谷浓度比较

CrCl(ml/min)	例次	万古霉素血药谷浓度(mg/L,$\bar{x}\pm s$)
＞90	71	9.76±8.38
50～90	116	12.26±9.72
10～50	238	15.32±10.56
＜10	33	8.56±13.34
F 值		5.26
P 值		0.541

2.4 万古霉素推荐剂量与实际剂量比较

由表 4 可知，CrCl＞90 ml/min 和 CrCl 50～90 ml/min 组患者经验性使用万古霉素实际剂量明显低于说明书推荐剂量，通过对亚组分析显示，CrCl＞90 ml/min 组未达标（＜10 mg/L）、达标（10～20 mg/L）和超标（＞20 mg/L）的实际剂量均低于推荐剂量，差异有统计学意义（P＜0.05）。CrCl 在 10～50 ml/min 和 CrCl＜10 ml/min 组患者经验性使用万古霉素实际剂量明显高于说明书推荐剂量，亚组分析显示，CrCl 10～50 ml/min 组未达标、达标和超标的实际剂量均高于推荐剂量，差异有统计学意义（P＜0.05）。

2.5 影响血药谷浓度的多因素分析

将患者性别、年龄、中重度外周水肿、BMI、CrCl 代入多元 Logistic 回归分析模型，结果显示年龄、中重度外周水肿、CrCl 及 BMI 为影响万古霉素血药谷浓度的相关因素，差异有统计学意义（P＜0.05）。见表 5。

表 4 万古霉素推荐剂量与实际剂量比较

CrCl(ml/min)	例次	万古霉素(g/d) 推荐剂量	万古霉素(g/d) 实际剂量	t 值	P 值
＞90	71	2.03±0.56	1.83±0.38	0.312	＜0.001
未达标	25(35.21)	1.94±0.27	1.79±0.42	0.654	＜0.001
达标	28(39.44)	1.98±0.62	1.87±0.48	3.593	＜0.001
超标	18(25.35)	2.13±0.39	2.01±0.51	2.543	0.03
50～90	116	1.96±0.35	1.83±0.24	1.879	0.021
未达标	36(31.03)	1.83±0.36	1.71±0.29	5.127	0.012
达标	50(43.10)	2.11±0.25	2.01±0.32	2.896	0.452
超标	30(25.86)	2.05±0.32	2.01±0.21	1.467	0.127
10～50	238	1.07±0.25	1.26±0.36	4.321	＜0.001
未达标	64(26.89)	0.93±0.47	0.97±0.47	5.546	＜0.001
达标	105(44.12)	1.06±0.32	1.12±0.21	12.354	＜0.001
超标	69(28.99)	1.13±0.28	1.15±0.21	21.261	0.008
＜10	33	0.53±0.26	0.59±0.32	15.346	0.021
未达标	6(18.18)	0.43±0.19	0.47±0.24	20.191	0.231
达标	10(30.30)	0.51±0.21	0.53±0.17	11.211	0.134
超标	17(51.52)	0.32±0.24	0.43±0.36	12.321	0.023

表 5 影响万古霉素血药谷浓度的多因素分析结果

变量	β	S.E.	β'	t	P	OR	95%CI
常量	12.348	6.897	—	4.632	0.015	2.654	1.34～3.54
年龄	8.543	5.438	0.632	7.432	0.014	3.532	2.17～4.72
中重度外周水肿	7.235	5.194	0.432	5.876	0.039	1.654	1.52～3.05
CrCl	8.593	4.321	0.654	4.193	0.023	4.187	1.11～2.76
BMI	8.764	3.738	0.543	6.980	0.026	2.154	2.43～3.95

注：β 表示偏回归系数，β'表示标准化回归系数：S.E.表示标准误；—为无数据

2.6 干预效果比较

观察组血药谷浓度达标率高于对照组，30 d 病死率及不良反应发生率低于对照组，差异有统计学意义（P＜0.05）。见表 6。

表 6 两组患者干预效果比较[例(%)]

组别	例数	血药谷浓度达标	30 d 病死	不良反应
对照组	86	28(32.56)	19(22.09)	18(20.93)
观察组	86	67(77.91)	4(4.65)	8(4.65)
χ^2 值		5.98	5.04	5.76
P 值		0.01	0.01	0.01

3 讨论

2013 年，美国感染疾病学会等组织联合发布万古霉素血药浓度检测指南，建议将原来推荐万古霉素谷浓度 5～10 mg/L 提高到 10～20 mg/L，指南同时做出了具体给药剂量推荐[7]。因此，万古霉素血药谷浓度应达 10～20 mg/L 已得到业界普遍认可，但对于重症感染、中枢神经系统感染等患者血药谷浓度应达 15～20 mg/L[8-9]。在国内，由于受不同生产厂家、患者基础情况（如年龄、体重）等因素影响，万古霉素血药谷浓度达标率较低，文献[10-11]报道均在 50%以下，而对于重症感染患者而言，受肾功能、白蛋白水平、液体循环等影响，万古霉素血药谷浓度达标率则更低。

通过本研究发现，患者年龄、中重度外周水肿、CrCl 及 BMI 为影响万古霉素血药谷浓度的主要因素。国内也有文献[10-12]报道，万古霉素血药谷浓度的影响因素可能还有很多，如种族、机体代谢水平等，这些因素均有可能参与了万古霉素血药谷浓度的变化。因万古霉素 90%以上以原型经肾脏排泄清除，因此，CrCl 的大小与万古霉素的清除直接相关。本研究发现，CrCl 正常患者，万古霉素血药谷浓度低于 10 mg/L 的比例更高。通过进一步深入分析发现，可能与实际使用剂量低于说明书/指南推荐给药剂量有关。临床使用万古霉素可根据 CrCl 或血药谷浓度适当增加用药剂量。本研究中，CrCl＜50 ml/min 患者中，万古霉素血药谷浓度高于 20 mg/L 患者比例明显增加，进一步分析发现，其实际剂量显著高于推荐药物剂量。值得注意的是，在 CrCl 10～50 ml/min 组患者中，浓度超标比例较高这一现象更为明显，可能由于患者本身肾功能减退，导致万古霉素排泄降低有关，也有可能是万古霉素使用造成肾损伤，导致药物清除率进一步降低所致。因此，对于 CrCl 下降患者，应及时严格根据 CrCl 调整万古霉素使用剂量，并加强血药浓度监测，避免肾毒性发生。

综上所述，万古霉素血药谷浓度的主要影响因素包括年龄、中重度外周水肿、CrCl 及 BMI。因此，临床经验性使用万古霉素过程中，应充分考量以上因素对血药谷浓度的影响，选择合适的给药剂量。与此同时，临床药师应根据上述影响因素给予个体化用药治疗建议，以提高万古霉素的临床治疗效果和防止不良反应的发生。本研究纳入患者例数较少，尽管排除大部分干扰因素，仍受部分不可控干扰因素影响，但在目前文献报道不多的情况下，仍有一定的参考价值，值得进一步深入研究。

参考文献

[1] Cataldo MA,Tacconelli E,Grilli E,et al.Continuous versus intermittent infusion of vancomycin forthetreatment of Gram-positiveinfections: systematic review and meta analysis[J].J Antimicrob Chemother, 2012,67(1):17-24.

[2] Ye ZK,Tang HL,Zhai SD.Benefits of therapeutic drug monitoring of vancomycin:a systematic review and meta-analysis[J].PLoS One, 2013,8(10):e77169.

[3] Rybak MJ,Lomaestro BM,Rotschafer JC,etal.Therapeutic monitoring of vancomycin in adults summary ofconsensus recommendations from the American Society of Health-System Pharmacists,the Infectious Diseases Society of America,and the Society of Infectious Diseases Pharmacists[J].Pharmacotherapy,2009,29(11):1275-1279.

[4] 唐喆,曹静,帅维维,等.新生儿万古霉素血药谷浓度影响因素分析[J].中国抗生素杂志,2019,44(4):493-502.

[5] 国家卫生计生委医政医管局,国家卫生计生委合理用药专家委员会.国家抗微生物治疗指南(第 2 版)[M].北京:人民卫生出版社,2017:56.

[6] 范洪伟主译，热病(新译第 48 版)[M].北京:中国协和医科大学出版社,2019:230.

[7] Davis SL,Scheetz MH,Bosso JA,et al.Adherence to the 2009 consensus guidelines for vancomycin dosing and monitoring practices: a cross-sectional survey of U.S. hospitals[J].Pharmacotherapy,2013, 33(12):1256-1263.

[8] 万古霉素临床应用剂量专家组.万古霉素临床应用剂量中国专家共识[J].中华传染病杂志,2012,30(11):641-646.

[9] 刘素琴,沈国琴.我院 ICU 老年感染患者万古霉素血药谷浓度的监测结果分析[J].中国药房,2018,29(24):3417-3421.

[10] 李静静,刘艺茜,唐莲,等.新生儿万古霉素的群体药动学研究[J].中国药学杂志,2017,52(16):1434-1441.

[11] 梁培,郭晓芳.高肌酐清除率重症患者万古霉素血药浓度监测分析[J].药学与临床研究,2017,25(6):493-496.

[12] 申庆荣,李刚,卢秋玉,等.万古霉素血药谷浓度的影响因素分析[J].中国抗生素杂志,2017,42(5):429-434.

（收稿日期：2022-01-20）

基于学科交叉的药学实验教学模式的改革与实践

梁 可，徐英辉，余 巧，李大炜，张新忠

（惠州卫生职业技术学院，广东 惠州 516025）

摘 要：本研究旨在探索和建立适合药学专业的创新实验教学模式，开展基于多学科交叉的综合大实验，提高学生的创新精神和实践能力，促进教学质量。

关键词：药学；学科交叉；综合性实验；教学改革

中图分类号：R91 G64　　文献标识码：A　　文章编号：1672-979X（2017）01-0050-03

Reform and Practice of Teaching Mode of Pharmaceutical Experiment Based on Interdisciplinary

LIANG Ke, XU Ying-hui, YU Qiao, LI Da-wei, ZHANG Xin-zhong

(*Huizhou Health Sciences Polytechnic, Huizhou* 516025, *China*)

Abstract: The purpose of this study is to explore and establish an innovative experimental teaching mode suitable for pharmacy specialty to carry out comprehensive experiments based on interdisciplinary, thus to improve the students ' innovative spirit and practical ability, and to promote the quality of teaching.

Key Words: pharmacy; interdisciplinary; comprehensive experiment; teaching reform

职业教育的最终目标是培养适应用人单位需求的高素质技能型人才，学生不仅应有扎实的理论基础，更重要的是应注重创新精神和实践能力的综合培养。提高学生核心竞争力，需要改革人才培养模式，将创新意识、实践技能的传授融进理论教学过程之中，培养药学专业学生“综合创新者”意识和“药学服务者”意识，以适应当前药学领域对药学人才的需求。实验教学是药学专业教学体系的重要组成部分[1]，在人才培养方案中占有的比例重，在培养学生理论联系实际的创新精神和实践能力方面有不可替代的作用，也是理论教学的重要补充和延伸。

1 改革背景

国内大部分高职院校开展的都是单一学科的独立验证型实验，实验教学模式单一，教师“填鸭式”灌输讲解示范，学生被动接受知识，“照葫芦画瓢”实验操作，缺乏实验学习的主动性和创造能力；此外，各学科实验内容各自为政，其他药学知识涉及深度和广度不够，没有体现出知识的系统性和连贯性[2-3]。如药物化学是合成实验，药剂学是制剂实验，药理学是药效实验，缺乏药物研制及生产之间的序贯性；再者，有些实训项目在不同学科中重复开设，如《药物化学》中“阿司匹林的合成与性质”与《药物分析》中“阿司匹林的质量分析”有重复的实验项目；《药剂学》中的“片剂的质量检查”与《药物分析》中“片剂的重量差异与溶出度检查”重复。根据对药学专业实习生及毕业生的评价跟踪，大部分用人单位认为目前我院的药学专业人才知识面单一，缺乏将所学的各门学科知识系统整合的

收稿日期：2016-12-06

基金项目：2013年惠州市教育科研立项课题（2013kt360），2013年院级研究课题立项（20130106）

作者简介：梁可（1983-），女，讲师，硕士，主要从事药学教育与研究工作 E-mail：17497108@qq.com

能力。这种传统实践教学模式培养出的学生，不能适应药学用人单位实际需求，毕业生需较长时间适应及融入岗位工作。

相对于单一简单的验证性实验，大型综合性实验不仅能检验学生基础理论掌握程度，也能培养学生的综合创新能力，并能构建健全的先进性教学手段。结合药学各学科实验教学相关环节，开设综合性大实验，减少重复性实验，让学生系统地完成药品生产、检验、销售等各环节的实验，不仅使学生更好理解与掌握各学科的理论基础知识和基本技能，还能培养学生综合知识应用和科学素质，并加深对多门课程的综合理解及掌握相关实验技能。将课堂理论与实验实践融为一体，改善教学的效果，实现了对传统教学模式的创新[4]，保证实验教学内容的完整性、先进性和科学性。

2 改革内容

我院的药学综合大实验是在药学专业主干学科实验课的基础上开设的，按照“实践、创新”的要求，以培养职业能力为本位，在专项技能训练的基础上，将《药物化学》、《天然药物学》、《药物分析》、《药剂学》、《药理学》、《药品市场营销》等课程中有关联的实验衔接起来，使之整合成一个有机的整体实训项目[5]，改革原有的以单一学科为中心，开展综合实验教学的模式，建立一体化多层次的实训教学内容体系，提高学生对专项技能的综合运用能力，对药学专业有一个全面系统的认识[6]。

2.1 建立健全实验课程的教学模式

根据课程教学计划、本学科领域的发展现状和趋势，本着注重基础理论和工艺、培养实际操作技能的目标，编制、修订《药学专业综合性实验教学大纲》和《药学专业综合性实验讲义》等教学校本教材，理顺各学科实验内容的关系，明确综合实验各阶段教学目标，构建综合实验体系和指导性方案。确定综合实验项目为《阿司匹林片的研制》和《板蓝根颗粒的研制》，前者为化学药物的代表，后者为中成药的代表。通过2个代表药物的化学合成、药材的有效成分提取、药效试验、制剂制备、质量分析、营销策划的综合性实验，模拟创新化学药物及中成药的生产、检测和营销过程。加深学生对于各主干课程相关理论基础知识及实践专项技能的综合理解与掌握，切实体会各学科之间的关联，培养学生相关实验技能、综合知识、系统设计方法和科学素质等方面的素养。

2.2 具体实施

我们将综合大实验项目纳入学生实习前的实践教学活动，为期两周，此时课程已全部讲授完成，学生已熟悉各学科的基本理论和专项技能。学生以组为单位，参照实验讲义设计实验方案，设计内容经相关教师审核后实施实验，实验中安排教师及实验员指导，最终完成实验报告；指导教师对实验预习、方案设计、原始记录、操作能力、实验报告、实验素养、营销技巧等进行量化考核。在实验过程中，学生为主体，变被动为主动学习，对实验中出现的各种问题进行讨论并寻求解决之道，始终保持互动协作式教学模式，极大提高学生分析总结、团结协作能力，为今后独立开展工作打下坚实的基础。

2.3 成效与体会

通过综合实验教学模式的改革，可使学生对药品的生产、检测、销售进行一次有意义的模拟演练，与传统实验教学模式相比，更好激发了学生学习的主动积极性，使学生获得较全面、系统、扎实的实践知识和操作技能，还能帮助学生理顺专业脉络，促进各学科知识的融会贯通[7]，掌握药物开发的基本步骤、主要研究内容和方法及研究报告的书写，培养学生综合运用所学知识去解决实际问题的能力，创新思维能力，学会研究性及创新性学习方法，加强团队合作精神，使学生更快融入工作岗位。

虽然药学综合实验模式的开展取得初步成功，但仍出现一些问题，如学生某些专项技能操

作不规范、基础理论和技能不够扎实、查阅文献能力较差；教师缺乏将各学科知识综合应用的能力，有时在学生实验过程中不能给予及时的指导。这提醒我们，需要进行教学改革，重视学生基础知识和基本技能的训练，并在开展综合实验前加大教师的培训力度，充分调动学生和教师的积极性，在实践中不断探求、改革和完善实验教学模式，进而不断提高实验教学质量，培养出高素质技能型药学人才。

参考文献

[1] 陈 琰，钟延强，鲁莹，等．药学多学科综合性实验改革的探索和体会[J]．药学实践杂志，2009，27（4）：309-310.

[2] 张 辉，喻莉萍，李强国，等．药学综合实验教学体系的构建及其实践[J]．中国现代药物应用，2010，4（11）：211-212.

[3] 林奇泗，张 玲，牟 杰，等．药学综合设计性实验教学的探索[J]．科技视界．2013，(30)：14-15.

[4] 梁香．药学专业中开展综合性实验的探讨[J]. 现代医药卫生，2008，24（1）：153-154.

[5] 蒋庆琳，郑向辉，王地娟，等．基于学科交叉的药学综合性与设计性实验改革与实践[J]．药学实践杂志，2012，30（5）：392-400.

[6] 李彩文，陈宝泉，刘玉明，等．药学综合实验的教学内容改革初探[J]．中国医药导报，2011，8（36）：125-126.

[7] 高春华，石向群，刘频建，等．药学综合实验教学改革探索[J]．九江学院学报，2011（1）：95-97.

基于职业能力的高职药学专业课程标准探究

徐英辉，申　茹，祁银德
（惠州卫生职业技术学院，广东 惠州 516000）

摘　要：从高职药学专业课程标准研制的实践出发，分析将职业能力融入课程标准建设的必要性及课程标准与职业能力精细化对接需要解决的问题，探讨基于职业能力精细化对接的高职药学专业课程标准建设策略，尝试为高职药学专业建设提供课程标准指引。

关键词：高职药学专业；课程标准；职业能力
中图分类号：G420　　**文献标识码：**A　　**文章编号：**1671-1246（2021）11-0038-03

课程标准是规定某一学科的课程性质、课程目标、内容目标、实施建议的教学指导性文件。它是教育质量评价的主要依据，也是高职院校进行教学诊断与改进的重要基础。教育部《关于深化职业教育教学改革全面提高人才培养质量的若干意见》（教职成[2015]0156 号）明确指出：省级教育行政部门要根据国家发布的相关标准，组织开发具有地方特色的专业教学指导方案和课程标准，积极开发与国际先进标准对接的专业教学标准和课程标准[1]。而职业能力是指人们在从事其职业过程中应具备的各种综合能力，具体包括专业能力、关键能力和社会能力[2]。专业能力指从事某一职业时能胜任岗位工作的专业能力；关键

基金项目：广东省高职教育医药卫生类专业教指委 2018 年度教育教学改革项目（2018LX045）

一是课程实践。在思政课中设计实践教学环节，分为课内实践和课外实践。课内实践包括案例分析、主题演讲或辩论、情景剧表演等。课外实践包括阅读分享、走访参观、公益和调查活动等，例如，鼓励学生积极参加由校内外各级单位组织的公益活动和志愿者服务活动，通过参加卫生宣教、义诊服务、心理咨询、兴农、支农、义务助教等系列实践活动，提高学生思政课实践教学参与度，使学生进一步了解国情、省情，提高判断社会现象、认识分析社会问题和解决社会问题的能力。

二是专项实践。每学期由辅导员及思政课专职教师带队，组织学生赴黄继光纪念馆、双流云华村等实践教学基地，以考察学习的形式开展专项实践教学，感知国家进步与时代挑战，弘扬革命精神，引领学生积极投身民族复兴的伟大事业。

三是社会实践。寒暑假依托校外实践教学基地，充分挖掘地方德育资源，学生围绕经济建设、政治建设、文化建设、社会建设、生态文明建设、党的建设等确定调研主题，通过参观、调研、考察、社会服务、科技服务等形式开展社会实践活动。

四是网络实践。建立四川护理职业学院思想政治理论课网络教学平台，发布教学信息，与学生在课前、课后展开交流讨论，充实、丰富、深化课堂教学内容。

2.4 整合教育资源，夯实教学支撑体系

思政课实践教学支撑体系建设要立足院校，多元整合校内外自然资源、红色资源、文化资源、体育资源、科技资源、国防资源和企事业单位资源，尤其是符合地方发展和专业特点的特色教育资源。通过校地共建、校企共建等途径，围绕生命教育、价值观教育、医德教育 3 方面进行实践教学基地建设，如爱国主义教育基地、新农村建设示范基地、区域经济发展示范基地、医疗新业态机构以及学院未来的校史馆等，丰富思政课教学内容，拓展思政课教学空间，改进思政课教学方式方法，增强学生体验感，推动思政课实践教学发展。

2.5 注重过程记录，完善效果评价体系

为确保思政课实践教学落到实处，必须注重对实践活动时间、地点、内容以及活动现场、活动认识、感受等基本要素的记录和呈现。采用过程与结果相结合、定性与定量相结合的评价方法，利用包括学校、教师、学生、社会在内的多元评价主体，制定科学可行的思政课实践教学考核评价标准、具体实施方案和细则，建立立体、互动的反馈机制，最大限度反映实践教学真实情况与教学效果，不断完善实践教学方案。

参考文献：

[1]习近平：用新时代中国特色社会主义思想铸魂育人　贯彻党的教育方针落实立德树人根本任务[N].人民日报，2019-03-19（01）.
[2]教育部.新时代高校思想政治理论课教学工作基本要求[Z].2018.
[3]中共中央办公厅，国务院办公厅.关于深化新时代学校思想政治理论课改革创新的若干意见[Z].2019.
[4]廖日文.确保每一个大学生都能参加社会实践[J].思想理论教育导刊，2011（1）：111-115.
[5]张丽.高职院校“思政课”实践教学体系的构建及相关创新模式研究[J].教育现代化，2019（12）：124-126.

（* 通讯作者：谢孝红）

能力包括跨职业的专业能力、社会能力、方法能力和个人能力4个方面；社会能力指一般的学习能力、人际交往能力、团队协作能力、对环境的适应能力、文字和语言运用能力，以及遇到挫折时良好的心理承受能力。

基于职业能力精细化对接的高职药学专业课程标准，即对药学专业就业的岗位需求进行充分的调研与分析，构建专业的课程体系，依据工作内容，对接职业能力，优化选取教学内容及课程标准，对专业基础课、专业课进行精细化对接[3]。在教学过程中积极推进课程标准的实施，优化教学模式，积极开展项目导向教学，做中学、学中做教学，案例分析式，问题讨论式等新的教学模式，进而拓展学生的专业综合素质与岗位适应能力[4]。本文以惠州卫生职业技术学院药学专业为例，探讨基于职业能力精细化对接的高职药学专业课程标准建设策略，进一步推动高职药学专业职业教育的健康协调发展，系统培养适应新时期经济社会发展需要的药学技能型人才。

1 课程标准与职业能力精细化对接是职业教育发展的必然趋势

高职教育的培养目标是培养高素质技能型专门人才，注重对学生职业能力的培养，文化知识、专业知识是基础，而实践技能、应变能力则是竞争的有力保障[5]。因此，为提高学生的综合职业能力，大力开展课程改革，将课程标准与职业能力精细化对接是职业教育发展的必然趋势。课程标准对高职教育教学具有指导性意义，其中包括课程定位与课程设计、课程目标、课程教学设计思路、课程实施条件及考核评价方式等，其在专业建设、教学改革方面起着至关重要的作用。同时课程标准也是高职教师、教育管理者开展教学研究、诊断与改进教学问题的基础，课程标准的建设亦是进一步深化“以服务企业发展为宗旨，以促进学生就业为导向，以职业能力提升为根本”的职业教学改革，关键在于精确分析专业岗位需求，提升学生职业能力，将课程教学目标与职业能力培养有机结合，努力提高课程的实用性、技能性和职业性，使学生的专业知识、实践技能同步提高，改革传统的教学方法，构建以职业能力培养为本位的专业课程体系，实现学生能力培养目标与用人单位岗位工作能力需要的紧密对接[6]。

2 课程标准与职业能力精细化对接是市场需求的内在要求

将职业能力与课程标准精细化对接，是深化校企融合的有效途径，也能使所培养学生快速适应用人单位的需求，提高学生的综合竞争力[7]。用人单位在招聘毕业生时，考核内容包括文化知识、专业知识，并且涵盖实践能力及学生分析问题、解决问题的灵活应变能力。而专业技能与职业能力中的一般职业能力相匹配，指在职业活动中不可缺少的能力，包括学习能力、人际交往、团队写作、实践操作能力。应变能力是职业能力中的关键，指对学生未来发展起关键作用，具有可迁移性的能力。由此可见，职业能力是企业对高职生的重要要求，知识理论水平高，但实践技能、应变能力低的学生是难以满足企业用人需求的。因此，培养职业能力是切实提高高职学生就业竞争力的有力手段。专业课程教学与企业职业岗位需求有效接轨，课程标准与职业能力精细化对接，高职院校课程教学目标与企业需求的职业能力相匹配，扎实开展以培养学生职业能力为目标的课程改革和开发具有高职院校特色的课程标准是当务之急。

3 课程标准与职业能力精细化对接需要解决的关键问题

3.1 分析岗位需求，培养职业能力，实现教学目标与职业能力的无缝对接

分析岗位需求，对药企、医院、药检所进行深入调研，了解医药行业发展对药学专业人才的需求状况，了解市场需求变化和对人才的具体要求，准确剖析具体岗位如药品生产、药品调剂、药品检验等对药学专业学生职业能力的要求[8]。针对专业培养目标及方向，适时调整专业人才培养方案，培养学生职业能力，加强校企、校院合作，共建校外实训基地，确保职业教育与当地社会发展和经济发展相适应，为药企、医院、药检所培养优秀的药学专业技能型人才。

3.2 将职业能力培养贯穿于整个专业课程体系，各门课程之间进行精细化对接[9]

职业能力的培养不仅限于专业课程，更不限于某一门课，应将职业能力培养渗透到整个专业课程体系，包括文化基础课、专业基础课、专业课、专业选修课等。将职业能力细化到每一门课程中，各门课程相互独立又紧密联系，课程教学目标的制定对应职业岗位需求，具体职业岗位的职业能力需求有其层次关系，各课程教学目标也应体现其前后递进关系，教师应依据课程教学目标，设计教学模块。

3.3 转变教师、行企业专家观念，推进课程标准的建设与实践

现阶段，高职院校教师在授课过程中往往更加注重对理论知识的讲授，对工作岗位需求的分析甚少，没有把教学目标与职业能力联系起来，使得学生缺乏对工作岗位的认知，难以满足用人单位需求。为建立新的课程标准，需要充分调动教师积极性，根据人才规格要求和市场需求变化，有针对性地进行课程改革，促进职业教育服务行业的发展[10]。同时，推进课程标准的建设需要行企业专家的大力配合，学校教师应深入企业调研、加强校企合作。校企合作包括校企联合申报横向课题，校企共同开发实训教材，教材内容要紧密结合岗位需求，教学内容要与岗位技能标准精细对接。

4 基于职业能力精细化对接的高职药学专业群课程标准建设策略

4.1 以行企业调研为基础，构建专业课程体系

对与药学专业紧密相关的药企、医院、药检所进行深入调研，认真听取用人单位对高职药学专业学生职业能力培养的建议，并深入了解药学专业毕业生对本专业人才课程体系知识结构、能力结构，课程设置和实习实践环节设置等方面的反馈意见。综合其对高职药学人才理论知识和实践技能的需求，确定专业面向的职业岗位（群）的主要工作要求，归纳若干个典型工作任务及其相应的职业能力，依据职业能力需求，构建专业课程体系，课程设置与学生今后就业方向相适应，课程内容选择服务于职业能力建构[11]。

4.2 以职业能力培养为核心，确立课程教学目标

明确分析专业课程体系中各门课程与专业职业能力之间的关系，从而确定该课程可以培养学生哪方面的职业能力，最终确定课程的定位与设计思路、教学目标[12]。课程目标包括具体的知识目标、技能目标、职业素质目标和态度目标，课程目标是

教师在课程教学设计与具体教学实施的重要依据。例如：药剂学是高职药学专业的核心课程之一，主要包括临床常用剂型的概念、特点、生产工艺流程、生产技术、质量控制，以及药物制剂的稳定性、药品调剂和药学服务等。高职药学专业学生毕业后可以在医院药房、药品生产企业、药品经营企业从事药品调剂、药品生产、药品经营等工作，需要具备临床各种常用剂型的制备及质量检查方法等职业能力。故在药剂学课程教学中，教师要对照职业能力，确定教学目标，细化教学要求。

4.3 以岗位能力需求为依据，确定课程教学内容

组建由药企、医院、药检所专家、课程专家等组成的课程建设指导委员会，对职业能力与岗位需求进行科学分析[13]，以典型项目为载体，将岗位工作内容与教学内容进行有机融合，将专业课程项目化、模块化。每个模块以任务的形式进行分解，明确知识目标、能力目标及态度目标，使学生在学习不同类型的课程后，逐步具备完成复杂项目所需的综合职业能力。对专业基础课、专业课进行精细化对接设计。例如：药物化学是药学专业的主干课程和专业课程，先修课程有无机化学、有机化学、生物化学、生理学等课程，学生学习本门课程需要有先期知识或技能，故在药物化学课程标准中对先修课程提出建议和要求：掌握杂环的分类、结构特点和命名，各类官能团的性质、水解反应、氧化反应、聚合反应、异构化反应、脱羧反应等反应原理等内容。实现专业课程与先修课程有机衔接，确定课程教学内容，进一步提升教学质量。

4.4 以学生为主体，设计课程教学方法

积极推进基于能力精细化对接的高职药学专业群课程标准的实施，探索符合高职特色的新型教学模式，如项目化、理实一体化、案例式、问题讨论式等新的教学模式[14]；强化学校、药企、医院、药检所的合作内涵，提高人才培养的针对性，进而拓展学生专业综合素质与岗位适应能力。在教学过程中，坚持以学生为主体，以职业能力提升为目标的教学理念，运用现代化信息教育手段，设计灵活多样的教学方法。采取任务驱动模式，通过任务驱动，带动学生查阅资料，指导学生制订工作计划，引导学生对计划进行可行性分析，然后由学生做出决策并实施计划，教师进行指导答疑。例如：在药物分析课程中“维生素 C 颗粒的含量测定及质量检查”内容，采用项目教学法，设计药检所对药品检测的情景，与教学内容的实训项目相匹配。这些实训项目因为和实际工作联系紧密，所以极大地调动了学生的学习热情，同时进一步提高了学生的实际操作能力，培养了学生的团队合作精神。

4.5 以专业技能提升为目标，建立考核评价体系

课程考核是高职院校教学活动的重要环节之一，除了要对学生的专业知识进行考核，更要重视对学生实践技能、应变能力的评价。改革以往的将期末考试等同于课程考核的方式，将学生课堂学习、实训操作、完成作业的全过程纳入考核范畴，以提升学生专业技能为目标，建立科学的考核评价体系[15]。在考核过程中，引导学生主动思考、积极探索，培养学生的自主学习能力。要做到评价主体多元化、评价形式多样化，形成以过程考核与结果考核，主观考核与客观考核，学校考核与药企、医院、药检所考核，教师考核与学生相互评价并重，并与药学专业相关的职业技能鉴定考核标准相衔接的评价体系。力争将一般职业能力、关键能力和专业能力进行全方位考核，有力提高学生的综合竞争力。

5 结语

开展基于职业能力精细化对接的高职药学专业课程标准探究，可以解决当前高职院校药学专业课程教学内容体系存在的重理论、轻实践，重知识、轻运用，重系统、轻能力等问题。将职业能力融入课程标准的研究又是一项系统、长期的项目，需要学校、药企、医院和社会共同推进。对职业能力的培养应始终贯穿于教育教学过程中，应融入每一门课程的课程标准中，职业能力与课程教学项目及评价标准精细化对接，使得学生职业能力不断积累并向职业能力提升过渡[16]。课程标准必须在充分调研和实践研究的基础上逐渐建立起来，并随社会和企业的需求变化不断完善和改进，从而推动高职药学专业教育改革的深入，提高人才培养质量，真正实现职业院校人才培养与企业需求的精准对接。

参考文献：

[1]席东梅.筑牢职业教育发展之根基：专家解读《关于深化职业教育教学改革全面提高人才培养质量的若干意见》[J].中国职业技术教育，2015(25)：10-14.

[2]陈晓兰.基于职业能力的高职课程标准建设与实践[J].教育教学论坛，2018(34)：234-236.

[3]覃国蓉，何涛.高职课程标准建设的探索与实践[J].中国职业技术教育，2012(8)：72-75.

[4]陆远蓉，许喜斌.基于手持智能终端的高职教学模式改革探析[J].职教论坛，2015(14)：64-68.

[5]陈晓兰.基于职业能力的高职课程标准建设的必要性和策略研究[J].卫生职业教育，2018，36(5)：4-5.

[6]景萌，李宏昌.高职院校课程建设质量标准开发和设计研究：以贵州省高职院校为例[J].职业技术教育，2019，40(29)：17-22.

[7]周茂东，张福堂.高职专业课程体系构建探析：兼评高职经济类专业教学标准中的课程体系[J].职业技术教育，2013，34(14)：19-22.

[8]沈惠惠.基于职业标准的高职院校课程改革困境与出路[J].教育与职业，2019(5)：105-108.

[9]周茂东，张福堂.从“课程体系与核心课程”看高职专业教学标准的修订[J].职业技术教育，2015，36(28)：33-36.

[10]鲁文娟，金一强.协同创新、内涵衔接的中高职三二分段衔接专业标准与课程标准研究[J].教育与职业，2015(22)：89-91.

[11]李继红.对接职业标准的高职中药学专业课程体系构建[J].辽宁农业职业技术学院学报，2016，18(6)：12-14.

[12]蔡扬帆.对高职药学教育的几点看法[J].卫生职业教育，2015，33(14)：22-23.

[13]于永军，陈俊荣，刘清新，等.高职药学专业“双主体”育人模式的探究与实践[J].中国医药导报，2017，14(1)：125-128.

[14]马仁海.高职特殊教育专业“行为矫正技术”课程标准的研究[J].教育与职业，2014(28)：139-141.

[15]林小文，周海霞.现代服务业专业技能课程标准开发实践研究：以宁波市北仑职业高级中学旅游专业为例[J].职业技术教育，2011，32(20)：22-25.

[16]陈晓琴.高职课程标准与职业岗位技能标准对接探究[J].职教论坛，2011(14)：16-18.

校企合作共建“双师型”教师团队的探索与实践
——以惠州卫生职业技术学院药学专业为例

徐英辉，申 茹
（惠州卫生职业技术学院，广东 惠州 516025）

摘要：高职院校的专业教师必须具备良好的理论教学水平，以及较强的实践操作技能，即具备“双师型”素质，才能承担起培养高素质技能型专门人才的重任。校企共建一支综合水平高，专兼结合的“双师型”教师团队是保证高职院校教学质量的根本，是提升高职院校核心竞争力的有效保证。文章以惠州卫生职业技术学院药学专业为例，通过建立完善“双师型”教师团队培养机制、校企共建“双师型”教师团队培养基地、加强专业教师下企业实践锻炼、聘请企业骨干担任兼职教师、校企合作开启订单培养新模式等具体措施，在实操层面探讨校企合作共建 “双师型”教师团队。

关键词：校企合作；双师型；教师团队

高职院校的办学特色在于培养适应生产、建设、管理、服务第一线需要的高素质技能型专门人才，具备良好的实践动手能力，能够实现零距离上岗工作[1]。因此，高职院校的专业教师必须具备较好的理论教学水平，以及较强的实践操作技能，即具备“双师型”素质，才能承担培养高素质技能型专门人才的重任。“双师型”教学团队的建设，也是高职院校发展的内在要求，相对于普通高等院校而言，高职院校的首要目标是使学生获得从事某个职业和行业的实际技能与知识，能在生产实践中熟练运用和发展，并具有适应职业变化的能力[2]。惠州卫生职业技术学院药学专业于2012年开办，是学院重点建设专业。多年来，坚持“以服务为宗旨、以岗位需求为导向”的培养目标，以提升教师综合素质能力这一任务为引领，以创建省级品牌专业为抓手，依托校企合作平台，制定切实可行的“双师型”教师团队的培养方案，采取了一系列有效的措施，取得了一定的成效。

一、建立完善“双师型”教师团队培养机制

学院以建立结构合理、专兼结合的高素质“双师型”教师团队为目标，规范教师团队建设，先后出台了一系列制度，如《惠州卫生职业技术学院“双师素质”教师认定与管理暂行办法》《专业带头人、骨干教师管理办法》《药学系“一加一”教师专项能力提升项目实施方案》《药学专业师资团队建设实施方案》等；修订了《专业教师到企业实践管理规定》《青年教师导师制》《兼职教师管理办法》等；完善了《教师教学工作量考核办法》《教师教学质量评价办法》等，以形成“双师型”教师培养认定、管理的良性运行机制，满足社会和企业对技能型人才的培养需求。

二、校企共建 “双师型”教师团队培养基地

学院药学专业自开办以来，先后与惠州市百姓

收稿日期：2017-10-30
基金项目：2015年度广东省教育研究院教育研究项目（2015-B-b097）
作者简介：徐英辉（1981-），女，惠州卫生职业技术学院药学系讲师，研究方向：职业教育、教学管理。

大药房连锁有限公司、惠州市百姓缘医药有限公司、惠州市卫康中西药业有限公司、惠州市先锋药业等企业建立了紧密合作关系，并聘请企业专家担任专业建设指导委员会成员，定期召开专业建设指导委员会工作会议，研究人才培养方案的制定、专业建设、课程建设和实训中心建设、“双师”素质教师培养、专业服务产业等具体事宜，充分发挥行业优势参与教学，促进药学专业建设。

（一）校企共建、共管、共享校内外实训基地

校企合作共建校内外专业实践基地，充分利用和配置双方资源，在资金、场所、设备和技术等方面合作，实现共建、共管、共享。通过多年与企业的紧密合作，学院药学专业已经开拓了一批以惠州市百姓大药房连锁有限公司为代表的融教学、培训、职业资格考核和顶岗实践锻炼于一体的校外实训基地，为“双师型”教师团队提供现实的操作空间，也为学生提供了实习平台，有利于培养技能型人才。

学院积极引企入校，拉近了学院与实践单位的距离，有效推进了校内药学实训大楼的建设。由惠州市百姓大药房连锁有限公司赞助建设的“模拟药房”已经开放使用，由惠州市先锋药业专家担任工程设计师的“GMP车间”正在建设，与惠州市卫康中西药业有限公司合作建设的“中药标本馆”已经顺利完工。校企合作共建的实训基地，注重技能实操的培养从源头上满足企业需求。

此外，利用现有的校内外实训基地，确保实践教学任务完成的同时，双方教师还承担了部分非学历职业技术技能培训任务，如医药商品购销员考试、中药传统技能竞赛等，发挥社会服务职能。兼职教师和专业教师共同参与培训，促进“双师型”教师职业技术技能的提升。

（二）校企合作推进课程建设，申报产学研课题

校企合作推进课程建设，构建理论与实践紧密结合，融知识、能力和素质教育于一体的课程体系。近年来，学院药学专业在企业的参与下，建成了多门核心课程的课程标准、技能标准、教学视频、授课计划、多媒体课件、实验实训教材等，如《药店创业》课程即是药学专业3名教师与3名兼职教师共同编写的校本教材，已经作为专业选修课开设，学生反映良好。另外，依据技能标准，还与企业共同研究编写了多本实训指导，如《药剂学实训指导》《药物分析实训指导》《药物化学实训指导》《药品市场营销学实训指导》《药事管理实训指导》，通过校企联合开发实训课程，使提高教师实践教学能力落到实处，促进“以能力为本位，以就业为导向”校企合作办学模式下的“双师型”教师团队建设[3]。

依托紧密合作的制药企业、医药公司联合申报产学研课题，既能满足药学类专业“层层递进，工学结合”实践教学内容的要求，又可以提升教师科研水平。例如，学院药学专业教师与合作企业联合申报的惠州市哲学社会科学项目《“纲要”指向下的惠州中职教育基础能力建设研究》、省级教改项目《新升格高职院校基于中高职衔接的专业建设研究与实践——以药学专业为例》已经顺利结题，并取得了较好的社会效益，有效地促进了教学改革。与惠州市新峰药业有限公司联合申报的《基于学科交叉的药学实验教学模式的改革与实践》，获2014年度惠州市教改课题研究立项。与惠州市百姓大药房连锁有限公司、惠州市百姓缘有限公司等企业联合申报的《校企共建药学专业“双师型”教师培养培训基地研究》教学改革课题，获2015年度广东省教育研究院教育研究立项。与企业联合申报实训课题，在增强实践教学内容的实用性及针对性，促进学生实践能力和综合技能提高的同时，也提升了教师的实践能力。

三、加强专业教师下企业实践锻炼

专业教师下企业实践锻炼是加快“双师型”专业教学团队建设的有效途径，是提高专业教师“双师”素质，更好地实现高职教育人才培养目标的有力保证，专业教师可通过企业顶岗实践、合作研发（提供技术服务）等多种形式下企业实践锻炼。

（一）鼓励要求专业教师企业顶岗实践

根据学院《专业教师临床（企业）实践管理规定》的要求，专业教师每5年必须参加不少于累计5个月的临床或企业实践，达不到实践时长者，不得晋升高一级职称。药学专业教师实行自找实践单位、学院指定实践单位以及选派青年教师参加省级企业实践培训课程等多样化模式的企业顶岗实

践。近年来，学院与惠州市新峰药业有限公司、惠州市百姓大药房连锁有限公司、惠州市百姓缘医药有限公司等多家合作企业建立教师实践基地，为教师到企业实践提供强有力的保障。具体做法：由共建企业提供教师实践工作场所，提供必要的办公用品，配备部门经理或专业技术人员对实践教师进行必要的工作指导，由学院给与基本工资待遇。专业教师通过参与企业实际工作，了解企业运营、行业企业的需求，有力地增强了教师实际操作能力，积累丰富了教学案例。同时，专业教师还参与企业实习生的管理与指导，达到资源共享，优势互补。近两年，药学专业共有 18 名教师完成了实践任务，5 名教师参加了省级或国家级的企业实践培训。

（二）选派骨干教师担任企业“科技特派员”

校企合作共建 “双师型”教师团队，在保证教学的同时，应为企业提供药品检测、技术人员培训、技术攻关等专业服务，从而拓宽校企合作内容，丰富合作内涵。近年来，学院选派了一批药学专业“双师型”骨干教师，深入到惠州市医药企业，按照市场需求和企业的实际需要，协助企业申报科技成果转化，通过 GSP 认证、GMP 认证、开展药学服务等。如本学年，学院药学专业共有 6 名教师先后赴惠州市泛生中药饮片厂等医药企业进行知识顾问和技术指导。实现了专业服务产业的社会目标，促进了校企合作关系的稳定和长期发展。

四、聘请企业骨干担任兼职教师

通过聘请具有行业影响力的企业专家、骨干作为学院兼职教师，由于这些兼职教师来自企业生产、销售、管理第一线，他们专业理论功底扎实、并且有着丰富的实践经验，了解行业的最新动态、实操能力强，可以把工作中的第一线的新技术、新工艺以及社会对人才素质的新要求带到教学中，可以有力地促进学生实践能力的培养[4]。如学院药学专业的《药店零售技术》《优良药房实务》《药店创业》《仪器分析》《药事管理》等多门专业课程均由兼职教师授课。在教学过程中实施企业职称特聘制，兼职教师承担的专业课采取“1 名兼职教师 +1 名学院专业教师”双主体的教学模式，共同完成该门专业课的教学任务。兼职教师、专业教师共同组织教学，一方面可以加强沟通，促进合作；另一方面通过相互学习，专业教师可以提升实践能力，而兼职教师在教育教学理论、教学基本功、教学管理能力等方面均会有很大程度的提高，切实实现校内专任教师与兼职教师的优势互补。

五、校企合作开启订单培养新模式

校企双方深度融合，加强合作，以订单班为切入点，加强“双师型”教师团队的建设。目前，学院与惠州市百姓大药房连锁有限公司、惠州市百姓缘医药有限公司合作开办了“百姓药剂班”“百姓缘药剂班”，专业教师和兼职教师共同授课，为医药公司、制药企业培养药品销售、药品生产、药品质检一线的药学技术人员，与岗位无缝对接，进一步强化“双师型”教师团队建设，提高教学的实用性。另外，合作企业会对订单班的专业教师进行定期培训，将企业的新知识、新技能、新需求传授给专业教师，不断提高专业教师的实践技能。因此，校企合作平台的“双师型”教师团队建设，需要与技术领先的企业开展合作，这样能够为高职院校的教师提供技术服务、培训等，使培养 “双师型”教师人才，构建“双师型”教师团队的目标落到实处[5]。

综上，校企共建“双师型”教师团队是保证高职院校教学质量的根本，是提升高职院校核心竞争力的有效保证。通过校企优势互补，实现高职院校的课程体系与企业职业岗位需求的无缝对接，我院药学专业校企合作仍处于起步阶段，“双师型”教师团队建设任重道远。因此，要继续深化合作力度，拓宽合作广度，为有效地提高高职院校教师的能力和水平，推动高职教学工作不断向前发展做贡献。

参考文献：

[1] 姜春华. 高职“双师型”师资团队建设探讨[J]. 科技资讯，2012，(24)：194- 196.
[2] 吴伟俊. 高职院校学前教育专业“双师型”师资队伍建设初探[J]. 职业时空，2012，8 (1)：13- 15.
[3] 许能生. 校企合作构建高职教育职业核心能力培养模式[J]. 江苏建筑职业技术学院学报，2013，13 (3)：39- 41.
[4] 王宇. 关于校企共建教师教学团队的思考[J]. 中国电力教育，2009，(9)：20- 21.
[5] 陆建军，高玉梅. 基于校企合作的高职院校双师型教师团队建设[J]. 市场周刊 (理论研究)，2013，(2)：120- 121.

[12] 唐秀胜，靳凤云，章 誉，等. HPLC 法测定贵州苗药铁筷子中东莨菪内酯的含量 [J]. 贵阳中医学院学报，2015，37(6)：24-27.
[13] 甄 攀，王治宝，白雪梅，等. 吴茱萸中吴茱萸碱和吴茱萸次碱的 HPLC 分析 [J]. 中成药，2004，26(3)：227-229.
[14] 曾金祥，刘 勇，黄碧涛，等. 吴茱萸 HPLC 指纹图谱的建立及 3 种成分含量的测定 [J]. 安徽农业科学，2011，39(14)：8273-8275，8278.
[15] 杨媛媛，陈志永，廖立平，等. 冯了性风湿跌打药酒中东莨菪素、东莨菪苷和绿原酸的测定 [J]. 中成药，2014，36(3)：551-553.

忍冬藤胶囊的制备及其质量标准

徐英辉[1]， 申 茹[1]， 郭玉岩[2*]
(1. 惠州卫生职业技术学院，广东 惠州 516000；2. 黑龙江中医药大学，黑龙江 哈尔滨 150040)

摘要：目的 制备忍冬藤胶囊，并建立其质量标准。**方法** 以休止角、吸湿率、堆密度为指标，制备忍冬藤胶囊。然后，TLC 法定性鉴别绿原酸、马钱苷，HPLC 法测定绿原酸、马钱苷含有量。**结果** 最佳制备工艺为微晶纤维素与淀粉比例 3∶1，吸湿率 10.7%，选用 1 号胶囊。TLC 斑点清晰，阴性对照无干扰；绿原酸、马钱苷分别在 10.2～306、7～525 mg/mL 范围内线性关系良好，平均加样回收率分别为 100.8%、98.67%，RSD 分别为 1.79%、2.41%。**结论** 该方法合理可行，专属性强，重复性好，可用于忍冬藤胶囊的质量控制。

关键词： 忍冬藤胶囊；制备；绿原酸；马钱苷；TLC；HPLC
中图分类号： R927.2 **文献标志码：** A **文章编号：** 1001-1528(2019)08-1790-05
doi: 10.3969/j.issn.1001-1528.2019.08.008

Preparation of Rendongteng Capsules and the quality standard

XU Ying-hui[1]， SHEN Ru[1]， GUO Yu-yan[2*]
(*1. Huizhou Health Sciences Polytechnic, Huizhou 516000, China; 2. Heilongjiang University of Chinese Medicine, Harbin 150040, China*)

KEY WORDS: Rendongteng Capsules; preparation; chlorogenic acid; loganin; TLC; HPLC

忍冬藤为忍冬科植物忍冬 *Lonicera japonica* Thunb. 的干燥茎枝，具有清热解毒、疏风通络功效，用于温病发热、热毒血痢、痈肿疮疡、风湿热痹、关节红肿热痛[1]，始见于梁代《名医别录》，四季均可用药，资源丰富[2]，其有效成分绿原酸、咖啡酸有显著的抗菌、抗病毒作用[3-6]，马钱苷具有抗炎作用[7-8]。课题组前期以绿原酸、马钱苷为指标，优化忍冬藤提取工艺[9]；本实验在此基础上，以休止角、堆密度、吸湿率[10]为指标，对忍冬藤胶囊的制备工艺进行研究，并对其进行质量控制，以期为今后工业化生产提供理论依据。

1 材料

1.1 仪器 Agilent 1260 高效液相色谱仪（美国安捷伦公司）；HH-8 数显恒温水浴锅（江苏金坛市环宇科学仪器厂）；JA3003 电子天平（上海舜宇恒平科学仪器有限公司）；BPG-9240A 鼓风干燥箱（上海百典仪器设备有限公司）；PS-40A 超声波清洁机（深圳市科洁超声科技有限公司）；ZF-7 暗箱三用紫外分析仪（上海和勤分析仪器有限公司）；AS-400 手工胶囊填充板（浙江奥尔特机械有限公司）；BZF-50 真空干燥箱（上海博迅实业有限公司）。

1.2 试药 药用乳糖、淀粉、糖粉、微晶纤维素（山东聊城华阳医药辅料有限公司）；1 号空心胶囊（吉林敖东顺合胶囊有限公司）。忍冬藤（批号 160601）购自亳州市宏大中药饮片有限公司，产

收稿日期：2018-07-07
基金项目：国家自然基金资助项目（81703724）；2016 年度惠州市科技专项资金资助项目（2016X0402017）
作者简介：徐英辉（1981—），女，硕士，讲师，从事药物制剂研究。E-mail：21806850@qq.com
* 通信作者：郭玉岩（1982—），女，博士，副教授，从事中药新药开发研究。E-mail：guoyuyan622@163.com

地山东，经惠州卫生职业技术学院中药教研室祁银德副教授鉴定为忍冬科植物忍冬 *Lonicera japonica* Thunb. 的干燥茎枝。绿原酸（批号 170309）、马钱苷（批号 170308）对照品购自北京世纪奥科生物技术有限公司。甲醇、乙腈为色谱纯；其他试剂均为分析纯；水为超纯水。

2 制备工艺

2.1 辅料筛选 以浓缩稠膏进行减压干燥时发现，干燥后呈块状黏连固体，而且容易吸潮，不利于胶囊剂填充，故选择湿法制颗粒。

2.1.1 单一辅料 取稠膏 5 g，加入一定量的淀粉、微晶纤维素、乳糖、糖粉混合制粒，以休止角、吸湿性、绿原酸及马钱苷含有量、成型状态为考察指标进行筛选，结果见表 1。由表可知，以上辅料均符合流动性与吸湿性的要求，其中微晶纤维素流动性最好，乳糖吸湿性最好，微晶纤维素成分含有量最高，而在辅料用量方面，糖粉用量最大，可排除；淀粉用量稍大，但价格低廉；微晶纤维素用量较少，但其成本高，不利于产业化。综合考虑，需将辅料混合后作进一步考察。

表 1 单一辅料考察结果

Tab. 1 Results of single excipient investigation

辅料	用量/g	休止角/(°)	吸湿率/%	绿原酸/%	马钱苷/%	成型状态
淀粉	20.2	15.45	6.10	0.169 2	0.350 7	成型性好，颗粒软，易成粉末
乳糖	47.7	19.65	1.48	0.076 1	0.139 5	成型性一般，颗粒松散
糖粉	77.1	15.52	4.85	0.061 2	0.108 7	成型性好，颗粒适中
微晶纤维素	6.2	15.38	7.65	0.425 1	0.867 3	不易成型，粉末量多

2.1.2 混合辅料 取稠膏 5 g，加入不同比例混合的微晶纤维素、淀粉、乳糖制备湿颗粒，以休止角、吸湿性、绿原酸及马钱苷含有量、成型状态为考察指标进行筛选，结果见表 2。由表可知，不同比例下颗粒休止角均小于 30°，颗粒流动性较好，符合吸湿性制剂要求，其中微晶纤维素与淀粉混合时辅料用量少，颗粒成型性好；随着微晶纤维素中淀粉量提高，辅料用量随之增加，绿原酸、马钱苷含有量随之降低，其中微晶纤维素-淀粉比例为 3∶1时两者含有量最高，而且颗粒适中。综合考虑有效成分含有量和患者服用量，最终选择混合辅料为微晶纤维素-淀粉（3∶1），稠膏与辅料的比例约为 1∶1.1。

表 2 混合辅料考察结果

Tab. 2 Results of mixed excipient investigation

辅料	配比	用量/g	休止角/(°)	吸湿率/%	绿原酸/%	马钱苷/%	成型状态
乳糖-淀粉	2∶1	30.2	18.78	4.91	0.117 7	0.242 7	好，颗粒适中
乳糖-淀粉	1∶1	21.1	14.34	4.57	0.153 8	0.330 3	好，颗粒适中
乳糖-淀粉	1∶8	28.0	23.20	4.98	0.106 0	0.234 1	差，易成粉末
微晶纤维素-乳糖	2∶1	7.1	11.31	7.80	0.346 4	1.004 9	差，粉末较多
微晶纤维素-乳糖	1∶1	8.8	9.46	6.84	0.281 0	0.807 8	一般，颗粒适中
微晶纤维素-乳糖	1∶2	9.3	12.53	5.95	0.282 9	0.807 9	好，颗粒适中
微晶纤维素-乳糖	1∶5	13.7	11.31	3.82	0.208 8	0.595 4	好，颗粒适中
微晶纤维素-淀粉	3∶1	5.6	9.46	10.71	0.648 8	1.303 9	好，颗粒适中
微晶纤维素-淀粉	2∶1	6.5	11.31	10.72	0.597 2	1.209 5	一般，颗粒软
微晶纤维素-淀粉	1∶1	7.2	9.46	11.17	0.559 1	1.137 5	好，颗粒适中
微晶纤维素-淀粉	1∶2	8.5	9.46	9.47	0.328 4	0.940 2	好，颗粒适中，硬度适中
微晶纤维素-淀粉	1∶3	10.2	13.13	9.16	0.281 7	0.805 7	好，颗粒适中
微晶纤维素-淀粉	1∶4	11.5	10.73	8.66	0.259 8	0.748 5	好，颗粒适中，硬度一般
微晶纤维素-淀粉	1∶5	10.3	11.92	9.46	0.277 8	0.805 5	好，颗粒适中，硬度一般
微晶纤维素-淀粉	1∶10	12.2	10.70	8.98	0.242 9	0.696 1	好，颗粒较大，硬度偏软

2.2 胶囊型号筛选

2.2.1 堆密度 精密称取 3 份颗粒（质量 m），填充于 10 mL 量筒中，由 5 cm 高度落在木板上，反复振动 3 次后测定体积（V），根据公式 $\rho = m/V$ 计算堆密度，测得其分别为 0.374、0.380、0.374 g/mL，平均 0.376 g/mL（RSD = 0.921%）。

2.2.2 胶囊装量 《中国药典》规定，忍冬藤用量为 9～30 g，绿原酸、马钱苷含有量均不低于 0.10%，以此折算，2 种成分用量为 9～30 mg，每天服用 9～18 粒。结合“2.2.1”项下结果，根据胶囊壳型号和近似容积的关系，选择 1 号空心胶囊（近似容积为 0.5 mL）分装，每粒装约 0.18 g。

2.3 验证试验 称取药材粗粉 400 g，按优化工艺进行提取，提取液在 80 ℃下减压浓缩至相对密度为 1.27 的稠膏备用，取 10、20、50 g，加入混合辅料（微晶纤维素-淀粉，3∶1），混合制粒，考察工艺稳定性，结果见表 3，可知所得颗粒成形性理想，大小适中，而且工艺稳定性好，操作简便。

表 3 验证实验结果

Tab. 3 Results of verification tests

稠膏质量/g	辅料用量/g	绿原酸/%	平均值/%	RSD/%	马钱苷/%	平均值/%	RSD/%
10	11	0.665 0			1.345 9		
20	22	0.665 8	0.658 8	1.73	1.345 3	1.337 2	1.09
50	55	0.645 7			1.320 3		

2.4 制备工艺 取药材粗粉 400 g，按优化工艺提取，80 ℃下减压浓缩，得稠膏约 105 g，相对密度为 1.27，加入混合辅料（微晶纤维素-淀粉，3∶1）120 g，制粒，干燥，装入胶囊即得，制成 1 000粒。

3 质量标准

3.1 TLC 定性鉴别

3.1.1 对照品溶液制备 精密称取绿原酸、马钱苷对照品适量，50%甲醇溶解，制成每 1 mL 分别含两者 0.3、0.57 mg 的溶液，即得。

3.1.2 供试品溶液制备 精密称取胶囊内容物 0.5 g，加入 10 mL 50%甲醇超声处理 30 min，滤过，取续滤液，即得。

3.1.3 对照药材溶液制备 精密称取对照药材 1 g，加入 10 mL 50%甲醇超声处理 30 min，滤过，取续滤液，即得。

3.1.4 空白辅料溶液制备 按照处方制备空白辅料并精密称取 0.5 g，加入 10 mL 50%甲醇超声处理 30 min，滤过，取续滤液，即得。

3.1.5 鉴别方法 按照薄层色谱法（通则 0502）试验[1]，吸取空白辅料、供试品、对照药材、对照品溶液各 5 μL，在同一硅胶 G 薄层板上点样，以乙酸丁酯-甲醇-甲酸-水（7∶1∶2∶1）为展开剂，展开，取出，晾干，在紫外光灯（365 nm）下检视，再喷以 10%硫酸乙醇溶液，于 105 ℃烘箱中加热，斑点显色清晰后停止，在日光下检视薄层板，结果见图 1。由图可知，对照药材、对照品、供试品色谱对应位置上显相同颜色的荧光斑点或斑点，阴性无干扰。

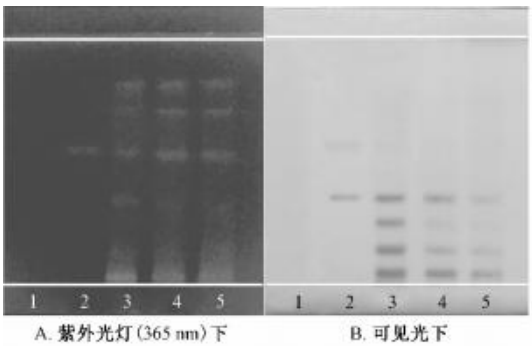

注：1 为空白辅料溶液，2 为对照品溶液，3 为对照药材溶液，4～5 为供试品溶液

图 1 样品 TLC 色谱图

Fig. 1 TLC chromatograms of samples

3.2 检查 按照 2015 年版《中国药典》四部通则胶囊剂项下规定，对胶囊进行水分、装量差异、崩解时限、微生物限度检查。

3.2.1 水分 取 3 批胶囊，每批 10 粒，依法检查[1]，发现均符合《中国药典》规定，见表 4。

3.2.2 装量差异 取 3 批胶囊，每批 20 粒，依法检查[1]，发现均符合《中国药典》规定，见表 4。

3.2.3 崩解时限 取 3 批胶囊，每批 3 粒，依法检查[1]，发现均符合《中国药典》规定，见表 4。

表 4 抽样检查结果

Tab. 4 Results of sampling inspection

检查项目	批号			标准
	20170607	20170608	20170609	
水分/%	3.8	4.1	3.9	<9.0
装量差异/%	符合规定	符合规定	符合规定	±10
崩解时限/min	11	12	11	<30

3.3 含有量测定

3.3.1 色谱条件 YMC-Pack ODS-A 色谱柱（4.0 mm×250 mm，5 μm）；流动相 0.04%磷酸-乙腈，梯度洗脱（0 min，88.5∶11.5；14 min，85∶15；20 min，69∶31；23 min，10∶90）；检测波长 240 nm（马钱苷）、327 nm（绿原酸）；体积流量 0.6 mL/min；柱温 20 ℃；进样量 5 μL。

3.3.2 对照品溶液制备 精密称取绿原酸、马钱苷对照品适量，50%甲醇溶解，制成每 1 mL 分别含两者 0.51、0.7 mg 的溶液，即得。

3.3.3 供试品溶液制备 精密称取胶囊内容物约 0.5 g，置于具塞锥形瓶中，加入 50%甲醇 25 mL，称定质量，超声（功率 250 W、频率 30 kHz）处

理 30 min，放冷，再称定质量，50%甲醇补足减失质量，摇匀，滤过，取续滤液，即得。

3.3.4 阴性样品溶液制备 取不含药材提取液的空白辅料颗粒 0.5 g，按“3.3.3”项下方法制备，即得。

3.3.5 系统适用性试验 取对照品、样品、阴性样品溶液，在“3.3.1”项色谱条件下进样测定，结果见图 2，可知各成分均能得到较好的分离，阴性无干扰。

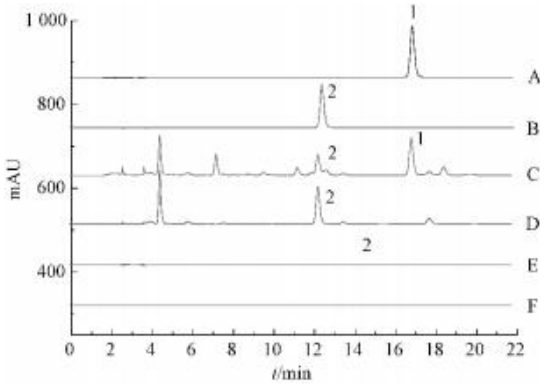

注：A～F 分别为马钱苷对照品溶液（240 nm）、绿原酸对照品溶液（327 nm）、供试品溶液（240 nm）、供试品溶液（327 nm）、阴性样品溶液（240 nm）、阴性样品溶液（327 nm）

1. 马钱苷 2. 绿原酸

1. loganin 2. chlorogenic acid

图 2 各成分 HPLC 色谱图

Fig. 2 HPLC chromatograms of various constituents

3.3.6 线性关系考察 取绿原酸对照品母液，依次稀释至 10.2、25.5、51、127.5、255、306 μg/mL，在“3.3.1”项色谱条件下各进样 5 μL测定。以溶液质量浓度为横坐标（X），峰面积为纵坐标（Y）进行回归，得方程 $Y=23\ 026X-57.274$（$r=0.999\ 7$），在 10.2～306 mg/mL 范围内线性关系良好。

取马钱苷对照品母液，依次稀释至 7、14、35、70、140、245、525 μg/mL，在“3.3.1”项色谱条件下各进样 5 μL 测定。以溶液质量浓度为横坐标（X），峰面积为纵坐标（Y）进行回归，得方程 $Y=11\ 345X-11.359$（$r=0.999\ 9$），在 7～525 mg/mL 范围内线性关系良好。

3.3.7 稳定性试验 取同一供试品溶液，于 0、2、4、8、12、24 h 在“3.3.1”项色谱条件下进样测定，测得绿原酸、马钱苷峰面积 RSD 分别为 0.24%、0.14%，表明供试品溶液在 24 h 内稳定性良好。

3.3.8 精密度试验 精密吸取供试品溶液 5 μL，在“3.3.1”项色谱条件下进样测定 6 次，测得绿原酸、马钱苷峰面积 RSD 分别为 0.11%、0.17%，表明仪器精密度良好。

3.3.9 重复性试验 精密称同一批供试品约 0.5 g，共 6 份，按“3.3.3”项下方法制备供试品溶液，在“3.3.1”项色谱条件下进样测定，测得绿原酸、马钱苷含有量 RSD 分别为 1.54%、1.47%，表明该方法重复性良好。

3.3.10 加样回收率试验 取含有量已知的同一胶囊 9 份，加入对照品溶液（绿原酸 0.6 mg/mL、马钱苷 1.3 mg/mL），按“3.3.3”项下方法制备供试品溶液，在“3.3.1”项色谱条件下进样 5 μL 测定，计算回收率，结果见表 5～6。

表 5 绿原酸加样回收率试验结果

Tab. 5 Results of recovery tests for chlorogenic acid

取样量/g	原有量/mg	加入量/mg	测得量/mg	回收率/%	平均回收率/%	RSD/%
0.100 9	0.602 9	0.3	0.912 2	103.11		
0.100 8	0.602 9	0.3	0.899 9	99.01		
0.101 4	0.602 9	0.3	0.900 9	99.32		
0.101 0	0.602 9	0.6	1.199 1	99.37		
0.101 4	0.602 9	0.6	1.197 2	99.04	100.80	1.79
0.100 8	0.602 9	0.6	1.218 5	102.60		
0.101 1	0.602 9	0.9	1.508 1	100.58		
0.101 7	0.602 9	0.9	1.533 7	103.43		
0.100 5	0.602 9	0.9	1.510 2	100.81		

表 6 马钱苷加样回收率试验结果

Tab. 6 Results of recovery tests for loganin

取样量/g	原有量/mg	加入量/mg	测得量/mg	回收率/%	平均回收率/%	RSD/%
0.100 9	1.310 8	0.65	1.957 8	1.00		
0.100 8	1.310 8	0.65	1.933 7	0.96		
0.101 4	1.310 8	0.65	1.951 5	0.99		
0.101 0	1.310 8	1.30	2.572 9	0.97		
0.101 4	1.310 8	1.30	2.566 7	0.97	98.67	2.41
0.100 8	1.310 8	1.30	2.605 5	1.00		
0.101 1	1.310 8	1.95	3.234 5	0.99		
0.101 7	1.310 8	1.95	3.339 5	1.04		
0.100 5	1.310 8	1.95	3.225 2	0.98		

3.3.11 样品含有量测定 取 5 批胶囊内容物，每批 0.5 g，按”3.3.3”项下方法制备供试品溶液，吸取对照品、供试品溶液各 5 μL，在”3.3.1”项色谱条件下进样测定，计算含有量，结果见表 7。

4 讨论

本实验对薄层色谱条件进行筛选时，采用乙酸丁酯-甲酸-水体系，发现马钱苷、绿原酸 R_f 值分别为 0.088、0.188，分离度不高；展开体系中有丙酮、甲醇等极性溶剂可提高 R_f 值，但加入前者

表 7 各成分含有量测定结果

Tab. 1 Results of content determination of various constituents

取样量/g	绿原酸峰面积	绿原酸含有量/%	平均值/%	马钱苷峰面积	马钱苷含有量/%	平均值/%
0. 500	2 991. 1	0. 662		3 030. 5	1. 341	
0. 501	3 019. 5	0. 668		3 054. 9	1. 351	
0. 501	3 038. 5	0. 672	0. 662	3 088. 9	1. 366	1. 341
0. 500	2 979. 4	0. 659		2 993. 6	1. 324	
0. 500	2 923. 7	0. 647		2 988. 8	1. 322	

时极性过大，分离度不高，拖尾现象严重，展开时间较长，而加入后者时成分分离度良好，最终确定乙酸丁酯-甲醇-甲酸-水（7∶1∶2∶1）作为展开条件。然后，对不同点样量（3、5、8、10 μL）进行考察，发现点样量越大条带越明显，但超过 5 μL时会影响分离效果，故选择 5 μL。接着，对不同条带宽度（2、4、6、8、10 mm）进行考察，发现条带越小，色谱图越窄，不能较好分离，故选择 10 mm。再对展开距离、温度、湿度进行考察，发现三者对薄层色谱图均无明显影响。

本实验对 HPLC 色谱条件进行筛选时，考察流动相甲醇-0. 04% 磷酸、乙腈-0. 1% 甲酸、乙腈-0. 04%磷酸，发现乙腈-0. 04%磷酸洗脱时有效成分分离效果最好，再对其进行优化，确定梯度洗脱比例。结果显示，绿原酸、马钱苷保留时间适当，峰形良好，分离度高。

参考文献:

[1] 国家药典委员会. 中华人民共和国药典: 2015 年版一部[S]. 北京: 中国医药科技出版社，2015: 193.

[2] 贾献慧，李 静，张永清. 忍冬藤化学成分研究进展[J]. 山东中医杂志，2015，34(8): 641-643.

[3] 张 聪，殷志琦，叶文才，等. 忍冬藤的化学成分研究[J]. 中国中药杂志，2009，34(23): 3051-3053.

[4] 赵娜夏，韩英梅，付晓丽. 忍冬藤的化学成分研究[J]. 中草药，2007，38(12): 1774-1776.

[5] 马 荣，殷志琦，张 聪，等. 忍冬藤正丁醇萃取部位的化学成分[J]. 中国药科大学学报，2010，41(4): 333-336.

[6] 纪瑞锋，刘素香，王文倩，等. 忍冬属植物环烯醚萜类成分研究概况[J]. 中草药，2012，43(6): 1226-1232.

[7] 齐乐辉，杨连荣，尹 蕊，等. 忍冬藤成份分析及在抗菌消炎等方面的研究进展[J]. 黑龙江科技信息，2010(3): 207.

[8] 胡若琪，饶娴宜. 獐牙菜甙对 *D*-氨基半乳糖性甙损伤保护作用的实验研究[J]. 临床肝胆病杂志，1988，4(3): 27.

[9] 徐英辉，申 茹，刘道军. 正交实验法优选忍冬藤中绿原酸和马钱苷的提取工艺研究[J]. 汕头大学医学院学报，2017，30(3): 139-140，155.

[10] 肖成燕，朱 毅，董 志. 水黄皮胶囊剂的制备工艺和质量标准[J]. 中成药，2016，38(1): 200-203.

[11] 国家药典委员会. 中华人民共和国药典: 2015 年版四部[S]. 北京: 中国医药科技出版社，2015.

以职业能力为导向的高职药品生产技术专业“药物制剂设备”课程标准制定研究

申　茹　梁　可　彭碧芬　徐英辉*
（惠州卫生职业技术学院，广东 惠州 516000）

【摘　要】“药物制剂设备”课程作为高职药品生产技术专业的重要核心课程之一，主要培养学生的制药技能，让学生系统学习制药设备的操作和维护，是一门综合性较强的技术学科。本研究结合惠州卫生职业技术学院药品生产技术专业人才培养方案及专业特色，以“药物制剂设备”课程为例，从课程定位、课程设计理念和思路、课程衔接、课程目标、教学实施、考核与评价等方面探讨基于职业能力培养的高职课程标准制定策略。

【关键词】药物制剂设备　课程标准　职业能力
DOI:10.19494/j.cnki.issn1674-859x.2022.06.007

教育部《关于深化职业教育教学改革全面提高人才培养质量的若干意见》（教职成〔2015〕6号）明确指出：完善教学标准体系，积极开发与国际先进标准对接的专业教学标准和课程标准[1]。课程标准是一门课程教学组织实施的指导性文件，包括课程定位、课程目标、教学内容、考核方式等，在高职专业课程中有着举足轻重的地位[2]。惠州卫生职业技术学院药品生产技术专业于2017年开办，现作为该校药学专业群两翼之一，发挥着不可替代的作用。该专业精准对接药品生产企业，培养药品生产操作、质量管理、质量检验岗位技能型人才。本研究以药品生产技术专业为例，将职业能力培养贯穿专业课程体系，制定“药物制剂设备”课程标准，进一步推动高职职业教育健康、协调发展，系统培养适应新时期经济社会发展需要的药品生产技术技能型人才[3]。

1　课程定位

“药物制剂设备”是高职药学、药物制剂技术、药品生产技术专业的一门重要的专业课程。课程的主要内容是以药物制剂生产过程中各岗位所需要的知识和技能为依据，以生产流程为主线，介绍常见的固体制剂、半固体制剂、液体制剂、无菌制剂和传统中药制剂等生产过程中制剂设备的结构、工作原理、设备操作和维护规程[4]。通过该课程的学习，学生可以掌握药物制剂设备的基本理论、基本知识和实操技能，为进入药品生产一线奠定良好的基础。

2　课程设计理念和思路

根据药品生产技术专业人才培养方案，依据《中华人民共和国职业分类大典》中药物制剂工职业群的要求，结合企业岗位需求，遵循“知识、技能、素质并行”的原则，以就业为导向，以能力为本位，以职业实践为主线，以项目化教学为主体，引入新知识、新方法和新技术，对教学内容进行整合和提升。将真实工作任务引入项目化教学，根据《药品生产质量管理规范》（GMP）的要求进行授课，根据技能大赛评分标准、药物制剂生产“1+X”职业等级证书考核标准进行考核评价[5]，重构了模块化内容、项目式实施、任务式驱动的“岗课赛证融通”课程体系，采用“探、学、践、拓”多步联动能力训练模式，采取理实一体化、线上线下混合式教学的方式，使学生“做中学、学中做、做中悟”，培养学生在制剂生产过程中设备操作的实践技能，并

基金项目：1. 惠州市2019—2020年度职业院校教育科学研究课题（项目编号：2020hzzjkt08）；2. 广东省职业技术教育学会第四届理事会科研规划项目2021—2022年度课题（项目编号：202103G171）；3. 2018年广东省高等职业教育品牌专业建设项目（项目编号：100）。

建立起工作任务与岗位技能、相关理论及职业知识的联系，在强化培养、训练学生职业岗位技能的同时，注重培养学生在复杂工作过程中对出现的问题能做出判断并采取正确行动的综合职业能力，注重培养学生在职业情境中“药德为先、药规为本、药技为重”的职业素养。

3 课程衔接

“药物制剂设备”是药品生产技术专业的主干核心课程，前期课程有“有机化学”“仪器分析”“生物化学”“天然药物化学”“药物制剂技术”“病原生物与免疫学基础”等。

开设本门课程需要以下知识或技能，故对选修课程的建议及要求如下。

（1）常见制剂的生产工艺流程。建议“药物制剂技术”课程要求学生掌握每个常见剂型的制备工艺流程。

（2）设备操作以及标准操作程序（SOP）。建议“仪器分析”课程和“有机化学”课程要求学生熟练掌握称量、配液等实验操作技能，具备动手操作能力。

（3）中药提取、浓缩等中药前处理内容。建议“天然药物化学”课程要求学生掌握中药有效成分的提取、浓缩、分离和纯化方法等内容。

（4）灭菌方法和培养基操作。建议“病原生物与免疫学基础”课程和“生物化学”课程要求学生掌握培养基配制和超净工作台的使用、灭菌等内容。

4 课程目标

4.1 知识目标

（1）掌握常见药物制剂设备的主要结构和工作原理。

（2）熟悉常见药物制剂设备的工艺流程、工序质量控制点和方法。

（3）了解制药设备分类、制药设备确认与验证。

4.2 技能目标

（1）能按照药物制剂生产中常见设备标准化流程进行操作。

（2）学会药品生产常见药物制剂设备的维护和保养。

（3）学会识别药品生产中常见的设备故障，分析故障原因并找到解决方法。

（4）能认真观察、记录实验现象，会分析实训结果，并写出实训报告。

4.3 素质目标

（1）具有专业应有的良好的职业道德、科学的工作态度。

（2）培养较强的团结协作能力和勇于奉献的精神。

（3）培养科学的思维能力和严谨的工作作风。

（4）培养安全意识、质量意识和环保意识。

5 教学实施

5.1 教学内容安排

按照高职药品生产技术专业课程目标和工作任务要求，结合学生的认知特点和“1+X”职业等级证书考核标准确定课程内容，授课中突出知识性、实践性和应用性，技能培养注重体现“以专业人才培养目标为依据，以岗位需求为导向，以增加学生就业创业能力为核心，以职业能力培养为根本”的职业教育理念。本课程开设在第四学期，共54学时，其中理论课28学时、实验课26学时（表1）。

表1 “药物制剂设备”课程内容安排

课程内容	学时数		
	理论	实验	合计
认识制药设备	2	2	4
固体制剂生产设备	10	10	20
液体制剂生产设备	4	4	8
无菌制剂生产设备	6	4	10
传统中药制剂生产设备	4	4	8
半固体制剂生产设备	2	2	4
总计	28	26	54

5.2 教学方法与手段

本课程围绕高技能人才培养要求，进行“课岗对接，课证融合，课赛融通”的一体化教学设计。针对主线任务，采用“探、学、践、拓”多步联动能力训练模式，在实施过程中化繁为简、化抽象为具体，以“任务驱动法”为主，辅以项目教学法、直观教学法、案例教学法、四阶段教学法、仿真训练法等，在理实一体化教学环境中

进行教学，实现“做中学、学中做、做中悟”。用最适合学生实际的教学方法，传授给学生最新的、最能满足企业行业需要的知识、能力和素养，培养学生的自学能力、知识拓展能力和创新能力，进而助推学生从“就业导向”迈向“企业需求导向”，达到以学生为中心、培养学生综合素质的教学目的。

5.2.1　任务驱动法

“药物制剂设备”课程的主要内容是各类制剂设备的结构、原理、操作使用、维护保养等。运用任务驱动法，先给学生布置任务，然后学生分成小组，自主选择一台设备，根据制定的评分细则完成任务，最后教师进行点评，调动学生的积极性，提高学生的能动性，培养学生的团结协作能力[6]。

5.2.2　项目教学法

“药物制剂设备”课程以药物制剂岗位操作技能标准为教学目标，项目教学法通过引导学生行为使学生完成既定的学习任务，让学生参与具体项目的设计和实施，激发学生的学习兴趣，充分体现以学生为中心的原则。使学生在探寻项目实施过程中遇到具体问题时[7, 8]，能够分析并学会解决问题，不断提升学生的实践能力和综合素质。

5.2.3　直观教学法

“药物制剂设备”课程涉及制剂设备的组成、结构、工作原理和不同机型的制备工艺等内容，传统教学方法耗费时间较多，学生理解较难。采用实物直观等手段将学生生疏、难以理解的知识点表现出来，可以吸引学生的注意力，激发学生的学习兴趣[9]。此外，还可以带学生参观固体制剂车间的小试、中试等生产设备，或者在课堂上利用Flash动画或教学视频，促进课堂教学效率提高。

5.2.4　案例教学法

教师根据教学内容的不同要求，采用案例展示的方式组织学生学习和讨论，进而培养学生的学习能力。注重理论与实践相结合，通过引入药品生产和科研实例，激发学生的学习兴趣，使学生由被动变为主动，有助于提升学生的理解能力和记忆水平[10]。

5.2.5　四阶段教学法

四阶段教学法教学过程主要由“准备、示范、模仿、归纳”4个阶段组成[11]，“药物制剂设备”课程注重学生综合素质和实践能力的培养。设置各剂型设备的问题场景，先由教师示范操作程序，再让学生按步骤重复教师的操作，教师在旁观察、点评，最后布置练习让学生独立完成。

5.2.6　仿真训练法

“药物制剂设备”是一门实践性非常强的课程，考虑到学校的实验设备大多数为小型设备，无法做到与企业零对接，故采用GMP仿真实训教学，通过计算机模拟典型药物制剂生产过程进行教学[12]，引导学生查找相关资料，主动进行模拟操作，学生可以直接观察剂型的实际生产过程和设备结构，有助于提高其学习的积极性。

5.3　教学资源开发与利用

5.3.1　教材编写与使用

优先选用国家高职高专药品生产技术专业精品课程教材、教育部高职高专相关医学类专业教学指导委员会推荐教材。同时，联合企业遵循“药物制剂设备”课程性质与任务共同编写《药物制剂设备学习指导》《药物制剂设备实训讲义》等校本教材，突出“三基”（基本理论、基本知识、基本技能）、“五性”（思想性、科学性、先进性、启发性、适用性）原则，既有利于教，也有利于学[13]。

5.3.2　数字化资源开发与利用

注重课程资源和现代化教学资源的开发与利用，优化教学手段，激发学生学习兴趣，促进学生对知识的理解和掌握。不断完善教学课件，增强教学指导的针对性和可操作性。充分利用超星学习通、智慧树等信息化学习平台的任务发布、问卷调查、资源下载、作品提交、在线考评等功能；利用虚拟仿真教学平台完成各剂型的线上模拟操作，使用平台配套的教学资源进行教学；结合符合《药品生产质量管理规范》的药品生产车间等线下实训场所进行学习和训练；充分开发联合培养企业工作现场的视频资料用于教学。

6　考核与评价

课程考核包括过程性考核（占40%）和终结性考核（占60%）。立足课程的性质和特点，以药物制剂职业岗位技能要求为依据，在教学实施过程中建立教师、学生、企业专家多主体参与的人

才培养质量评价体系，采取全过程、立体化、多元化的评价方式，不仅要求学生理解知识、掌握技能，还注重培养学生运用知识解决实际问题的能力。

过程性考核包括课前预习考核（占10%）、课中学习考核（占60%）、课后拓展考核（占10%）和项目考核（占20%）。课前预习考核包括学生任务点的完成情况、课前测试结果；课中学习考核包括学生的出勤情况、随堂练习、课堂参与度等；课后拓展考核包括实验报告、微视频录制、参与话题等作业完成情况；项目考核主要包括项目测试结果。各环节根据需要分别引入学生评价、生生互评、教师评价、企业专家评价。

终结性考核包括理论考核成绩（占50%）和技能考核成绩（占50%）。技能考核主要以教师评价、企业专家评价为主，考查学生的动手能力和在实践操作过程中分析问题、解决问题的能力。

7 结语

“药物制剂设备”作为高职药品生产技术专业的核心课程，以培养“药德为先、药规为本、药技为重”的高素质人才为目标，在教学过程中遵循“重技强能，乐学致用”的教学理念。以任务为驱动，培养学生科学化、规范化、系统化完成各剂型设备使用流程等任务，熟练掌握相应的操作技能及安全生产知识。同时，将课程思政教育浸润教学全过程，同步培养学生的知识、能力、素质，培养学生的药物制剂职业能力和职业素养，为学生走上工作岗位打下坚实的基础。教师要针对药物制剂生产设备的发展和需求，逐步调整课程标准，优化教学内容，提升教学效果。

参 考 文 献

[1] 席东梅. 筑牢职业教育发展之根基：专家解读《关于深化职业教育教学改革全面提高人才培养质量的若干意见》[J]. 中国职业技术教育，2015（28）：26–31.

[2] 胡辰. 以职业能力为导向的课程标准制定研究：以“电动汽车结构与维修”课程为例[J]. 职业技术，2020，19（5）：55–59.

[3] 徐英辉，申茹，祁银德. 基于职业能力的高职药学专业课程标准探究[J]. 卫生职业教育，2021，39（11）：38–40.

[4] 杨宗发，庞心宇，蒋猛. 常用制药设备使用与维护[M]. 北京：高等教育出版社，2021.

[5] 陈晓琴. 高职课程标准与职业岗位技能标准对接探究[J]. 职教论坛，2011（14）：16–18.

[6] 庞心宇. 多种教学方法在高职“药物制剂设备”教学中的综合应用[J]. 高教学刊，2017（2）：79–81.

[7] 孔明霞. 基于项目化教学的药物制剂技术课程教学实践[J]. 黑龙江科学，2021，12（17）：118–119.

[8] 尚平. 项目教学法在《药物制剂与设备》课程中的应用[J]. 科技风，2018（10）：17.

[9] 宋新焕，张晓军. 技工院校药物制剂设备课程教学方法初探[J]. 职业，2019（36）：58–59.

[10] 布秀娟，刘畅. “药物制剂设备”课程的教学探索[J]. 现代职业教育，2018（1）：106.

[11] 王小娟. 四阶段教学法在汽车类专业课程中的创新应用：以“汽车发动机构造与维修”课程为例[J]. 汽车维护与修理，2017（16）：53–55.

[12] 方伟光，许阳，胡文林. 虚拟仿真平台辅助的药物制剂实训课程教学模式构建与探讨[J]. 安徽化工，2020，46（1）：128–131.

[13] 孙绍华. 高职教材管理改革的探索[J]. 辽宁税务高等专科学校学报，2006（1）：73–74.

***通讯作者：徐英辉　电子邮箱：**21806850@qq.com

高职高专院校药剂学教学方法改革探讨与实践

申茹，徐英辉，梁可，余巧，莫颖华
(惠州卫生职业技术学院，广东 惠州 516000)

[摘 要]药剂学为高职高专药学专业的主干课程之一，具有实践性、综合性强等特点。药剂学中剂型繁多，记忆量大，学生学习难度较大，为了培养学生的学习兴趣，提升学生学习能力、实践能力和创新能力等综合素质。本文结合我院专业特色，对药剂学课程教学方法进行改革和探讨。

[关键词]药剂学；教学方法；改革
[中图分类号]TQ [文献标识码]A [文章编号]1007-1865(2021)07-0235-02

Discussion and Practice on Teaching Method Reform of Pharmaceutical in Higher Vocational Colleges

Shen Ru, Xu Yinghui, Liang Ke, Yu Qiao, Mo Yinghua
(Huizhou Health Sciences Polytechnic, Huizhou 516000, China)

Abstract: Pharmaceutics is one of the main courses of pharmacy specialty in higher vocational colleges, which has the characteristics of practicality and comprehensiveness. In pharmacy, there are many dosage forms, large memory, and students are difficult to learn. In order to cultivate students ' interest in learning, improve students' comprehensive quality of learning ability, practical ability and innovation ability. In this paper, the teaching method of pharmaceutics was reformed and discussed according to the specialty characteristics of our hospital.

Keywords: pharmaceutics；teaching method；reform

教高[2000]2 号《教育部关于加强高职高专教育人才培养工作的意见》文件中明确指出：“高职高专教育是我国高等教育的重要组成部分，其任务是培养拥护党的基本路线，适应生产、建设、管理、服务第一线需要的，德、智、体、美等方面全面发展的高等技术应用性专门人才[1]。”高职高专院校药剂学课程是研究药物制剂的生产理论、生产技术、质量控制与合理应用等内容的综合性应用技术科学[2]。药剂学在药学领域中的地位是举足轻重的，不仅是转换枢纽的作用，还对其他学科起到了承上启下的作用。药品是一类特殊商品，使用过程中与人的生命息息相关，要求从事药品生产、调剂、质控的人员必须熟练掌握规范的操作程序，这就需要药学专业技术人员具有扎实的理论知识和熟练的操作能力，才能满足社会对药学人员的需求。

以往药剂学都是传统教学方法，每节课信息量大，系统性差，学生缺乏自主学习的动力，学习兴趣差，参与互动少。运用信息化教学手段，改变传统的教学方法，充分调动学生学习的主观能动性，提高学生课堂参与度，激发学生自主学习的积极性。笔者多年从事药剂学理论和实践教学工作，并结合学科特色，对药剂学教学方法进行改革和探讨，旨在不断提高教学效果，培养药学专业技术应用型专门人才。

1 问题导入式教学—引发学生思考

提高学生兴趣是一节课成功的开始，学习兴趣离不开教师的有效引导，以生活中常见的事例为例，让学生充分思考并进行解答，如同学们小时候有没有吹过泡泡，用什么吹？衣服脏了怎么办？用什么来清洗，为什么肥皂和洗衣粉具有去污作用，学生们以问题为学习起点，积极思考、展开讨论，有效的活跃了课堂气氛，充分提高了学习的积极性。针对学生讨论结果，教师进行重点总结，引出课堂所学内容为表面活性剂的概念和应用。再比如讲解到固体制剂流动性时，提出问题：“面粉和细沙哪个流动性比较好？分别将面粉和细沙倒入漏斗中想象物料通过的情况？物料流动性会对剂量造成影响吗？”学生充分思考、讨论结束后，主讲教师对流动性的概念和表示方法进行讲解。将日常生活中的例子转化成与教学内容想匹配的问题，可以充分激发学生分析问题、探究真相的能力，灵活运用所学理论知识解决实际问题。

2 多媒体教学—创设生动的教学情境

药剂学课程重点为各种剂型的特点及制备工艺，难点为各种制药设备的工作原理、操作流程。传统的教学方法以讲授为主，较为枯燥，学生难以生动形象的理解和掌握相应的知识点。多媒体教学可以使教学内容生动形象，教学情境有趣直观，有效弥补传统教学方法的缺点和不足。将剂型中难懂和难学的内容制作为多媒体课件，采用图片、Flash 动画、视频、声音等多媒体信息，使教学内容更跃然纸上、扣动学生心弦，激发学生的独立思考能力、思维能力、想象能力，学生通过观看，理解剂型的制备过程和注意事项[3]，明确作为药学专业技术人员责任重大，更能激发学生的学习使命和对生命的理解。

3 案例式教学—理论联系实践

案例式教学法起源于美国，其特点是通过分析典型案例讲解相应的理论知识[4]。在教学过程中，对应知识点设置相关案例，通过案例分析，培养学生独立思考、自主探究、理论联系实践的能力。以就业为导向，以提高岗位能力为目的，更需要教师将经典案例讲授给学生，加深对知识的认知度。药剂学中的注射剂是常见剂型之一，制备要求严格，尤其是药品必须经过灭菌处理。2006 年发生的“欣弗事件”导致出现严重不良反应，致人死亡，经过调查发现是注射剂制备过程中缩短了相应的灭菌时间，擅自降低了灭菌温度，同时增加了灭菌柜的装药量，完全没有按照要求的工艺参数灭菌，导致灭菌效果受到影响。通过真实的案例分析，不仅可以使学生全面掌握“热原的危害、注射剂灭菌的作用”等知识点，而且加深了学生们对“制剂安全、有效、稳定”的理解、对“药学专业技术人员的社会责任和职业道德”感同身受。

在讲授注射剂章节时，以“齐二药”药害事件案例导入，引导学生自主分析齐齐哈尔第二制药厂药害事件主要原因为药物溶剂选择错误，以工业原料二甘醇代替了丙二醇，导致药物投入市场后，出现严重不良反应，13 人因此死亡。真实的案例不仅让学生牢固掌握所学重点难点，更使学生们意识到作为药学专业技术人员的社会责任，应具备严谨认真的工作态度[5]。

4 对比式教学—便于学生记忆

药剂学中剂型有几十种，每种剂型都要讲授概念、特点、分类、制备方法、质量控制等内容，应用传统的教学方法记忆，相似的知识点也容易混淆，学生学习效果差。采用对比式教学法[6]，对不同剂型的特点及制备方法等教学内容进行列表对比，不仅可以使内容简单化，学生对知识点的印象深刻，还可以通过举一反三，达到事半功倍的效果，提高学生的自我学习的能力。比如在讲解液体制剂制备方法时，可以将溶液剂、芳香水剂、醑剂、糖浆剂、甘油剂、混悬剂、乳剂的概念和特点进行列表，找到相同点和不同点，便于同学们对知识的理解和巩固。在表面活性剂的讲解中，内容较多，不易理解，可以将表面活性剂的分类、特点、特性和应用进行对比，加深对内容的理解，提高学习效率。

[收稿日期] 2021-01-28
[基金项目] 广东省高职教育医药卫生专业教学指导委员会 2018 年教育教学改革课题(2018LX068)
[作者简介] 申茹(1981-)，女，黑龙江人，硕士研究生，主要研究方向为药学教育教学。

5 微课—提高学习效率

微课是微课程的简称，由美国新墨西哥州圣胡安学院率先提出并开展实践研究[7]。微课也是“信息化时代”的历史产物，它是现代教学手段中起到举足轻重的作用，它具有主题突出、短小精悍、资源丰富多样等特点。微课是将理论和实验课上的难点、重点拍摄成 5-10 分钟的短片，学生只要拿出手机便能在网上自由点击学习，由于内容简便易懂，重点突出，学生容易巩固接受，根据视频中的讲解，独立思考，提出疑问。

药剂学是一门理论与实践紧密结合性学科，是培养学生所需的专业知识和岗位技能。剂型的制备方法和设备讲解中学生理解难度较大，理论知识不扎实如何进行实践操作呢，通过微课程不仅可以将剂型制备工艺流程、设备的操作过程和工作原理展示给学生，简单灵活，可反复利用。尤其在实验教学中发挥更大的作用。传统的实验教学方式是老师先示范讲解，学生按部就班的操作，不经大脑思考，很容易遗忘，则会出现做一步看一步，甚至有些同学因实验步骤繁琐，实验量大而手忙脚乱，不仅影响实验进度，还得不到准确的实验结果，最终草草了事，学生的动手操作能力和思考能力得不到充分锻炼。有了微课后，实验前将视频发送给实验小组，小组成员先了解实验步骤，并分析讨论实验中的关键环节，这样学生不仅可以的高效的完成实验，更有助于实验过程中团队精神的培养。实验全部结束后，学生需要完成实验项目思考题部分，书写实验报告，教师要对结果进行点评，并评选出优秀作品。

6 Moodle 平台—实现碎片化学习

随着互联网信息技术的迅速发展，信息工具的普及，教育信息化思想已经深入人心，各种网络教学平台相继出现。Moodle 教学平台包括课程管理、教学资源、实验教学、专题讲座、在线测试、期末考核等模块，具有操作简单、使用方便等特点[8]。作为高职高专教师，要想培养药类职业人，就要跟随时代步伐，与时俱进，采用现代化的的网络教学平台，促进师生互动，强化学生的自学能力，利用碎片时间随时学习，提高教学质量。

Moodle 教学平台可以为学生提供丰富多样的教学资源，灵活自主的学习时间，信息化的教学模式，学生通过移动终端，查阅相关资料，独立完成教师课前布置的学习任务，课中认真理解，培养学生的实践能力和创新意识，变被动学习为主动学习，自主学习效果显著。

7 总结

综上所述，高职高专药剂学课程教学，应根据就业岗位的需求着手，细化典型工作任务，积极倡导问题导入式教学、多媒体教学、案例式教学、对比式教学、微课等教学方法，应用 Moodle 教学平台，增强学生的动手操作能力、综合运用能力，提升学生职业技能和综合素质。通过教学方法的改革，使学生除具有扎实的专业知识外，更具有分析问题、解决问题的专业实践能力，不断提高药剂学学科的教学水平[9]，培养理论与实践能力具备的应用型人才。

参考文献

[1]匡瑛．“双高计划”背景下高职高等性意涵及其实现[J]．高等工程教育研究，2020(1)：148-152.
[2]张琦岩．药剂学[M]．第 2 版．北京：人民卫生出版社，2013.
[3]廖乃英，黄欣碧．“3+2”高职药剂学教学内容与方法探讨[J]．广西教育，2014(3)：139-140.
[4]Kanfam DM，Mann KV．Basis sciences in problem based learning and conventional carricula：students’ attitudes[J]. Medical Education，1997，31(3)：177-180.
[5]申茹，徐英辉，莫颖华，等. 高职院校药学专业药剂学教学改革探讨[J]. 广东职业技术教育与研究，2015(6)：68-70.
[6]鄢海燕．药剂学教学改革与探索[J]．中国医药指南，2013，11(24)：742-743.
[7]胡铁生，黄明燕，李民．我国微课发展的三个阶段及其启示[J]．远程教育杂志，2013(4)：36-42.
[8]王冰寒，颜巧元，朱琴，等．基于 Moodle 的护理科研课程网络学习平台的设计与应用[J]．护理教育，2017，17(8)：1052-1056.
[9]邢蓉，陈根德，王秀．药剂学教学方法改革的探讨与实践[J]．中国药事，2010，24(10)：1027-1029.

（本文文献格式：申茹，徐英辉，梁可，等．高职高专院校药剂学教学方法改革探讨与实践[J]．广东化工，2021，48(7)：235-236）

(上接第 238 页)

课堂活动较少，实践内容不足，上课效果一般；其次，当前的大多教材都是按照传统的理论知识体系进行内容架构，而不是根据学生学情和实际应用来编排知识，这就会造成学生上课时脱节，甚至产生厌学等情绪。

目前，关于药学英语相关的教材数量一般，但适合高职药学类专业的教材选择较少，而适合本院师生的教材更是少之又少。因此，出版一本适合我校学生的药学英语校本教材已是迫在眉急。

2.2 学生学习积极性较差

我院的高职生生源结构较为复杂，素质和水平参差不齐。他们的英语基础普遍比较薄弱，英语课的学习兴趣弱，尤其是对于有一定难度的《专业英语》。这两个因素导致学生的学习积极性较差。

2.3 教学方式单一

目前课堂主要的授课方式就是讲授法，以教师讲解为主，学生做笔记。这种方式仍然属于“填鸭式教学”，因此很难提升学生的学习兴趣。

3 我校药学《专业英语》课程改革方向

3.1 “以实用为导向”开发立体化教材

在现有的医药英语教学内容的基础上融入四六级考试和专升本考试的相关内容，以学生实用为导向，开发一本对于学生英语技能考试具有实际指导作用的融合性《药学实用英语》立体化教材。教材分为三大模块，一是基于《医药英语》第 2 版的教材内容，选择药物历史(History of Medicine)、制药行业(Pharmaceutical Profession)和药品管理(Management of Medicine)等部分内容，二是专升本英语相关内容，三是 CET-4 相关考试内容。

3.2 “以学情为基础”优选教学内容

学生对于药学《专业英语》的学习兴趣不高，主要的原因是基础薄弱和教材内容难度较大。因此根据学生学情选择合适的教学内容，比如重点讲解中药历史(History of TCM)、西药历史(History of Western Medicine)、中药(Traditional Chinese Medicine)等学生熟悉的传统文化进行英语教学，提升学生学习兴趣，同时也可以有效地提高课堂效率。同时在教学过程中注入思政教学理念，大力培养学生的爱国主义情怀。此外，在每节课的教学中，教学生拼读单词，巩固音标等基础内容，帮助基础差的同学有所进步。同时选择四级考试真题中的完形填空和阅读文章给学生逐句分析，为学生考级做好铺垫。

3.3 “以学生为主体”多元教学手段，丰富课程实践

课堂教学不能只是一味的灌输，而应该充分发挥学生的主体作用。课堂上可采用小组教学，每一小组进行一段课文的解析，比如对药品说明书进行解读或者翻译；其次，以小组为单位布置英文简历的书写，并进行面试者与面试官的轮流扮演交流，将英文简历活学活用。同时，把模拟购药情景、参观中药历史名人文化墙并进行交流等增设为实践教学内容，打造英语生活剧。一个学习小组成员可分别扮演患者、导购员、执业药师、收银员、导游等角色，教师规定基本要素后，让学生自由发挥，小组间进行评比，以学生为主体进行教学，提高学习积极性，丰富课程实践。

参考文献

[1]黄新蓉．高职院校药学《专业英语》的教学改革研究[D]．湖南师范大学，2014.

（本文文献格式：李绣菊，黄芳，李玉龙，等．高职院校药学《专业英语》课程改革研究——以铜仁职业技术学院为例[J]．广东化工，2021，48(7)：237-238）

药品生产技术专业人才需求与职业岗位能力分析

申 茹,徐英辉,梁 可,莫颖华
(惠州卫生职业技术学院,广东 惠州 516000)

摘 要:通过对药品生产技术专业的人才需求分析,明确药品生产企业的主要工作岗位及职业能力,从而确定本专业的人才培养目标,构建与企业岗位深度融合的人才培养模式,以及以职业能力为核心的专业课程体系。

关键词:药品生产技术专业;人才需求;职业岗位能力
中图分类号:G420 文献标识码:A 文章编号:1671-1246(2019)04-0027-02

药学事业是与人民生命和健康息息相关的事业,要求从业人员必须具备高超的药学技能和良好的职业道德,尤其在药品生产环节,不仅具有娴熟的药品生产专业技能,还要有严谨规范的管理能力[1]。因此,药品生产技术专业既要适应国家政策需要,也要满足学生的就业需求。如何制订该专业的人才培养模式、构建专业课程体系成了当前亟待解决的问题。本文针对药品生产技术专业的人才需求、岗位需求和职业能力分析,对医药企业和医疗机构等进行充分调研,确定该专业的培养目标和专业定位。

1 调研背景

随着医药科技的发展,人们生活水平不断提高,自我保健意识不断增强,对药品安全也越发关注。以近十几年内发生的药害事件为例,2006 年的"欣弗"事件引起了社会各界的关注,同年齐二药"亮菌甲素注射液"事件震动全国,把药品安全问题提上了议事日程。生产环节关系到药品质量,所以要生产高质量、安全、有效的药品,必须从生产环节抓起。因此培养高素质的生产技能型人才,是医药卫生类高等院校义不容辞的责任。

为使药品生产技术专业更好地适应市场需求,课程教学更适应岗位需求,对相关行业发展现状与趋势、岗位设置情况及变化趋势进行了调研。本次调研对象为广东省医药企事业单位,包括药品生产企业、药品经营企业等,调研方式为实地调研,采取问卷调查与行业负责人交谈、个别访谈、参观交流、专家座谈等方式。其中包括药品生产企业 5 家,医疗机构 3 家,药品经营企业 5 家,毕业生 40 人,实习生 40 人。调研内容包括就业单位对学生知识、能力和素养要求的认知程度,从事药品生产、质量检验、质量管理等岗位能力和工作任务剖析,并对该专业教学模式和人才培养方案等方面的建议等。

2 药品生产技术专业人才及岗位需求情况分析

2.1 人才需求分析

设置药品生产技术专业是落实国家学科建设与人才发展战略,培养国际化紧缺人才的需要[2]。该专业目前在广东省只有 6 所高等职业院校开设。经过对广东省医药行业调研,药品生产技术专业毕业生就业方向主要集中在药品生产、药品检验和药品销售等领域。

广东省大、中、小型药品生产企业共有 730 多家,其中有 50 多家为股份制医药企业,中药饮片厂 250 多家,注册许可的医疗器械生产企业近 900 家,药品批发企业 1 600 多家,零售药店 53 000 多家,学生就业前景非常广阔。

2.2 岗位需求分析

药品生产技术专业现只有高职层次,呈现供不应求的状态。通过对用人单位对人才学历水平的要求进行调查,22.5%的用人单位需要本科及以上学历人才,70.8%的用人单位需要高职高专学历人才,仅有 5.5%的用人单位需要中专学历人才,1.2%的用人单位对学历无要求。用人单位本专业就业毕业生主要选择以下几个岗位:一是药品生产企业生产操作、质量管理、质量检验岗位;二是药品经营企业中药调剂、药品营销岗位。为提高学生专业知识和实践能力水平,学院在人才培养过程中应加大实训力度,使学生的动手操作能力、分析问题和解决问题能力得到较大提高,才能在制药岗位上得心应手。

2.3 企业对药品生产技术专业人才素质和能力的要求

了解企业对人才能力的需求是本专业人才培养方案和教学计划制订的依据。通过对制药企业中技术工人、车间管理人员及生产管理人员进行问卷调查,结果显示,制药企业对人才的能力和专业素质要求包括剂型生产操作能力、制药设备操作能力、制剂生产在线质量控制能力、生产后清场能力、生产文件记录能力、GMP 相关知识、生产工艺设计能力、创新能力、生产过程中解决问题能力,除此之外还要具有良好的药学职业道德、敬业精神、实事求是的态度和责任意识。

2.4 药品生产技术专业职业岗位与职业能力要求分析

通过调研,分析企业对药品生产技术专业人才素养、知识和能力的需求,制订该专业的职业岗位与能力要求见表 1。

3 讨论

根据专业的人才需求、岗位需求和职业岗位能力分析来看,药品生产技术专业应着重培养与广东制药行业企业相适应的,满足社会就业岗位需求,具有较高职业道德和素养,能从事药品生产、药品检验、药物制剂设备使用与维护、药品营销等工作的高素质技能型专门人才。

以药品生产技术岗位群能力要求为基础,确定核心工作岗位、职业能力要求,构建课程体系,建议该专业核心课程可开设:实用药物学基础、药物制剂技术、药物检测技术、药物制剂

基金项目:惠州卫生职业技术学院"创新强校工程"(2016—2020 年)项目"药品生产技术专业教学标准研制"(CQ2017—3.1.82)

中高职护理专业基础医学课程体系衔接探讨

张　敏
（韶关学院医学院，广东　韶关　512026）

摘　要：目前中高职基础医学课程体系存在课程重复问题，如何进一步完善中高职护理专业基础医学课程体系衔接，关键在于科学设置、有效整合与衔接课程模块。立足护理专业，结合就业实际与教学现状，统筹考虑中高职护理专业基础医学课程设置，建议将基础医学课程解剖学和组织学与胚胎学整合为正常人体结构，将生理学和生物化学整合为正常人体功能，将病理学、病原生物学与免疫学整合为疾病学基础，同时探讨整合后的课程标准。

关键词：中高职衔接；护理专业；基础医学课程；课程标准
中图分类号：G420　　文献标识码：A　　文章编号：1671-1246（2019）04-0028-03

中高职衔接是指按照建设现代职业教育体系的要求，推动中等和高等职业教育协调发展，系统培养适应经济社会发展需要的技能型特别是高端技能型人才。为适应社会经济的发展需求，2017 年国务院提出应大力发展现代职业教育和继续教育，加快培养经济社会发展急需人才，推行产教融合的职业教育模式，坚持面向市场、服务发展、促进就业的办学方向，科学确定各层次各类型职业教育培养目标，创新技术技能人才培养模式。因此，如何完善中高职衔接成为目前职业教育重点关注的课题之一。目前国内护理专业中高职衔接存在诸多问题，其中课程重复最为突出[1]。解决课程重复难题是促进中高职课程体系衔接的重点之一。国外许多国家已形成较成熟的对接模式，国内部分省份开设护理专业的高职院校近年来也逐步推进相关课程改革[2]，而我省尚待开启此项工作。因此需探索打破“以学科为中心”的教学模式，努力实现课程的有机整合，形成“以职业为基础，以能力为本位”的一体化课程体系，使学生更好地掌握医学基础知识和技能，为后续临床课程的学习及今后职业发展奠定基础[3]。

1　中高职护理专业基础医学课程体系衔接思路

我院设有中职和高职两个层次的护理专业，从就业的实际情况分析，在中高职课程体系衔接改革中应坚持以就业为导向，从学生可持续发展角度分析，认真思考基础医学课程设置问题。围绕中高职护理专业培养目标，结合临床实际护理岗位工作需求，减少重复内容的教学，加强理论与临床的联系和素质培养。

2　中高职护理专业基础医学课程体系衔接探讨

2.1　人才培养目标和指导原则

基金项目：广东省高职教育医药卫生类教学改革项目立项课题“护理专业中高职衔接医学基础课程体系的探讨与实践”（20171075）

表 1　药品生产技术专业职业岗位与职业能力要求分析

核心工作岗位及相关工作岗位	岗位描述	职业能力要求
药品生产	从事各类剂型生产和中药拣选、清洗、提取与分离以及制药设备使用和养护等工作	掌握常用剂型的生产工艺相关知识、中药前处理流程、提取和分离设备使用操作，具备药物制剂生产与技术保障能力，具备常用制剂设备使用和维护能力，具备药品生产质量管理规范相关知识，具备较强的动手操作、分析问题和解决问题能力，具备高度的责任心和科学严谨的工作态度
质量监督	从事药品生产过程质量监控和管理等工作	了解生产车间现场的清场工序，掌握药品生产安全知识，了解生产管理文件内容，能对车间药品生产全过程进行质量监控，掌握半成品的重量差异等项目检验和药品各个工序外观检查步骤，具备评价审核药品质量的能力，具备发放、整理和审核药品生产记录能力
质量检验	从事药品检验前工作以及抽样、检验操作和检验结束后管理等工作	掌握常用药物的结构特点、化学性质和分析方法，掌握试剂、试液、对照品、检验设备、容器工具的调试等准备流程，具备制定物料、产品质量和检验标准操作流程的能力，熟悉检验记录书写和出具检验报告书，具备检验结束后对检验仪器、用具清洁和维护能力
仓储、物流管理	从事药品采购、运输、入库验收、储存、养护、出库等管理工作	掌握药品供销配运知识，掌握药品性质，对药品进行分库、分区、分类放置，具备药品入库验收、贮存、养护、安全管理能力，具备正确规范填写药品购销记录能力
药品应用与服务	从事药品调剂和用药咨询与指导等工作	掌握药事管理法律法规知识，熟悉常见疾病的典型症状、病因、治疗原则和常用药物种类，掌握临床常用药物的药理作用、临床应用、用法用量、不良反应、药物间相互作用，具备处方接收、审查、调配、复核和发药能力，具备指导用药、解答用药疑难问题能力
药品营销	从事药品销售、营销服务、定价谈判、药品促销、营业推广等工作	具备预测药品销售形式、确定销售方向和方式能力，掌握常用药物的药理作用、临床应用、不良反应等知识，了解促销工具的选择和营业推广方法，具有能根据不同药品的特性分析市场和消费者心理，选择合适策略成功营销的能力

设备、药事管理与法规；专业课程可开设：生药学、天然药物化学、药物辅料与包装材料、临床医学概要、药品安全生产管理、中药制药生产技术、药学服务实务等。

参考文献：

[1]马彦，徐刚.校企合作开发的药品生产技术课程改革与实践[J].广东职业技术教育与研究，2017（1）：78-80.
[2]陶娟.浅谈高职院校开展药品生产技术专业的理由[J].现代职业教育，2016（9）：168.▲